# Taylor-Couette flow for shear-thinning fluids

S Topayev

UNIVERSITE DE LORRAINE

**Laboratoire d'Energétique et de Mécanique Théorique et Appliquée**
ECOLE DOCTORALE SIMPPÉ

# Thèse

Présentée et soutenue publiquement pour l'obtention du titre de

DOCTEUR DE l'UNIVERSITE DE LORRAINE

Mention : Mécanique et Energétique

par **Sultan Topayev**

Sous la direction de **Chérif Nouar**

# Taylor-Couette flow for shear-thinning fluids

Soutenue le 17 Decembre 2021

**Membres du jury :**

| | | | |
|---|---|---|---|
| *Directeur de thèse :* | Chérif Nouar | - | Directeur de Recherche CNRS, Université de Lorraine |
| *Président de jury :* | Sandra Lerouge | - | Professeur, Université Paris Diderot |
| *Rapporteurs :* | Innocent Mutabazi | - | Professeur, Université Le Havre Normandie |
| | Eric Serre | - | Directeur de Recherche CNRS, Université d'Aix Marseille |
| *Examinateurs :* | Cécile Lemaitre | - | Maitre de Conférences, HDR, Université de Lorraine |
| | Jan Dusek | - | Professeur, Université de Strasbourg |

# Table des matières

# Chapitre 1

# Introduction générale

Les phénomènes d'instabilité et de transition vers la turbulence revêtent une importance primordiale dans la maitrise des procédés industriels ainsi que dans la compréhension de certains phénomènes naturels en géophysique ou en astrophysique. Très souvent, les fluides rencontrés sont non-Newtoniens du fait d'une interaction non linéaire entre la micro-structure du fluide et l'hydrodynamique. Le travail présenté ici à pour objectif de contribuer à comprendre l'influence du comportement non-Newtonien sur les mécanismes d'apparition des instabilités et l'évolution vers la turbulence. Dans cette perspective, on s'est intéressé à un type d'écoulement dit de Taylor-Couette, confiné entre deux cylindres coaxiaux pouvant tourner indépendamment l'un de l'autre. On a fait ce choix en raison de la grande richesse des phénomènes rencontrés illustrée par la carte des écoulements secondaires stationnaires ou instationnaires (1.4) observés par Andereck et al. [1].

Les paramètres géométriques qui décrivent l'écoulement sont le rapport $\eta$ entre les rayons $R_1$ et $R_2$, respectivement des cylindres inérieur et extérieur,

$$\eta = \frac{R_1}{R_2}, \tag{1.1}$$

et le rapport d'aspect $L$, rapport entre la hauteur $l$ du fluide dans l'espace annulaire et l'épaisseur de l'entrefer $d$,

$$L = \frac{l}{R_2 - R_1} = \frac{l}{d}. \tag{1.2}$$

La dynamique de l'écoulement est caractérisée par les nombres de Reynolds interne $Re_1$ et externe $Re_2$,

$$Re_1 = \frac{\rho \Omega_1 R_1 d}{\mu}; \qquad Re_2 = \frac{\rho \Omega_2 R_2 d}{\mu}. \tag{1.3}$$

où $\rho$ est la masse volumique du fluide, $\mu$ sa viscosité dynamique et $\Omega_1$ et $\Omega_2$ sont les

vitesses de rotation des cylindres inérieur et extérieur.
Dans la littérature, le nombre de Taylor est aussi utilisé pour décrire l'écoulement

$$Ta = \sqrt{\frac{d}{R_1}} Re_1. \tag{1.4}$$

D'autres expressions de Ta et de $Re_1$ sont proposées dans la littérature. À faible vitesse de rotation, l'écoulement est purement azimuthale. Une particule fluide est alors en équilibre sous l'effet de la force centrifuge et du gradient radial de pression centripète. Dans le cas d'un fluide parfait, selon le critère de Rayleigh (1916) la condition nécessaire et suffisante de stabilité de l'écoulement est que la dérivée du carré du moment angulaire $M = rV_b$ où $V_b$ est la vitesse (azimuthale/de l'écoulement), soit positive dans tout l'entrefer,

$$\frac{d}{dr}(rV_b)^2 > 0; \quad pour\ tout\ r \in [R_1, R_2]. \tag{1.5}$$

Cette condition de stabilité est matérialisée dans le plan $(Re_2, Re_1)$, par la ligne de Rayleigh,

$$Re_1 = \frac{Re_2}{\eta} \tag{1.6}$$

Cette ligne est en fait située dans le demi-plan $Re_2 > 0$ (cylindres corotatifs). En dessous de cette ligne, l'écoulement est stable et au-dessus de cette ligne l'écoulement est instable. Dans le cas d'un fluide visqueux, le critère Rayleigh ne peut pas être utilisé car la viscosité à un effet stabilisant. En 1923, Taylor [2] a mis en évidence expérimentalement l'existence d'un écoulement secondaire axisymétrique schématisé par la figure 1.1 et caractérisé par des rouleaux contrarotatifs sur toute la hauteur de l'espace annulaire. Cet écoulement axisymétrique et stationnaire est appellé Taylor Vortex Flow (TVF). Une étude théorique a été développée par Taylor [2] dans le cas limite où $L \to +\infty$ et $\eta \to 1$. La valeur critique $Ta_c$ du nombre de Taylor à partir de laquelle l'écoulement de Couette circulaire bifurque vers le régime TVF a été déterminée, $Ta_c = 1708$. Les structures tourbillonnaires ont une taille pratiquement égale à cette de l'entrefer $d$. Ce qui conduit à un nombre d'onde $k \approx \pi/d$.

**Influence des paramètres géométriques**

Des corrélations empiriques sont proposées dans la littérature qui donnent le nombre de Reynolds critique en fonction du rapport des rayons $\eta$. On cite en particulier la corrélation d'Esser et Grossmann [3] :

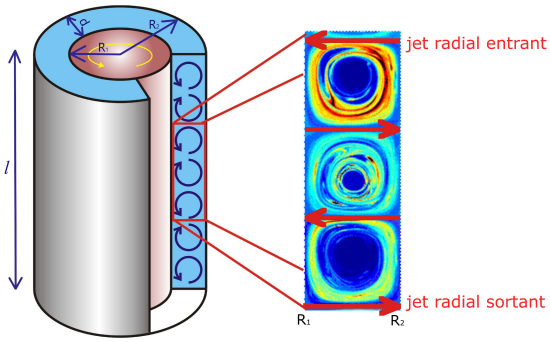


FIGURE 1.1 – Représentation schématique du régime d'écoulement de Taylor-Vortex : les jets radiaux entrant et sortant sont représentées par des flèches rouges

$$Re_c = \frac{1}{\alpha}\frac{(1+\eta)^2)}{2\eta\sqrt{(1-\eta)(3+\eta)}} \quad avec \quad \alpha = 0.1556 \tag{1.7}$$

Des résultats plus récents ont été proposés par Dutcher & Muller [4]. Dans le cas où le cylindre extérieur est fixe, la corrélation suivante est proposée.

$$Re_c = 10.81294/\eta + 41.45025/(1-\eta)^{1/2} - 11.67578. \tag{1.8}$$

Pour ce qui est de l'influence du rapport d'aspect, les résultats de la littérature indiquent que la valeur critique du nombre de Reynolds n'est pas affectée par les effets de bord lorsque $L \gtrsim 8$. La taille des structures tourbillonnaires ainsi que le sens de rotation de ces structures peut-être affecté lorsque le rapport d'aspect et très faible (Cliffe & Mullin [5]). Une étude détaillée de ce problème a été décrite par Czarny et al. [6]. Lorsque les cylindres sont de longueur finie, le profil idéal de Couette circulaire est déformé par les conditions de non-glissement aux extrêmités de la géometrie. Cette déformation est due au pompage d'Ekman dans la couche limite visqueuse qui se développe au niveau des parois rigides aux extrêmités. Globalement, la pression est pratiquement uniforme le long de l'espace annulaire. La différence entre le gradient radial de pression et la force centrifuge au voisinage de la paroi rigide génère un écoulement radial entrant. Du fait de l'incompressibilité du fluide un écoulement axial se développe au voisinage de la paroi du cylindre conduisant à la formation d'une recirculation dans le plan $(r, z)$. Par entrainement visqueux des tourbillons contrarotatifs dont l'intensité décroit exponentiellement avec la distance (Ahlers et al. [7]) sont générés. Ceux-ci vont par la suite sélectionner le sens de rotation des cellules de Taylor. Des situations particulierès se produisent lorsque le rapport d'aspect est très court (Benjamin & Mullin [8]), où les tourbillons de Taylor tournent dans le sens opposé à celui inité par les tourbillons d'Ekman.

**Influence de la montée en vitesse du cylindre intérieur**

Burkhalter et Koschmieder [9] ainsi que Lim et al. [10] ont démontré expérimentalement la non-unicité des écoulements TVF qui pouvaient se différencier par une longueur d'onde axiale différente. Un facteur majeur à l'origine de cette différence réside dans le protocole mis en œuvre pour atteindre le régime TVF. Une forte augmentation de la vitesse de rotation du cylindre intérieur et une augmentation quasi-statique conduisent à des longueurs d'onde axiale différentes.

## 1.1 Instabilité du régime TVF

### 1.1.1 Instabilité vis-à-vis de perturbations azimuthales : bifurcation vers le régime WVF

Lorsqu'on augmente davantage la vitesse de rotation du cylindre intérieur, le régime TVF devient à son tour instable. Cette deuxième instabilité a été observée expérimentalement par Coles [11]. Les lignes de séparation des cellules de Taylor présentent des ondulations azimutales comme le montre la figure 1.2. Ce type d'écoulement est appelé Wavy Vortex Flow. Il est tridimensionnel, instationnaire et il est caractérisé par deux nombres d'onde : axiale $k$ et azimutal $m$. Une description détaillée de la structure de l'écoulement à partir des mesures PIV 2D a été donnée par Wereley et Lueptow [12]. Une illustration de leurs résultats est montrée par la figure 1.3. On observe clairement un transfert de fluide entre deux cellules adjacentes. Néanmoins, sur une période, le bilan de transfert de masse est nul. Le mécanisme physique à l'origine de la bifurcation du régime TVF au régime WVF à été clairement mis en évidence par Martinand et al. [13]. Selon ces auteurs, dans le cas d'une géometrie à faible entrefer, l'apparition de stries de haute et basse vitesse azimutales induits par les jets radiaux entrant et sortant est à l'origine de l'instabilité inflexionnelle du régime TVF. Ce point de vue a été confirmé récemment par Dessup et al. [14], en adoptant le modèle d'un processus de cycle auto-entreteur (Self Sustaining Process, SSP) proposé par Waleffe [15]. Les rouleaux de Taylor conduisent à la formation de stries, qui développent des instabilités inflexionnelles, qui elles-mêmes, lors de leur évolution non-linéaire formeront à nouveau les rouleaux de Taylor, refermant ainsi le cycle.

#### Influence des paramètres géométriques

Pour des géométries à faible entrefer $0.7 \leq \eta \leq 0.9$ et un rapport d'aspect $L \geq 20$, il a été observé expérimentalement (Coles [11] ; Cole [17] ; Wereley et Lueptow [12]) que le régime de TVF reste stable sur une étroite gamme de $Re$ compris entre $Re_c$ et 1.1 à 1.3 $Re_c$. Pour des rapports de rayons $\eta$ plus faible ($\eta < 0.7$) le régime TVF reste stable sur une plus grande gamme de Re (Jones [18] ; Snyder et Lambert [19] ; King et al. [20] ; Meincke et Egbers [21] ; Razzak et al. [22]). Pour $\eta = 0.5$ Razzak et al., moyennant une simulation numérique avec des conditions aux limite périodique, trouve que le régime TVF bifurque vers le WVF à $Re = 8.45 Re_c$. Il convient aussi de noter que le nombre de

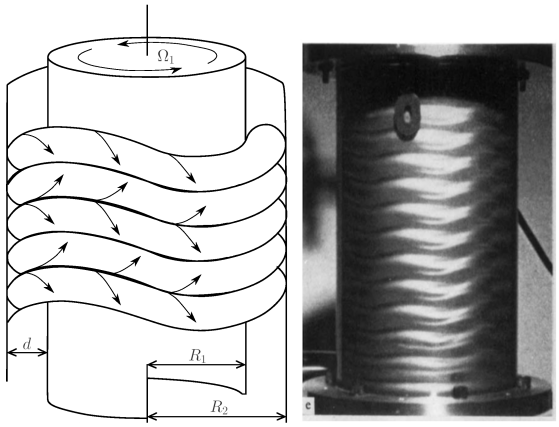


FIGURE 1.2 – **(a)** Vue schématique du régime Wavy Vortex Flow ; **(b)** Wavy Vortex Flow régime obtenu par Coles [11]

Reynolds critique à l'apparition du régime WVF augmente fortement lorsque le rapport d'aspect diminue.

#### Influence de la montée en vitesse du cylindre intérieur

Plusieurs études expérimentales (Cole [17] ; Edward ; Tagg [23] ; Swinney 1991 ; Benjamin et Mullin [8]) ont mis en évidence pour les mêmes paramètres géométriques des écoulements WVF avec des nombre d'onde azimutale variant de 1 à 8. Cette multiplicité des solutions a par origine la forte sensibilité du régime WVF au protocole de montée en vitesse du cylindre intérieur.

### 1.1.2 Instabilité vis-à-vis de perturbations axisymétriques

Lorsque le nombre de Reynolds dépasse la valeur critique $Re_c$, toute une bande de nombres d'onde $\delta k$ centrée sur $k_c$ ont un taux de croissance positif comme le montre la figure 1.5. En effet au voisinage de $Re_c$, un développement en série de Taylor du taux de croissance $\sigma$ de la perturbation est donné par

$$\sigma(Re, k) = \frac{1}{\tau_0}\frac{Re - Re_c}{Re_c} - \frac{\xi_0^2}{\tau_0}(k - k_c)^2, \tag{1.9}$$

où $\tau_0$ désigne le temps de relaxation des perturbations et $\xi_0$ la longueur de cohérence (Manneville [24]).

L'existence de cette gamme de nombres d'onde instables va induire une modulation spatiale de la taille des cellules de Taylor. Du fait de cette modulation, les cellules de

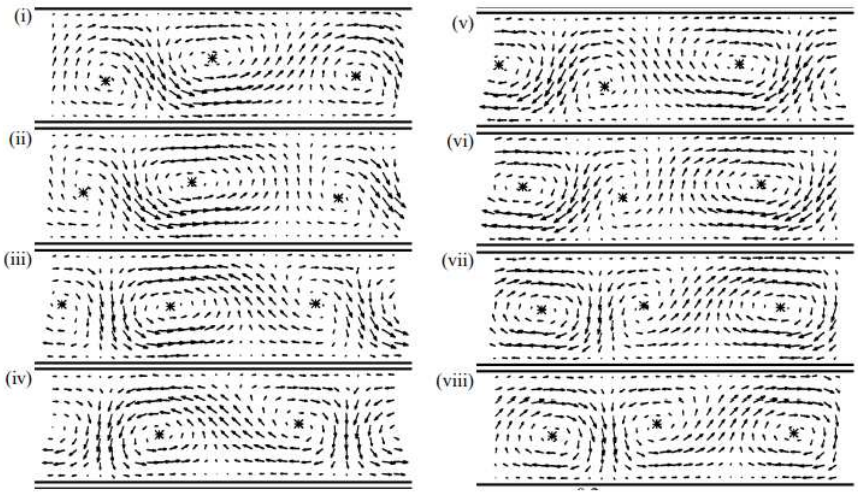


FIGURE 1.3 – Wavy Taylor-Vortex flow régime utilisant l'analyse de vélocimétrie par image de particules (PIV 2D) à Re $= 253$ ; $\eta = 0.83$, $L = 47.7$, $Re_c = 103$ (Wereley & Lueptow, [12]). Mise en évidence d'un phénomène cyclique de transfert entre deux vortex adjacents.

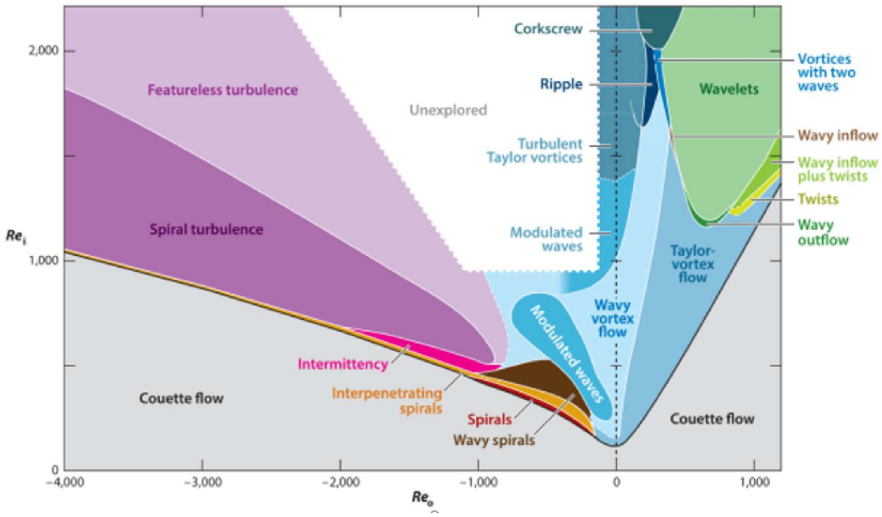


FIGURE 1.4 – Diagramme de transition d'écoulement dans un plan du nombre de Reynolds du cylindre externe $R_o$ au nombre de Reynolds du cylindre interne $R_i$ (Andereck et al. [1] ; version colorée tirée de [16])

Taylor peuvent subir une instabilité dite d'Ekhaus qui est une instabilité de compression/dilatation de grande longueur d'onde. Dans le domaine où le nombre d'onde est très inférieur à $k_c$ (rouleaux dilatés), l'écoulement devient temporairement instable et ajuste la longueur d'onde en créant une nouvelle paire de rouleaux. La structure finale qui en résulte a un nombre d'onde plus proche de $k_c$. Si au contraire, la structure initiale est formée de rouleaux comprimés ($k \gg k_c$), le réajustement se fait par fusion de deux cellules. Le domaine de stabilité d'Ekhaus peut être déterminé aisément à partir de l'équation

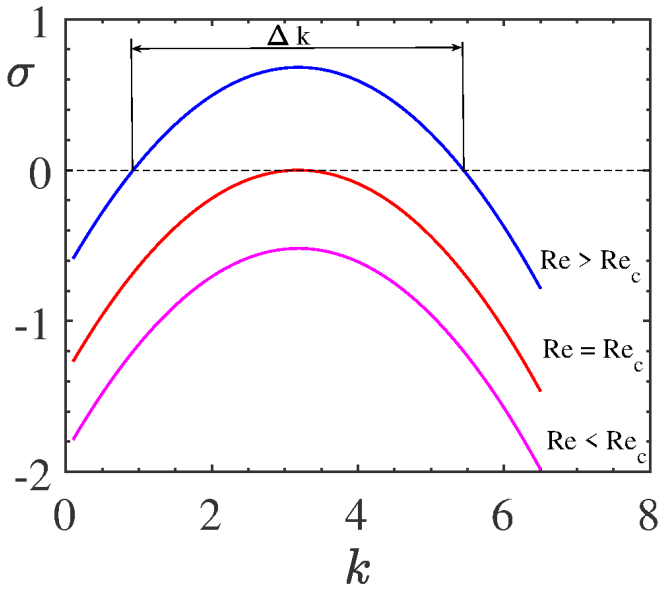


FIGURE 1.5 – Taux de croissance en fonction du nombre d'onde k pour différents nombres de Reynolds

d'amplitude (Manneville [24], Hoyle [25]) qui n'est valide qu'au voisinage des conditions critiques. Le régime TVF est stable vis-à-vis de perturbations axisymétriques de grande longueur d'onde si

$$\varepsilon < \varepsilon_E = 3q^2\xi_0^2; \tag{1.10}$$

où $q = k - k_c$ et $\xi_0$ la longueur de cohérence.
Pour de faibles rapports de rayons, disons $\eta \leq 0.5$, l'étude de la stabilité des rouleaux vis-à-vis des perturbations axisymétriques peut être effectuée pour des nombres de Reynolds loins des conditions critiques puisque l'instabilité azimuthale est repousée à $Re > 4Re_c$ pour $\eta = 0.5$. Riecke & Paap [26] et Paap & Riecke [27] ont calculé la solution rouleaux par une méthode de continuation et pour un nombre d'onde $k \neq k_c$. La stabilité de cette solution vis-à-vis de perturbations axisymétriques est ensuite étudiée par la méthode de Floquet. Pour un nombre de Reynolds $Re = 2Re_c$, l'instabilité affecte une paire de tourbillons sur toute la hauteur de l'espace annulaire. On parle alors d'instabilité de courte longueur d'onde. Néanmoins, après réajustement, le système redevient stationnaire et stable.
Les frontières du domaine de stabilité d'Eckhaus ont été déterminées expérimentalement par Dominguez-Lerma et al. [28]. Pour une géométrie avec un rapport de rayons $\eta = 0.75$, un très bon accord avec la théorie est observée pour $\varepsilon = (Re - Re_c)/Re_c \leq 0.1$. Au delà de cette valeur le domaine de stabilité exprérimental est plus restreint que celui prévu théoriquement. D'autres expériences ont été conduits par Linek & Ahlers [29] avec $\eta = 0.74$, en considérant la situation où les deux frontières axiales de la géométrie sont rigide-rigide et rigide-surface libre. Les auteurs constatent que le domaine de stabilité est

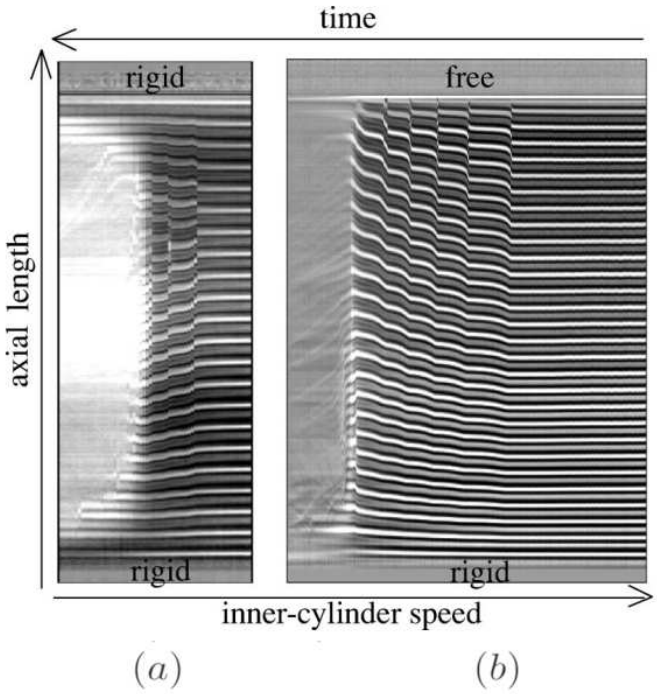


FIGURE 1.6 – Annulation des tourbillons en cas de (a) frontières rigides et (b) frontière libre au sommet du système. (Linek & Ahlers, 1998)

encore plus restreint dns le cas où on a une surface libre. En outre dans ce dernier cas, les modifications se produisent au voisinage de la surface libre, alors que dans le cas rigide-rigide, les modifications ont lieu à l'intérieur du système comme le montre la figure 1.6. Dennin et al. [30] ont effectué des expériences pour un rapport de rayons $\eta = 0.5$. Leurs résultats relatifs aux instabilités de petite longueur d'onde sont en bon accord avec les études theorique et numérique de Paap et Riecke [27].

## 1.2 Ecoulement de Taylor-Couette pour des fluides non-Newtoniens

Les fluides non-Newtoniens interviennent dans de nombreux procédés industriels tels que ceux rencontrés dans les industries pétrolière, pharmaceutique, ... . Ces fluides se présentent souvent sous forme de solution de polymères, de molécules tensio-actives ou de suspension de particules. Ils possèdent une microstructure susceptible de se modifier sous l'effet d'un écoulement à des échelles de temps plus où moins différents de celles associées à l'écoulement. La microstructure peut aussi se réorganiser complètement conduisant à une viscosité qui peut dépendre fortement du taux de cisaillement. Globalement, deux propriétés sont fréquemment rencontrées dans les fluids complexes : la rhéofluidification (diminution de la viscosité avec le cisaillement) et la viscoélasticité qui se traduit par une différence de contraintes normales induite par l'allongement des macromolécules.

### 1.2.1 Influence du comportement viscoélastique

En utilisant des fluides dits de Boger, solutions de polyisobutylène dans un solvant très visqueux, 100 à 1000 fois la viscosité de l'eau, il a été observé que la viscoélasticité peut induire une instabilité de l'écoulement de Couette à très faible vitesse de rotation (Larson [31] et Larson et al. [32]). Cette instabilité dite purement élastique peut être décrite à l'aide du nombre de Weissenberg qui est le rapport entre le temps caractéritique de relaxation sur le temps caractéristique de cisaillement. À mi-chemin entre les instabilités inertielles observées pour les fluides Newtoniens et les instabilités purement élastiques se situent les régimes dits inertio-élastiques, pour lesquels les modes d'instabilité observés présentent une nature différente de celle observée avec des fluides Newtoniens tout en étant pour l'essentiel régi par les forces d'inertie (Groismann et Steinberg[33], Crumeyrolle et al. [34]). En utilisant des solutions de xanthane dans un mélange eau-glycerol et en faisant varier la concentration en glycerol, Lacassagne et al. [35] ont pu étudier la compétition entre le caractère rhéofluidifiant et le caractère viscoélastique dans les transitions en écoulement de Taylor-Couette. Globalement pour des faibles degrés de rhéofluidification et une forte élasticité, les auteurs retrouvent la transition d'un écoulement de Couette circulaire vers un état chaotique. Au contraire pour des fluides fortement rhéofluidifiants, on retrouve la transition classique CCF $\rightarrow$ TVF $\rightarrow$ WVF, même si le caractère viscoélastique est très marqué.

### 1.2.2 Influence du comportement rhéofluidifiant sur la stabilité d'un écoulement de Taylor-Couette

L'écoulement de Couette pour un fluide rhéofluidifiant est principalement caractérisé par une stratification radiale de la viscosité. Cet effet est d'autant plus important que le caractère rhéofluidifiant est marqué et l'entrefer large. Le mécanisme physique de l'instabilité de l'écoulement de Couette décrit précédemment pour les fluides Newtoniens s'applique aussi pour des fluides purement visqueux. Cependant les conditions critiques sont modifiées du fait de la modification d'une part de la dissipation visqueuse et d'autre part du gradient pariétal de la vitesse qui intervient dans l'échange d'énergie entre l'écoulement de base et la perturbation : le cisaillement augmente au niveau du cylindre intérieur et décroît que niveau du cylindre extérieur. L'analyse linéaire de stabilité fait aussi apparaître une anisotropie dans le déviateur du tenseur des contraintes liée à la perturbation (Agbessi et al. [36]). En fait, les calculs montrent que cette anisotropie ne joue pas un rôle majeur dans la sélection du mode critique (Agbessi et al. [36]). Le nombre de Reynolds critique et le nombre d'onde axial critique ont été déterminés par plusieurs auteurs pour différents modèles des fluides rhéofluidifiants et pour différents rapport de rayons. Une analyse critique des résultats de la littérature a été effectuée par Alibenyahia et al. [37] et ensuite par Agbessi et al. [36]. À titre d'exemple, dans le cas où le cylindre extérieur est fixe, on peut retenir que le mode critique est axisymétrique et stationnaire et que le nombre d'onde axial critique augmente (taille des rouleaux de Taylor diminue) lorsque le

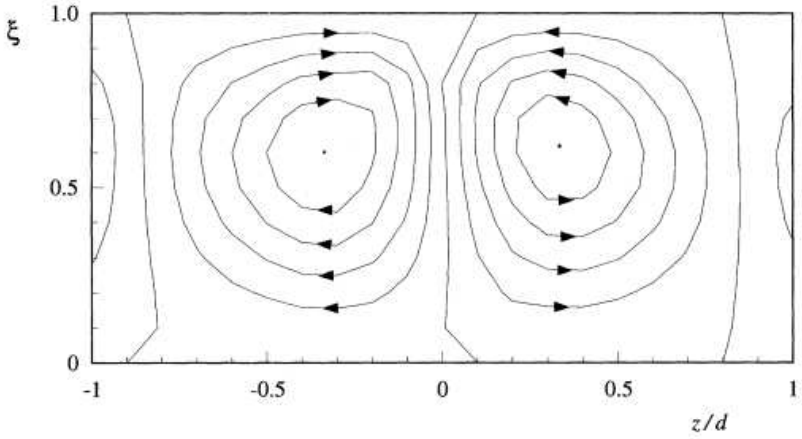


FIGURE 1.7 – La forme des tourbillons de Taylor en utilisant la solution Xanthane (Escudier et al., 1995), où $\xi$ est la position radiale non dimensionnelle, $\xi = (R_2 - r)/(R_2 - R_1)$

caractère rhéofluidifiant devient plus marqué. L'étude énergétique montre que l'échange d'énergie entre l'écoulement de base et la perturbation ainsi que la dissipation visqueuse ont lieu essentiellement au voisinage de la paroi du cylindre intérieur. Par conséquent, l'interprétation des résultats quant à l'influence des effets rhéofluidifiant doit être faite en utilisant un nombre de Reynolds défini avec la viscosité évaluée à la paroi du cylindre intérieur. Dans ce cas, il est montré que la rhéofluidification a un effet stabilisant. Cette stabilisation est due à une réduction de l'échange d'énergie entre l'écoulement de base et la perturbation. D'un point de vue pratique, les auteurs utilisent plutôt la viscosité nominale pour un fluide en loi puissance, ou la viscosité à cisaillement nul pour un fluide de Carreau dans la définition du nombre de Reynolds. Dans ce cas, les résultats montrent au contraire un effet déstabilisant (Li & Khayat [38]). D'autres auteurs (Masuda et al. [39] ; Elçiçek et Güzel [40]) suggèrent d'utiliser une viscosité moyennée sur tout l'espace annulaire. Pour conclure sur cette partie, on pense que la sélection d'une viscosité de référence est juste une question de choix. D'un point de vue expérimental, Escudier et al. [41] ont étudié l'évolution des tourbillons de Taylor en régime supercritique pour un fluide non-Newtonien rhéofluidifiant. Le dispositif expérimental a un rapport de rayons $\eta = 0.5$ et un rapport d'aspect $L = 233$. Les fluides utilisés sont des solutions aqueuses de xanthane et de laponite. Les composantes axiale et azimuthale de la vitesse sont mesurées par vélocimétrie laser Doppler. Il a été constaté que le centre du tourbillon était décalé vers la paroi de cylindre intérieur où la viscosité est plus faible et vers le jet radial sortant comme le montre la figure 1.7.

Ces études ont été reprises plus tard par Cagney et Balabani [42] en utilisant un dispositif ayant un rapport de rayons $\eta = 0.883$ et un rapport d'aspect $L = 13$. Les fluides utilisés sont des solutions de xanthan dans un mélange eau-glycerol (75% eau - 25% glycerol). Les caratéristiques de l'écoulement sont déterminées par visualisation et par des mesures PIV 2D. Comme dans le cas Newtonien, le jet radial sortant est plus

intense que le jet radial entrant. Néanmoins, cette différence augmente avec le caractère rhéofluidifiant du fluide. Les auteurs se sont intéressés à la deuxiéme instabilité, i.e. la transition du régime TVF au régime WVF. Ils constatent une variation non monotone du nombre de Reynolds critique $Re_s$ en fonction du caractère rhéofluidifiant. Ceci est probalement du au choix de la viscosité de référence dans la définition de Re. Les auteurs notent aussi que l'amplitude des oscillations est plus importante dans le cas d'un fluide rhéofluidifiant que dans le cas Newtonien, au niveau des jets radiaux sortant et entrant.
Des expériences similaires sur la stabilité du régime TVF ont été refaites par les mêmes auteurs (Cagney et al. [43]) avec les mêmes fluides (solutions de xanthane dans un mélange 75% eau - 25% glycerol) mais en utilisant une géométre ayant un rapport de rayons $\eta = 0.77$ et un rapport d'aspect $L = 21.5$. Comme dans leur premier article, les auteurs observent une transition classique CCF $\rightarrow$ TVF $\rightarrow$ WVF. Excepté que cette fois-ci les auteurs observent dans le régime WVF une fusion des tourbillons de Taylor au voisinage des frontières rigides qui délimitent axialement la géométrie. En fait, le même résultat a été observé dans le cas Newtonien par Park & Crawford [44] et Crawford et al. [45]. Cette fusion de cellules en régime WVF et aux extrêmités de la géometrie serait liée au rapport d'aspect qui n'est pas suffisamment important.
Des résultats complétement différents ont été obtenus expérimentaux par Elçiçek et Güzel [40] pour deux configurations géometriques ($\eta = 0.883, L = 42$) et ($\eta = 0.643, L = 16$). Les fluides utilisés sont des solutions aqueuses de xanthane. Les essais expérimentaux sont basés uniquement sur la visualisation de la structure de l'écoulement. Les auteurs observent dans certaines situations une succession de transitions très complexes telle que : CCF $\rightarrow$ SVF (Spiral Vortex Flow) $\rightarrow$ TVF $\rightarrow$ MVF (Modulated Wavy Vortex Flow) $\rightarrow$ Chaotic state ou d'autres motifs avec des instabilités de glissement (drifting instability). On pense que cette complexité de l'écoulement est due à une forte concentration en particules utilisées pour la visualisation et peut être aussi à des montées en vitesse trop rapides. Il est clair que les résultats récents relatifs à la stabilité du régime TVF dans des fluides rhéofluidifiants nécessite des études supplémentaires.

## 1.3 Objectifs et méthodologie

L'objectif principal de notre travail de recherche est d'examiner l'influence du caractère rhéofluidifiant d'un fluide non-Newtonien sur la stabilité du régime TVF. On a considéré délibérément le cas d'un large entrefer (faible valeur du rapport de rayons), avec l'idée d'une part de retarder l'apparition du régime WVF à des nombres de Reynolds suffisamment élevés pour pouvoir étudier le régime TVF et son évolution sur une large gamme de nombres Reynolds, et d'autre part accentuer les effets rhéofluidifiants en augmentant en particulier la stratification de la viscosité. La méthodologie suivie s'appuie sur des approches théorique, numérique et expérimentale. L'approche théorique consiste en une analyse faiblement non linéaire qui est effectuée pour rendre compte de l'influence des termes non linéaires d'inertie et des termes non linéaires visqueux sur la

structure de l'écoulement. Le modèle de Carreau est adopté. L'intérêt de cette approche est double, d'une part identifier les termes les plus significatifs qui interviennent dans l'organisation de l'écoulement et d'autre part avoir une solution quasi-analytique au voisinage des conditions critiques permettant une analyse paramétrique pour une large gamme de paramètres rhéologiques, dynamique et géométriques en un temps assez-court. Dans l'approche numérique, les équation de conservation de masse et de quantité de mouvement couplées avec la loi de comportement rhéologique du fluide (modéle de Carreau) sont résolues numériquement dans le cas axisymétrique afin de se focaliser sur les instabilités axiales de grande où de petite longueur d'onde. La comparaison des résultats théoriques/numériques avec des résultats expérimentaux permettra de confirmer où d'infirmer les différentes hypothèses adoptées.

## 1.4 Organisation du manuscrit

Le manuscrit est organisé en trois chapitres en plus de l'introduction et de la conclusion générale. La présentation sous forme d'articles introduit inévitablement certaines répétitions. Le chapitre II est consacré à une analyse faiblement non linéaire d'un écoulement de Taylor-Couette pour un fluide rhéofluidifiant purement visqueux. Un développement asymptotique en amplitude jusque'à l'ordre 7 est mis en œuvre. Les résultats obtenus montrent que le caractère rhéofluidifant modifie de manière significative la structure de l'écoulement. Le centre d'une cellule de Taylor est décalé vers le cylindre intérieur et vers le jet radial sortant (du cylindre intérieur vers le cylindre extérieur). Celui-ci est plus fin et plus intense. L'écoulement radial entrant a une intensité plus faible et une étendue plus importante. On pense que c'est cette modification qui est à l'origine des instabilités axiales observées expérimentalement et numériquement. Le chapitre III comporte une partie expérimentale et une partie numérique. Dans la partie expérimentale, le dispositif expérimental, les fluides utilisés et les techniques de mesure mises en œuvre pour la visualisation et les mesures de vitesse par PIV sont décrites. Dans la partie numérique, la méthode numérique utilisée pour la resolutions des equations de conservation de quantité de mouvement sont présentées en basant sur le solver de Freefem++. Des résultats originaux ont été obtenus avec un très bon accord entre le numérique et l'expérience. On montre que pour un fluide rhéofluidifiant, le régime TVF devient instable vis-à-vis de perturbations axiales. Cette instabilité se caractérise par un processes continu et répétitif de création et de fusion de tourbillons.

Il était question d'étendre cette étude au cas des fluides présentant une contrainte seuil d'écoulement. On était particulièrement intéressé par la situation où le fluide dans l'espace annulaire n'est que partiellement cisaillé, i.e. avec une zone non-cisaillée attachée à la paroi du cylindre extérieur. Le cas où tout l'espace annulaire est cisaillé, devrait se rapprocher du problème traité au chapitre II. On a commencé par une analyse faiblement non linéaire en utilisant un fluide modèle du type Bingham : c'est l'objective du chapitre IV. Une des

difficultés réside dans le traitement des conditions aux limites à la surface séparant les phases liquide et "solide".Des résultats préliminaires sur la perturbation de la frontière de la zone non-cisaillée et sur la structure de l'écoulement sont présentés. Une synthèse des résultats les plus pertinents ainsi que les différentes perspectives qui découlent de ce travail seront présentées à la fin de ce manuscrit.

## Bibliographie

[1] C. D. Andereck, S. S. Liu, and H. L. Swinney. Flow regimes in a circular Couette system with independently rotating cylinders. *J. Fluid Mech.*, 164 :155–183, 1986.

[2] G. I. Taylor. Stability of a viscous liquid contained between two rotating cylinders. *Trans. R. Soc. Lond. A*, 223 :289–343, 1923.

[3] A. Esser and S. Grossmann. Analytic expression for Taylor-Couette stability boundary. *Phys. Fluids*, 8(7) :1814–1819, 1996.

[4] C.S. Dutcher and S.J. Muller. Explicit analytic formulas for Newtonian Taylor-Couette primary instabilities. *Phys. Rev. E*, 75(4) :047301, 2007.

[5] K.A. Cliffe and T. Mullin. A numerical and experimental study of anomalous modes in the Taylor experiment. *J. Fluid Mech.*, 153 :243–258, 1985.

[6] O. Czarny, E. Serre, P. Bontoux, and R. M. Lueptow. Interaction between Ekman pumping and the centrifugal instability in Taylor-Couette flow. *Phys. Fluids*, 15(2) :467–477, 2003.

[7] G. Ahlers, D.S. Cannell, M.A. Dominguez-Lerma, and R. Heinrichs. Wavenumber selection and Eckhaus instability in Couette-Taylor flow. *Phys. D : Nonlinear Phenom.*, 23(1-3) :202–219, 1986.

[8] T. B. Benjamin and T. Mullin. Notes on the multiplicity of flows in the Taylor experiment. *J. Fluid Mech.*, 121 :219–230, 1982.

[9] J.E. Burkhalter and E.L. Koschmieder. Steady supercritical Taylor vortices after sudden starts. *Phys. Fluids*, 17(11) :1929–1935, 1974.

[10] T.T. Lim, Y.T. Chew, and Q. Xiao. A new flow regime in a Taylor-Couette flow. *Phys. Fluids*, 10(12) :3233–3235, 1998.

[11] D. Coles. Transition in circular Couette flow. *J. Fluid Mech.*, 21(3) :385–425, 1965.

[12] S. T. Wereley and R. M. Lueptow. Spatio-temporal character of non-wavy and wavy Taylor-Couette flow. *J. Fluid Mech.*, 364 :59–80, 1998.

[13] D. Martinand, E. Serre, and R. M. Lueptow. Mechanisms for the transition to waviness for Taylor vortices. *Phys. Fluids*, 26(9) :094102, 2014.

[14] T. Dessup, L.S. Tuckerman, J.E. Wesfreid, D. Barkley, and A.P. Willis. Self-sustaining process in Taylor-Couette flow. *Phys. Rev. Fluids*, 3(12) :123902, 2018.

[15] F. Waleffe. On a self-sustaining process in shear flows. *Phys. Fluids*, 9(4) :883–900, 1997.

[16] Arjun Anantharaman. Suspension taylor-couette flow : Investigation of particle loading effects on transitions between flow regimes. 2019.

[17] J.A. Cole. Taylor-Vortex instability and annulus-length effects. *J. Fluid Mech.*, 75(1) :1–15, 1976.

[18] C. A. Jones. The transition to wavy Taylor vortices. *J. Fluid Mech.*, 157 :135–162, 1985.

[19] H.A. Snyder and R.B. Lambert. Harmonic generation in Taylor vortices between rotating cylinders. *J. Fluid Mech.*, 26(3) :545–562, 1966.

[20] G.P. King, Y. Li, W. Lee, H. L. Swinney, and P. S. Marcus. Wave speeds in wavy Taylor-Vortex flow. *J. Fluid Mech.*, 141 :365–390, 1984.

[21] O. Meincke and C. Egbers. Routes into chaos in small and wide gap Taylor-Couette flow. *Phys. Chem. Earth Pt. B*, 24(5) :467–471, 1999.

[22] M. A. Razzak, B. C. Khoo, and K. B. Lua. Numerical study on wide gap Taylor Couette flow with flow transition. *Phys. Fluids*, 31(11) :113606, 2019.

[23] R. Tagg. The Couette-Taylor problem. *Nonlinear Sci. Today*, 4 :1–25, 1994.

[24] P. Manneville. *Instabilities, chaos and turbulence*, volume 1. World Scientific, 2010.

[25] R. Hoyle. *Pattern formation : an introduction to methods.* Cambridge University Press, 2006.

[26] H. Riecke and H-G. Paap. Stability and wave-vector restriction of axisymmetric Taylor vortex flow. *Phys. Rev. A*, 33(1) :547, 1986.

[27] H-G. Paap and H. Riecke. Wave-number restriction and mode interaction in Taylor vortex flow : Appearance of a short-wavelength instability. *Phys. Rev. A*, 41(4) :1943, 1990.

[28] M.A. Dominguez-Lerma, D. S. Cannell, and G. Ahlers. Eckhaus boundary and wave-number selection in rotating Couette-Taylor flow. *Phys. Rev. A*, 34(6) :4956, 1986.

[29] M. Linek and G. Ahlers. Boundary limitation of wave numbers in Taylor-Vortex flow. *Phys. Rev. E*, 58(3) :3168, 1998.

[30] M. Dennin, D. S. Cannell, and G. Ahlers. Measurement of a short-wavelength instability in Taylor vortex flow. *Phys. Rev. E*, 49(1) :462, 1994.

[31] R. G. Larson. Instabilities in viscoelastic flows. *Rheol. Acta*, 31(3) :213–263, 1992.

[32] R.G. Larson, E.S.G. Shaqfeh, and S.J. Muller. A purely elastic instability in Taylor-Couette flow. *J. Fluid Mech.*, 218 :573–600, 1990.

[33] A. Groisman and V. Steinberg. Mechanism of elastic instability in Couette flow of polymer solutions. *Phys. Fluids*, 10 :2451–2463, 1998.

[34] O. Crumeyrolle, I. Mutabazi, and M. Grisel. Experimental study of inertioelastic Couette-Taylor instability modes in dilute and semidilute polymer solutions. *Phys. Fluids*, 14(5) :1681–1688, 2002.

[35] T. Lacassagne, N. Cagney, and S. Balabani. Shear-thinning mediation of elasto-inertial Taylor-Couette flow. *J. Fluid Mech.*, 915, 2021.

[36] Y. Agbessi, B. Alibenyahia, C. Nouar, and L. Choplin. Linear stability of Taylor-Couette flow of shear-thinning fluids : modal and non-modal approaches. *J. Fluid Mech.*, 775 :354–389, 2015.

[37] B. Alibenyahia, C. Lemaître, C. Nouar, and N. Ait-Messaoudene. Revisiting the stability of circular Couette flow of shear-thinning fluids. *J. Non-Newtonian Fluid. Mech.*, 183 :37–51, 2012.

[38] Z. Li and R.E. Khayat. A non-linear dynamical system approach to finite amplitude Taylor-Vortex flow of shear-thinning fluids. *Int. J. Numer. Methods Fluids*, 45(3) :321–340, 2004.

[39] H. Masuda, T. Horie, R. Hubacz, M. Ohta, and N. Ohmura. Prediction of onset of Taylor-Couette instability for shear-thinning fluids. *Rheol. Acta*, 56(2) :73–84, 2017.

[40] H. Elçiçek and B. Güzel. Effect of shear-thinning behavior on flow regimes in Taylor-Couette flows. *J. Non-Newtonian Fluid. Mech.*, 279 :104277, 2020.

[41] M. P. Escudier, I. W. Gouldson, and D. M. Jones. Taylor vortices in Newtonian and shear-thinning liquids. *Proc. Roy. Soc. Lond. A.*, 449 :155–176, 1995.

[42] N. Cagney and S. Balabani. Taylor-Couette flow of shear-thinning fluids. *Phys. Fluids*, 31(5) :053102, 2019.

[43] N. Cagney, T. Lacassagne, and S. Balabani. Taylor-Couette flow of polymer solutions with shear-thinning and viscoelastic rheology. *J. Fluid Mech.*, 905, 2020.

[44] K. Park and G. L. Crawford. Deterministic transitions in Taylor Wavy-Vortex flow. *Phys. Rev. Letters*, 50(5) :343, 1983.

[45] G. L. Crawford, K. Park, and R.J. Donnelly. Vortex pair annihilation in Taylor Wavy-Vortex flow. *Phys. Fluids*, 28(1) :7–9, 1985.

# Chapitre 2

# Taylor-vortex flow in shear-thinning fluids

## Sommaire

## 2.1 Introduction

Instabilities of Couette flow between two coaxial cylinders are considered as prototypes for general studies in hydrodynamic instability and transition to turbulence. A survey of the literature on the Taylor-Couette problem can be found in Koschmieder [1] and Tagg [2]. In the classical configuration, the inner cylinder is rotating and the outer one is fixed. The basic state, a circular Couette-flow (CCF), is purely azimuthal with a balance between the centrifugal force and the pressure gradient pointing inward. In this situation, the angular momentum decreases with the radius. According to Rayleigh criterion [3], CCF is unstable in the inviscid limit with respect to axisymmetric three-dimensional perturbation. Taylor [4] determined theoretically and experimentally the influence of the fluid viscosity on the stability boundary. The primary instability results in axisymmetric meridional rolls (Taylor vortices) periodically spaced in the axial direction and separated by radial jets. When the inner cylinder rotation rate is increased, a Hopf bifurcation to a rotating wave occurs, i.e. the Taylor vortex flow (TVF) acquires a periodicity along the azimuthal direction $\theta$. The resulting state is the wavy vortex flow (WVF). The Reynolds number $Re$ for onset of time-dependent wavy vortices was computed numerically by Jones [5]. It is shown that for a radius ratio, $\eta = R_1/R_2$, close to 1, say $\eta \geq 0.85$, the supercritical Reynolds number regime in which the axisymmetric vortices are stationary is very small. As the radius ratio is decreased, the wavy vortices set in at higher and higher Reynolds numbers. This result was confirmed experimentally. For instance, in experiments performed by Snyder & Lambert [6] with a gap of radius ratio $R_1/R_2 = 0.5$, the first appearance of significant azimuthal waviness was reported at $Re \approx 10\, Re_c$. Furthermore, they suggested that this was probably due to end effects of the cylinders. For the same radius ratio, i.e. $\eta = 0.5$, Meincke & Egbers [7] observed experimentally a transition to WVF at $Re \approx 16\, Re_c$. Thus, from experimental point of view, it is not clear at which Reynolds number the flow in a wide gap undergoes a transition to wavy-mode. The disagreement between experimental results could be related to the influence of the aspect ratio (AR = column length/gap width). Indeed in [6] $AR \approx 30$, whereas in [7], $AR \approx 4$.

For moderate or small gap width (say $\eta > 0.75$), increasing further $Re$, the system undergoes a bifurcation from wavy-vortex-flow (WVF) to modulated wavy-vortex-flow (MWVF), characterized by the presence of a second frequency modulating the rotating waves as described by Andereck *et al.* [8]. Subsequent bifurcations lead generally to turbulence after few steps. This orderly progression of nonlinear flow states makes Taylor-Couette flow as an attractive model for studying transition to turbulence.

In the case of non-Newtonian fluids (polymer solutions, suspensions, emulsions, ...), mechanisms of the instability and transition to turbulence may be modified by the non-linearity of the rheological behavior. Most non-Newtonian fluids have two common properties, viscoelasticity and shear-thinning. Polymer solutions, colloïdal suspensions as well as particulate dispersions display this behavior above a certain concentration threshold. There was a significant interest in inertialess viscoelastic Taylor-Couette instability since the pioneering work of Giesekus [9]. This instability was then analyzed by Muller *et al.* [10], Larson *et al.* [11] and Shaqfeh *et al.* [12]. In the laminar state, the rotation produces a shear which stretches the polymer molecule along the curved stream lines. This leads to a first normal stress difference which acts against the centrifugal force. Groisman and Steinberg (1998) [13] showed experimentally that elastic instability leads to a strong non-linear flow transition at vanishing inertia.
Hereafter, we focus on shear-thinning fluids, for which the elastic response can be neglected. Typically, stiff polymer solutions, show significant nonlinear decrease of the viscosity with the shear-rate, with almost negligible elastic effects [14]. The shear-thinning behavior, i.e. a nonlinear decrease of the viscosity with the shear rate, arises from the reorganization of the internal fluid structure to reduce the viscous dissipation. The characteristic time of the reorganization of the flow structure is supposed much smaller than all characteristic times of the problem. In other words, the fluid is assumed purely viscous and its response to an applied shear-stress is instantaneous.

### 2.1.1 Brief Review on Taylor-Couette flow of shear-thinning fluids

Circular Couette flow of a shear-thinning fluid is mainly characterized by a viscosity stratification in the annular space, which is more significant as the shear-thinning effects are stronger and the annular space is wider. With increasing shear-thinning effects, the shear rate increases at the inner wall and decreases at the outer one. Furthermore, the nonlinear variation of the viscosity with the shear rate introduces at the linear level an anisotropy in the deviatoric tensor associated to the perturbation. This latter point is discussed in section 2.2.4.
The mechanism of instability of CCF of shear-thinning fluids is the same as for a Newtonian fluid and results in axisymmetric counter rotating vortices separated by radial inflow and outflow jets of angular momentum emanating from the fluid layers adjacent to the cylinders' wall. However, the critical conditions are different because of the radial viscosity stratification and the modification of the azimuthal velocity profile. In the case where the inner cylinder is rotating and the outer one is at rest, the critical Reynolds and axial wave numbers are given in the literature for power-law and Carreau fluids, for wide and narrow annular spaces, see for instance Agbessi *et al* [15] and Alibenyahia *et al* [16] and the references therein. When both the inner and the outer cylinders are rotating, the critical conditions were determined by Agbessi *et al* [15] for a narrow and a wide annular space.

It is shown that when the Reynolds number is defined using the inner wall-shear viscosity, the shear-thinning delays the appearance of Taylor vortices. It is explained that this delay is due to the reduction of the energy exchange between the base flow and the perturbation. A radically different conclusion may be reached if one uses the zero-shear viscosity of the fluid as viscosity scale. In the narrow gap-limit and weakly shear-thinning behavior of the fluid, Li & Khayat [17] found that the critical Reynolds number defined with the zero-shear viscosity becomes lower as shear-thinning effects increase. Similar tendency is observed when free (slip) boundary conditions are used [18, 19, 20]. Recently Masuda *et al.* [21] suggested to use an average viscosity weighted by the strain-rate squared. They found that the critical Reynolds number defined with this average viscosity is the same as for a Newtonian fluid. However, this result is limited only to a narrow annular space with a radius ratio $\eta > 0.7$.

From experimental point of view, Escudier *et al.* [22] suggested to determine the critical conditions by focusing on the development of the axial velocity component, near the inner wall at a radial position $r$ such $(R_2 - r)/(R_2 - R_1) = 0.8$.

Sinevic et al. [23] measured the torque acting on the inner cylinder for three shear-thinning fluids described by a power-law model ($n_p = 0.4$, 0.45 and 0.57). They found that in the Taylor-vortex flow region, the power number $Po$ behaves as $Po \propto Re_w^{-0.7}$, where, $Re_w$ is the Reynolds number defined with the inner wall shear-viscosity. Concerning the flow structure, for a wide gap, it is shown theoretically [16, 15] and experimentally [22] that with increasing shear-thinning effects, the vortex eye is shifted toward the inner cylinder, because of the viscosity stratification : the viscosity increases from the inner cylinder to the outer one. Escudier *et al.* [22] investigated the flow structure in a Taylor-Couette geometry with a radius ratio of 0.5. Axial and tangential velocity measurements were made using Laser Doppler Anemometry for a 0.15% aquesous solution of xanthan gum, whose rheological behavior is described by a power-law model with a shear-thinning index $n_p \approx 0.45$. The results show an axial shift of the vortices towards the radial outflow boundary slightly more pronounced for a shear-thinning fluid than for a Newtonian fluid. Except for this issue dealing with the position of the vortex, results are very sparse. For instance, there is no indication on the influence of shear-thinning effects on the strength of the radial outflow and radial inflow, nor on the azimuthal streaks in outflow and inflow regions, nor on the modification of the viscosity field by Taylor vortices particularly in a wide annular space and strong shear-thinning effects. It is clear that a more clear understanding and characterization of supercritical Taylor vortex flow of a shear-thinning fluid is needed.

To our best knowledge, there are no theoretical nor numerical studies on shear-thinning effects in Taylor vortex flow structure.

### 2.1.2 Objectives, methodology and outline of the paper

The objective of the present work is to examine the effects of the nonlinear relation between the viscosity and the shear rate on the flow structure, the viscosity field and the

torque applied on the inner cylinder. Actually, there is an interplay between nonlinear inertia terms and nonlinear viscous terms. Based on the experimental results such the streamline patterns in Taylor vortices represented by Escudier et al. [22] and the spatio-temporal plots reported by Cagney and Balabani [24] for different shear-thinning fluids, the Taylor vortex flow observed can be considered as periodic with a wavenumber $k$ close to the critical value $k_c$. Here we take $k = k_c$ and we concentrate on solutions that consist of this mode plus modes that can be generated from it through the nonlinearity. A weakly nonlinear analysis based on the amplitude expansion method is used as a first approach to study nonlinear effects. This method was pioneered by Watson [25] and Stuart [26] who used such expansion to describe the subcritical modes in plane Poiseuille flow below the linear instability threshold. Herbert [27] and Sen & Venkateswarlu [28] improved Watson's expansion method by making a definition of the disturbance amplitude clear. Another alternative is the multiple scales method. Fujimura [29] demonstrated the complete equivalence between these two methods. Here, we focus on the case of a wide gap with $\eta = 0.4$, where shear-thinning are more pronounced. The case of a narrow gap is briefly discussed in the last section.

The chapter is organized as follows. In § 2.2, we formulate the physical problem, state the governing equations and define the dimensionless parameters. The velocity and viscosity profiles of the base state are discussed and the perturbation equations are derived. Subsequently, the linear stability analysis is presented in section 2.3. In § 2.4, the main steps of the weakly nonlinear analysis are outlined. The results are presented and discussed in § 2.5. The contribution of the nonlinear viscous terms on the saturated coefficient at cubic order in the amplitude equation is analysed. Departing from the onset, the weakly nonlinear analysis is carried out up to seventh-order in the amplitude equation. The influence of shear-thinning effects on the flow structure, the viscosity field and the torque applied on the inner cylinder is highlighted. Finally, § 2.6 is devoted to a concluding discussion.

## 2.2 Physical and mathematical model

### 2.2.1 Basic formulation

We consider the flow of an incompressible shear-thinning fluid between two coaxial cylinders of inner and outer radii $\hat{R}_1$ and $\hat{R}_2$ respectively. The radius ratio is $\eta = \hat{R}_1/\hat{R}_2$. The outer cylinder is at rest and the inner cylinder rotates with an angular velocity $\hat{\Omega}_1$. The cylinders are assumed to be infinite. The incompressibility condition and the momentum equations read

$$\mathbf{div}\,\boldsymbol{U} = 0 \tag{2.1}$$

$$\partial_t \boldsymbol{U} + Re\,(\boldsymbol{\nabla U})\cdot\boldsymbol{U} = -\boldsymbol{\nabla} P + \mathbf{div}\,(\boldsymbol{\tau})\ , \tag{2.2}$$

where $\boldsymbol{U} = U\mathbf{e}_r + V\mathbf{e}_\theta + W\mathbf{e}_z$ is the velocity vector in cylindrical coordinates $(r, \theta, z)$, $P$ a generalized pressure which includes the effect of gravity, $\hat{\boldsymbol{\tau}}$ the deviatoric extra-stress tensor, and $Re$ is the Reynolds number :

$$Re = \hat{\rho}\,\hat{\Omega}_1\hat{R}_1\hat{d}/\hat{\mu}_0\,. \tag{2.3}$$

The quantities defined with a hat $(\hat{.})$ are dimensional, while quantities without $(\hat{.})$ are dimensionless. To scale these equations, we have followed Chossat & Iooss [30], with the aim of maintaining some compatibility between the notations used here and those found in the literature for Newtonian fluids. Lengths are scaled with the annular gap $\hat{d} = \hat{R}_2 - \hat{R}_1$. Velocities are scaled with $\hat{R}_1\hat{\Omega}_1$. Time is scaled with a viscous diffusion time $\hat{\rho}\,\hat{d}^2/\hat{\mu}_0$, where $\hat{\rho}$ and $\hat{\mu}_0$ are the density a characteristic viscosity of the fluid. The pressure and the deviatoric stress are scaled with $\hat{\mu}_0\hat{R}_1\hat{\Omega}_1/\hat{d}$. To the previous equations, we add the no-slip and impermeability conditions at the walls,

$$U = W = 0,\ V = 1 \quad \text{at} \quad r = R_1, \tag{2.4}$$

$$U = V = W = 0 \qquad \text{at} \quad r = R_2, \tag{2.5}$$

where $R_1 = \eta/(1-\eta)$ and $R_2 = 1/(1-\eta)$. The fluid is assumed to be purely viscous. The constitutive equation reads :

$$\boldsymbol{\tau} = \mu(Re, \Gamma)\dot{\boldsymbol{\gamma}} \quad \text{with} \quad \dot{\boldsymbol{\gamma}} = \boldsymbol{\nabla U} + (\boldsymbol{\nabla} U)^T\,, \tag{2.6}$$

where the second invariant of the strain-rate tensor is expressed as

$$\Gamma = \frac{1}{2}\dot{\boldsymbol{\gamma}} : \dot{\boldsymbol{\gamma}} = \frac{1}{2}\dot{\gamma}_{ij}\dot{\gamma}_{ij}\,. \tag{2.7}$$

In Equation 2.7, the Einstein's summation convention for repeated indices is used.

### 2.2.2 Carreau model

Although the equations derived here are valid for any nonlinear purely viscous fluid, for numerical applications, a rheological model has to be chosen to describe the shear-thinning behavior. We have chosen the Carreau model [31] because it has a sound theoretical basis and is $C^\infty$ with respect to $\Gamma$, unlike the power-law model or Carreau-Yasuda model which are singular at $\Gamma = 0$. The Carreau's law reads [32]

$$\frac{\hat{\mu} - \hat{\mu}_\infty}{\hat{\mu}_0 - \hat{\mu}_\infty} = \left(1 + \hat{\lambda}^2\hat{\Gamma}\right)^{(n_c-1)/2}\,, \tag{2.8}$$

where $\hat{\mu}_0$ and $\hat{\mu}_\infty$ are the dynamic viscosity at low and high shear rate, $n_c < 1$ the shear-thinning index and $\hat{\lambda}$ the characteristic time of the fluid. The location of the transition from the Newtonian plateau to the shear-thinning regime is determined by $\hat{\lambda}$ since $1/\hat{\lambda}$ defines the characteristic shear rate for the onset of shear-thinning. Increasing $\hat{\lambda}$ reduces

the Newtonian plateau to lower shear rates. The infinite shear viscosity $\hat{\mu}_\infty$ is generally associated with the breakdown of the fluid and is frequently significantly smaller, $(10^3 - 10^4)$ times smaller than $\hat{\mu}_0$ see Bird *et al* [32] and Tanner [33]. The ratio $\hat{\mu}_\infty/\hat{\mu}_0$ will be thus neglected in the following. This leaves three rheological parameters : $\hat{\mu}_0$, $\hat{\lambda}$ and $n_c$. The Newtonian behavior, $\hat{\mu} = \hat{\mu}_0$ is recovered by setting $n_c = 1$ or $\hat{\lambda} = 0$. It is interesting to note that when the characteristic time $\hat{\lambda}$ of the fluid is larger than the advection time $\left(\hat{d}/\hat{R}_1\right)\hat{\Omega}_1^{-1}$, the Carreau model tends towards the power-law model $\hat{\mu} = \hat{K}\hat{\Gamma}^{(n_c-1)/2}$ with a consistency $\hat{K} = \hat{\mu}_0\hat{\lambda}^{(n_c-1)/2}$. Examples of the values of the Carreau parameters can be found in the literature, particularly for solutions of xanthan gum, stiff-rode-like polymer [21, 34, 35]. Typically, the characteristic time of the fluid $\hat{\lambda}$ is of order of seconds or tens of seconds and the zero shear viscosity is of order 0.1 Pa.s or 10 Pa.s. The shear thinning index $n_c \in ]0, 1[$. In dimensionless form the Carreau's law reads

$$\mu\left(Re, \Gamma\right) = \frac{\hat{\mu}}{\hat{\mu}_0} = \left[1 + \left(\lambda Re\right)^2 \Gamma\right]^{\frac{n_c-1}{2}} \quad \text{with} \quad \lambda = \frac{\hat{\lambda}}{\hat{\rho}\,\hat{d}^2/\hat{\mu}_0}. \tag{2.9}$$

### 2.2.3 Base flow

For sufficiently small Reynolds number, the circular Couette flow is a solution of the system (3.7), (3.8), satisfying the boundary conditions (2.4) and (2.5). It is given by :

$$\boldsymbol{U}_b = (0, V_b(r), 0) \quad , \quad \frac{d}{dr}\left(r^2 \tau_{r\theta_b}\right) = 0 \quad \text{with} \quad V_b(R_1) = 1 \text{ and } V_b(R_2) = 0\,, \tag{2.10}$$

where,

$$\tau_{r\theta b} = \mu_b\left(\frac{dV_b}{dr} - \frac{V_b}{r}\right) \quad \text{with} \quad \mu_b = \mu\left(Re, \Gamma_b\right) = \left[1 + \left(\lambda Re\right)^2 \Gamma_b\right]^{(n_c-1)/2}. \tag{2.11}$$

The system (2.10), (2.11) is solved numerically using an iterative process combined with a polynomial Chebyshev approximation of the azimuthal velocity profile [16, 15]. One must notice that contrarily to the Newtonian case, for a non-Newtonian fluid, the dimensionless base flow $\boldsymbol{U}_b$ also depends on $Re$. However, for the sake of simplicity, this dependence is left implicit. Figure 2.1 shows the effect of the shear-thinning index on the velocity and viscosity profiles at $\eta = 0.4$ and $\lambda\mathcal{R} = 100$. With increasing shear-thinning effects, the curvature of the velocity profile becomes more pronounced. The shear rate increases at the inner wall and decreases at the outer one. This results in a viscosity stratification within the gap. The viscosity as well as the degree of viscosity stratification defined by $d\mu_b/dr$ increases from the inner to the outer wall. For sufficiently strong shear-thinning effects, a thick layer of the fluid with low shear-rate and large viscosity forms at the outer wall as shown by the curve (4) in Fig. 2.1(b). In the figure 2.1(a), the velocity profiles are almost

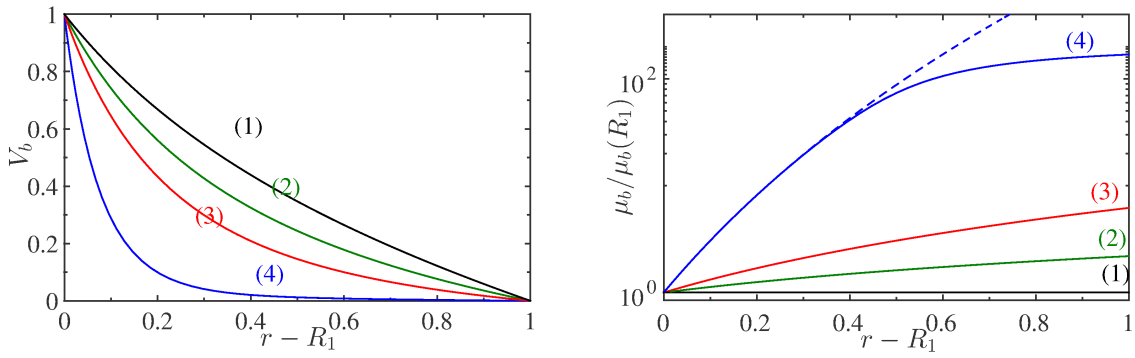


FIGURE 2.1 – (Color online) Base flow for Carreau fluids at $\eta = 0.4$ and $\lambda Re = 100$. Influence of shear-thinning index $n_c$ on the velocity **(a)** and viscosity **(b)** profiles. (1) $n_c = 1$ (Newtonian fluid) ; (2) $n_c = 0.7$ ; (3) $n_c = 0.5$ and (4) $n_c = 0.2$. Dashed line is the viscosity profile for a power-law fluid with $n_p = 0.2$.

the same as those obtained for a power-law fluid,

$$V_b(r) = \frac{r}{R_1}\left[1 - \left(\frac{1}{R_2^{2/n_p}} - \frac{1}{R_1^{2/n_p}}\right)^{-1}\left(\frac{1}{r^{2/n_p}} - \frac{1}{R_1^{2/n_p}}.\right)\right] \tag{2.12}$$

It is the same for the viscosity profiles except for $n_c = 0.2$ and $\eta = 0.4$, where a difference is observed near the outer cylinder. Actually at $\eta = 0.4$, the numerical results show that there is no significant difference between Carreau and power-law velocity profiles when $\lambda Re \geq 10$. However, for the viscosity profiles a larger value of $\lambda Re$ is needed to reduce the difference observed near the outer cylinder, particularly for low values of $n_c$.

### 2.2.4 Perturbation equations

The velocity $\boldsymbol{U}$ and the pressure $P$ are splitted into the basic field (with the subscript b) and the disturbance :

$$\boldsymbol{U} = \boldsymbol{U}_b + \boldsymbol{u} \qquad \text{and} \qquad P = P_b + p\,. \tag{2.13}$$

Substituting $\boldsymbol{U}$ and $P$ by their expressions in (3.7) and (3.8) leads to

$$\boldsymbol{\nabla} \cdot u = 0\,, \tag{2.14}$$

$$\partial_t \mathbf{u} = -Re\left[\mathbf{u} \cdot \boldsymbol{\nabla}\mathbf{u} + \boldsymbol{U}_b \cdot \boldsymbol{\nabla}\boldsymbol{u} + \boldsymbol{u} \cdot \boldsymbol{\nabla}\boldsymbol{U}_b\right] - \boldsymbol{\nabla} p + \boldsymbol{\nabla} \cdot \left(\boldsymbol{\tau}(\boldsymbol{U}_b + \boldsymbol{u}) - \boldsymbol{\tau}(\boldsymbol{U}_b)\right)\,, \tag{2.15}$$

where, $\tau_{ij}\left(\boldsymbol{U}_b + \boldsymbol{u}\right) = \mu\left(\boldsymbol{U}_b + \boldsymbol{u}\right)\dot{\gamma}_{ij}\left(\boldsymbol{U}_b + \boldsymbol{u}\right)$. The boundary conditions are :

$$\boldsymbol{u} = 0 \qquad \text{and} \qquad \partial_r(\boldsymbol{u} \cdot \boldsymbol{e}_r) = 0 \quad \text{at} \quad r = R_1,\, R_2\,. \tag{2.16}$$

The second condition arises from the continuity equation. For a small amplitude disturbance, the viscosity of the perturbed flow can be expanded around the base flow as :

$$\mu\left(\boldsymbol{U}_b+\boldsymbol{u}\right)=\mu_b+\mu_1\left(\boldsymbol{u}\right)+\mu_2\left(\boldsymbol{u},\boldsymbol{u}\right)+\mu_3\left(\boldsymbol{u},\,\boldsymbol{u},\,\boldsymbol{u}\right)+\ldots, \tag{2.17}$$

where,

$$\mu_1\left(\boldsymbol{u}\right) = \left[\frac{\partial\mu}{\partial\dot{\gamma}_{ij}}\right]_b\dot{\gamma}_{ij}\left(\boldsymbol{u}\right), \tag{2.18}$$

$$\mu_2\left(\boldsymbol{u},\,\boldsymbol{u}\right) = \frac{1}{2}\left[\frac{\partial^2\mu}{\partial\dot{\gamma}_{ij}\partial\dot{\gamma}_{k\ell}}\right]_b\dot{\gamma}_{ij}\left(\boldsymbol{u}\right)\dot{\gamma}_{k\ell}\left(\boldsymbol{u}\right), \tag{2.19}$$

$$\mu_3\left(\boldsymbol{u},\,\boldsymbol{u},\,\boldsymbol{u}\right) = \frac{1}{6}\left[\frac{\partial^3\mu}{\partial\dot{\gamma}_{ij}\partial\dot{\gamma}_{k\ell}\partial\dot{\gamma}_{pq}}\right]_b\dot{\gamma}_{ij}\left(\boldsymbol{u}\right)\dot{\gamma}_{k\ell}\left(\boldsymbol{u}\right)\dot{\gamma}_{pq}\left(\boldsymbol{u}\right), \tag{2.20}$$

The deviatoric stresses in the disturbed flow can also be written as

$$\tau_{ij}\left(\boldsymbol{U}_b+\boldsymbol{u}\right)=\tau_{ij}\left(\boldsymbol{U}_b\right)+\tau_{1,ij}\left(\boldsymbol{u}\right)+\tau_{2,ij}\left(\boldsymbol{u},\boldsymbol{u}\right)+\tau_{3,ij}\left(\boldsymbol{u},\,\boldsymbol{u},\,\boldsymbol{u}\right)+\ldots, \tag{2.21}$$

with,

$$\tau_{1,ij}\left(\boldsymbol{u}\right) = \mu_b\dot{\gamma}_{ij}\left(\boldsymbol{u}\right)+\mu_1\left(\boldsymbol{u}\right)\dot{\gamma}_{ij}(\boldsymbol{U}_b), \tag{2.22}$$

$$\tau_{2,ij}\left(\boldsymbol{u},\,\boldsymbol{u}\right) = \mu_2\left(\boldsymbol{u}\,,\boldsymbol{u}\right)\dot{\gamma}_{ij}\left(\boldsymbol{U}_b\right)+\mu_1\left(\boldsymbol{u}\right)\dot{\gamma}_{ij}\left(\boldsymbol{u}\right), \tag{2.23}$$

$$\tau_{3,ij}\left(\boldsymbol{u},\,\boldsymbol{u}\right) = \mu_3\left(\boldsymbol{u}\,,\boldsymbol{u}\,,\boldsymbol{u}\right)\dot{\gamma}_{ij}\left(\boldsymbol{U}_b\right)+\mu_2\left(\boldsymbol{u},\,\boldsymbol{u}\right)\dot{\gamma}_{ij}\left(\boldsymbol{u}\right). \tag{2.24}$$

In the case of a circular Couette flow of a viscous fluid, we have $\dot{\gamma}^b_{ij}=0$, if $ij\neq r\theta$, $\theta r$ and $\dot{\gamma}^b_{r\theta}=DV^b-V^b/r$, where $D\equiv d/dr$. Setting $\Gamma_b=\left(\dot{\gamma}^b_{r\theta}\right)^2$ and $\Gamma_2=(1/2)\dot{\gamma}_{ij}(\boldsymbol{u})\dot{\gamma}_{ij}(\boldsymbol{u})$, the expressions of $\mu_1,\mu_2$ and $\mu_3$ can be simplified,

$$\mu_1 = 2\left[\frac{d\mu}{d\Gamma}\right]_b\dot{\gamma}^b_{r\theta}\dot{\gamma}_{r\theta}(\boldsymbol{u}), \tag{2.25}$$

$$\mu_2 = \left[\frac{d\mu}{d\Gamma}\right]_b\Gamma_2+2\left[\frac{d^2\mu}{d\Gamma^2}\right]_b\Gamma_b\dot{\gamma}^2_{r\theta}(\boldsymbol{u}), \tag{2.26}$$

$$\mu_3 = 2\left[\frac{d^2\mu}{d\Gamma^2}\right]_b\dot{\gamma}^b_{r\theta}\dot{\gamma}_{r\theta}(\boldsymbol{u})\Gamma_2+\frac{4}{3}\left[\frac{d^3\mu}{d\Gamma^3}\right]_b\left(\dot{\gamma}^b_{r\theta}\right)^3\dot{\gamma}^3_{r\theta}(\boldsymbol{u}). \tag{2.27}$$

Replacing $\mu_1$, $\mu_2$, $\mu_3$ by their expressions (2.25)-2.27) into equations (2.22)-(2.24), we obtain

$$\tau_{1,ij} = \mu_b \dot{\gamma}_{ij}(\boldsymbol{u}) \qquad \text{if} \qquad ij \neq r\theta, \theta r\,, \tag{2.28}$$

$$\tau_{1,r\theta} = \left[\mu_b + 2\left(\frac{d\mu}{d\Gamma}\right)_b \left(\dot{\gamma}^b_{r\theta}\right)^2\right] = \mu_t \dot{\gamma}_{r\theta}(\boldsymbol{u})\,, \tag{2.29}$$

$$\tau_{2,ij} = \mu_1 \dot{\gamma}_{r\theta}(\boldsymbol{u}) \qquad \text{if} \qquad ij \neq r\theta, \theta r\,, \tag{2.30}$$

$$\tau_{2,r\theta} = \mu_2 \dot{\gamma}^b_{r\theta} + \mu_1 \dot{\gamma}_{r\theta}(\boldsymbol{u})\,, \tag{2.31}$$

$$\tau_{3,ij} = \mu_2 \dot{\gamma}_{r\theta}(\boldsymbol{u}) \qquad \text{if} \qquad ij \neq r\theta, \theta r\,, \tag{2.32}$$

$$\tau_{3,r\theta} = \mu_3 \dot{\gamma}^b_{r\theta} + \mu_2 \dot{\gamma}_{r\theta}(\boldsymbol{u})\,. \tag{2.33}$$

In equation (2.29), $\mu_t$ is the tangent viscosity. For one dimensional shear flow with the velocity $V_b(r)$ in the azimuthal direction, the tangent viscosity is given by $\mu_t = (\partial\mu/\partial\dot{\gamma}_{r\theta})_b$. Note that for simplicity of writing, we preferred to write the viscosity as a function of $\boldsymbol{U_b}$ and $\boldsymbol{u}$ rather than $Re, \Gamma_b$ and $\Gamma_2$.
Here, we consider axisymmetric disturbances. For generalized Newtonian fluids and in the case where the outer cylinder is fixed and the inner one is rotating, the numerical tests performed by Alibenyahia *et al* [16] and Agbessi *et al* [15], for a large range of rheological parameters, showed that the least stable mode is axisymmetric. In this case, the continuity simplifies and is satisfied via introduction of a streamfunction $\psi$

$$u = -\frac{1}{r}\frac{\partial\psi}{\partial z} \quad \text{and} \quad w = \frac{1}{r}\frac{\partial}{\partial r}(\psi)\,. \tag{2.34}$$

However, it is found that it is more convenient to work with $\phi = \dfrac{\psi}{r}$ in terms which

$$u = -\frac{\partial\phi}{\partial z} \quad \text{and} \quad w = \frac{1}{r}\frac{\partial}{\partial r}(r\phi) \tag{2.35}$$

Cross-differentiating $r$- and $z$- momentum equations and eliminating the pressure, we obtain

$$\frac{\partial\Omega}{\partial t} = Re\left[\frac{\partial\phi}{\partial z}D\Omega - D_*\phi\frac{\partial\Omega}{\partial z} - \frac{1}{r}\frac{\partial\phi}{\partial z}\Omega - \frac{2}{r}v\frac{\partial v}{\partial z} - 2\frac{V_b}{r}\frac{\partial v}{\partial z}\right] + \left(DD_* - \frac{\partial^2}{\partial z^2}\right)\tau_{rz} + \frac{\partial}{\partial z}\left(D\tau_{zz} - D_*\tau_{rr} + \frac{\tau_{\theta\theta}}{r}\right) \tag{2.36}$$

$$\frac{\partial v}{\partial t} = Re\left(\frac{\partial\phi}{\partial z}D_*v - D_*\phi\frac{\partial v}{\partial z} + \frac{\partial\phi}{\partial z}D_*V_b\right) + \frac{1}{r^2}D\left(r^2\tau_{r\theta}\right) + \frac{\partial}{\partial z}\tau_{\theta z}\,, \tag{2.37}$$

where, $D \equiv \dfrac{\partial}{\partial r}$, $D_* \equiv D + \dfrac{1}{r}$ and $\Omega = \left(DD_* + \dfrac{\partial^2}{\partial z^2}\right)\phi$ the azimuthal vorticity.

## 2.3 Linear stability analysis

The linearized version of the disturbance equations (2.36) and (2.37) is

$$\frac{\partial \Omega}{\partial t} = -2Re\frac{V_b}{r}\frac{\partial v}{\partial z} + \left(DD_* - \frac{\partial^2}{\partial z^2}\right)\tau_{1,rz} + \frac{\partial}{\partial z}\left(D\tau_{1,zz} - D_*\tau_{1,rr} + \frac{\tau_{1,\theta\theta}}{r}\right), \quad (2.38)$$

$$\frac{\partial v}{\partial t} = Re(D_*V_b)\frac{\partial \phi}{\partial z} + \frac{1}{r^2}D\left(r^2\tau_{1,r\theta}\right) + \frac{\partial}{\partial z}\tau_{1,\theta z}\,. \quad (2.39)$$

### 2.3.1 Direct mode

Using the invariance of equations (2.38), (2.39) (by translation along the axial direction, reflection $z \to -z$ ), we seek the eigenmodes in the following form :

$$(\phi,\, v) = (F_{11}(r),\, V_{11}(r))\exp\left(st + ikz\right)\,, \quad (2.40)$$

where $k \in \mathbb{R}$, is the axial wavenumber and $s = s_r + is_i$ a complex eigenvalue. Its real part $s_r$ is the growth-rate of the disturbance and the imaginary part allows to define the axial phase velocity. Substituting (2.40) into (2.38) and (2.39) :

$$s\left(DD_* - k^2\right)F_{11} = -2ikRe\frac{V_b}{r}V_{11} + \left(DD_* - k^2\right)\left[\mu_b\left(DD_* - k^2\right)F_{11}\right] + 2k^2\left(D^2\mu_b\right)F_{11}\,, \quad (2.41)$$

$$sV_{11} = ikRe\left(D_*V_b\right)F_{11} + \frac{1}{r^2}D\left[r^2\mu_t\left(DV_{11} - \frac{V_{11}}{r}\right)\right] - k^2\mu_bV_{11}\,, \quad (2.42)$$

with

$$F_{11} = DF_{11} = V_{11} = 0 \quad \text{at} \quad r = R_1, R_2\,. \quad (2.43)$$

The set of differential equations (2.41) and (2.42) is an eigenvalue problem where $s$ is an eigenvalue and $\boldsymbol{X}_{11} = (F_{11}, V_{11})$ the eigenvector. It can be written formally as

$$s\boldsymbol{M}\cdot\boldsymbol{X}_{11} = \boldsymbol{L}\cdot\boldsymbol{X}_{11}\,. \quad (2.44)$$

Since any multiple of the eigenvector $\boldsymbol{X}_{11}$ is also solution of (2.43), $\boldsymbol{X}_{11}$ can be normalized such that

$$\max(V_{11}) = 1. \quad (2.45)$$

The eigenvalue problem (2.44) with the boundary conditions (2.43) is solved using a spectral collocation method based on Chebyshev polynomials evaluated at $N+1$ collocation points of the Gauss-Lobatto method. The matrix eigenvalue problem that results is solved using QZ algorithm with Matlab. To test the convergence of the numerical method, the computations of the critical conditions are made with different spectral truncation

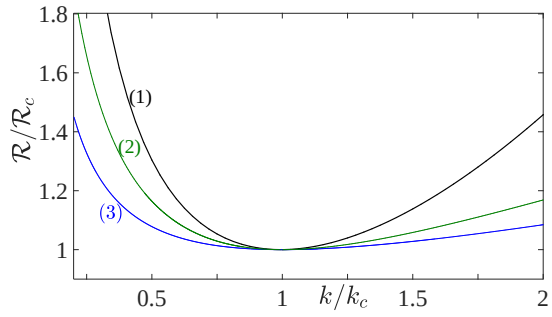


FIGURE 2.2 – (Color online) Normalized marginal stability curves at $\eta = 0.4$ for a Newtonian fluid (1) where $Re_c = 68.3$, and $k_c = 3.183$ and Carreau fluids : (2) $n_c = 0.5$, $\lambda = 1$, $Re_c = 16.57$, $k_c = 3.487$ ; (3) $n_c = 0.2$, $\lambda = 44$, $Re_c = 2.282$, $k_c = 8.355$.

$N$. It is observed that 40 collocation points provide sufficient accuracy for the rheological parameters considered here. The results given in the paper are obtained with $N = 50$. Marginal stability curves are determined for different rheological parameters ($n_c$ and $\lambda$). The minimum of these curves gives the critical conditions $Re_c$ and $k_c$. In Figure 2.2, normalized marginal stability curves, $Re/Re_c$ vs $k/k_c$ are shown for a Newtonian fluid and for Carreau fluids. It is interesting to observe that the marginal stability curves flatten with increasing shear-thinning effects. The curvature at threshold allows to define the coherence length of perturbations $\xi_0 = \frac{1}{2Re_c}\left(\frac{\partial^2 Re}{\partial k^2}\right)_{Re_c,k_c}$. To evaluate the second derivative, we have followed the methodology described in [36]. The variation of $\xi_0$ as a function of the shear-thinning index $n_c$ for different values of $\lambda$ is shown in figure 2.3. It can be observed that the coherence length of perturbations decreases with decreasing $n_c$. This effect is particularly significant for very low values of $n_c$.

A second feature of shear-thinning effects is highlighted by eigenvalues spectra. They are shown in Fig. 2.4 at the critical conditions with $\eta = 0.4$, for a Newtonian and a Carreau-fluid with $n_c = 0.2$ and $\lambda = 44$. The eigenvalues are real or complex conjugate [37]. However, the first eigenvalue that crosses the real axis is always real in agreement with the principle of stability exchange [37]. One can note that with increasing shear-thinning effects, the relaxation times of the eigenmodes become closer one to another. For instance, for a Newtonian fluid at the critical conditions, the first eigenvalue is $s_1 = -8.0 \times 10^{-6}$ and the second one is $s_2 = -44.5$ while for a Carreau fluid with $n_c = 0.2$, $\lambda = 44$, we have $s_1 = -1.808 \times 10^{-6}$ and $s_2 = -1.726$. The variation of the critical Reynolds number as a function of the shear-thinning index $n_c$, at $\eta = 0.4$ is shown in figure 2.5(a) for different values of the dimensionless characteristic time $\lambda$. With the definition (3.6) of $Re$, the influence of shear-thinning appears destabilizing. Opposite effects can be found by using a Reynolds number defined with the viscosity $\mu_{bw}$ evaluated at the inner wall, $Re_w = Re/\mu_{bw}$. The selection of the viscosity scale may be considered a matter of choice, however the conclusion that one reaches by comparing shear-thinning fluids among themselves and against Newtonian fluid can be radically different from one choice to another. The influence of the

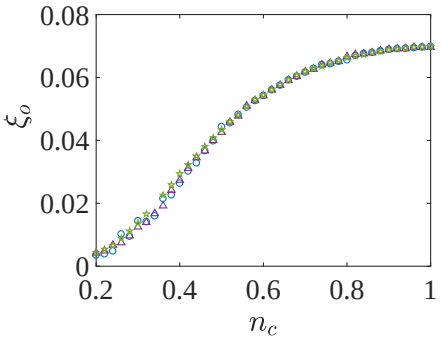


FIGURE 2.3 – (Color online) Variation of characteristic length $\xi_0$ as a function of the shear-thinning index $n_c$ for different values of $\lambda : \lambda = 1(\star), \lambda = 10(\triangle), \lambda = 100(\circ)$.

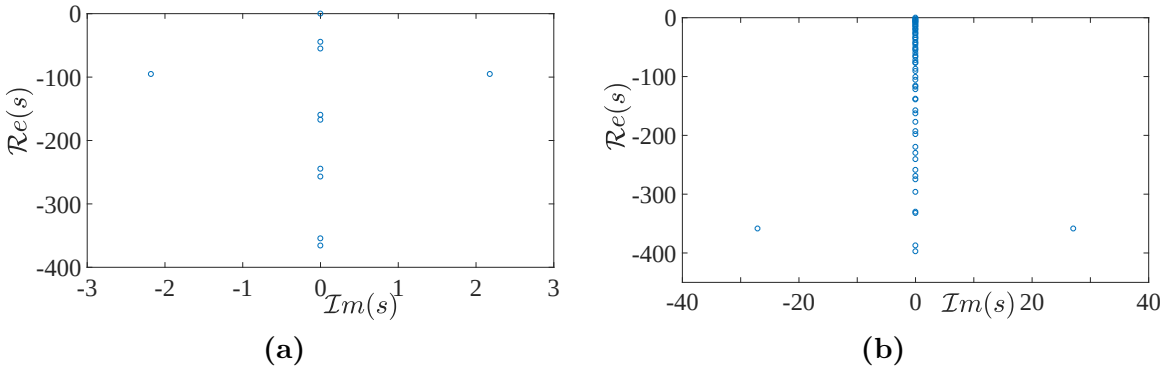


FIGURE 2.4 – (Color online) Eigenspectra for axisymmetric perturbations at critical conditions with $\eta = 0.4$. **(a)** Newtonian fluid at $Re_c = 68.296$, $k_c = 3.183$. **(b)** Carreau fluid with $n_c = 0.2$, $\lambda = 44$ at $Re_c = 2.282$, $k_c = 8.355$ .

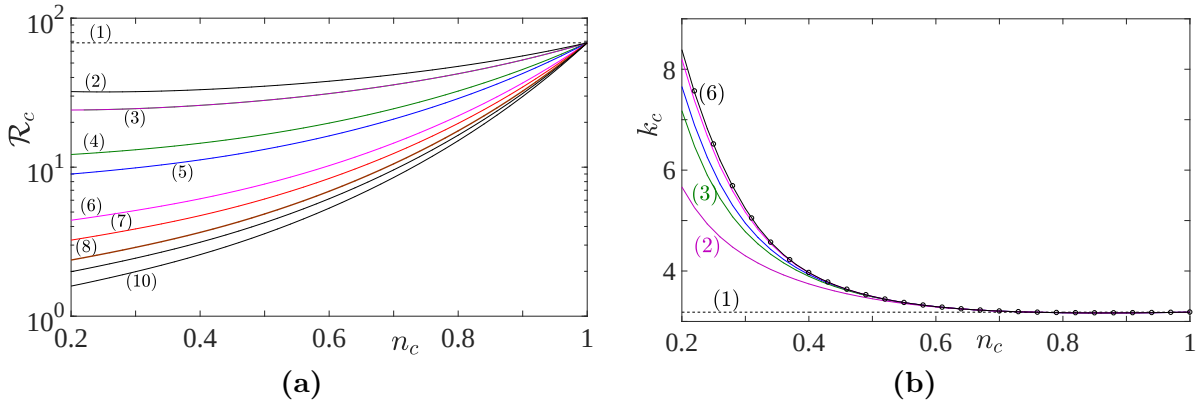


FIGURE 2.5 – (Color online) Carreau fluid. **(a)** Variation of the critical Reynolds number as function of shear-thinning index for different values of dimensionless constant time $\lambda$. (1) $\lambda = 0$ (Newtonian fluid) ; (2) $\lambda = 0.1$ ; (3) $\lambda = 0.2$ ; (4) $\lambda = 1$ ; (5) $\lambda = 2$ ; (6) $\lambda = 10$ ; (7) $\lambda = 20$ ; (8) $\lambda = 40$ ; (9) $\lambda = 60$ ; (10) $\lambda = 100$. **(b)** Variation of the critical axial wavenumber as function of shear-thinning index for different values of $\lambda$. (1) $\lambda = 0$ (Newtonian fluid) ; (2) $\lambda = 0.2$ ; (3) $\lambda = 1$ ; (4) $\lambda = 2$ ; (5) $\lambda = 10$ ; (6) $\lambda = 100$. The symbol ($\circ$) corresponds to a power-law fluid.

rheological parameters $n_c$ and $\lambda$ on the axial wave number and therefore on the size of the Taylor vortices is represented in figure 2.5(b). With increasing shear-thinning effects, the axial wavelength, $2\pi/k_c$ decreases significantly because of a strong viscosity stratification. As indicated in the analysis of the base flow, for weak values of $n_c$ and large values of $\lambda$, a highly viscous fluid layer adjacent to the outer wall is formed.

The structure of the critical eigenfunctions is depicted in figure 2.6 for $\lambda = 44$ and different values of $n_c$. Here $V_{11}(r)$ is a real-valued function, whereas $F_{11}(r)$ is purely imaginary. With increasing shear-thinning effects, variations of $F_{11}(r)$ and $V_{11}(r)$ are mainly confined in a thin layer adjacent to the inner cylinder where the viscosity is lower, and a large part of the annular space is unaffected by the perturbation : the vortices are squeezed against the inner wall. Furthermore, the eigenfunction and consequently the associated radial and axial velocity components are strongly reduced.

**Remarks**

- The validity of our program has been tested by comparing our results to the ones of Chandrasekhar [38] for a Newtonian fluid at different radius ratios $\eta$. A very good agreement is found as indicated by Tab. 3.4 (in Appendix 2.A). For the Carreau model, the critical Reynolds number can be recalculated in terms of the inner wall shear viscosity and compared with the values given by Alibenyahia et al. [16]. Again, a very good agreement is found as shown by Tab. 3.5 (Appendix 2.A).

- The bifurcation from a stationary circular Couette flow to a stationary Taylor vortex flow discussed above is not specific to Carreau model. Actually, the principle of exchange of stability holds for any purely viscous non-Newtonian fluid, where the instability of the circular Couette flow is inertial. Therefore, the oscillating mode observed for instance by

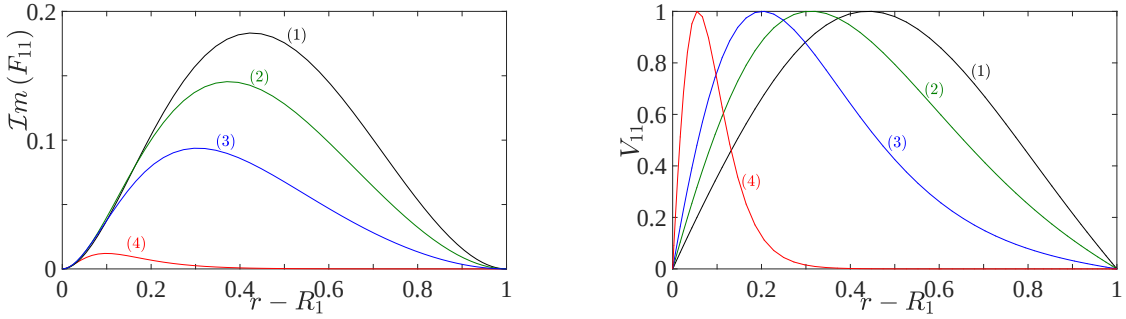


FIGURE 2.6 – (Color online) Critical eigenfunctions at $\eta = 0.4$, for Carreau fluids with $\lambda = 44$ and different values of the shear-thinning index : (1) $n_c = 1$, $Re_c = 68.296$ ; (2) $n_c = 0.7$, $Re_c = 10.301$ ; (3) $n_c = 0.5$, $Re_c = 4.702$ and (4) $n_c = 0.2$, $Re_c = 2.282$.

Crumeyrolle *et al.* [39] at the onset for some polymer solutions which are viscoelastic and shear-thinning is a signature of the emergence of elastic effects.

### Linear energy equation

The linear energy equation is derived by multiplying (2.41), (2.42) by $r$ times the complex conjugate $(F_{11}^*, V_{11}^*)^T$ then integrating between the two cylinders. One obtains

$$Ree(s)\left\langle k^2|F_{11}|^2 + |V_{11}|^2 + |D_* F_{11}|^2 \right\rangle = ReJ_I - J_{\mu_b} + J_{\mu_b - \mu_t}, \tag{2.46}$$

where $\langle(.)\rangle = \int_{R_1}^{R_2} (.) r \, \mathrm{d}r$, $J_I$, $J_{\mu_b}$ and $J_{\mu_b - \mu_t}$ denote inertial and viscous contributions to the kinetic energy growth of the perturbation. They are defined by :

$$J_I = -\left\langle \dot{\gamma}^b_{r\theta} \left(-ik_c F_{11}\right) V_{11}^* \right\rangle, \tag{2.47}$$

$$J_{\mu_b} = \left\langle \mu_b \left[ \frac{1}{2} \left( \left|\dot{\gamma}'_{\theta\theta}\right|^2 + \left|\dot{\gamma}'_{zz}\right|^2 + \left|\dot{\gamma}'_{rr}\right|^2 \right) + \left|\dot{\gamma}'_{rz}\right|^2 + \left|\dot{\gamma}'_{r\theta}\right|^2 + \left|\dot{\gamma}'_{\theta z}\right|^2 \right] \right\rangle, \tag{2.48}$$

$$J_{\mu_b - \mu_t} = \left\langle \left(\mu_b - \mu_t\right) \left|\dot{\gamma}'_{r\theta}\right|^2 \right\rangle, \tag{2.49}$$

with $\dot{\gamma}'_{ij} = \dot{\gamma}_{ij}(\boldsymbol{u})$. At criticality, the transfer of energy from the base flow to the perturbation $Re\, J_I$ is exactly balanced by the viscous dissipation $(J_{\mu_b} - J_{\mu_b - \mu_t})$. The decrease of the critical Reynolds number with increasing shear-thinning effects means that

$$Re_c = \frac{J_{\mu_b} - J_{\mu_b - \mu_t}}{J_I} \tag{2.50}$$

decreases with increasing shear-thinning effects. The term $J_{\mu_b - \mu_t}$ originates in the viscosity perturbation. It is positive definite and produces a reduction of the viscous dissipation and thus a decrease of the critical Reynolds number. This decrease is quite modest as it is shown by figure 2.7, where $Re_c$ is compared with that obtained when the viscosity per-

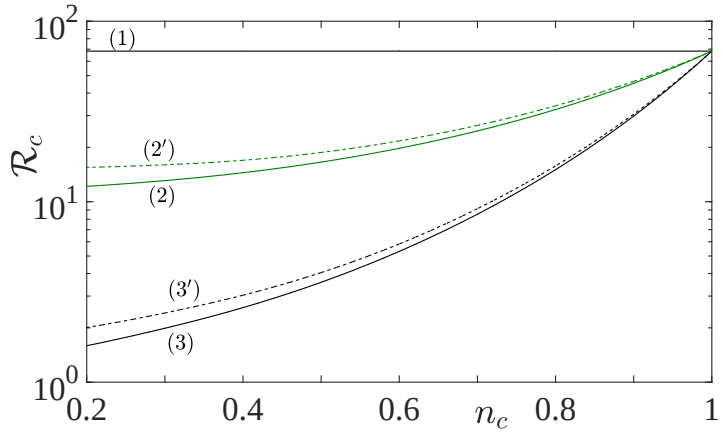


FIGURE 2.7 – (Color online) Critical Reynolds number as a function of the shear-thinning index for Carreau fluids at $\lambda = 1$, curves (2) and (2') and $\lambda = 100$, curve (3) and (3'). In the curves (2) and (3), the viscosity perturbation is taken into account. In the curves (2') and (3'), the viscosity perturbation is not taken into account. Curve (1) is represented as a reference and corresponds to the Newtonian case.

turbation is not taken into account.

The numerical results show that $J_I$ and $J_{\mu_b}$ decrease with increasing shear-thinning effects. However, $J_{\mu_b}$ decrease faster than $J_I$. Thus $Re_c$ decreases with increasing shear-thinning effects. The integrand of $J_I$ contains $\dot{\gamma}_{r\theta b}$ and the quadratic product of the eigenfunctions. The integrand of $J_{\mu_b}$ contains $\mu_b$, the quadratic product of the eigenfunctions and their first derivatives. The eigenfunctions are normalized such that $max\,(V_{11}) = 1$.

The variations of $J_I$ and $J_{\mu_b}$ with shear-thinning effects, has to be due to change with $n_c$ (for instance), in either $\dot{\gamma}_{r\theta b}$, $\mu_b$ or the eigenfunctions.

Figure 10(a) shows that the integrand of $J_{\mu_b}$ decreases with increasing shear-thinning effects. Figure 10(b) shows that the eigenfunctions contribute to increase the viscous dissipation. Therefore the decrease of $J_{\mu_b}$ is due to $\mu_b$.

Analysis of figures 9(a) and 10(a), show that the eigenfunctions contribute to a decrease of $J_I$. The shear rate $\dot{\gamma}_{r\theta b}$ attenuates this decrease and amplifies the transfer of energy from the base flow to perturbation. Consequently, it appears that changes in the eigenfunctions with shear-thinning effects cannot be responsible for the decrease of $Re_c$ and the effect has to be due to the change in the base flow : increase of the shear-rate and decrease of the viscosity near the inner wall.

### 2.3.2 Characteristic time

In the neighborhood of the critical conditions such that $(Re - Re_c)/Re_c = \epsilon << 1$, the growth rate can be approximated using Taylor expansion

$$s = \frac{\epsilon}{\tau_0} + O\left(\epsilon^2\right), \tag{2.51}$$

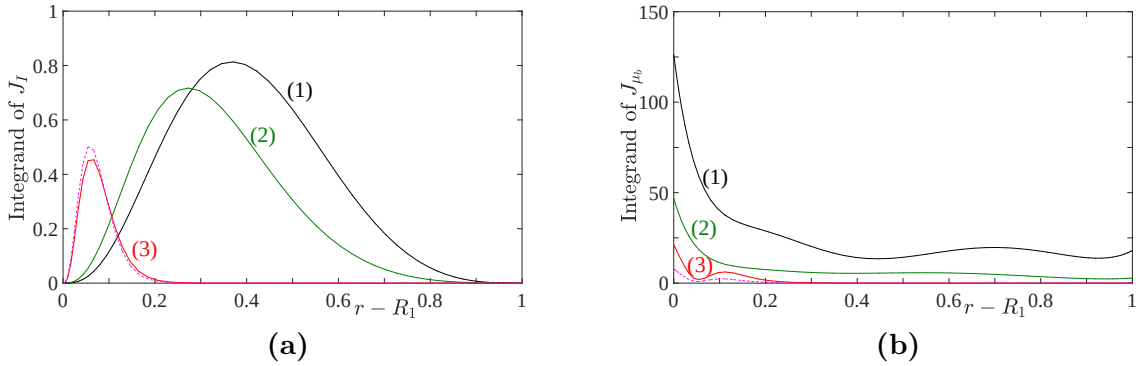


FIGURE 2.8 – (Color online) Integrands of $J_I$ **(a)** and $J_{\mu_b}$ **(b)** at critical conditions : (1) Newtonian fluid ; (2) Carreau fluid with $n_c = 0.7, \lambda = 1$ ; (3) Carreau fluid with $n_c = 0.2$, $\lambda = 1$ ; (4 dashed line) Carreau fluid with $n_c = 0.2, \lambda = 10$.

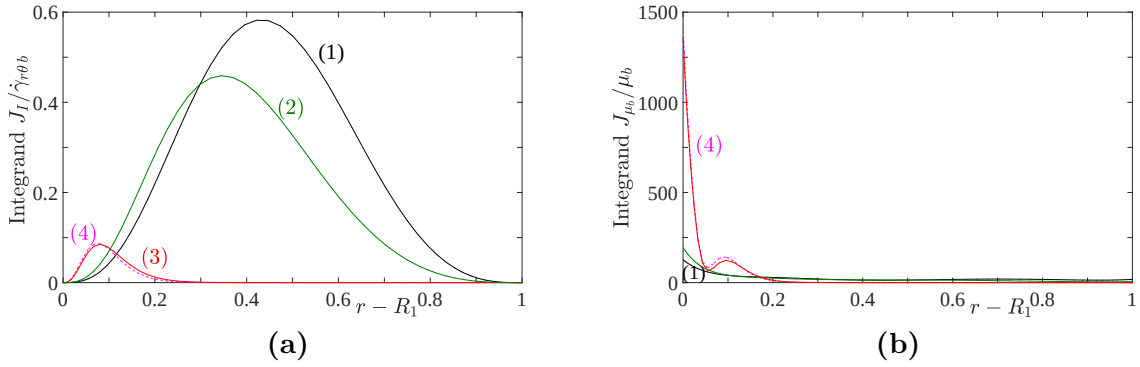


FIGURE 2.9 – (Color online) Integrands of $J_I/\dot{\gamma}_{r\theta b}$ **(a)** and $J_{\mu_b}/\mu_b$ **(b)** at critical conditions : (1) Newtonian fluid ; (2) Carreau fluid with $n_c = 0.7, \lambda = 1$ ; (3) Carreau fluid with $n_c = 0.2$, $\lambda = 1$ ; (4 dashed line) Carreau fluid with $n_c = 0.2, \lambda = 10$.

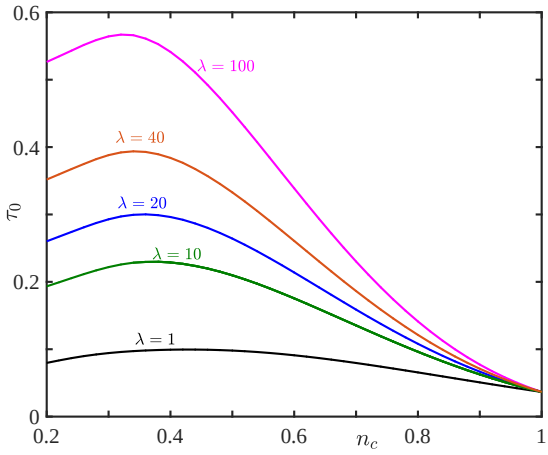


FIGURE 2.10 – (Color online) Variation of the characteristic time of circular Couette flow instability as function of the shear-thinning index for different values of the dimensionless constant-time of the fluid. The radius ratio is $\eta = 0.4$.

where $\tau_0$ is the characteristic time for the instability to grow. The determination of $\tau_0$ can be obtained by evaluating $\left(\frac{ds}{d\epsilon}\right)_{\epsilon=0}$ ($s$ is calculated for different values of $\epsilon$, around $\epsilon = 0$). Figure 2.10 shows for a Carreau fluid, the variation of $\tau_0$ as a function of the shear-thinning index $n_c$ for different values of $\lambda$. The characteristic time for the instability to grow increases significantly with $\lambda$, reaches a maximum at $n_c \approx 0.3$ then decreases slightly as $n_c$ decreases. These results reveal that the onset of Taylor vortex flow is much more gradual for a shear-thinning fluid than for a Newtonian fluid.

### 2.3.3 Adjoint mode

To the direct problem (2.44) is associated the adjoint problem

$$s\boldsymbol{M}^{+} \cdot \boldsymbol{X}_{ad} = \boldsymbol{L}^{+} \cdot \boldsymbol{X}_{ad} \quad \text{with} \quad \boldsymbol{X}_{ad} = (F_{ad}, V_{ad}) \; . \tag{2.52}$$

The adjoint operators $\boldsymbol{M}^{+}$ and $\boldsymbol{L}^{+}$ are defined by

$$\langle \boldsymbol{X}_{ad}, \boldsymbol{M} \cdot \boldsymbol{X} \rangle = \langle \boldsymbol{M}^{+} \cdot \boldsymbol{X}_{ad}, \boldsymbol{X} \rangle \quad \text{and} \quad \langle \boldsymbol{X}_{ad}, \boldsymbol{L} \cdot \boldsymbol{X} \rangle = \langle \boldsymbol{L}^{+} \cdot \boldsymbol{X}_{ad}, \boldsymbol{X} \rangle \, , \tag{2.53}$$

with the inner product between two vector functions $\boldsymbol{f}(r)$ and $\boldsymbol{g}(r)$,

$$\langle \boldsymbol{f}, \boldsymbol{g} \rangle = \int_{R_1}^{R_2} \boldsymbol{f}^{*} \cdot \boldsymbol{g} \, r \, dr \, , \tag{2.54}$$

where $f^*$ is the complex conjugate of $f$. The adjoint problem associated to (2.41), (2.42) is

$$s\left(DD_*-k^2\right)F_{ad}=ikRe\frac{V_b}{r}V_{ad}+\left(DD_*-k^2\right)\left[\mu_b\left(DD_*-k^2\right)F_{ad}\right]+ 2k^2\left(D^2\mu_b\right)F_{ad}\,, \tag{2.55}$$

$$sV_{ad}=-2ikRe\left(D_*V_b\right)F_{ad}+\frac{1}{r^2}D\left[r^2\mu_t\left(DV_{ad}-\frac{V_{ad}}{r}\right)\right]-k^2\mu_bV_{ad}\,, \tag{2.56}$$

with

$$F_{ad}=DF_{ad}=V_{ad}=0\quad\text{at}\quad r=R_1,R_2. \tag{2.57}$$

## 2.4 Weakly nonlinear stability analysis

### 2.4.1 Principle and formulation

A weakly nonlinear analysis using the amplitude expansion method is used as a first approach to investigate nonlinear effects. Near the bifurcation point, the dynamics are assumed to be determined by the fundamental mode with wavenumber $k=k_c$, its higher harmonics generated by the the nonlinear self-interactions and the modification of the base state due to the interactions with the complex conjugate. It is natural to write the nonlinear perturbation as the Fourier series

$$\left[\phi\left(r,z,t\right),\,v\left(r,z,t\right)\right]=\sum_{n=-\infty}^{+\infty}\left[\phi_n\left(r,t\right),v_n\left(r,t\right)\right]E^n\quad\text{with}\quad E^n=e^{ink_cz}. \tag{2.58}$$

The transient evolution of the perturbation is taken into account by the temporal evolution of the Fourier coefficients $\phi_n$ and $v_n$. Because $\phi$ and $v$ are real, we have $\phi_{-n}=\phi_n^*$ and $v_{-n}=v_n^*$, where the star denotes the complex conjugate. Substituting (2.58) into (2.36) and (2.37) and separating out the coefficients of similar exponentials, we obtain a set of nonlinear partial differential equations for the Fourier components $\phi_n$ and $v_n$ :

$$\frac{\partial}{\partial t}\mathcal{S}_n\phi_n=\mathcal{S}_n\left[\mathcal{S}_n\left(\mu_b\phi_n\right)\right]-2inkRe\frac{V_b}{r}v_n+\left[NI1\right]_{E^n}+\left[NV1\right]_{E^n}\,, \tag{2.59}$$

$$\frac{\partial}{\partial t}v_n=ink_cRe\left(D_*V_b\right)\phi_n+\frac{1}{r^2}D\left[r^2\mu_t\left(Dv_n-v_n/r\right)\right]+\left[NI2\right]_{E^n}+\left[NV2\right]_{E^n} \tag{2.60}$$

with

$$\mathcal{S}_n=DD_*-n^2k_c^2, \tag{2.61}$$

$[NI]_{E^n}$ and $[NV]_{E^n}$ the coefficients of $E^n$ in the nonlinear inertial and nonlinear viscous terms respectively. The nonlinear viscous terms arise from the shear-thinning behavior. As in references [26, 25, 28, 27, 40, 41], the amplitude $A(t)$ of the fundamental mode $(\phi_1,v_1)$ is considered as small, therefore the Fourier components $\phi_n$ and $v_n$ can be sought using a

perturbation method expanding around the solution of the linear problem :

$$[\phi_1(r,t), v_1(r,t)] = A(t)\,[F_1(r,t), V_1(r,t)]\ . \tag{2.62}$$

The amplitude of the perturbation is defined by setting

$$A(t) = max(v_1(r,t))\,. \tag{2.63}$$

It is clear that if the linear solution is $O(A)$, the leading term of $(\phi_2, v_2)$ is $O(A^2)$ because of the interaction of the fundamental with itself. The same reasoning applied to higher harmonics shows that $(\phi_n, v_n)$ can be written as

$$[\phi_n(r,t), v_n(r,t)] = A^n(t)\,[F_n(r,t), V_n(r,t)] \quad \text{if} \quad n > 0, \tag{2.64}$$

and

$$[\phi_0(r,t), v_0(r,t)] = A^2(t)\,[F_0(r,t), V_0(r,t)]\ . \tag{2.65}$$

Substituting (2.64) and (2.65) into (2.59) and (2.60) and equating similar powers of $A(t)$, leads to the following set of equations for $F_n$ and $V_n$

$$\left(\frac{\partial}{\partial t} + ng\right)\mathcal{S}_n F_n = \mathcal{S}_n\left[\mathcal{S}_n\left(\mu_b F_n\right)\right] - 2ink Re\frac{V_b}{r}V_n + [NI1]_{A^n E^n} + [NV1]_{A^n E^n}\,, \tag{2.66}$$

$$\left(\frac{\partial}{\partial t} + ng\right)V_n = ink_c Re\left(D_* V_b\right)F_n + \frac{1}{r^2}D\left[r^2\mu_t\left(DV_n - V_n/r\right)\right] + [NI2]_{A^n E^n} + [NV2]_{A^n E^n}\,. \tag{2.67}$$

The time evolution of the amplitude $A(t)$ is given by the Stuart-Landau equation

$$g = \frac{1}{A}\frac{dA}{dt} = \sum_{m=0} g_m\,|A|^{2m}\ , \tag{2.68}$$

where $g_0 = s$ is the linear eigenvalue, and $g_m$ with $m > 1$, the $m$th Landau coefficient. Since $F_n(V_n)$ is $O(1)$ or $O(A^2)$ as $A \to 0$, the nonlinearities generate terms in ascending power of $A^2$. Hence, $F_n$ and $V_n$ are expanded as follows

$$F_n(r,t) = \sum_{m=0}^{+\infty} F_{n,2m+n}(r)A^{2m}\ , \quad V_n(r,t) = \sum_{m=0}^{+\infty} V_{n,2m+n}(r)A^{2m}. \tag{2.69}$$

Substituting (2.69) into (2.66) and (2.67) and using (2.68) yields the differential equations for $F_{n,2m+n}$ and $V_{n,2m+n}$,

$$\begin{aligned} L1_{nm}F_{n,2m+n} + L2_{nm}V_{n,2m+n} &= [NI1]_{E^nA^{2m+n}} + [NV1]_{E^nA^{2m+n}} \\ &- \sum_{j=1}^{m} [2(m-j)+n]\, g_j \mathcal{S}_n F_{n,2(m-j)+n} \qquad (2.70) \\ L3_{nm}F_{n,2m+N} + L4_{nm}V_{n,2m+n} &= [NI2]_{E^nA^{2m+n}} + [NV2]_{E^nA^{2m+n}} \\ &- \sum_{j=1}^{m} [2(m-j)+n]\, g_j V_{n,2(m-j)+n}\,, \qquad (2.71) \end{aligned}$$

with

$$L1_{nm} = (2m+n)\, s\mathcal{S}_n - \mathcal{S}_n\,(\mu_b \mathcal{S}_n) \quad , \quad L2_{nm} = -2ink_c Re V_b/r\,, \qquad (2.72)$$

$$L3_{nm} = -ink_c Re\,(D_* V_b) \quad , \quad L4_{nm} = (2m+n)\, s - \frac{1}{r^2} D\left[r^2 \mu_t\,(D - 1/r)\right] \qquad (2.73)$$

### 2.4.2 Solution procedure

The system of differential equations (2.70) and (2.71) is solved sequentially beginning from $n = 1$ and $m = 0$. The problem $n = 1$, $m = 0$ is the linear problem (2.41) and (2.42). The problem $n = 0, m = 1$ yields the first correction to the base flow, the problem $n = 2$, $m = 0$ yields the second harmonic mode; $n = 1$, $m = 1$ yield the coefficient $g_1$ of feedback on the fundamental mode. More precisely, $g_1$ is determined using the solvability condition to the equation which gives the modification of the fundamental mode. For each $(n, m)$, the system of differential equations (2.70), (2.71) with the associated boundary conditions is solved numerically using a spectral collocation method based on Chebyshev polynomials as in the linear problem (2.41)-(2.43).

## 2.5 Results and discussion

### 2.5.1 Modification of the base flow

The interaction of the fundamental $AF_{11}$, $AV_{11}$ with its complex conjugate through the nonlinear quadratic terms produces a correction of the basis state : $A^2F_{02}$ and $A^2V_{02}$. Equations for $F_{02}$ and $V_{02}$ are obtained by setting $n = 0$ and $m = 1$ in (2.70)-(2.73). The factor of $A^2E^0$ arising from the nonlinear inertial and nonlinear viscous terms in (2.70) vanish, therefore

$$F_{02} = 0\,. \qquad (2.74)$$

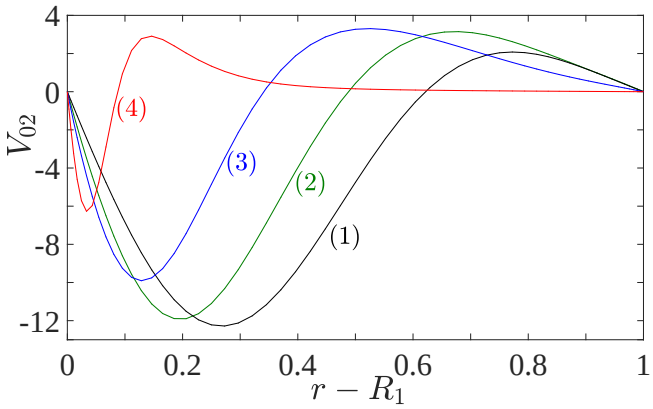


FIGURE 2.11 – (Color online) Modification of the base flow at $\eta = 0.4$, for Carreau fluids with $\lambda = 1$ and different values of the shear-thinning index : (1) $n_c = 1$ Newtonian fluid ; (2) $n_c = 0.7$ ; (3) $n_c = 0.5$ and (4) $n_c = 0.2$.

The modification of the base flow satisfies the following equation

$$\frac{1}{r^2}D\left[r^3\mu_t D\left(\frac{V_{02}}{r}\right) - 2sV_{02}\right] = -Re\left(\frac{\partial\phi}{\partial z}D_*v - D_*\phi\frac{\partial v}{\partial z}\right)_{A^2E^0} - \frac{1}{r^2}D\left(r^2\tau_{2,r\theta}\right)_{A^2E^0}, \tag{2.75}$$

with the boundary conditions

$$V_{02} = 0 \quad \text{at} \quad r = R_1, R_2\,. \tag{2.76}$$

In equation (2.75), $(\cdot)_{A^2E^0}$ means the coefficient of $A^2E^0$ in the nonlinear inertial or nonlinear viscous terms. Figure 2.11 shows the modification of the base flow at order $A^2$ for $\lambda = 1$ and different values of $n_c$. One notes that with increasing shear-thinning effects (decreasing $n_c$), $V_{02}(r)$ becomes more concentrated in the neighborhood of the inner cylinder because of the viscosity stratification. Furthermore, the numerical results indicate that from $\lambda = 1$, there is practically no influence of this parameter.

The profiles of $V_{02}$ are related to the radial inflow and outflow jets. The radial inflow jet carries fluid particles with low azimuthal momentum from the outer cylinder inward, decreasing the azimuthal velocity near the inner cylinder. The radial outflow jet carries fluid particles with high azimuthal momentum from the inner cylinder outward, increasing the azimuthal velocity near the outer cylinder. This reorganization of the azimuthal flow tends to increase $|dV/dr|$ at the walls and to reduce $|dV/dr|$ in the fluid interior. Note also that the deficit of the azimuthal velocity near the inner cylinder is higher than the surplus near the outer cylinder. Canceling artificially, the nonlinear viscous terms in (2.75) allows to highlight the contribution of the nonlinear inertial terms and vice-versa, to highlight the contribution of the nonlinear viscous terms on the modification of the base flow.

The contribution of the nonlinear viscous terms, which arise from the viscosity pertur-

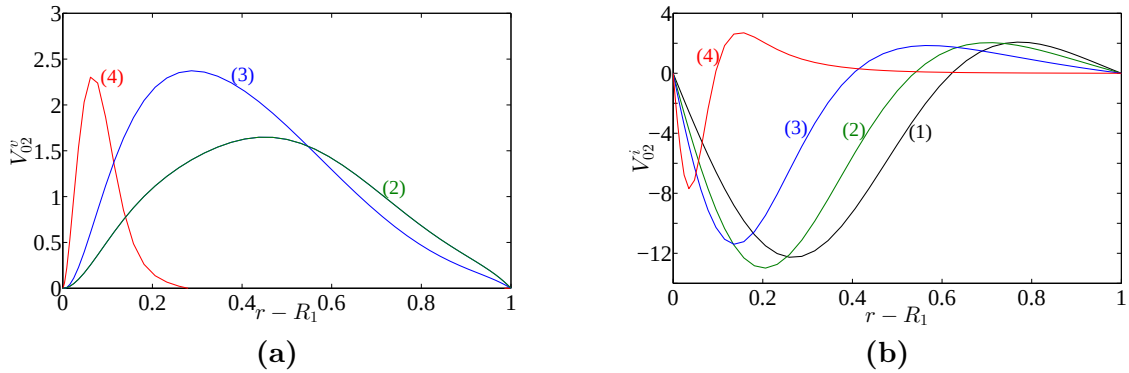


FIGURE 2.12 – (Color online) Modification of the base flow at $\eta = 0.4$, for Carreau fluids with $\lambda = 100$ and different values of the shear-thinning index : (1) $n_c = 1$ ; (2) $n_c = 0.7$ ; (3) $n_c = 0.5$ and (4) $n_c = 0.2$. **(a)** Contribution of nonlinear viscous terms ; **(b)** contribution of nonlinear inertial terms.

bation is shown in Fig. 2.12(a). The azimuthal velocity is increased in practically all the annular space, and mainly near the inner cylinder for strong shear-thinning effects. This is a consequence of the reduction of the viscous dissipation described by the term $J_{\mu_b - \mu_t}$ in equation (2.49). The modification of the base flow by the nonlinear viscous terms is weaker, but of the same magnitude order, than that induced by the nonlinear inertial terms shown in figure 2.12(b). The difference between these two contributions decreases with increasing shear-thinning effects.

### 2.5.2 Second harmonic mode

Interaction of the fundamental $(AF_{11}, AV_{11})$ with itself through the quadratic nonlinear terms in the perturbations equations (2.36), (2.37) generates the second harmonic, $A^2\,(F_{22}, V_{22})$. Equations for $F_{22}$ and $V_{22}$ are obtained by setting $n = 2$, $m = 0$ in (2.70) and (2.71) and extracting the factors of $A^2E^2$ in the nonlinear terms. At order $n = 2$, $m = 0$, equations (2.70) and (2.71) reduce to

$$L1_{22}F_{22} + L2_{22}V_{22} = [NI1]_{A^2E^2} + [NV1]_{A^2E^2}\,, \tag{2.77}$$

$$L3_{22}F_{22} + L4_{22}V_{22} = [NI2]_{A^2E^2} + [NV2]_{A^2E^2}\,,. \tag{2.78}$$

The boundary conditions read

$$F_{22} = DF_{22} = V_{22} = 0 \quad \text{at} \quad r = R_1, R_2\,. \tag{2.79}$$

Radial profiles of $\mathcal{I}m(F_{22})$ and $V_{22}$ are shown in figure 2.13 for $\lambda = 10$ and different values of $n_c$. As for the fundamental mode, with increasing shear-thinning effects, the variations of $F_{22}$ and $V_{22}$ are confined in a thin layer adjacent to the inner wall, i.e the second harmonic is squeezed against the inner cylinder. Furthermore, with increasing shear-thinning effects

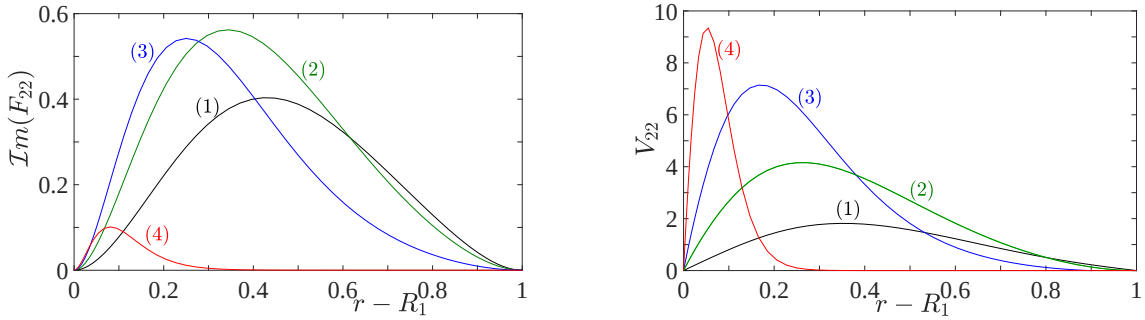


FIGURE 2.13 – (Color online) Second harmonic mode at the critical conditions for $\eta = 0.4$, $\lambda = 10$ and different values of the shear-thinning index : (1) $n_c = 1$ Newtonian case ; (2) $n_c = 0.7$ ; (3) $n_c = 0.5$ ; (4) $n_c = 0.2$. **(a)** Radial profile of $\mathcal{I}m(F_{22})$ ; **(b)** azimuthal velocity $V_{22}$.

the maximum of the azimuthal velocity $V_{22}$ is amplified, whereas the radial velocity is reduced.

### 2.5.3 Modification of the fundamental mode at cubic order : Cubic Landau constant

The nonlinear interactions between the fundamental, the second harmonic and the modification of the base flow lead to a cubic correction $O\left(A^3\right)$ to the fundamental mode. The first Landau coefficient $g_1$ accounts for these nonlinear interactions on the fundamental mode. The modification of the fundamental mode at order $|A|^2A$ is governed by (2.70) and (2.71) with $m = n = 1$, i.e.

$$L1_{13}F_{13} + L2_{13}V_{13} = [NI1]_{|A|^2AE^1} + [NV1]_{|A|^2AE^1} - g_1\mathcal{S}_1\, F_{11}\,, \tag{2.80}$$

$$L3_{13}F_{13} + L4_{13}V_{13} = [NI2]_{|A|^2AE^1} + [NV2]_{|A|^2AE^1} - g_1V_{11}\,. \tag{2.81}$$

The boundary conditions are

$$F_{13} = DF_{13} = V_{13} = 0 \quad \text{at} \quad r = R_1, R_2\,. \tag{2.82}$$

The system (2.80) and (2.81) can be written

$$\boldsymbol{L}\cdot\boldsymbol{X}_{13} = -g_1\boldsymbol{M}\cdot\boldsymbol{X}_{11} + \boldsymbol{NI} + \boldsymbol{NV} \quad \text{with} \quad \boldsymbol{X}_{13} = (F_{13}, V_{13})\,. \tag{2.83}$$

At the critical conditions, (2.83) has a non-trivial solution if the Fredholm solvability condition is satisfied, i.e. orthogonality of the inhomogeneous part of (2.83) to the null-space of the adjoint operator of $\boldsymbol{L}$. The cubic Landau constant is then readily obtained,

$$g_1 = g_1^I + g_1^V = \left(g_{10}^I + g_{12}^I\right) + \left(g_{10}^V + g_{12}^V + g_{1-11}^V\right)\,, \tag{2.84}$$

with

$$g_{10}^{I} = \frac{\langle \boldsymbol{NI}\left(\boldsymbol{X}_{02}|\boldsymbol{X}_{11}\right), \boldsymbol{X}_{ad}\rangle}{\langle \boldsymbol{M}\cdot\boldsymbol{X}_{11}, \boldsymbol{X}_{ad}\rangle} \quad , \quad g_{10}^{V} = \frac{\langle \boldsymbol{NV}\left(\boldsymbol{X}_{02}|\boldsymbol{X}_{11}\right), \boldsymbol{X}_{ad}\rangle}{\langle \boldsymbol{M}\cdot\boldsymbol{X}_{11}, \boldsymbol{X}_{ad}\rangle} \tag{2.85}$$

$$g_{12}^{I} = \frac{\langle \boldsymbol{NI}\left(\boldsymbol{X}_{22}|\boldsymbol{X}_{-11}\right), \boldsymbol{X}_{ad}\rangle}{\langle \boldsymbol{M}\cdot\boldsymbol{X}_{11}, \boldsymbol{X}_{ad}\rangle} \quad , \quad g_{12}^{V} = \frac{\langle \boldsymbol{NV}\left(\boldsymbol{X}_{12}|\boldsymbol{X}_{-11}\right), \boldsymbol{X}_{ad}\rangle}{\langle \boldsymbol{M}\cdot\boldsymbol{X}_{11}, \boldsymbol{X}_{ad}\rangle} \tag{2.86}$$

$$g_{1-11}^{V} = \frac{\langle \boldsymbol{NV}\left(\boldsymbol{X}_{11}, \boldsymbol{X}_{11}|\boldsymbol{X}_{-11}\right), \boldsymbol{X}_{ad}\rangle}{\langle \boldsymbol{M}\cdot\boldsymbol{X}_{11}, \boldsymbol{X}_{ad}\rangle}\,, \tag{2.87}$$

where $\boldsymbol{X}_{-11} = \boldsymbol{X}_{11}^{*}$, $g_{10}^{I}$ and $g_{10}^{V}$ are the feedback of the mean flow correction onto the fundamental through the nonlinear inertial and nonlinear viscous terms respectively, $g_{12}^{I}$ is the feedback of the second harmonic onto the fundamental, etc. The vertical bar notation in (2.85)-(2.87) may be better defined through an example of a nonlinear term. For instance $\left(D_{*}\phi\dfrac{\partial v}{\partial z}\right)(\boldsymbol{X_{22}}|\boldsymbol{X_{-11}}) \rightarrow D_{*}F_{22}(-ikV_{11}^{*}) + D_{*}F_{11}^{*}(2ikV_{22})$. The integrals in (2.85)-(2.87) are evaluated by means of the Clenshaw and Curtis method. In figure 2.14(a), $g_1$ is plotted as a function of $n_c$ for different values of $\lambda$. The sign of $g_1$ is negative indicating a supercritical nature of the bifurcation. As expected for weakly shear-thinning effects, the contribution of the nonlinear viscous terms $g_1^V$, on the first Landau coefficient, play a minor role and $\left|g_1^I\right| >> g_1^V$. With increasing the shear-thinning effects (decreasing $n_c$), the contribution of the nonlinear inertial terms $g_1^I$ and nonlinear viscous terms $g_1^V$ become of the same order, however $|g_1^I|$ remains larger than $g_1^V$, as shown in figure 2.14(b). Note that $g_1^V$ is positive, i.e. nonlinear viscous terms favor a subcritical bifurcation. Contributions of the different terms $g_{10}^I$, $g_{12}^I$, $g_{12}^V$ ... that control the value of $g_1$ are given in Appendix 2.B. The data show that for a Newtonian fluid, $g_1$ is dominated by the feedback of the base flow correction onto the fundamental. With increasing shear-thinning effects, the feedback of the second harmonic becomes more significant.

### 2.5.4 Features of the perturbation near the threshold

Besides the Landau coefficient, the amplitude of the perturbation $A$ is an important quantity in the nonlinear stability analysis. It is obtained by setting $dA/dt = 0$ in (2.68). In the neighbourhood of the critical conditions, to lowest order in $\epsilon$, the amplitude is

$$A = \sqrt{\frac{-\epsilon}{\tau_0\, g_1}}\,. \tag{2.88}$$

The numerical values of the Landau coefficient and hence the values the perturbation amplitude $A$ depend upon the normalization condition used for the eigenfunction in the linear theory. However, the physical velocity components, i.e. the product of the amplitude with the eigenfunctions of the linear theory are independent of the normalization. For instance, we can consider the mean kinetic energy of the perturbation or the torque applied on the inner cylinder.

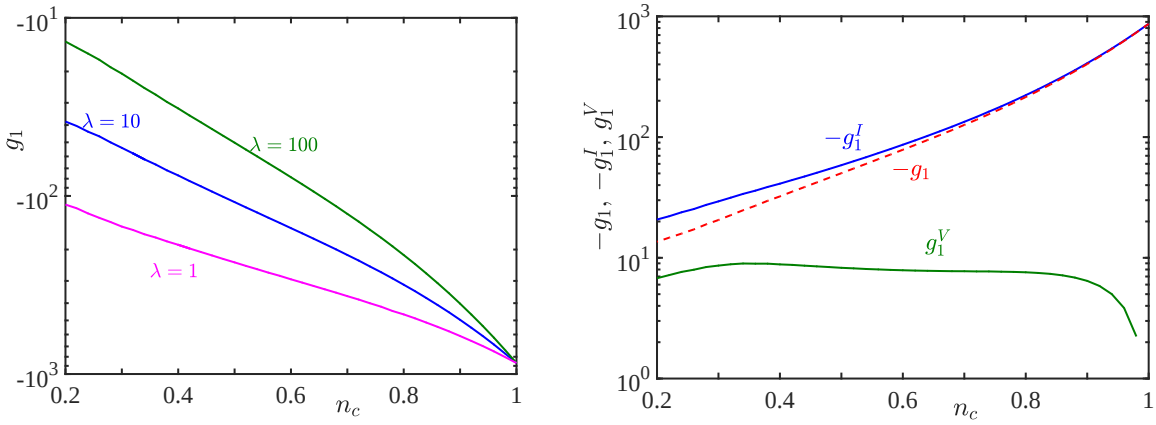


FIGURE 2.14 – (Color online) **(a)** Cubic Landau constant, $g_1$, as a function of $n_c$ for different values of the dimensionless constant time $\lambda$ with $\eta = 0.4$. **(b)** Contribution of the nonlinear inertial terms $(-g_1^I)$ and nonlinear viscous terms $g_1^V$ at $\lambda = 100$.

### Mean kinetic energy

At order $A^2$, the mean kinetic energy is defined by

$$\xi = A^2 \int_{R_1}^{R_2} \left( k_c^2 \left| F_{11} \right|^2 + \left| V_{11} \right|^2 + \left| D_* F_{11} \right|^2 \right) r \mathrm{d}r \,. \tag{2.89}$$

Figure 2.15(a) plots $\xi$ as a function of $\epsilon$ for different values of the shear-thinning index $n_c$. The dimensionless constant time is fixed $\lambda = 10$. The curves are practically identically to those obtained for a power-law fluid. As it can be observed the kinetic energy of the perturbation decreases with increasing shear-thinning effects. Figure 2.15(b) shows that the azimuthal kinetic energy is much larger than the radial and axial ones. For instance at $n_c = 0.2$, more than 95% of the kinetic energy is concentrated on the azimuthal velocity. The decrease of the kinetic energy with increasing shear-thinning effects is due to the viscosity stratification. Indeed, with increasing shear-thinning effects, the Taylor vortices are confined in the thin region near the inner wall where the viscosity is low (the perturbations are suppressed in the highly viscous fluid at a short distance from the inner cylinder) and their strength becomes weaker as shown in figure 2.6a.

### Torque

The determination of the torque $\hat{T}$ applied on the inner cylinder is of great interest. It provides information about the energy dissipation since the energy injected in the fluid per unit of time is obtained by multiplying the torque by the velocity of the inner cylinder. Dubrulle [42] and Eckhardt [43] demonstrated that the dimensionless torque $G = \hat{T}/2\pi\hat{\rho}\hat{\nu}^2\hat{h}$ where $\hat{\nu}$ is the kinematic viscosity and $\hat{h}$ the height of the inner cylinder, is related to the angular momentum flux. By analogy with the heat transfer in Rayleigh-Bénard convec-

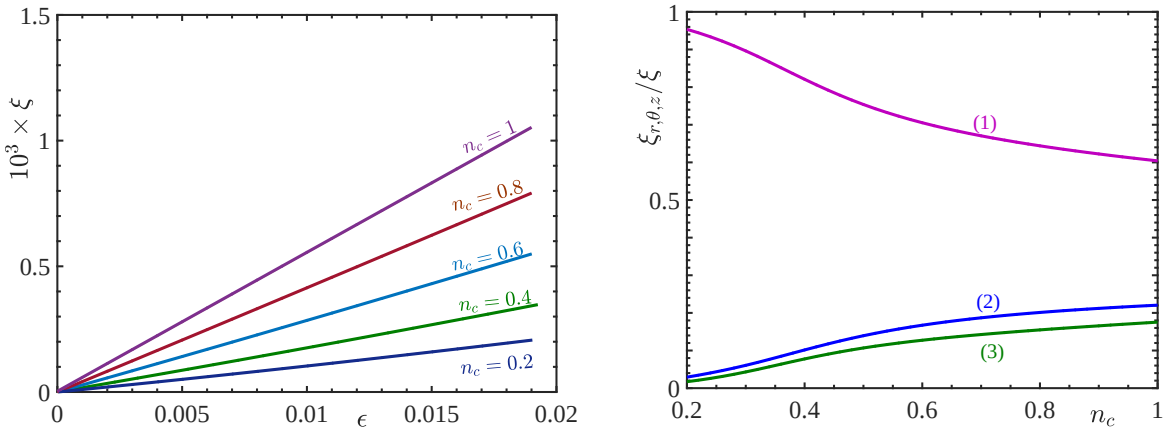


FIGURE 2.15 – (Color online) **(a)** Kinetic energy at order $A^2$ for different values of the shear-thinning index $n_c$ with $\lambda = 10$ and $\eta = 0.4$. **(b)** Ratio of azimuthal $\xi_\theta$ (curve 1), radial $\xi_r$ (curve 2) and axial $\xi_z$ (curve 3) kinetic energy to the total kinetic energy $\xi$.

tion, the previous authors defined a pseudo-Nusselt number, $Nu_*$ for a Taylor Couette flow as the ratio of $G$ to the dimensionless torque of the laminar flow $G_b$. Hence, for a purely viscous fluid,

$$Nu_* = \frac{G}{G_b} = \frac{\int_0^{2\pi/k_c} (\mu\dot{\gamma}_{r\theta})_{r=R_1}\,\mathrm{d}z}{(2\pi/k_c)\,(\mu_b\dot{\gamma}_{r\theta b})_{r=R_1}}\,. \tag{2.90}$$

Using (2.17) and (2.28)-(2.33), $Nu_*$ can be written as

$$Nu_* = 1 + \left(\frac{\mu_t}{\mu_b}\right)_{R_1} \frac{\int_0^{2\pi/k_c} (\dot{\gamma}_{r\theta})_{r=R_1}\,\mathrm{d}z}{(\dot{\gamma}_{r\theta b})_{r=R_1}} + \frac{\int_0^{2\pi/k_c} (\mu_1\dot{\gamma}_{r\theta} + \mu_2\dot{\gamma}_{r\theta b})_{r=R_1}\,\mathrm{d}z}{(\mu_b\dot{\gamma}_{r\theta b})_{r=R_1}} + \ldots \tag{2.91}$$

In the laminar regime, the angular momentum flux is diffusive and $Nu_* = 1$. In the TVF regime, the pseudo-Nusselt number at order $A^2$ is given by

$$Nu_* = 1 + A^2 \left(\frac{\mu_t}{\mu_b}\right)_{R_1} \left(\frac{DV_{02}}{DV_b}\right)_{R_1} + 2\frac{A^2}{(\mu_b)_{r=R_1}} \left(\frac{\mathrm{d}\mu_b}{\mathrm{d}\Gamma_b}\right)_{R_1} \left(3\,|DV_{11}|^2 + \left|D^2F_{11}\right|^2\right)_{R_1} + 4\frac{A^2}{(\mu_b)_{r=R_1}} \left(\frac{\mathrm{d}^2\mu_b}{\mathrm{d}\Gamma_b^2}\right)_{R_1} |DV_{11}|^2_{R_1} + O\left(A^4\right)\,. \tag{2.92}$$

Using (2.88), the pseudo-Nusselt number can be written formally as

$$Nu_* = 1 + K\epsilon\,. \tag{2.93}$$

For a Newtonian fluid, the expression of the slope $K$ reduces to

$$K = -\frac{1}{\tau_0 g_1} \frac{(DV_{02})_{R_1}}{\left(\dot{\gamma}^b_{r\theta}\right)_{R_1}} \quad \text{with} \quad \dot{\gamma}^b_{r\theta} = -\frac{2}{\eta\,(1+\eta)} \tag{2.94}$$

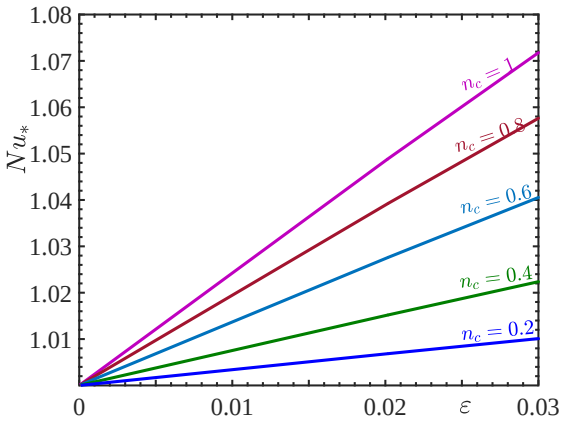


FIGURE 2.16 – (Color online) Torque applied on the inner cylinder, at order $A^2$, versus $\epsilon$ for different values of the shear-thinning index $n_c$ with $\lambda = 10$.

In this case, the increase of the torque applied on the inner cylinder is due to the increase of the inner wall shear rate of the mean flow, via the term $(DV_{02})_{R_1}$. For non-Newtonian shear-thinning fluids, there is an additional term arising from the viscosity perturbation as indicated by (2.92). Figure 2.16 shows the variation of $Nu_*$ with $\epsilon$, for different values of $n_c$. The dimensionless constant time of the fluid is fixed at $\lambda = 10$. The pseudo-Nusselt number decreases with increasing shear-thinning effects, in agreement with the decrease of the kinetic energy of the perturbation. The intensity of the Taylor vortices diminishes and thus the modification of the shear-rate at the inner wall is weaker. However, the analysis of the different terms in equation (2.91) shows that for a strong shear-thinning fluid, the term $\mu_1 \dot{\gamma}_{r\theta}(\boldsymbol{u})$ plays a significant role in the reduction of $Nu_*$. This term called "non-Newtonian Reynolds-stress" in [44] contributes to the reduction of the viscous dissipation.

### 2.5.5 Validation by computing higher-order Landau constants

Figures 2.15 and 2.16 indicate that the kinetic energy of the perturbation and the pseudo-Nusselt number $Nu_*$ decrease with increasing shear-thinning effects. This result was obtained by truncating the series (2.68) to the first Landau constant, at cubic order in $A$. For a significant deviation from the critical condition, terms of higher order become large and should be taken into account. A weakly nonlinear expansion was then carried out up to seventh-order in amplitude. As in the Newtonian case, for shear-thinning fluids, the Landau constants are of the same sign and increase very fast, i.e. $A$ has to be very small to satisfy the assumption of the weakly nonlinearity. This increase is stronger with increasing shear-thinning effects as it is shown by the data in table 2.5 (Appendix 2.C). The representation of the equilibrium amplitude versus $\epsilon$ at figure 2.27 (Appendix 2.C), at the third-, fifth- and seventh-order shows that the correction brought by adding a new term decreases.

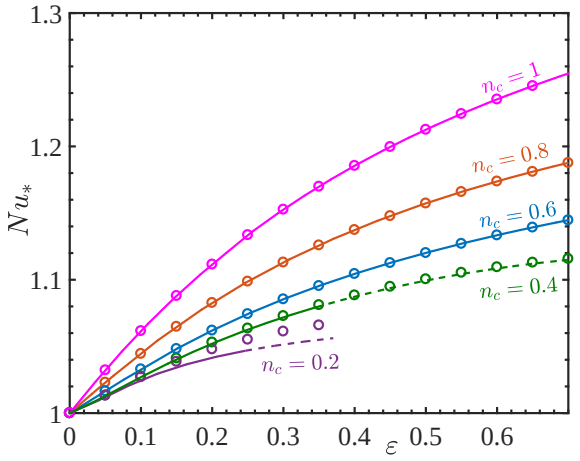


FIGURE 2.17 – (Color online) Influence of shear thinning effects on the pseudo-Nusselt number at $\eta = 0.4$ and $\lambda = 10$. The symbols correspond to a power-law model for the same shear-thinning index.

Figure 2.17 shows the variation of the pseudo-Nusselt number as a function of $\epsilon$ for different values of $n_c$. As it can be observed, the decrease of $Nu_*$ with increasing shear-thinning effects is confirmed at least for a reasonable distance from the critical conditions. Curves for Carreau and power-law models are not distinguishable except for $n_c = 0.2$. In this last case, a higher value of $\lambda$ is needed.

Similarly, the numerical results show that for a reasonable departure from the critical conditions, the kinetic energy of the perturbation decreases with increasing shear-thinning effects and it is mainly concentrated on the azimuthal velocity component.

**Remarks**

- Our results for $Nu*$ are compared with those obtained experimentally by Donnelly & Simon [45] for a Newtonian fluid with $\eta = 0.5$. A good agreement is found at least up to $\epsilon = 0.5$ as it is illustrated by Tab. 2.3 (Appendix 2.A). With the exception of one point, the relative difference is less than 1 %.

- For $n_c = 0.2$ and 0.4, the curves $Nu_*$ versus $\epsilon$ are dashed when $\epsilon$ exceeds a particular value say $\epsilon_0$. Actually, harmonics analysis done in §2.5.7 shows that for sufficiently strong shear-thinning effects, the fourth harmonic overtakes the third one when $\epsilon > \epsilon_0$, which may delimit the range of validity of the results.

- Departing sufficiently from the critical conditions, we can no longer assume $s = 0$ in the equations that describe the modification of the fundamental mode. Hence, these equations become unconditionally solvable. To calculate the Landau coefficients, an iterative process was used as suggested by Sen & Venkateswarlu [28] (See also Bouteraa et al. [46] and Bouteraa & Nouar [47]).

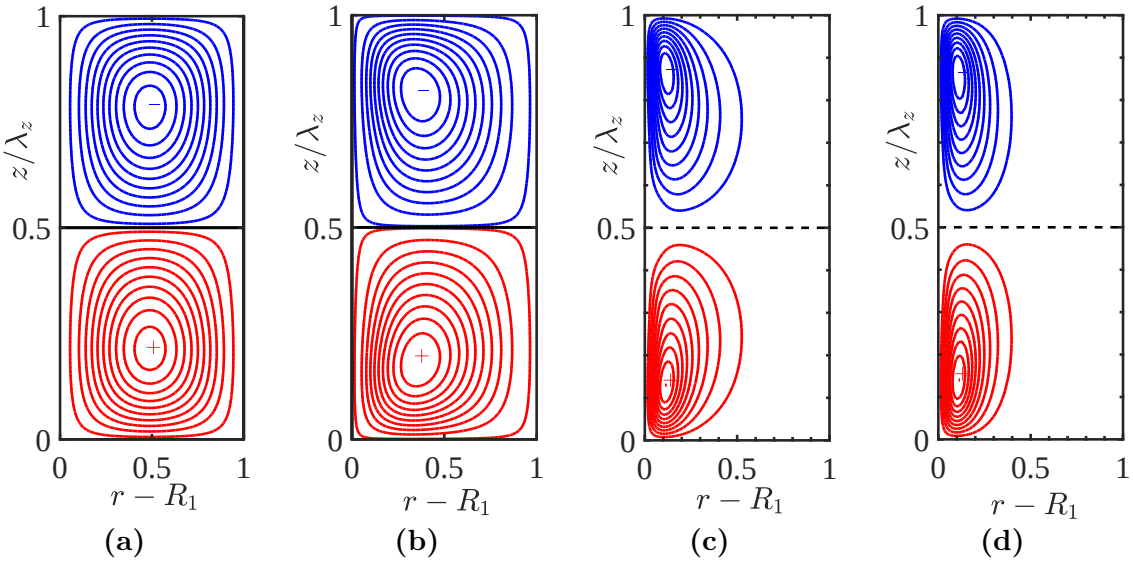


FIGURE 2.18 – (Color online) Contours of streamfunction at $\epsilon = 0.1$ for **(a)** Newtonian fluid, with ($\psi_{max} = 2.2\,10^{-2}$) ; **(b)** Carreau fluid with $n_c = 0.5$, $\lambda = 1$ ($\psi_{max} = 1.05510^{-2}$) ; **(c)** Carreau fluid with $n_c = 0.2$, $\lambda = 1$, ($\psi_{max} = 2.082\,10^{-3}$) ; **(d)** Carreau fluid with $n_c = 0.2$, $\lambda = 10$, ($\psi_{max} = 2.1\,10^{-3}$). The increment between lines is $\Delta\,\psi = \psi_{max}/10$.

### 2.5.6 Description of the flow field

The change in the flow structure with increasing shear-thinning effects is described by contours of stream function $\psi$, azimuthal vorticity and velocity components $u$, $v$ and $w$. Figure 2.18 shows isolines of constant $\psi$ on one wavelength $\lambda_z = 2\pi/k_c$ (two cells), for Newtonian and Carreau fluids at a reduced Reynolds number $\epsilon = 0.1$. Positive and negative values of $\psi$ correspond to anticlockwise and clockwise rotation. The vortices lose the symmetry along the horizontal axis through the cell center. The eye of vortices is shifted towards upper and lower cell boundaries, i.e. $z/\lambda_z = 0$ and 1. This effect is weak for a Newtonian fluid (figure 2.18(a) and becomes more pronounced with decreasing the shear-thinning index $n_c$. This axial shift of the vortex eye is coupled with the radial shift towards the inner cylinder due to the viscosity stratification discussed in § 2.2.3. The displacement of the vortex center in the direction of higher shear-stress and lower viscosity leads to an increasing concentration of vorticity near the inner wall at $z/\lambda_z = 0$ and 1 as it is shown in figure 2.19 where isolines of contours of $\Omega$ are displayed for different rheological parameters. In contrast with the build-up of vorticity near the inner cylinder and at the corners $z = 0$ and $z = \lambda_z$, the region between the two cells, around $z/\lambda_z = 0.5$, which is practically void of vorticity increases in area with increasing shear-thinning effects.

This build-up of the vorticity with increasing shear-thinning effects and the change in the vortices can be related to the evolution of the radial flow from the inner to the outer cylinder (outflow) at $z/\lambda_z = 0$ and $z/\lambda_z = 1$ and from the outer to the inner one (inflow), around $z/\lambda_z = 0.5$. Figure 2.20 shows the radial velocity component at the vortex eye

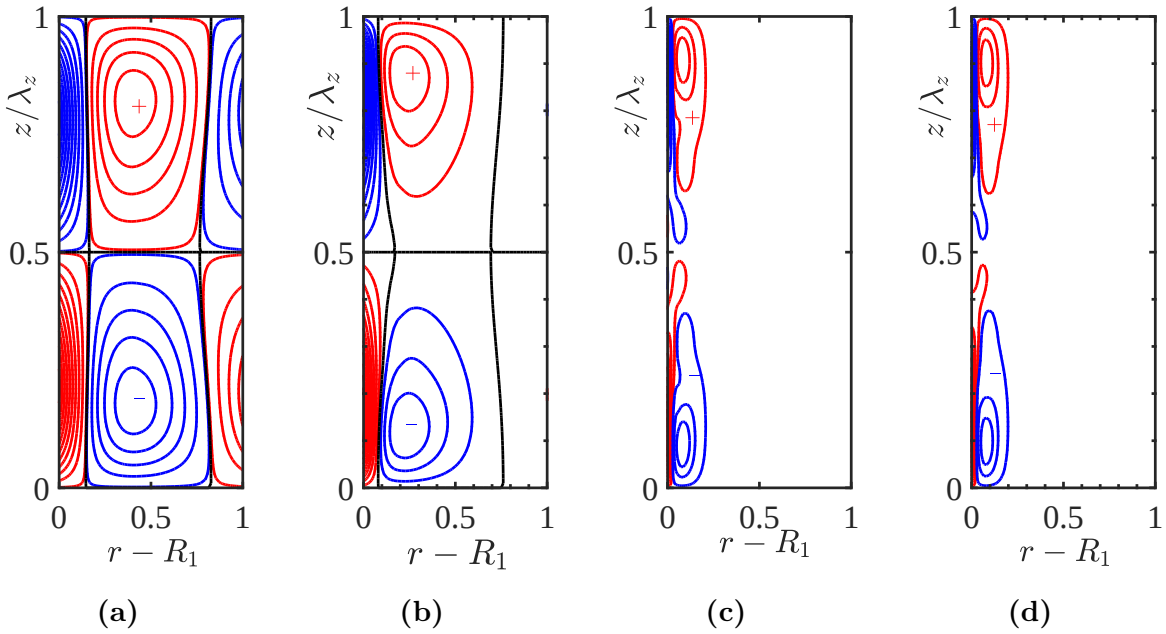


FIGURE 2.19 – (Color online) Contours of vorticity for **(a)** Newtonian fluid, $n_c = 1$, with $\Omega_{max} = 1.121$ ; **(b)** Carreau fluid with $n_c = 0.5$, $\lambda = 1$, $\Omega_{max} = 1.625$ ; **(c)** Carreau fluid with $n_c = 0.2$, $\lambda = 1$, $\Omega_{max} = 3.965$ ; **(d)** Carreau fluid with $n_c = 0.2$, $\lambda = 10$, $\Omega_{max} = 4.199$. The increment between lines is $\Delta\,\Omega = \Omega_{max}/10$.

center, versus $z$ for Newtonian and Carreau fluids. It can be observed that the radial outflow is stronger than the radial inflow.

The ratio $r_u$ between the intensity ($\max|u|$) of the radial outflow and that the radial inflow, increases with increasing shear-thinning effects. At $\epsilon = 0.1$, $r_u$ increases from 1.6 for a Newtonian fluid to 4.5 for a Carreau fluid with $n_c = 0.2$ and $\lambda = 10$. The width of the radial outflow zone decreases with decreasing $n_c$ and the region of inflow increases accordingly. For instance, at $\epsilon = 0.1$ and for a Carreau fluid with $n_c = 0.2$ and $\lambda = 10$, the ratio between the axial extent of radial outflow and that of inflow is practically 3, whereas for a Newtonian fluid, the ratio is slightly larger than 1. With increasing Reynolds number $Re$, the radial outflow becomes stronger, increasingly jet-like, and the ratio $r_u$ between $\max|u|$ in outflow and inflow increases. At $\epsilon = 0.3$, $r_u \approx 6.5$ for a Carreau fluid with $n_c = 0.2$, $\lambda = 10$, whereas for a Newtonian fluid, $r_u \approx 2.1$.

Fluctuations in the radial inflow, observed with decreasing $n_c$, might be related to the influence of harmonics discussed in the Section 2.5.7.

The change of the flow with increasing shear-thinning effects is also shown from consideration of the azimuthal velocity distribution. Contours of $v$ are displayed in figure 2.22 for Newtonian and Carreau fluids at $\epsilon = 0.1$. Positive azimuthal streaks evolve in the outflow region, $z/\lambda_z = 0$ and 1, where high azimuthal momentum fluid is carried outward from near the inner cylinder. Similarly, negative azimuthal streak evolves in the inflow region, $z/\lambda_z = 0.5$, where low azimuthal momentum fluid is carried inward from near the outer

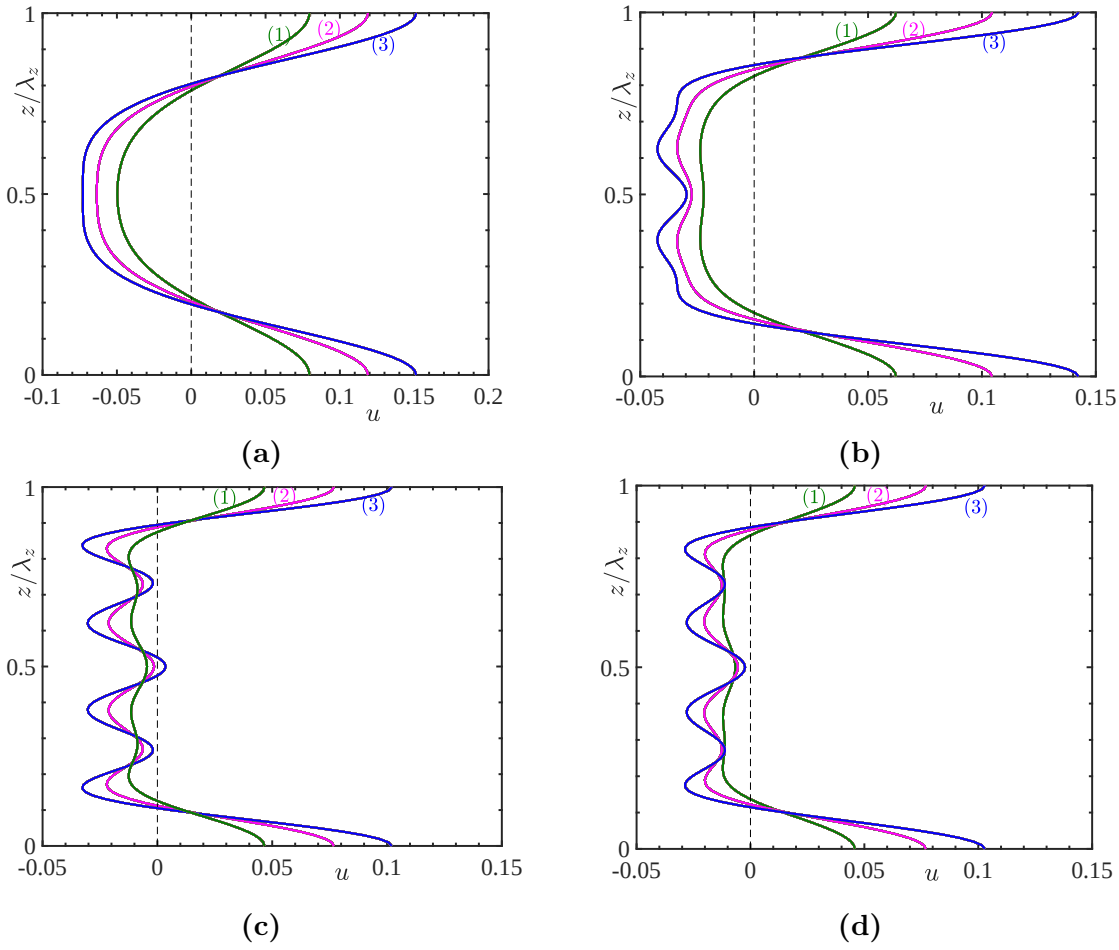


FIGURE 2.20 – (Color online) Radial component of velocity versus $z$ at a fixed radial position corresponding to the vortex eye center. **(a)** Newtonian fluid ; **(b)** Carreau fluid with $n_c = 0.5$, $\lambda = 1$ ; **(c)** Carreau fluid with $n_c = 0.2$, $\lambda = 1$ ; **(d)** Carreau fluid with $n_c = 0.2$, $\lambda = 10$. (1) $Re = 1.1\,Re_c$, (2) $Re = 1.2\,Re_c$ , (3) $Re = 1.3\,Re_c$

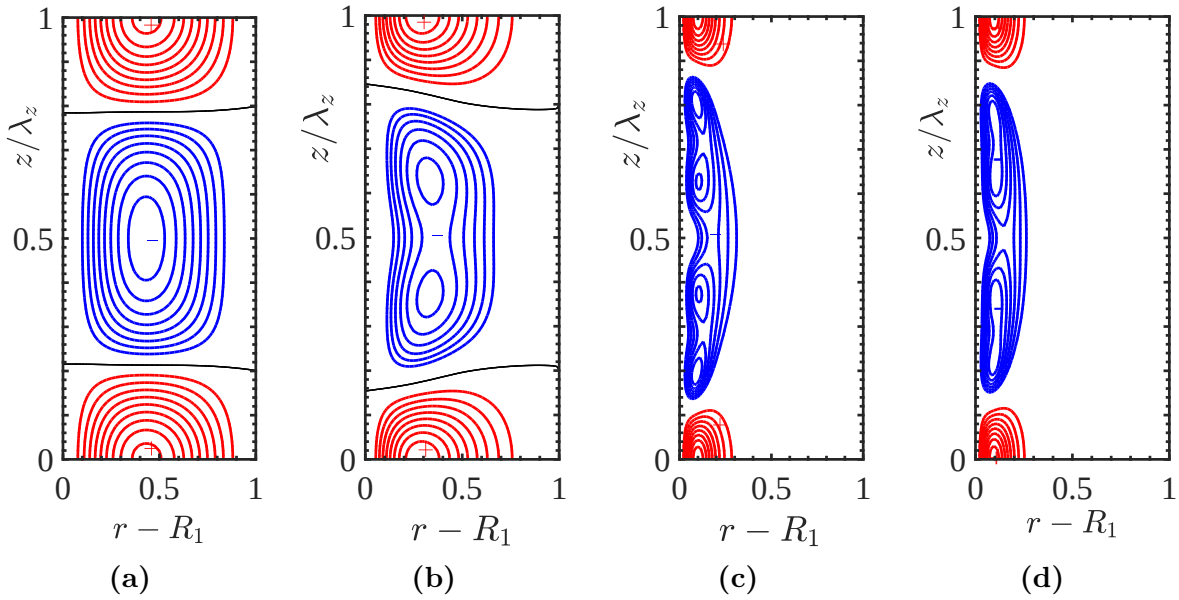


FIGURE 2.21 – (Color online) Contours of radial velocity component at $\epsilon = 0.1$ for **(a)** Newtonian fluid, $u_{max} = 0.077$, $u_{min} = -0.049$ ; **(b)** Carreau fluid with $n_c = 0.5$, $\lambda = 1$, $u_{max} = 0.057$, $u_{min} = -0.021$ ; **(c)** Carreau fluid with $n_c = 0.2$, $\lambda = 1$, $u_{max} = 0.0466$, $u_{min} \approx -0.012$ ; **(d)** Carreau fluid with $n_c = 0.2$, $\lambda = 10$, $u_{max} = 0.046$, $u_{min} = -0.012$. The increment between lines is $\Delta u = u_{max}/10$ for positive values and $\Delta u = u_{min}/10$ for negative values.

cylinder. With increasing shear-thinning effects, contours lines of $v$ are more concentrated in the vicinity of the inner cylinder, and the positive azimuthal streaks of narrow width are separated by a negative streak of a large extent. The evolution of the positive and negative azimuthal streaks with increasing Reynolds number is illustrated by plotting in figure 2.23 the axial profile of $v$ at a fixed radial position (center of patterns) and different values of $\epsilon$. The positive azimuthal streak increases strongly with $\epsilon$ and shear-thinning effects, whereas $v$ varies relatively little in the inflow region. This asymmetry between the inflow and the outflow can be described in terms of local Reynolds number defined with the local azimuthal velocity and the local viscosity.

The influence of shear thinning effects on the flow structure is also illustrated by contours of the axial component of the velocity $w$, represented in the figure 2.24. With increasing the shear-thinning behavior, the maximum of $w$ is shifted radially towards the inner cylinder and axially towards the outflow boundaries $z/\lambda_z = 0$ and 1. Hence, in a very thin region across the outflow boundary, $w$ changes from positive extremum to negative extremum and vice versa.

The change in the flow structure with $Re$ and shear-thinning effects modifies the second invariant $\Gamma$ of strain-rate tensor $\dot{\gamma}$ and therefore the viscosity. Analysis of the different components $\dot{\gamma}_{ij}$ show that $\Gamma$ is dominated by the term $(\dot{\gamma}_{r\theta}(\boldsymbol{U_b} + \boldsymbol{u}))^2 \approx (\dot{\gamma}^b{}_{r\theta})^2 + 2\dot{\gamma}^b_{r\theta}\dot{\gamma}_{r\theta}$. In the outflow region, according to the contours of the azimuthal velocity (2.22), $\dot{\gamma_{r\theta}}(u)$ is

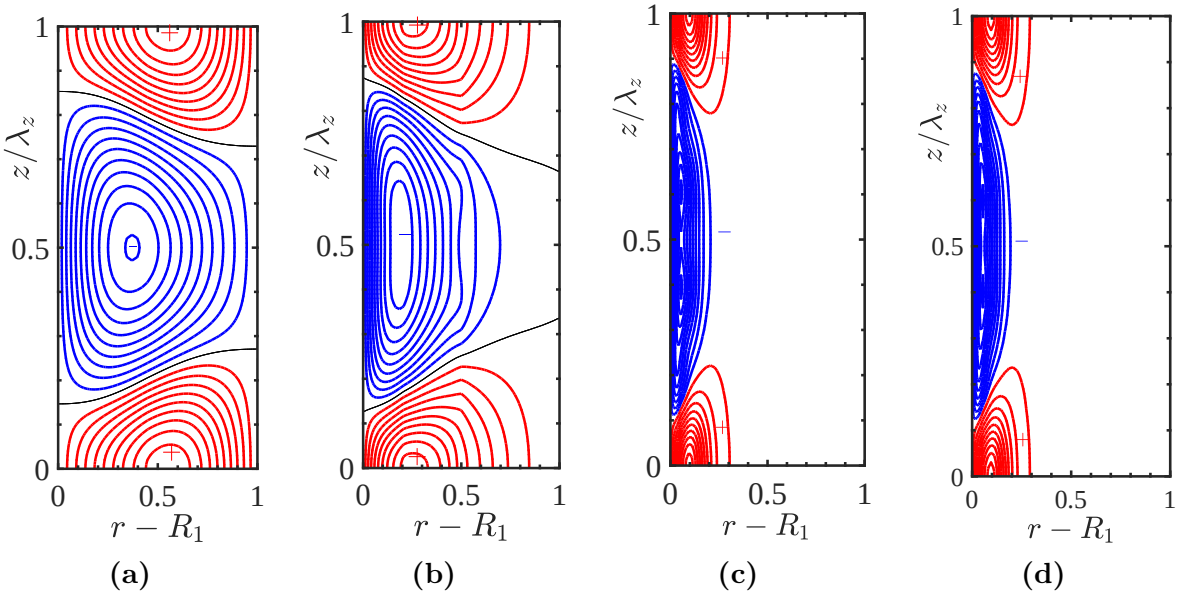


FIGURE 2.22 – (Color online) Contours of azimuthal velocity $v$ at $\epsilon = 0.1$ for **(a)** Newtonian fluid, $v_{max} \approx 0.1$, $v_{min} \approx -0.12$ ; **(b)** Carreau fluid with $n_c = 0.5$, $\lambda = 1$, $v_{max} = 0.11$, $v_{min} \approx -0.093$ ; **(c)** Carreau fluid with $n_c = 0.2$, $\lambda = 1$, $v_{max} \approx 0.225$, $v_{min} \approx -0.12$ ; **(d)** Carreau fluid with $n_c = 0.2$, $\lambda = 10$. The increment between lines is $\Delta v = v_{max}/10$ for positive values and $\Delta v = v_{min}/10$ for negative values .

positive and maximum at the inner cylinder ($\Gamma < \Gamma_b$), then decreases, vanishes ($\Gamma = \Gamma_b$) around the center of the pattern, and becomes negative ($\Gamma > \Gamma_b$). Similar description can be done for the inflow region, but with opposite signs. This variation of $\Gamma$ explains the shape of the viscosity contours (Figure 2.25). For sufficiently strong shear-thinning effects, the vortices are confined near the inner cylinder with a quite large fluid layer adjacent to the outer cylinder where the perturbation is practically inexistent. In this case, the viscosity contours remain straight lines near the outer cylinder as it is shown by figure 2.25 (b) where the viscosity contours are represented at $\epsilon = 0.1$ for a Carreau fluid with $n_c = 0.2$ and $\lambda = 10$.

### 2.5.7 Harmonics

Nonlinearities of inertial and viscous terms generate spatial harmonics (in the axial direction) of the fundamental mode. From equations (2.58), (2.64), (2.65) and (2.69), the flow variables ($u$, $v$, $w$) can be written as sum of Fourier components. For instance for $v$ :

$$v(r,z) = v_0(r) + \sum_{n=1}^{\infty} v_n \cos nk_c z \tag{2.95}$$

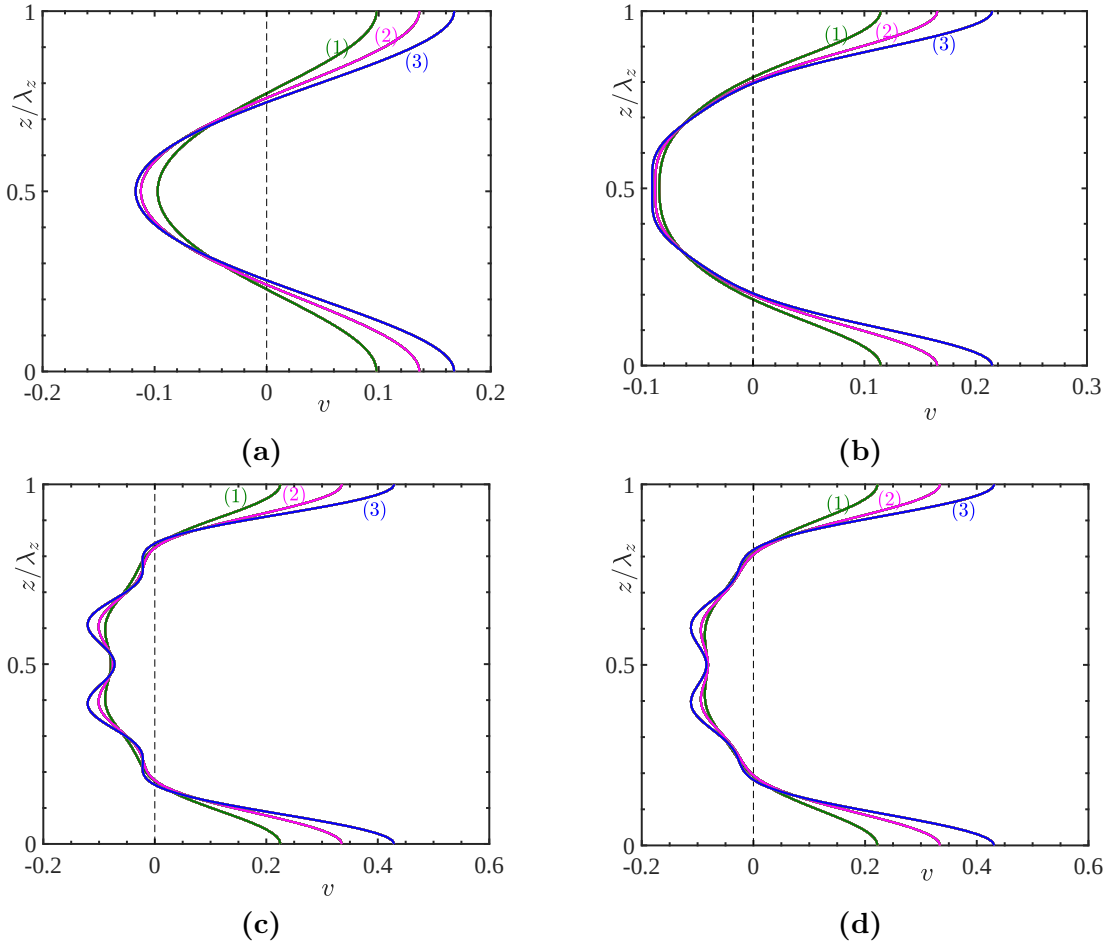


FIGURE 2.23 – (Color online) Azimuthal component of velocity versus $z$ at fixed radial position (center of pattern) and different Reynolds number. **(a)** n = 1 Newtonian fluid, **(b)** Carreau fluid with $n_c = 0.5$, $\lambda = 1$, **(c)** Carreau fluid with $n_c = 0.2$, $\lambda = 1$, **(d)** Carreau fluid with $n_c = 0.2$, $\lambda = 10$. (1) $Re = 1.1\,Re_c$, (2)$Re = 1.2\,Re_c$, (3) $Re = 1.3\,Re_c$

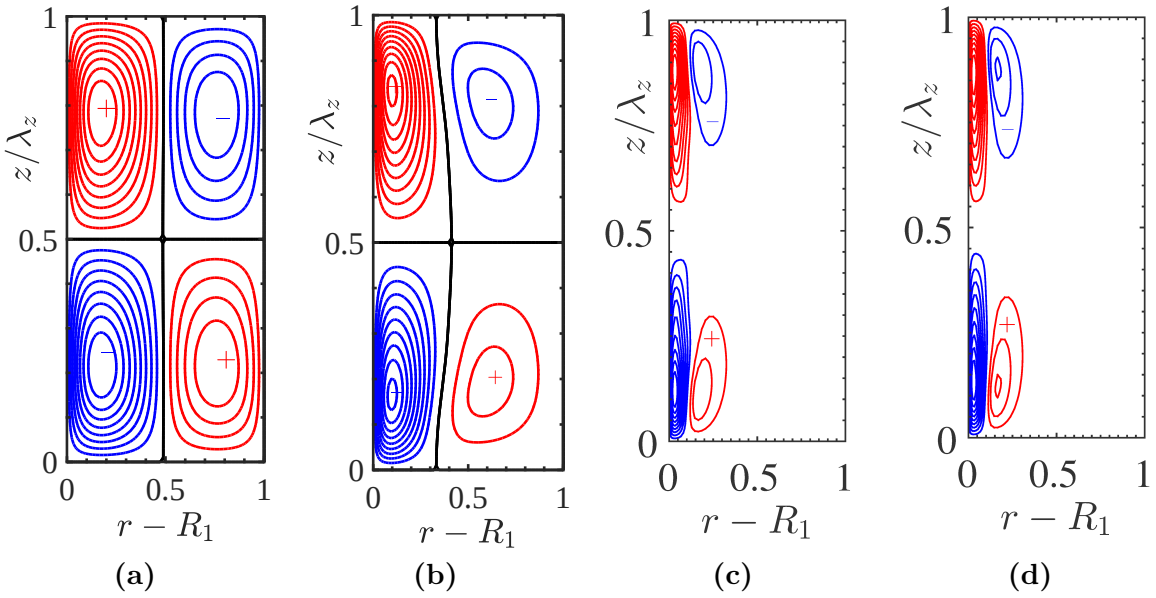


FIGURE 2.24 – (Color online) Contour of axial velocity component $w$ at $\epsilon = 0.1$ for **(a)** Newtonian fluid, $w_{max} = 0.082$ ; **(b)** Carreau fluid with $n_c = 0.5$, $\lambda = 1$, $w_{max} = 0.063$ ; **(c)** Carreau fluid with $n_c = 0.2$, $\lambda = 1$, $w_{max} = 0.05$ , **(d)** Carreau fluid with $n_c = 0.2$, $\lambda = 10$, $w_{max} = 0.048$. The increment between lines is $\Delta w = w_{max}/10$ for positives values and $\Delta w = -w_{max}/10$ for negative values.

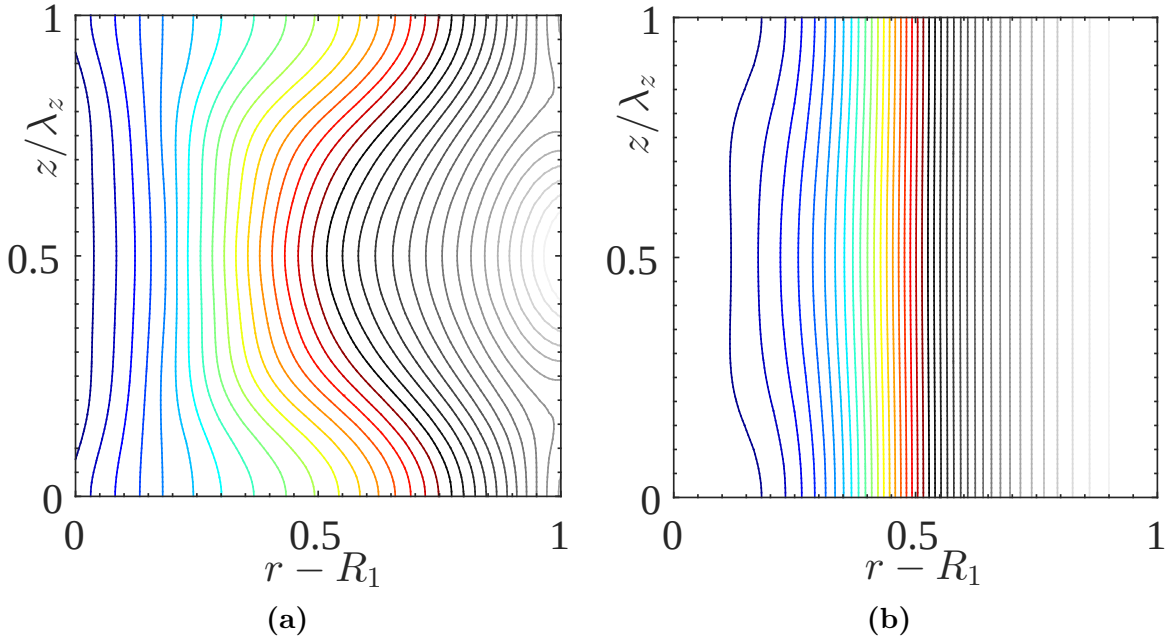


FIGURE 2.25 – (Color online) **(a)**Viscosity contours at $\epsilon = 0.1$ for : Carreau fluid with $n_c = 0.5$, $\lambda = 1$, $\mu_{max} = 0.63$, $\mu_{min} = 0.094$, the increment between lines is $\Delta\mu = 0.015$. **(b)** Carreau fluid with $n_c = 0.2$, $\lambda = 10$, $\mu_{min} = 0.0046$, $\mu_{max} = 0.86$, the increment between lines is $\Delta\mu = 0.02$.

with

$$v_0 = \sum_{m=0}^{\infty} A^{2m} V_{0,2m} \quad \text{and} \quad v_n = 2 \sum_{m=0}^{\infty} A^{2m+n} V_{n,2m+n}. \tag{2.96}$$

The amplitude $A$ is the stationary solution of the amplitude equation (2.68). The form of the $u$-component is similar to $v$ except that $v_0$ is omitted. The $w$-component is like $u$ except that the $z$-dependency is in $\sin nk_c z$. In order to describe the growth of harmonics with Reynolds number, the Fourier amplitude $v_n$ in (2.95) are averaged over the gap width, as in [48] and [6],

$$\overline{v_n} = \frac{1}{R_2 - R_1} \int_{R_1}^{R_2} v_n(r) r \mathrm{d}r. \tag{2.97}$$

We recall that $v_0$ corresponds to the modification of the base flow, $v_1$ to the distorted fundamental mode, $v_2$ to the second harmonic, etc ... In Figure 2.26, we have represented, the growth of the averaged Fourier amplitudes as the Reynolds number is increased, for Newtonian and shear-thinning fluids. The initial amplification of the fundamental mode $n = 1$ is stronger for a Newtonian fluid than for a shear-thinning fluid. At $\epsilon = 0.3$, $\overline{u_1}$(Newtonian fluid) $\approx 10 \times \overline{u_1}$(shear-thinning fluid). The zeroth-mode becomes more significant as the Reynolds number is raised. For example, at $\epsilon = 0.3$, $\overline{v_0} = 0.77 \times \overline{v_1}$ for a Newtonian fluid and $\overline{v_0} = 0.84 \times \overline{v_1}$ for the shear-thinning fluid. Higher harmonics, $n = 2$, 3, 4 grow faster with Reynolds number for shear-thinning fluids than for a Newtonian fluid. Note also in figure 2.26 (d) that for sufficiently strong shear-thinning behavior, the harmonic numbered (4) may overtake the harmonic numbered (3).
All in all, nonlinearities of the viscous terms combined with that of the inertial terms lead to a stronger amplification of higher harmonics.

## 2.6 Conclusion

Taylor-vortex flow (TVF) regime in shear-thinning fluids is considered in the present work. We focused mainly on the wide gap configuration. The fluid is assumed purely viscous. Compared to the Newtonian case, an additional nonlinearity appears in the momentum equations, via the rheological law. This additional nonlinearity is more complex than the quadratic nonlinear inertial terms. A weakly nonlinear analysis is used as a first approach to take into account nonlinear effects. The amplitude expansion Landau-Stuart method is adopted. The Carreau model is used as a typical rheological model.
As a first step, the critical Reynolds number, $Re_c$, for the onset of Taylor vortices was determined for a large range of rheological parameters. It is shown that, $Re_c$ defined with the zero shear viscosity decreases with increasing shear-thinning effects. This is the consequence of the increase of the shear-rate and decrease of the viscosity near the inner wall. Furthermore, the characteristic time for the growth of the vortices increases significantly with increasing shear-thinning effects. Computation of the first Landau coefficient $g_1$, indi-

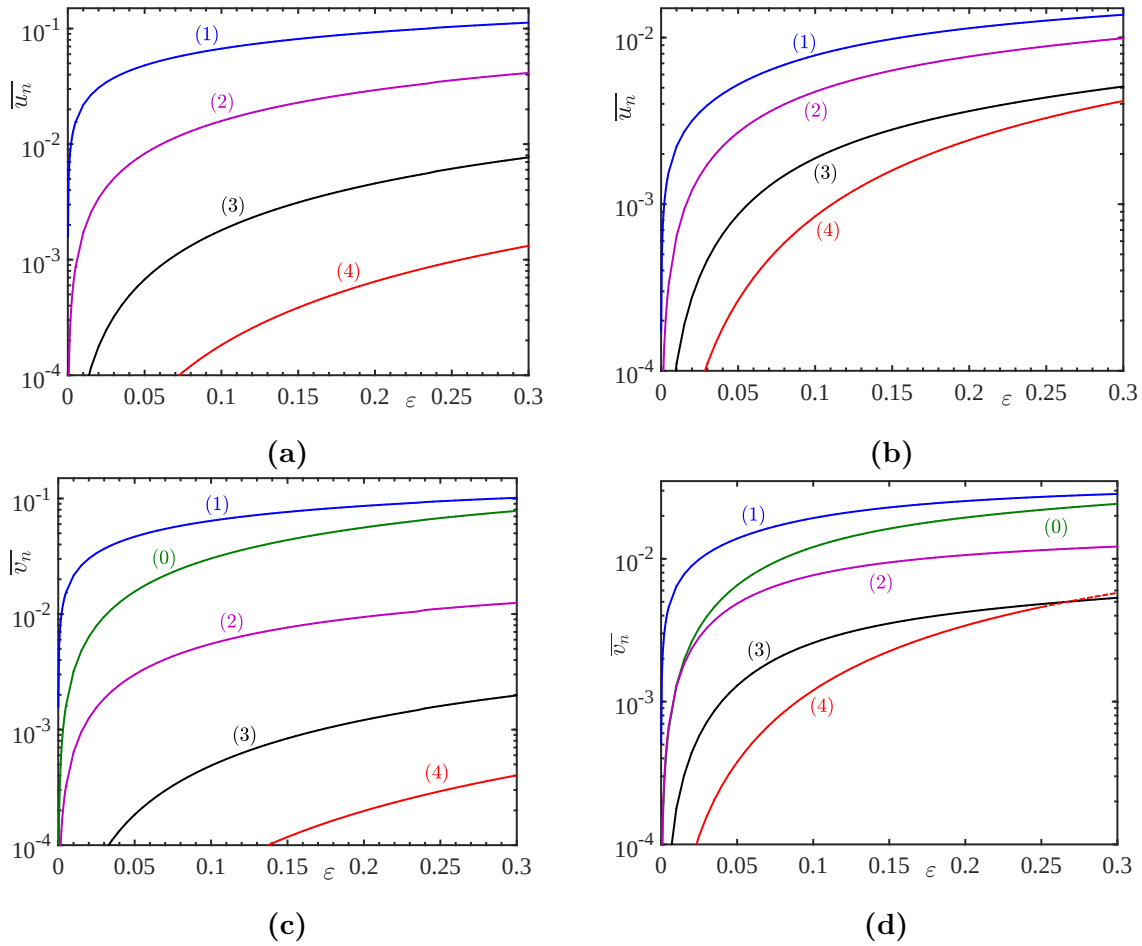


FIGURE 2.26 – (Color online) Evolution of the harmonics (averaged over a width gap) as a function of the reduced Reynolds number for a Newtonian fluid, frame **(a)** and **(c)** and a Carreau fluid, frame **(b)** and **(d)**, with $n_c = 0.2$, $\lambda = 10$.

cates that it is dominated by the feedback of the base flow correction onto the fundamental mode, when the Newtonian fluid is considered. For a shear-thinning fluids, the feedback of the first harmonic becomes more and more significant as the shear-thinning index decreases. The kinetic energy $\xi$ of the fundamental mode was determined. It is shown that $\xi$ decreases with increasing shear-thinning effects and more than 90 % of $\xi$ is concentrated on the azimuthal component.

Detailed analysis of the flow structure in the TVF regime at moderate distance from the onset was obtained by considering amplitude equation at seventh-order. It is shown that with increasing shear-thinning effects, Taylor vortices are squeezed against the inner cylinder and the center of the patterns are axially shifted towards the outflow boundaries ($z = 0$, $z/\lambda_z = 1$). Associated with this shift of the patterns is the increasing concentration of vorticity at these positions. Furthermore, the outflow becomes more stronger than the inflow and the area of the inflow increases accordingly. Positive azimuthal streaks induced by the radial outflow is more and more significant. Whereas, the negative azimuthal streak

is weak and occupies a large region. The change in the flow structure modifies the viscosity field. The numerical results show that this modification is mainly related to the variation of the shear-rate $\dot{\gamma}_{r\theta}(\boldsymbol{U_b} + \boldsymbol{u})$. The pseudo-Nusselt number $Nu_*$ is another feature of the flow structure. It is found that $Nu_*$ decreases with increasing shear-thinning effects. Besides this, analysis of the Fourier coefficients shows that even at moderate distance from the onset, higher harmonics become more relevant comparatively to the Newtonian case. Additional computations were performed for a narrow gap configuration. In this case, the azimuthal velocity profiles of the base flow get close to the linear profile, the viscosity stratification is weak and the range of $Re$ where the TVF regime is stable is quite limited. According to Coles [49] and Jones [5], for $\eta \geq 0.9$, transition to wavy vortex flow is observed at $Re \approx 1.2\, Re_c$ ($\epsilon = 0.2$). Some results are reported in Appendix 2.D for radius ratio $\eta = 0.9$.

For strong shear-thinning effects, the marginal stability curve flattens and the coherence length of the perturbation decreases significantly. In this case, modes of different wavenumbers (delimited by the Eckhaus boundary) exist close to the onset of the primary bifurcation. These modes may interact with each other leading to a secondary bifurcation with a more complex dynamic. The interaction of modes of different wavenumber limits the range of validity of the weakly nonlinear analysis. Nevertheless, we think that the modifications of the flow structure described in this study plays a fundamental role in triggering an eventual secondary bifurcation. To understand the interaction between different modes, a fully nonlinear method based on the numerical continuation can be used [50]. This approach could be useful to clarify the influence of shear-thinning on the coupling between the fundamental mode and the second harmonic observed experimentally by Crumeyrolle et al. [51] for semi-dilute aqueous solutions of high molecular weight polyethylenoxide.

## 2.A Validation

| Radius ratio $\eta$ | Chandrasekhar [38] ($Re_c$) | Our results ($Re_c$) |
|---|---|---|
| $\eta = 0.975$ | 260.9476 | 260.9496 |
| $\eta = 0.950$ | 184.98 | 184.99 |
| $\eta = 0.925$ | 151.48 | 151.4772 |
| $\eta = 0.900$ | 131.6131 | 131.6145 |
| $\eta = 0.875$ | 118.157 | 118.1571 |
| $\eta = 0.850$ | 108.3119 | 108.3131 |
| $\eta = 0.750$ | 85.7764 | 85.7765 |
| $\eta = 0.650$ | 74.9622 | 74.9623 |
| $\eta = 0.500$ | 68.1862 | 68.1863 |

TABLE 2.1 – Newtonian fluid. Critical Reynolds number at different radius ratios. Comparison with Chandrasekhar's results [38]

.

| Rheological parameters | Alibenyahia et al. [16] $(Re_c)/\mu_w$ | Our results $(Re_c)/\mu_w$ |
|---|---|---|
| $n = 0.7$, $\lambda = 20$ | 260.9476 | 260.9496 |
| $n = 0.5$, $\lambda = 20$ | 184.98 | 184.99 |
| $n = 0.3$, $\lambda = 20$ | 151.48 | 151.4772 |

TABLE 2.2 – Carreau fluid. Critical Reynolds number defined with the inner wall shear viscosity. Comparison with Alibenyahia et al. [16]

.

| $Re$ | $Nu_*$ Our results | $Nu^*$ Donnelly & Simon [45] |
|---|---|---|
| 69.1 | 1.012422 | 1.016190 |
| 70.2 | 1.027175 | 1.024306 |
| 73.0 | 1.063204 | 1.053082 |
| 75.3 | 1.090811 | 1.076942 |
| 78.8 | 1.129259 | 1.111199 |
| 85.1 | 1.188594 | 1.167744 |
| 94.8 | 1.260240 | 1.246044 |
| 107.0 | 1.326927 | 1.279206 |
| 121.0 | 1.383261 | 1.394628 |

TABLE 2.3 – Newtonian fluid. Variation of the Pseudo-Nusselt number $Nu_*$ versus Reynolds number at $\eta = 0.5$. Comparison between our results and those obtained experimentally by Donnelly & Simon [45]

## 2.B Contribution of nonlinear inertial and nonlinear viscous terms

The feedback of the mean flow correction and that of the first harmonic on the fundamental mode through the nonlinear inertial and nonlinear viscous terms are given in table 2.4 for $\lambda = 10$ and different values of the shear-thinning index $n_c$.

| $n_c$ | $g_1$ | $g_{10}^I$ | $g_{10}^V$ | $g_{12}^I$ | $g_{12}^V$ | $g_{1-11}^V$ |
|---|---|---|---|---|---|---|
| 0.2 | -38.235 | -29.561 | 6.721 | -28.098 | 25.534 | -12.831 |
| 0.3 | -53.698 | -33.737 | 5.724 | -42.354 | 26.268 | -9.598 |
| 0.4 | -76.801 | -45.024 | 3.527 | -52.555 | 24.690 | -7.438 |
| 0.5 | -108.301 | -65.101 | 9.766 | -60.968 | 22.549 | -5.758 |
| 0.6 | -151.688 | -95.215 | -1.276 | -71.688 | 20.446 | -3.956 |
| 0.7 | -214.583 | -140.846 | -3.006 | -86.899 | 18.018 | -1.849 |
| 0.8 | -315.127 | -215.481 | -4.105 | -110.776 | 14.775 | 4.592 |
| 0.9 | -496.243 | -351.458 | -3.970 | -152.723 | 9.693 | 2.216 |
| 1.0 | -867.033 | -632.705 | 0.000 | -234.329 | 0.000 | 0.000 |

TABLE 2.4 – Cubic Landau constant and contributions of nonlinear inertial and nonlinear viscous terms at the critical conditions

## 2.C Landau constants

The Landau coefficients $g_1$, $g_2$, $g_3$ are given in table 2.5 for $\lambda = 10$ and different values of the shear-thinning index.

## 2.D Flow structure and viscosity field for $\eta = 0.9$

In the figure 2.28 we have represented contours of the stream function, the vorticity and the viscosity distribution at $\epsilon = 0.1$, for a Carreau fluid with $n_c = 0.2$ and $\lambda = 10$.

| $n_c$ | $g_1$ | $g_2$ | $g_3$ |
|---|---|---|---|
| 0.2 | -38.217 | -11496.709 | -2411946.180 |
| 0.3 | -53.698 | -16939.108 | -5604408.660 |
| 0.4 | -76.647 | -21517.202 | -8480701.020 |
| 0.5 | -108.271 | -25742.819 | -10761822.517 |
| 0.6 | -151.684 | -31643.773 | -13182598.598 |
| 0.7 | -214.583 | -33736.107 | -12116764.641 |
| 0.8 | -315.127 | -38383.606 | -11625135.458 |
| 0.9 | -496.243 | -48609.312 | -12000787.340 |
| 1.0 | -867.033 | -62111.466 | -12310212.318 |

TABLE 2.5 – Landau constants at the critical conditions for different values of the shear-thinning index

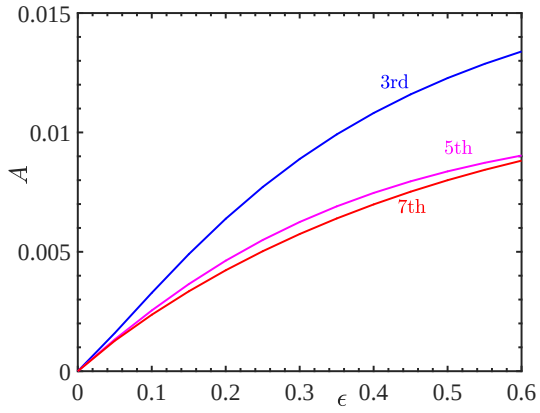


FIGURE 2.27 – (Color online) Evolution of the amplitude $A$ versus $\epsilon = (Re - Re_c)/Re_c$ for a shear-thinning fluid with $n_c = 0.5$, $\lambda = 10$, at cubic, fifth and seventh-order in the amplitude expansion.

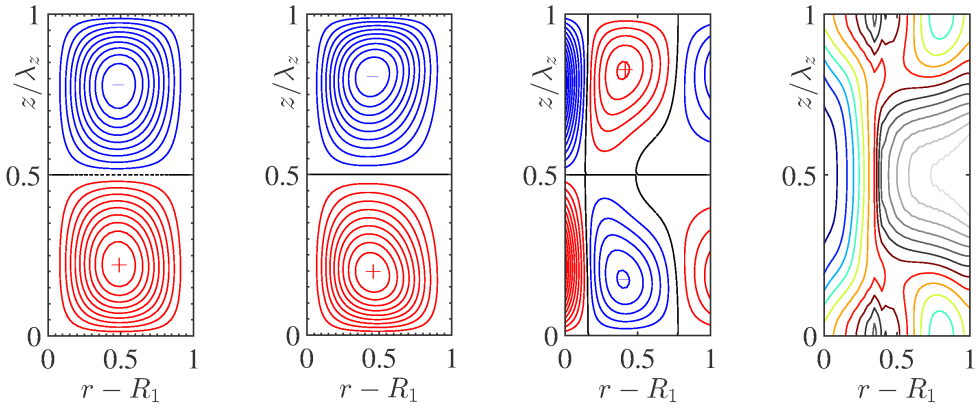


FIGURE 2.28 – (Color online) Narrow gap, $\eta = 0.9$. Flow field structure for a Newtonian fluid and a Carreau fluid with $n_c = 0.2$, $\lambda = 10$. **(a)** Contours of the stream function for a Newtonian fluid, $\psi_{max} = 0.12$, $\Delta\psi = \psi_{max}/10$. **(b)** Contours of the stream function for the Carreau fluid,$\psi_{max} = 0.072$, $\Delta\psi = \psi_{max}/10$ . **(c)** Contours of vorticity for a Carreau fluid, $\Omega_{max} = 0.35$, $\Delta\Omega = \Omega_{max}/10$. **(d)**, Contours of the viscosity for the Carreau fluid, $\mu_{max} = 0.0843$, $\mu_{min} = 0.02$, $\Delta\mu = 0.004$.

## Bibliographie

[1] E. L. Koschmieder. Bénard cells and Taylor vortices. *Cambridge Monogr. Mech.*, 844 :37–51, 1993.

[2] R. Tagg. The Couette-Taylor problem. *Nonlinear Sci. Today*, 4 :1–25, 1994.

[3] P. G. Drazin and W. H. Reid. Hydrodynamic stability. *Cambridge Mathematical Library. Cambridge University Press.*, 1981.

[4] G. I. Taylor. Stability of a viscous liquid contained between two rotating cylinders. *Trans. R. Soc. Lond. A*, 223 :289–343, 1923.

[5] C. A. Jones. The transition to wavy Taylor vortices. *J. Fluid Mech.*, 157 :135–162, 1985.

[6] H.A. Snyder and R.B. Lambert. Harmonic generation in Taylor vortices between rotating cylinders. *J. Fluid Mech.*, 26(3) :545–562, 1966.

[7] O. Meincke and C. Egbers. Routes into chaos in small and wide gap Taylor-Couette flow. *Phys. Chem. Earth Pt. B*, 24(5) :467–471, 1999.

[8] C. D. Andereck, S. S. Liu, and H. L. Swinney. Flow regimes in a circular Couette system with independently rotating cylinders. *J. Fluid Mech.*, 164 :155–183, 1986.

[9] H. Giesekus. Zur stabilität von strömungen viskoelastischer flüssigkeiten. *Rheol. Acta*, 5(3) :239–252, 1966.

[10] S. J. Muller, R.G. Larson, and E.S.G. Shaqfeh. A purely elastic transition in Taylor-Couette flow. *Rheol. Acta*, 28(6) :499–503, 1989.

[11] R.G. Larson, E.S.G. Shaqfeh, and S.J. Muller. A purely elastic instability in Taylor-Couette flow. *J. Fluid Mech.*, 218 :573–600, 1990.

[12] E.S.G. Shaqfeh, S.J. Muller, and R.G. Larson. The effects of gap width and dilute solution properties on the viscoelastic Taylor-Couette instability. *J. Fluid Mech.*, 235 :285–317, 1992.

[13] A. Groisman and V. Steinberg. Mechanism of elastic instability in Couette flow of polymer solutions. *Phys. Fluids*, 10 :2451–2463, 1998.

[14] A. Lindner, D. Bonn, and J. Meunier. Viscous fingering in a shear-thinning fluid. *Phys. Fluids*, 12(2) :256–261, 2000.

[15] Y. Agbessi, B. Alibenyahia, C. Nouar, and L. Choplin. Linear stability of Taylor-Couette flow of shear-thinning fluids : modal and non-modal approaches. *J. Fluid Mech.*, 775 :354–389, 2015.

[16] B. Alibenyahia, C. Lemaître, C. Nouar, and N. Ait-Messaoudene. Revisiting the stability of circular Couette flow of shear-thinning fluids. *J. Non-Newtonian Fluid. Mech.*, 183 :37–51, 2012.

[17] Z. Li and R.E. Khayat. A non-linear dynamical system approach to finite amplitude Taylor-Vortex flow of shear-thinning fluids. *Int. J. Numer. Methods Fluids*, 45(3) :321–340, 2004.

[18] N. Ashrafi and R.E. Khayat. Shear-thinning-induced chaos in Taylor-Couette flow. *Phys. Rev. E*, 61(2) :1455, 2000.

[19] N. Ashrafi. Stability analysis of shear-thinning flow between rotating cylinders. *Appl. Math. Model*, 35(9) :4407–4423, 2011.

[20] N. Ashrafi. Effect of nonlinearity on the Taylor-Couette flow in the narrow-gap. *J. Mech. Sci. Technol.*, 25(9) :2247, 2011.

[21] H. Masuda, T. Horie, R. Hubacz, M. Ohta, and N. Ohmura. Prediction of onset of Taylor-Couette instability for shear-thinning fluids. *Rheol. Acta*, 56(2) :73–84, 2017.

[22] M. P. Escudier, I. W. Gouldson, and D. M. Jones. Taylor vortices in Newtonian and shear-thinning liquids. *Proc. Roy. Soc. Lond. A.*, 449 :155–176, 1995.

[23] V. Sinevic, R. Kuboi, and A.W. Nienow. Power numbers, Taylor numbers and Taylor vortices in viscous Newtonian and non-Newtonian fluids. *Chem. Eng. Sci.*, 41(11) :2915–2923, 1986.

[24] N. Cagney and S. Balabani. Taylor-Couette flow of shear-thinning fluids. *Phys. Fluids*, 31(5) :053102, 2019.

[25] J. Watson. On the non-linear mechanics of wave disturbances in stable and unstable parallel flows. part 1. the development of a solution for plane Poiseuille flow and for plane Couette flow. *J. Fluid Mech.*, 9 :371–389, 1960.

[26] J. T. Stuart. On the non-linear mechanics of wave disturbances in stable and unstable parallel flows. part 1. the basic behaviour in plane Poiseuille flow. *J. Fluid Mech.*, 9 :353–370, 1960.

[27] T. Herbert. On perturbation methods in nonlinear stability theory. *J. Fluid Mech.*, 126 :167–186, 1983.

[28] P.K. Sen and D. Venkateswarlu. On the stability of plane Poiseuille flow to finite-amplitude disturbances, considering the higher-order Landau coefficients. *J. Fluid Mech.*, 133 :179–206, 1983.

[29] K. Fujimura. The equivalence between two perturbation methods in weakly nonlinear stability theory for parallel shear flows. *Proc. R. Soc. Lond. A*, 424(1867) :373–392, 1989.

[30] P. Chossat and G. Iooss. *The Couette-Taylor Problem*, volume 102. Springer Science & Business Media, 2012.

[31] P.J. Carreau. Rheological equations from molecular network theories. *T. Soc. Rheol.*, 16(1) :99–127, 1972.

[32] R. B. Bird, R. Amstrong, and O. Hassager. *Dynamics of polymeric liquids*. Wiley-Interscience, New York, 1987.

[33] R. Tanner. Engineering rheology. Oxford University Press, New York, 2000.

[34] M. Darbouli, C. Métivier, S. Leclerc, C. Nouar, M. Bouteraa, and S. Didier. Natural convection in shear-thinning fluids : Experimental investigations by MRI. *Int. J. Heat Mass Transfer*, 95 :742–754, 2016.

[35] A.S. Haase, A.J. Wood, L.M.J. Sprakel, and R.G.H. Lammertink. Inelastic non-Newtonian flow over heterogeneously slippery surfaces. *Phys. Rev. E*, 95(2) :023105, 2017.

[36] M.A. Dominguez-Lerma, G. Ahlers, and D.S. Cannell. Marginal stability curve and linear growth rate for rotating Couette–Taylor flow and Rayleigh–Bénard convection. *Phys. Fluids*, 27(4) :856–860, 1984.

[37] R.C. DiPrima and P. Hall. Complex eigenvalues for the stability of Couette flow. *Proc. R. Soc. Lond. A*, 396(1810) :75–94, 1984.

[38] S. Chandrasekhar. *Hydrodynamic and hydromagnetic stability.* Dover Publications, 1981.

[39] O. Crumeyrolle, I. Mutabazi, and M. Grisel. Experimental study of inertioelastic Couette-Taylor instability modes in dilute and semidilute polymer solutions. *Phys. Fluids*, 14(5) :1681–1688, 2002.

[40] K. Fujimura and S. Yamada. Hexagons and triangles in the Rayleigh-Bénard problem : quintic-order equations on a hexagonal lattice. *Proc. R. Soc. A*, 464 :2721–2739, 2008.

[41] S.C. Generalis and K. Fujimura. Range of validity of weakly nonlinear theory in the Rayleigh-Bénard problem. *J. Phys. Soc. Jpn*, 78 :1–11, 2009.

[42] B. Dubrulle and F. Hersant. Momentum transport and torque scaling in Taylor-Couette flow from an analogy with turbulent convection. *Eur. Phys. J. B*, 26(3) :379–386, 2002.

[43] B. Eckhardt, S. Grossmann, and D. Lohse. Torque scaling in turbulent Taylor-Couette flow between independently rotating cylinders. *J. Fluid Mech.*, 581 :221–250, 2007.

[44] A. Esmael, C. Nouar, A. Lefevre, and N. Kabouya. Transitional flow of a non-Newtonian fluid in a pipe : Experimental evidence of weak turbulence induced by shear-thinning behavior. *Phys. Fluids*, 22(10) :101701, 2010.

[45] R.J. Donnelly and N.J. Simon. An empirical torque relation for supercritical flow between rotating cylinders. *J. Fluid Mech.*, 7(3) :401–418, 1960.

[46] M. Bouteraa, C. Nouar, E. Plaut, C. Métivier, and A. Kalck. Weakly nonlinear analysis of Rayleigh–Bénard convection in shear-thinning fluids : nature of the bifurcation and pattern selection. *J. Fluid Mech.*, 767 :696–734, 2015.

[47] M. Bouteraa and C. Nouar. Weakly nonlinear analysis of Rayleigh-Bénard convection in a non-Newtonian fluid between plates of finite conductivity : Influence of shear-thinning effects. *Phys. Rev. E*, 92(6) :063017, 2015.

[48] H. Fasel and O. Booz. Numerical investigation of supercritical Taylor-vortex flow in a wide gap. *J. Fluid Mech.*, 138 :21–52, 1984.

[49] D. Coles. Transition in circular Couette flow. *J. Fluid Mech.*, 21(3) :385–425, 1965.

[50] R. Meyer-Spasche and H. B. Keller. Some bifurcation diagrams for Taylor Vortex flows. *Phys. Fluids*, 28(5) :1248–1252, 1985.

[51] O. Crumeyrolle, A. Latrache, I. Mutabazi, and A.B. Ezersky. Instabilities with shear-thinning polymer solutions in the Couette-Taylor system. In *J. Phys. Conf. Ser.*, volume 14, page 78. IOP Publishing, 2005.

# Chapitre 3

# Secondary instabilities in Taylor Couette flow of shear-thinning fluids

**Sommaire**

## 3.1 Introduction

The Taylor-Couette flow of a viscous incompressible fluid between two coaxial cylinders that are infinitely long is a paradigm for studies of stability and transition to turbulence. A survey of the literature on the Taylor-Couette problem can be found in Koschmieder [1] and Tagg [2]. In the usual case, the inner cylinder of radius $R_1$ is rotating with angular velocity $\Omega_1$ and the outer cylinder of radius $R_2$ is stationary. The radius ratio will be denoted

$$\eta = R_1/R_2 < 1. \tag{3.1}$$

The axial length $\ell$ is, in most implementations, much larger than the gap,

$$d = R_2 - R_1, \tag{3.2}$$

i.e. the aspect ratio

$$L = \ell/d \tag{3.3}$$

is much larger than 1 ($L \gg 1$). In the basic state, commonly called circular Couette flow (CCF), only the azimuthal velocity $u_\theta$, $\theta$ standing for the azimuthal angle, is non zero and it is a decreasing function of only the radius $r$.

### 3.1.1 Taylor vortex flow in Newtonian fluids

As demonstrated by Taylor [3], as inertial effects start to dominate over viscous ones, CCF becomes unstable giving rise to the Taylor vortex flow (TVF) characterized by stationary counter-rotating vortices stacked along the axial direction. The onset of instability can be parameterized by the Reynolds number (3.5). Equivalently, the Reynolds number can be used. In most common configurations the outer cylinder is at rest and the inner one rotates with angular velocity $\Omega_1$. This defines the velocity scale

$$U_{ref} = R_1\Omega_1. \tag{3.4}$$

In an incompressible Newtonian flow with uniform viscosity $\mu$ and density $\rho$ where kinematic viscosity $\nu = \mu/\rho$ is well defined, the standard definition of the Reynolds number

using the gap $d$ as length scale results in :

$$\mathrm{Re} = R_1\Omega_1 d/\nu. \tag{3.5}$$

The critical Reynolds number of the onset of TVF will be denoted $Re_c$. The canonical configuration, most convenient for theoretical study, consists in considering a small gap $\eta \to 1$ and an infinite aspect ratio $L \to \infty$ (Taylor [3]). However, in practical cases, in particular, experimental implementations, large gaps and finite aspect ratios occur. The values of the critical Reynolds for several values of the radius ratio are available in the literature (see for instance Table 1 in DiPrima et al.[4]). Approximate expressions of $\mathrm{Re}_c(\eta)$ can be found in Esser & Grossmann [5] and Dutcher & Muller [6]. Concerning the influence of the aspect ratio, Cole [7] has shown experimentally that there is practically no effect of the annulus length on the critical Reynolds number for an aspect ratio $L$ as low as 8. The interaction between the endwall boundary layer and the centrifugal Taylor instability has been studied numerically by Czarny et al. (2003) for a particularly low value of aspect ratio $L = 6$.

### 3.1.2 Stability of Taylor vortices in Newtonian fluids

For small gap width, the range of Reynolds number $Re$, in which the axisymmetric vortices remain stable is small. For instance, in the experiments of Cole [7] where $\eta = 0.95$ and $L = 60$, the Taylor vortex flow becomes unstable with respect to azimuthal disturbances at $Re_s = 1.05Re_c$. A bifurcation from TVF to the wavy vortex flow (WVF) is observed. The structure of the WVF and the doubly periodic (axially and in time) motion was first studied experimentally by Coles (1965). Unlike the transition to TVF, the Reynolds number $Re_s$ of the onset of the secondary instability yielding WVF depends significantly on the aspect ratio $L$. It increases strongly when the aspect ratio $L$ is reduced below 40, as it has been shown experimentally by Cole [7]. For $L \geq 40$, with $\eta > 0.89$, $Re_s$ changes by only few percent. The azimuthal wavenumber varies on a much wider range. It ranges from 2 to 8 depending on the conditions by which the second transition is approached (Coles [8], Cole [7], Mullin [9], Dutcher & Muller [10]. The non-uniqueness of this flow has been also observed through the existence of hysteresis phenomena Coles [8]. In other words, multiple stable flow states could be reached for a given Reynolds number. Concerning the physical mechanisms that drive the transition from TVF to WVF, they were discussed by Martinand et al. [11] and Dessup et al.[12].

For $\eta < 0.75$, $Re_s$ increases rapidly as $\eta$ decreases [13]). For instance, for $\eta = 0.67$, $Re_s \approx 5Re_c$ . This tendency is in agreement with the experimental results of Snyder & Lambert[14], Meincker & Egbers[15] and King et al.[16]. A recent direct numerical simulation by Razzak et al.[17] in a wide gap setup $\eta = 0.5$ yielded $Re_s \approx 8.45Re_c$. In their study, a four wavelengths fluid column is considered ($L = 4\,\Lambda = 7.944$) with periodic boundary conditions in the axial direction. For this relatively small aspect ratio, Razzak et al. [17] evidenced an intermediate step between TVF and WVF in the interval

$6.2\,\mathrm{Re}_c \leq \mathrm{Re} \leq 8.45\,\mathrm{Re}_c$. They found that the flow becomes non-axisymmetric with a strong azimuthal wave in the inflow region (inward oriented flow of the TVF vortex array) as compared to the outflow region. Three decades earlier, the linear stability of the Taylor vortices was investigated by Jones [13] for the same radius ratio $\eta = 0.5$. The axisymmetric solution was determined using a Fourier expansion in the axial direction with a period of one or two axial wavelengths, and a Chebychev polynomials in the radial direction. He found that the results depend on the axial wavelength $\Lambda$ selected. For $\Lambda < 2$ (1.6 and 1.7 in the table 1 of his paper ), Jones [13] detected a wavy outflow boundary (WOB) mode at $\mathrm{Re} \approx 5\,\mathrm{Re}_c$. In this mode, the oscillation amplitude is localized in the outflow boundary jet and adjacent outflow boundaries jets oscillate in antiphase, i.e. the flow is axial subharmonic with respect to the period of Taylor vortices. If $\Lambda > 2$ a direct transition to wavy vortex flow is observed. Still earlier, Lorenzen et al. [18] observed experimentally for $\eta$ around 0.5 a transition from TVF to WOB mode when the axial wavelength is less than 2 (the size of one vortex is less that the gap width). In their experiments, the number of vortices was kept constant as $L$ is varied so that the size of individual vortices varied.
Hence for a wide gap, $\eta$ around 0.5, wavy modes different from the conventional wavy vortex flow are obtained numerically and experimentally. The type of wavy mode observed is probably very sensitive to the aspect ratio, the size of vortices and may be also to the type of boundary conditions. Furthermore, the wavy mode obtained by Razzak et al. [17] was not predicted by the linear stability analysis done by Jones [13]. Therefore, we believe that additional experimental or numerical data are needed for a wide gap geometry. Concerning, the effect of endwalls on the wavy vortex flow, it has been shown numerically by Czarny et al. [19], that this effect does not penetrate far from the endwall. The waviness is already present one or two vortices far from the endwall.

Configurations with finite aspect ratio $L$ or given axial period lead to restrictions of the axial wavenumber of axisymmetric TVF. At the critical Reynolds number $\mathrm{Re}_c$, the axial wavenumber $k$ can have only a single, unique value, $k_c$. For $\mathrm{Re} > \mathrm{Re}_c$, TVF solutions to the equations of motion exist for a range of wavenumbers which depends on the reduced Reynolds number $\epsilon = \dfrac{\mathrm{Re} - \mathrm{Re}_c}{\mathrm{Re}_c}$ and the boundary conditions. However, the resulting solutions of such a system are not all stable. The stability of these solutions with respect to axisymmetric perturbations is a fundamental mechanism which delimits the width of the stable band of wavenumbers. Close to the marginal stability curve of the Couette flow, the limits of the stable band can be determined using amplitude expansion up to third order (Kogelman & DiPrima [20]). A first detailed investigation of the stability of TVF solutions with respect to axisymmetric perturbations was done numerically by Riecke & Paap [21] for three radius ratios : $\eta = 0.892$, 0.75 and 0.5. It was followed by that of Paap & Riecke [22] for $\eta = 0.5$ and larger values of $\epsilon$. Overall, a stationary TVF solution for a given wavenumber $k$ is computed, at different values of $\epsilon$, using a Galerkin method with Fourier expansion in the axial direction and Chebyshev polynomials in the

radial direction. Using the Floquet theory, the linear stability analysis of this solution, with respect to infinitesimal perturbations with wavenumber $\widetilde{k}$ leads to an eigenvalue problem, the least stable eigenvalue of which is real, i.e. represents the growth-rate $\sigma\left(\widetilde{k}\right)$ of a stationary perturbation. A TVF solution with a wavenumber $k$ is unstable when the growth rate $\sigma\left(\widetilde{k}\right)$ is positive for some value of $\widetilde{k}$. Two types of instabilities can be distinguished according to the value of $\widetilde{k}$ for which $\sigma\left(\widetilde{k}\right)$ first becomes positive. The first one corresponds to the case where $\sigma\left(\widetilde{k}\right)$ first exceeds zero near $\widetilde{k} = 0$, the instability is of Eckhaus type, i.e. of long wavelength [21, 22, 23]. In this case, the adjustment of the wavenumber is done by creation of a pair of vortices (if $k$ is too low) or pairing of vortices (if $k$ is too large) and a new stationary stable state is reached. The second type of instability corresponds to the case where $\sigma\left(\widetilde{k}\right)$ first exceeds zero near $\widetilde{k} = k/2$. It is called short-wavelength instability. In this case, the adjustment of the wavenumber is done by merging every two vortex pairs into a single one (when $k$ is too high) or by adding a vortex pair between every two base vortex pairs (when $k$ is too low). Riecke & Paap [21] and Paap & Riecke [22] found that the band of stable wavenumbers is mainly delimited from either low $k$- or high $k$- side by the Eckhaus instability mechanism. However, for $\epsilon > 1$ and from high k-side, the stable band is delimited by the short wavelength instability. Excellent agreement exists between the theoretical results of Riecke & Paap [21] and Paap & Riecke [22] and the experimental observations of Dominguez-Lerma et al. [24] and Dennin et al.[23]. Similar theoretical calculations done by Guo & Finlay [25] lead to the same results. Riecke & Paap [21] and Paap & Riecke [22] have noticed that the width of the band of stable wavenumbers is much smaller than that predicted from amplitude expansion. Furthermore, this behavior is more pronounced with lowering the radius ratio. It was also observed theoretically and experimentally that on the low $k$-side, the stability limits departs rather suddenly from the amplitude expansion result with increasing $\epsilon$. According to Riecke & Paap [21] this structure arises from the interaction of modes with resonating wavenumbers. The first such resonance occurs between $k$ and $2\,k$. This point has been discussed by Meyer-Spasche & Keller [26].

Note that, for a narrow gap, when $Re$ is increased further, the wavy vortex flow bifurcates to modulated wavy vortex flow (MWVF) characterized by two incommensurate temporal frequencies (Andereck et al. [27]). Shortly after the onset of the second frequency, the flow becomes chaotic or weakly turbulent (Brandsater et al. [28]). This orderly progression of nonlinear states makes the Taylor-Couette flow an attractive model for studying the influence of rheology of non-Newtonian fluids on the instability mechanisms and transition to turbulence.

### 3.1.3 Brief Review on Taylor-Couette flow of shear-thinning fluids

A common feature of many non-Newtonian fluids is the shear-thinning behavior, i.e. a nonlinear decrease of the viscosity when the shear rate increases. Polymer and colloid solutions as well as particulate dispersions exhibit this behavior above a certain concentration threshold. Actually, these fluids are also viscoelastic to varying degrees. Hereafter, we focus on shear-thinning fluids for which the elastic response does not play a significant role. Typically, stiff polymers show significant nonlinear decrease of viscosity with the shear-rate, with almost negligible elastic effect (Lindner et al. [29]). The shear-thinning behavior arises from the reorganization of the internal fluid structure reducing the viscous dissipation. We will assume that the characteristic time of the reorganization of the flow structure is much smaller than all characteristic times of the problem.
Several works have been devoted to the influence of shear-thinning behavior on threshold instabilities in Taylor-Couette flow as well as to the features of Taylor vortices.

Circular Couette flow of a shear-thinning fluid is mainly characterized by a viscosity stratification in the annular space, which is the more significant the stronger the shear-thinning effects and the wider the annular space. With increasing shear-thinning effects, the shear rate increases at the inner wall and decreases at the outer one. Furthermore, the nonlinear variation of viscosity with the shear rate introduces, at the linear level, an anisotropy of the deviatoric tensor associated to the perturbation.
The mechanism of instability of CCF of shear-thinning fluids with negligible viscoelasticity is the same as for a Newtonian fluid and results in axisymmetric counter rotating vortices separated by radial inflow and outflow jets emanating from the fluid layers adjacent to the cylinders' wall. However, the critical conditions are different because of the radial viscosity stratification and the modification of the azimuthal velocity profile. In the case where the inner cylinder is rotating and the outer one is stationary, the critical Reynolds and axial wave numbers were determined using linear stability analysis, for power-law and Carreau fluids, for wide and narrow annular spaces, see for instance Alibenyahia et al. [30], Li & Khayat [31], Agbessi et al.[32] and Topayev et al. [33] and the references therein. It is shown that the wavelength increases slightly with increasing shear-thinning effects when $\eta > 0.7$ and decreases significantly with increasing shear-thinning effects for a wide gap ($\eta < 0.6$). In shear-thinning flows the Newtonian definition (3.5) of the Reynolds number requires an additional specification of the viscosity scale $\mu_{ref}$ to replace $\nu = \mu_{ref}/rho$ where $\rho$ is the fluid density. A frequent choice is $\mu_{ref} = \mu_0$, where $\mu_0$ is the zero-shear viscosity :

$$\mathrm{Re} = \rho\,\Omega_1 R_1 d/\mu_0\,. \tag{3.6}$$

The critical Reynolds number defined using the zero-shear viscosity decreases with increasing shear-thinning effects. A radically different conclusion may be reached if one uses the inner wall-shear viscosity of the fluid as viscosity scale. Masuda et al. [34] used

an average viscosity weighted by the strain-rate squared. They found that the critical Reynolds number defined using this average viscosity is the same as for a Newtonian fluid. However, this result is limited only to a narrow annular space with a radius ratio $\eta > 0.7$. Recently, Elcicek & Guzel [35] suggested to use an average Reynolds number $Re_G$, defined as an average over the annular space of the local Reynolds number calculated using the local velocity and the local viscosity. With this definition, it is observed that the critical Reynolds number increases with increasing shear-thinning effects. The selection of the reference viscosity defining the Reynolds number may be considered to be simply a matter of choice, however, it changes the conclusions concerning the effect of shear thinning.

From an experimental point of view, Sinevic et al.[36] determined the onset of Taylor vortices based on changes in the scaling relationship between the measured torque exerted on the rotating inner cylinder and $Re$. The results were obtained for two radius ratios $\eta = 0.7$ and 0.9, the rheological behavior of the used fluids, CMC and Carbopol solutions, were described by the power-law model. Using a Taylor-Couette system with a radius ratio $\eta = 0.5$, Escudier et al. [37] determined the transition from CCF to TVF by focusing on the development of the axial velocity component near the inner wall at a radial position $r$ such $(R_2 - r)/(R_2 - R_1) = 0.8$. The Reynolds number is defined using the inner wall shear viscosity. The used fluids were a glucose solution as a Newtonian fluid reference, an aqueous solution of xanthan gum 1500 ppm which is shear thinning and a Laponite suspension which is shear-thinning and thixotropic. The radius ratio and the aspect ratio of the Taylor Couette configuration are $\eta = 0.506$ and $L = 233$. In their experimental work, the authors focus mainly on the development of Taylor vortices. It is indicated that for shear-thinning fluids, the onset of Taylor vortices is much more gradual than that for a Newtonian fluid.

Concerning the flow structure in the TVF regime, the theoretical [30, 32, 33] and experimental [37, 38, 39] results indicate that the flow undergoes a significant change with increasing shear-thinning effects. Indeed it is shown that with increasing shear-thinning effects : (i) for a wide gap, the vortex eye is shifted towards the inner cylinder, because of the viscosity stratification : the viscosity increases from the inner cylinder to the outer one ; (ii) the vortices are shifted axially towards the radial outflow boundaries ; (iii) this axial shift leads to increasing concentration of the vorticity at these boundaries ; (iv) the vorticity in the outflow becomes stronger than n the inflow and the extent of the inflow zone increases accordingly ; (v) the strength of the vortices becomes weak as compared to the velocity of the inner cylinder. Note that, using a weakly non linear analysis, Topayev et al. [33] demonstrated for a large range of rheological parameters that the transition to TVF regime for purely viscous shear-thinning fluids remains supercritical.

### 3.1.4 Stability of Taylor vortices in shear-thinning fluids

As far as the stability of the Taylor vortex flow is concerned, the results are sparse. In the experiments of Escudier et al. [37] at $Re_c < Re < 2.5\,Re_c$, with $\eta = 0.506$, it was noticed for xanthan gum solution 1500 ppm and Laponite solution, that the vortices exhibit a slow axial drift. A constant drift velocity of $3 - 4\,\mu$.m/s was reported.
In a geometrical configuration with a narrow gap, $\eta = 0.883$ and $L = 12.97$, the transition from TVF to WVF was detected and studied by Cagney et al.[38] and [39] using particle image velocimetry and visualization. Their results (Table III in Cagney et al. [39]) indicate that the transition to WVF occurs at $\mathrm{Re}_s \approx 8\,\mathrm{Re}_c$ for a Newtonian fluid and at $\mathrm{Re}_s > 8\,\mathrm{Re}_c$ for shear-thinning fluids. However, one can note that for the Newtonian fluid, the value of $Re_s$ is much larger than that predicted by Cole [7] for a similar geometry. Furthermore, Cagney et al.[39] noticed that the amplitude of the wave varies with the axial position. It may be a consequence of endwalls effects.

In a more recent paper, using xanthan gum solutions in a mixture glycerol-water (25% glycerol and 75% water) in a wider gap ($\eta = 0.77$) and a larger aspect ratio $L = 21.5$, than previously, Cagney et al. [40] observed the same progression of regimes ($CCF \rightarrow TCF \rightarrow WVF$) as for a Newtonian fluid. However, unlike in their previous study, the authors observed merger events mainly in a WVF regime at some Reynolds numbers. These merger events occur near the ends of their system and are followed by a drifting and splitting of vortices. Actually, the process of vortex merger was also observed for a Newtonian fluid in WVF regime near the ends of the Taylor-Couette geometry by Park et al. [41] ; Ahlers et al. [42] and Crawford et al. [43]. Ahlers et al. [42] have analyzed this process in terms of stability of the WVF regime in the plane (axial wavenumber, Reynolds number). According to these authors, near the ends the local wavenumber (wavelength) is large (small). The system reacts by eliminating one pair of vortices and makes the structure "enter" into the stable band of wavenumbers. They have also found that the side boundaries of stability domain of WVF are very aspect ratio dependent. This might explain why Cagney & Balabani [39] did not observe merger events since the aspect ratio was smaller than that in their paper Cagney et al. [40].
Elçiçek and Güzel [35] studied experimentally the influence of shear-thinning on flow structure and transition thresholds in a Taylor Couette flow for narrow ($\eta = 0.883, L = 42$) and wide ($\eta = 0.643, L = 16$) gaps. The used fluids are aqueous solutions of xanthan gum at 1000 and 2000 ppm. The rheological behavior of these fluids is described by a power-law model with a shear-thinning index $n_p = 0.45$ and 0.38 for 1000 and 2000 ppm concentration respectively. Unlike Cagney et al. [38] and [39] the transition from TVF to WVF is not observed. A direct transition from TVF to MWVF followed by a chaotic flow is observed. Furthermore, the authors highlighted the existence of non-axisymmetric modes between CCF and TVF.
It is clear from the above literature review, that additional experimental, theoretical and

numerical work is needed to understand the influence of shear-thinning behavior on the stability of the Taylor vortex flow. The scenario of the instability of the TVF regime depends probably on the aspect ratio.

### 3.1.5 Objectives, methodology and outline of the paper

The aim of the present article is to study the stability of Taylor vortex flow in shear-thinning fluids both experimentally and numerically. The novelty of the present work is to consider a wide gap configuration such that the onset of WVF regime would be delayed and the axisymmetric instabilities could develop. In this configuration, the observed creation and merging of vortices is not confined to the ends of the fluid domain. The experimental approach is based on visualization and particle image velocimetry measurements. The paper is structured as follows. In Section 2, we introduce the equations of the problem with the boundary conditions and we define the dimensionless parameters. In Section 3, we present the numerical method used. The validation of the numerical code is presented in Section 4. The experimental details of the Taylor-Couette flow setup as well as the measurement techniques are described in Section 5, along with the rheology of the used fluids. Experimental and numerical results are discussed in Sections 6 and 7. Section 6 concerns the primary bifurcation and Section 7 deals with the secondary bifurcation. In the conclusion section, we summarize the most relevant results and we give some perspectives to our work.

## 3.2 Mathematical formulation

We consider the flow of an incompressible shear-thinning fluid of uniform density $\rho$ and negligible viscoelasticity in an annular cavity characterized by a radius ratio (3.1) aspect ratio (3.3). The inner cylinder is rotating with an angular velocity $\Omega_1$ and the outer one is at rest. Non-dimensionalizing the velocity by the velocity scale (3.4) and the lengths by the gap $d$ we obtain the flow equations in the following form :

$$\mathbf{div}\,\boldsymbol{u} = 0 \tag{3.7}$$

$$\partial_t \boldsymbol{u} + (\boldsymbol{\nabla u})\cdot\boldsymbol{u} = -\boldsymbol{\nabla} p + \mathbf{div}\,(\boldsymbol{\tau})\ , \tag{3.8}$$

where $\boldsymbol{u} = u_r\mathbf{e}_r + u_\theta\,\mathbf{e}_\theta + u_z\mathbf{e}_z$ is the velocity vector in cylindrical coordinates $(r,\theta,z)$ and $p$ the pressure non-dimensionalized by the pressure scale $\rho\,U_{ref}^2$. $\boldsymbol{\tau}$ is the non-dimensionalized deviatoric stress tensor related to the strain-rate tensor :

$$\dot{\boldsymbol{\gamma}} = \nabla\boldsymbol{u} + (\nabla\boldsymbol{u})^T \tag{3.9}$$

by the relation

$$\boldsymbol{\tau}(\mathrm{Re},\dot{\boldsymbol{\gamma}}) = \frac{1}{Re}\,\frac{\mu}{\mu_0}\dot{\boldsymbol{\gamma}} \tag{3.10}$$

where Re is the Reynolds number (3.6) and the viscosity $\mu$ is modeled by the Carreau model [44] :

$$\frac{\mu-\mu_\infty}{\mu_0-\mu_\infty}=\left(1+\hat{\lambda}^2\Gamma\right)^{(n_c-1)/2}. \tag{3.11}$$

In the Carreau model (3.11), $\Gamma=\frac{1}{2}\dot{\boldsymbol{\gamma}}\!:\!\dot{\boldsymbol{\gamma}}$ is the second-invariant of the strain-rate tensor (3.9), $\mu_\infty$ is the dynamic viscosity at high shear rate, $n_c<1$ the shear-thinning index and $\hat{\lambda}=\lambda_f\,U_{ref}/d$, where $\lambda_f$ is the characteristic time of the fluid. The location of the transition from the Newtonian plateau to the shear-thinning regime is determined by $\lambda_f$ since $1/\lambda_f$ defines the characteristic shear rate for the onset of shear-thinning. Increasing $\hat{\lambda}$ reduces the Newtonian plateau to lower shear rates. The infinite shear viscosity $\mu_\infty$ is generally associated with the breakdown of the fluid and is frequently significantly smaller, $(10^3-10^4)$ times smaller than $\mu_0$ see Bird et al. [45] and Tanner [46]. The ratio $\mu_\infty/\mu_0$ will thus be neglected in the following. This leaves three rheological parameters : $\mu_0$, $\lambda$ and $n_c$ and the nondimensional viscosity in Eq. (3.10) writes

$$\frac{\mu}{\mu_0}=\left[1+(\lambda\mathrm{Re})^2\,\Gamma\right]^{\frac{n_c-1}{2}}. \tag{3.12}$$

In Eq. (3.12) we changed the original non-dimensionalization of the characteristic time $\hat{\lambda}$ by the time scale $d/U_{ref}$ to that by the viscous diffusion time scale $\rho d^2/\mu_0$ which resulted in replacing $\hat{\lambda}=\lambda\mathrm{Re}$. This makes the parameter $\lambda$ independent of the Reynolds number. Assuming axisymmetric flow, the velocity components depend only on two cylindrical coordinates $(r,z)$. The domain of these space variables is the rectangle $\mathcal{D}=\left[\frac{\eta}{1-\eta},\frac{1}{1-\eta}\right]\times[0,L]$.

Equations (3.7), (3.8), (3.10) and (3.12) have to be completed by appropriate boundary conditions. On the cylindrical boundaries, the dimensionless velocity $(u_r,u_\theta,u_z)$ obeys the no-slip condition

$$u_r=u_z=0,u_\theta=1,\ \text{at } r=r_1\equiv\frac{\eta}{1-\eta},\quad z\in\,]0;L] \tag{3.13}$$

$$u_r=u_z=0,u_\theta=0,\ \text{at } r=r_2\equiv\frac{1}{1-\eta},\quad z\in[0;L]\,, \tag{3.14}$$

Concerning the upper ($z=L$) and bottom ($z=0$) boundaries, we have considered two situations.

- In the first one, and in order to get as close as possible to the experimental conditions, we have considered a no slip boundary condition at the motionless bottom wall $z=0$, and a stress-free boundary condition on the upper boundary $z=L$. In this case, the free surface is assumed flat, and the surface tension is neglected, so that the surface is a pure

slip boundary.

$$u_r = u_z = u_\theta = 0, \text{ at } z = 0, \quad r \in [r_1; r_2] \tag{3.15}$$

$$u_z = 0, \ \tau_{rz} = \tau_{r\theta} = 0, \text{ at } z = L, \quad r \in [r_1; r_2]\,. \tag{3.16}$$

The boundary condition at the bottom boundary is complicated by the difficulty in handling the singularity in the azimuthal velocity $u_\theta$ at the corner where the cylinder has a different rotational speed than the lower surface (at $z = 0$ and $r = r_1$). To handle this, the velocity of the inner cylinder is set equal to 1, except very near the singularity, where the change of the velocity to zero is made progressive using a quadratic function :

$$\begin{aligned} &u_\theta = 1, \text{ at } r = r_1, \ L_1 \leq z \leq L\,, \\ &u_\theta = \frac{z}{L_1}\left(2 - \frac{z}{L_1}\right) \text{ at } r = r_1, \ 0 \leq z \leq L_1. \end{aligned} \tag{3.17}$$

The height $L_1$ is set to $L_1 = L/100$. Additional numerical tests were made with $L_1 = L/200$.

- In the second situation, following several authors, [17], [47], [48], [49], we have assumed axial periodic boundary conditions at the upper and lower endwalls, i.e.

$$f(r, 0, t) = f(r, L, t)\,, \tag{3.18}$$

where $f$ represents any of the dependent variables. Note that the height $L$ of the domain is an integer multiple of the expected wavelength. In this case, the velocity field $\boldsymbol{u}$ and the pressure $p$ were split into the basic field $(\boldsymbol{u}_b, \boldsymbol{p}_b)$ corresponding to a Couette flow solution between infinite coaxial cylinders and a disturbance : $\boldsymbol{u} = \boldsymbol{u}_b + \boldsymbol{u}'$ and $p = p_b + p'$. Substituting $\boldsymbol{u}$ and $p$ by their expressions into equations (3.7) and (3.8) lead to perturbation equations that are solved numerically.
Concerning the height of the computational domain, we have used $L = 10$ for fixed bottom endwall and stress-free at the top wall, and $L = 7\,\lambda_z$ for periodic boundary conditions. Here, $\lambda_z$ is the axial wavelength at the primary bifurcation.

## 3.3 Numerical method

### 3.3.1 Weak formulation

The governing equations (3.8) and (3.7) combined with (3.10) and (3.12) are solved numerically using the finite element solver FreeFem++ [50]. The weak formulation of

equations (3.7,3.8) reads :

$$\int_\Omega q\boldsymbol{\nabla}\cdot\boldsymbol{u}d\Omega = 0\,, \tag{3.19}$$

$$\int_\Omega (\partial_t\boldsymbol{u} + (\boldsymbol{u}\cdot\boldsymbol{\nabla})\boldsymbol{u})\cdot\boldsymbol{v}\,d\Omega = \int_\Omega (p\boldsymbol{\nabla}\cdot\boldsymbol{v} - \boldsymbol{\tau} : \boldsymbol{\nabla}\boldsymbol{v})\,d\Omega \tag{3.20}$$
$$+ \int_{\partial\Omega} \boldsymbol{v}\cdot(-p\boldsymbol{I} + \boldsymbol{\tau})\cdot\boldsymbol{n}\,d\partial\Omega.$$

where $\Omega$ is the volume occupied by the fluid and $\partial\Omega$ is its boundary. Given the axisymmetry of the problem, cylindrical coordinates are used and the integration over $\theta$ yields the factor $2\pi$ so that $d\Omega = 2\pi r dr dz$ and $d\partial\Omega = 2\pi r dl$, where $dl$ is the length of an elementary segment of the 2D boundary $\partial\mathcal{D}$ in the axial-radial plane. In what follows, the common factor $2\pi$ will be left out and a 2D formulation is obtained. In this formulation, $\boldsymbol{n}$ is the unit vector normal to the boundaries, pointing outward of the rectangle $\mathcal{D}$. The test functions $q$ and $\boldsymbol{v}$ are associated to the pressure $p$ and the velocity $\boldsymbol{u}$, respectively. $\boldsymbol{I}$ stands for the identity tensor. The surface term is zero for all the three types of boundary conditions specified in the previous section.

### 3.3.2 Time and space discretization

Discretizing the time derivative term by a first order backward Euler scheme and treating the nonlinear inertial terms and the nonlinear viscosity explicitly [51], we get

$$\int_\mathcal{D} q\boldsymbol{\nabla}\cdot\boldsymbol{u}_{n+1} r dr dz = 0\,, \tag{3.21}$$

$$\int_\mathcal{D} \left[\frac{\boldsymbol{u}_{n+1}}{\Delta t}\cdot\boldsymbol{v} - p_{n+1}\boldsymbol{\nabla}\cdot\boldsymbol{v} + \mu(\boldsymbol{u}_n)\dot{\boldsymbol{\gamma}}(\boldsymbol{u}_{n+1}) : \boldsymbol{\nabla}\boldsymbol{v}\right] r dr dz = \tag{3.22}$$
$$\int_\mathcal{D} \left[\left(\frac{\boldsymbol{u}_n}{\Delta t} - (\boldsymbol{u}_n\cdot\boldsymbol{\nabla})\boldsymbol{u}_n\right)\cdot\boldsymbol{v}\right] r dr dz\,.$$

For the space discretization of equations (3.21) and (3.22), a triangular mesh with $40\times 40L$ identical rectangles in the domain $\mathcal{D}$, each of them is divided into two triangles of equal area is used. A convergence test has also been performed with $60\times 60L$ rectangles. The finite element spaces used to discretize the velocity and the pressure are the Inf-Sup stable Taylor-Hood finite elements P2P1, i.e. quadratic continuous functions for velocity trial and test functions and piecewise continuous linear functions for pressure trial and test functions. The resulting algebraic system is solved with an iterative Uzawa Conjugate Gradient algorithm with a Cahouet-Chabart preconditionner [50, 52]. The matrix inversions are performed with the UMFPack solver embedded in FreeFem++. During the transient stages, the time step must satisfy the CFL condition to insure the accuracy and the numerical stability. In our simulations, the time step $\Delta t$ always verifies $\Delta t \leq \dfrac{h}{u_{max}}$, where $h$ is the smallest equivalent diameter of mesh elements and $u_{max}$ is the maximum value of the norm of $\boldsymbol{u}$.

Concerning the initial conditions, the flow field at $t = 0$ is given by specifying the initial values of the velocity components in the entire domain. We have used the Couette flow solution of a Carreau fluid between infinite cylinders as initial conditions at a Reynolds number below the critical value. This Couette flow solution determined numerically has been first regularized to take into account the singularity in the azimuthal velocity at the lower surface. A continuation method is then used where each new simulation is started with the permanent regime solution corresponding to the closest set of parameters as initial condition.
In the case of axial periodic boundary conditions, the initial condition is a velocity field which corresponds to divergence-free rolls :

$$\boldsymbol{u}'(r, z, t = 0) = A_0 \left( u'_r \boldsymbol{e}_r + u'_z \boldsymbol{e}_z \right), \tag{3.23}$$

where $A_0$ is the initial amplitude of the perturbation, and

$$u'_r = \cos(kz) \left(r - r_1\right)^2 \left(r - r_2\right)^2 , \tag{3.24}$$

$$u'_z = -\sin(kz) \left(r - r_1\right) \left(r - r_2\right) \frac{4r - 2\left(r_1 + r_2\right) + \frac{(r-r_1)(r-r_2)}{r}}{k} . \tag{3.25}$$

The shear-thinning behavior of the Carreau model (3.12) depends on the shear-thinning index $n_c$ and the dimensionless constant time $\lambda$. Shear-thinning effects increase either by increasing $\lambda$ or by decreasing $n_c$. Here, we have fixed $\lambda = 200$ and the numerical results are presented for $n_c = 0.5$ and $n_c = 0.2$. For $n_c = 0.5$, Taylor vortices fill all the annular space, whereas for $n_c = 0.2$, Taylor vortices are strongly squeezed against the inner wall. One can also recall that when $\lambda \geq 30$, this parameter has practically no effect on the base flow as well as on the size of vortices [30, 33].

## 3.4 Validation of the numerical method

### 3.4.1 Comparison with linear theory

Taylor-Couette configuration with periodic boundary conditions is used as a model to approximate infinite cylinders. To determine the threshold of the primary bifurcation, we compute the transient evolution of the velocity, starting with initial conditions (3.23)-(3.25), with a very small amplitude $A_0 = 10^{-6}$. For a Newtonian fluid and a radius ratio $\eta = 0.4$, we compute the time evolution of the flow at $\mathrm{Re} = 68.08$ and $\mathrm{Re} = 68.5$, i.e. around the value of the critical Reynolds number $\mathrm{Re}_c = 68.296542$ [30, 33]. From exponential fits of the time series, we extract the linear growth rates $\sigma(\mathrm{Re} = 68.08) = -0.086391$ and $\sigma(Re = 68.5) = 0.081148$. A linear fit between these values provides a critical value $\mathrm{Re}_c = 68.2972$ very close to that given in the literature.
A similar result was obtained for a shear-thinning fluid. For instance, for a Carreau fluid with $n_c = 0.5$, $\lambda = 100$ and $\eta = 0.4$, the linear stability analysis [30, 33] gives $Re_c =$

| Re<br>Reynolds number | Torque<br>method of Sec. 3.3 | Torque, theoretical<br>Topayev et al.[33] | Torque, theoretical<br>Davey [53] | Torque<br>Fasel & Booz [49] |
|---|---|---|---|---|
| 70.0 | 17.1594 | 17.1572 | 17.1544 | 17.1537 |
| 75.0 | 18.1741 | 18.2090 | 18.1089 | 18.1627 |
| 80.0 | 19.0700 | 19.1164 | 18.6183 | 19.0527 |
| 85.0 | 19.8707 | 19.8909 | 19.5375 | 19.8490 |
| 90.0 | 20.5954 | 20.5543 | 20.0800 | 20.5692 |
| 95.0 | 21.2567 | 21.1265 | 20.5391 | 21.2267 |

TABLE 3.1 – Newtonian fluid with $\eta = 0.5$. Variation of the torque at the inner cylinder as a function of Reynolds number. Comparison with weakly nonlinear stability results of Topayev et al.[33] as well as with the experimental results of Donnelly & Simon [54]

3.5770645. Using the same initial condition as previously, linear growth-rates are computed using the method of Sec. 3.3 at two Reynolds numbers around $\mathrm{Re}_c$. After exponential fits, we obtain $\sigma(\mathrm{Re} = 3.5663) = -0.0075602$ and $\sigma(\mathrm{Re} = 3.5871) = 0.0064292$. A linear fit between these two values leads to a critical Reynolds number of $\mathrm{Re}_c = 3.5775708$ very close to that given predicted by the linear theory for infinite cylinders[33].

### 3.4.2 Comparison with weakly nonlinear theory

In table 3.1 the torque obtained using the method of Sec. 3.3 for a Newtonian fluid at $\eta = 0.5$ is compared with the weakly nonlinear stability calculations of Davey [53] and those of Topayev et al.[33]. Here the torque $T$ has been non-dimensionalized by the reference torque $T_{ref} = \mu R_1^2 \Omega_1 \ell$ where $\ell$ is the length of the cylinders.

In the low supercritical regime the agreement with both Davey's and Topayev *et al.*'s data is very good. Nevertheless, one can note that our numerical solutions are closer to Topayev *et al.*'s results than to Davey's ones. This is not surprising since Davey's analysis is based on expansion at cubic order about the critical Reynolds number, whereas in Topayev et al.[33], the expansion is pushed until seventh order.

Comparison with weakly nonlinear theory in the case of a shear-thinning fluid is displayed in table 3.2 A Carreau fluid with $n_c = 0.5$ and $\lambda = 100$ is considered. The radius ratio is $\eta = 0.4$. As it can be observed, our numerical solutions are in very good agreement with Topayev *et al.*'s results.

### 3.4.3 Comparison with literature in strongly nonlinear regime

To validate the numerical tool described in Sec. 3.3, in a strongly nonlinear regime, our numerical results are compared with those obtained by Fasel & Booz [49] for a Newtonian fluid at $\eta = 0.5$. In their numerical study, the computations were carried out under the assumption of axisymmetric flow structure, with $L = 2$ and periodic boundary conditions

| Re<br>Reynolds number | Torque<br>method of Sec. 3.3 | Torque, theoretical<br>Topayev et al.[33] |
|---|---|---|
| 3.5810 | 0.54993 | 0.54975 |
| 3.9348 | 0.56953 | 0.56572 |
| 4.2925 | 0.58656 | 0.580353 |
| 4.6502 | 0.59795 | 0.59242 |

TABLE 3.2 – Carreau fluid with $n_c = 0.5$, $\lambda = 100$ and $\eta = 0.4$. Variation of the torque at the inner cylinder on Reynolds number. Comparison with weakly nonlinear stability results of Topayev et al.[33]

| Re<br>Reynolds number | Torque<br>method of Sec. 3.3 | Torque<br>Fasel & Booz [49] |
|---|---|---|
| 100 | 21.8653 | 21.8352 |
| 125 | 24.3584 | 24.3199 |
| 150 | 26.3074 | 26.2646 |
| 175 | 27.9669 | 27.9276 |
| 200 | 29.4749 | 29.4266 |

TABLE 3.3 – Newtonian fluid with $\eta = 0.5$. Variation of the torque at the inner cylinder on Reynolds number. Comparison with numerical results of Fasel & Booz [49]

at both ends of cylinders. Note that $L = 2$ is very close to a the axial wavelength at critical conditions $\Lambda = 1.9858$. Our numerical solutions obtained using a single wavelength fluid column with periodic boundary conditions presented in table 3.3 at different Reynolds numbers show excellent agreement with the DNS study of Fasel & Booz [49]. Additional computations done with two wavelengths fluid column gives the same results.

## 3.5 Experimental setup, Fluids used and Protocol

### 3.5.1 Experimental cell

The Couette-Taylor configuration used in our experiments consists of two coaxial cylinders with vertical axis. The outer cylinder is made of Plexiglas and has a radius $R_2 = 5\,\text{cm}$. The inner cylinder is made of stainless steel, has a radius $R_1 = 2\,\text{cm}$ and is painted in black to avoid light reflections. The gap between the two cylinders is $d = R_2 - R_1 = 3\,\text{cm}$. The height of the working fluid in the annular gap is $\ell = 96\,\text{cm}$. Consequently, the dimensionless parameter that describe the geometry are the radius ratio $\eta = R_1/R_2 = 0.4$ and the aspect ratio $L = \ell/d = 32$. There is an additional box filled with water in order to minimize distortion effects of refraction due to curvature of the outer cylinder during optimal measurements. The outer cylinder is fixed, while the inner one is driven by a DC servomotor at the frequency angular $\Omega_1$.

The bottom end wall is fixed and at the top, the working fluid contacts with air and the surface is free. The height of the working fluid is slightly lower (2 cm) than that of the

cylinders.

### 3.5.2 Flow visualization

For the purpose of visualization of flow structures, the working fluid is mixed with a small amount, 1 g of Iriodin [55, 56, 57]. These thin and flat reflective mica platelets of typical size $0.1 \times \mu m$ thick and $\approx 20\,\mu m$ across are oriented by the flow. The intensity of the light reflected depends on the particle orientation, revealing the flow structure. The region where the normal vectors of particles are in the bisectional direction between the incident light and the line of sight, appears bright. Furthermore, these particles respond very quickly to any local change in the flow pattern giving a change in the light reflectance pattern whenever a change in the velocity occurs [58, 59, 60]. The light reflectance can be recorded and digitized using a CCD camera.
In our experiments, the flow was illuminated from the top at an angle and visualized on the front side. In presence of counter rotating vortices, upward rotating at the outer wall is seen as brighter region and downward rotating is seen as darker region Majji et al.[61]. By plotting the reflected light intensity $I(z,t)$ along the axial direction in the Taylor-Couette cell, at regular time interval (0.1 s) a space-time diagram $I(z,t)$ of flow patterns is obtained. The recorded length is $12\,\mathrm{d} = 36\,\mathrm{cm}$ in the central part of the system corresponding to a spatial resolution of 86 pixels / cm.
For some experiments, the flow was also visualized in the $(r-z)$ plane by illuminating the gap between the cylinders using a He-Ne Laser sheet in the central part of the system. Space-time plots are generated by extracting single line of pixel intensity at a particular radial position.

### 3.5.3 Velocity measurements

Velocity fields in a vertical plane $(r,z)$ were measured using a particle image velocimetry (PIV) system. The working fluid was seeded with silver-coated hollow glass spheres with density $1.4\,g/cm^3$ and an average density of $10\,\mu m$. The particles are illuminated by a vertical laser sheet of thickness $b \approx 1\,\mathrm{mm}$ produced by a double pulsed Nd-Yag New-wave laser ($2 \times 120\,\mathrm{mJ}$, 532 nm). Images are acquired with a high resolution camera (Flow SenseEO $1280 \times 1024\,\mathrm{pixels}^2$, 4096 gray levels), synchronized with the laser at a rate of 1 frame pair per $0.1\,s$. The time delay between two laser pulses typically ranges from 1 to 8 ms depending on the azimuthal velocity component. The $1280 \times 1024\,\mathrm{pixels}^2$ observation window corresponds to physical size of $30 \times 90\mathrm{mm}^2$. For each PIV measurements, 500 pairs of images of size $1280 \times 1024$ pixels were recorded and analyzed using the adaptative-correlation technique of the 'Dynamic Studio' (Software of Dantec). Each image of a pair was sampled into a window of $64 \times 64$ pixels with a recovering of 50 %.

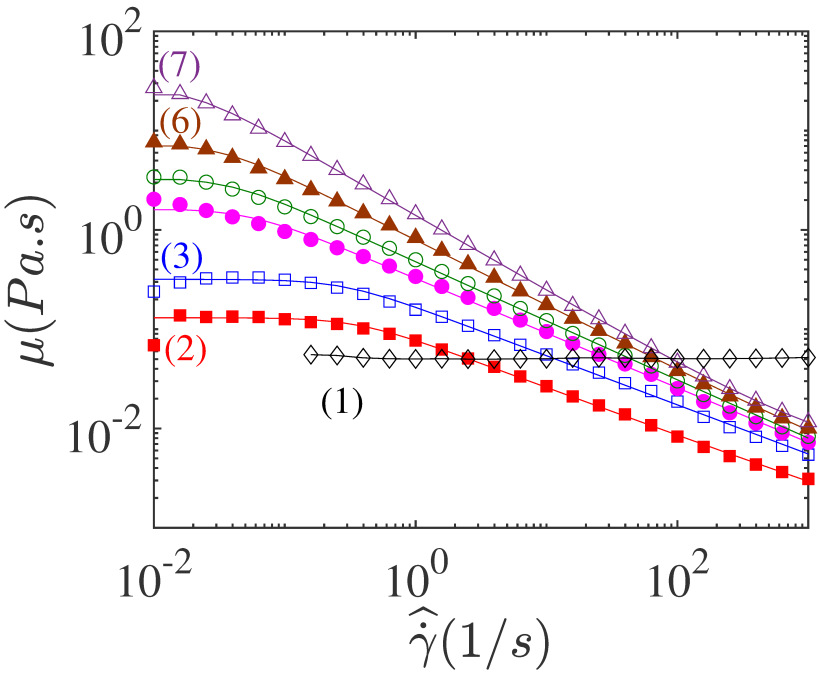


FIGURE 3.1 – Variation of the viscosity $\mu$ versus shear rate $\hat{\dot{\gamma}}$ for (1) a 80 % by volume glycerol aqueous solution and (2)-(7) different concentrations xanthan gum aqueous solutions.

### 3.5.4 Fluids used : preparation and rheology

The working fluids used are : a 80% by volume glycerol aqueous solution, which is Newtonian fluid, and aqueous xanthan gum (semi-rigid polymer) solutions at different concentrations : between 850 ppm, and 3000 ppm. Xanthan gum belongs to one class of cellulose gum with fairly rigid branched chains. The samples were supplied by *Arlès* (France) as *Satiaxane CX91*. For each set of experiments, 10 litters of xanthan gum solution were prepared by dispersing the required amount of xanthan gum powder in deionized water. The solutions were continuously stirred during 24 hours. A small amount of Formaldehyde is added to minimize the bacterial degradation. The solutions were then refrigerated at least during 24 hours. One day before a set of experiments, the solution is mixed with a visualization or PIV particles. The rheological behavior of the fluids used has been determined using a controlled torque rheometer (TA Instrument AR2000) with a cone and plate geometry (60 mm diameter, 28 $\mu$m truncature, angle 1.036°). The variation of the shear viscosity $\mu$ with the dimensional shear rate $\hat{\dot{\gamma}}$ is shown in the figure 3.1(b). For the xanthan gum solutions, the flow curves ($\mu$ *vs* $\hat{\dot{\gamma}}$) are fitted by the Carreau model in the range of shear rate encountered in our experiments. The rheological parameters are given in Table 3.4. The shear-thinning becomes more prominent as xanthan concentration in the solution increases. The zero shear-rate viscosity and the characteristic time of the fluid $\lambda_f$ increase significantly with increasing the concentration. The variation of the storage $G'$ and loss $G''$ modulus versus the shear-rate oscillation $\omega$ applied by the rheometer are

| # | Concentration | $n_c$ | $\mu_0(Pa.s)$ | $\lambda_f(s)$ | $\lambda$ |
|---|---|---|---|---|---|
| (1) | glycerol aqueous solution | 1 | 0.052 | - | - |
| (2) | 850 ppm | 0.52 | 0.13 | 2.78 | 0.40 |
| (3) | 1000 ppm | 0.5 | 0.33 | 8.48 | 3.14 |
| (4) | 1200 ppm | 0.45 | 1.64 | 18.93 | 34.5 |
| (5) | 1500 ppm | 0.41 | 3.38 | 26.51 | 99.6 |
| (6) | 2000 ppm | 0.34 | 5.85 | 30.36 | 197.4 |
| (7) | 3000 ppm | 0.23 | 27.48 | 47.66 | 1455.2 |

TABLE 3.4 – The main rheological parameters of aqueous xanthan gum solution : shear-thinning index $n_c$, zero shear viscosity $\mu_0$ and characteristic time of the fluid $\lambda_f$, at different concentrations.

reported in figure 3.2 at a strain amplitude $\gamma = 1\%$ which is within the linear viscoelastic region identified through strain sweep tests. The relaxation time $\tau_R$ is defined as $\tau_R = 1/\omega_c$ according to Maxwell model where $\omega_c$ is the crossover frequency for the $G'$ and $G''$ curves. When the concentration increases both $G'$ and $G''$ increase and the crossover point shifts to lower shear-rate oscillations. For instance, the relaxation time $\tau_R$ is 2.5 s, 10.9 s and 63.1 s for 1000, 2000 and 3000 ppm xanthan concentration respectively.
According to [62, 63] , the structure of xanthan gum solutions could be described by a network formed by a parallel packing of xanthan chain segments cross-linked by bonds with a finite lifetime. These bonds are not disrupted by low amplitude oscillatory strain in the linear viscoelastic region but are reversibly disrupted under large shear strain. This could explain the marked shear-thinning behavior of xanthan gum solutions. The high values of the relaxation times indicate that the mean lifetime of the cross-links between xanthan chains increase with increasing the concentration.

**Remark**
Although we followed the same protocol in the fluid preparation, the time of storage before experiments and the duration of these experiments (up to 10 hours) may affect the rheological parameters of the fluid. To avoid misunderstandings, the rheology of the fluid is measured before and after each experiment.

### 3.5.5 Experimental protocol

To observe flow structures corresponding to various Re in the Taylor-Couette geometry, the Reynolds number is slowly increased with time starting from a stationary inner cylinder. Actually, we have first evaluated the critical Reynolds number, $\mathrm{Re}_c$, for the onset of Taylor vortices from the linear theory. The velocity of rotation of the inner cylinder is increased from $\mathrm{Re} = 0$ to $\mathrm{Re} = 0.8\,\mathrm{Re}_c$ in one hour. In this first step, the ramping rate agrees with the criterion of Dutcher & Muller [10] : the nondimensional acceleration rate $\mathrm{d}Re/\mathrm{d}t_d$, where $t_d$ is the time dimensionalized with the viscous diffusion time scale $\rho\, d^2/\mu$, should be less than unity to ensure that the flow can be considered to be quasisteady. The

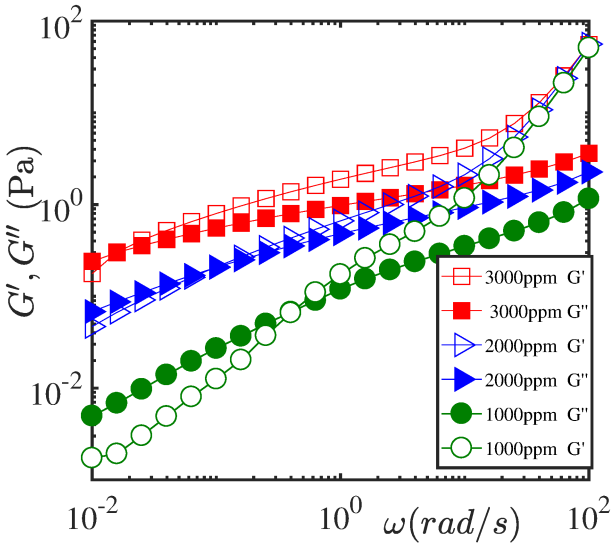


FIGURE 3.2 – Variation of the elastic $G'$ and viscous $G''$ as a function of the shear oscillation $\omega$ for different concentration of xanthan gum solutions.

| # | Concentration | $d\Omega_1/d\hat{t}\,(rad/s^2)$ | $dRe/dt_d$ |
|---|---|---|---|
| (1) | glycerol aqueous solution | 0.872e-3 | 1.006e-2 |
| (2) | 1000 ppm | 0.909e-3 | 1.97e-2 |
| (3) | 2000 ppm | 0.691e-3 | 2.01e-4 |
| (4) | 3000 ppm | 2.035e-3 | 1.51e-6 |

TABLE 3.5 – Experimental conditions used in the various experiments : acceleration rate during the phase where the velocity of the inner cylinder is increased from 0 to $0.8\,\mathrm{Re}_c$.

values of $dRe/dt_d$ and $d\Omega_1/d\hat{t}$ are listed in Table 3.5, with $\hat{t}$ the dimensional time. In the second step, i.e. for $Re = 0.8Re_c$, $\Omega_1$ was increased in small steps of $\Delta\Omega_1$ with waiting times sufficiently long to assure static conditions. Typical values of $\Delta\Omega_1$ is 0.21 rad/s. Above the onset of TVF, the step $\Delta\Omega_1$ and the waiting time period were adapted to have a balance between the need to avoid unsteady effects and the requirements that the measurements were performed over a reasonable time. Experiments typically lasted approximately 6 to 10 hours. Temperature measurements of the working fluid before and after an experiment indicated that the temperature change was less than 1°C.

## 3.6 Primary bifurcation : onset of Taylor vortex flow

### 3.6.1 Influence of the endwalls : Numerical results

The objective of this section is to check if the endwall boundary conditions have an effect on the onset of Taylor vortices in the case of purely viscous shear-thinning fluid for

a quite small aspect ratio $L = 10$.
For a purely viscous fluid, at Re $<<$ Re$_c$ and far from the endwalls, the stable flow is geostrophic. The fluid is in equilibrium under the centrifugal force and the pressure gradient. Close to the stationary bottom endwall, the no-slip boundary condition results in an azimuthal velocity lower than that far from the endwall. The imbalance between the pressure gradient force and the centrifugal force near the bottom endwall, results in a force that drives the fluid radially inwards (Czarny et al.[64]). This radial inflow induces an axial downward flow near the outer cylinder and an axial upward flow near the inner one, yielding a vortex situated at the bottom wall. As the Reynolds number is increased more counter rotating vortices appear. Below Re$_c$, the strength of the vortices decays exponentially [65, 66, 67]. However, the exponential decay length diverges as $|\epsilon|^{-1/2}$. Hence, a finite system of length $L$ will be completely filled with detectable vortices for $\epsilon \geq -L^{-2}$ (Ahlers et al.[65]). These counter-rotating vortices appear quite similar to Taylor vortices and have almost the same axial extent (Czarny et al. [64]). Numerical simulations done with $L = 10$, for a Carreau fluid of rheological parameters $n_c = 0.2$ and $\lambda = 200$ show that around the middle of the annular domain and at $\epsilon \leq -0.01$, the vortices induced by the endwalls boundary conditions are very weak. This is clearly shown by figure 3.3 where we have represented the radial velocity profile along the axial line, $r = 0.8$, passing through the center of vortices (position of minimum speed in the radial plane, $\sqrt{u_r^2 + u_z^2}$). At $\epsilon = -0.01$, the maximum radial velocity is about 0.7% of the surface speed of the inner cylinder reached near the bottom endwall. When $\epsilon > 0$, vortices due to centrifugal instability are observed and their strength increases with increasing Reynolds number. Around the middle of the height of the annular space ($z = 5$), we have found a wavenumber $k^{num} = 8.39$ which is in very good agreement with the theoretical value $k_c = 8.4055$ [33]. Therefore, there is practically no effect of endwalls boundary conditions on the onset of TVF even for a quite small aspect ratio $L = 10$. At the middle of the height of the annular space, the periodicity of the cells is well described by the linear theory.
Note that in the TVF regime the maximum outflow (positive) velocity is larger than the maximum inflow (negative) velocity. For instance, at $\epsilon = 0.06$, the ratio between the maximum outflow and the maximum inflow is $\approx 3.6$ and the width of the inflow region is 2.4 times that of the outflow region as measured between zero-crossings.

### 3.6.2 PIV measurements

In order to check if the viscoelasticity of the fluid plays any role on the onset of Taylor vortices, PIV measurements were performed at Re around Re$_c$. The increase of the velocity of the inner cylinder follows the protocol given in section 3.5.5. At Re below Re$_c$, PIV measurements did not detect radial or axial velocity. At Re slightly above Re$_c$, Taylor vortices are detected. They are illustrated in figure 3.4, where the velocity field measured just above Re$_c$, at $\epsilon \approx 0.01$, is shown for glycerol solution and xanthan gum solutions at 1000 ppm ($n_c = 0.51$, $\lambda = 5.3$) and 2000 ppm ($n_c = 0.33, \lambda = 262$). The

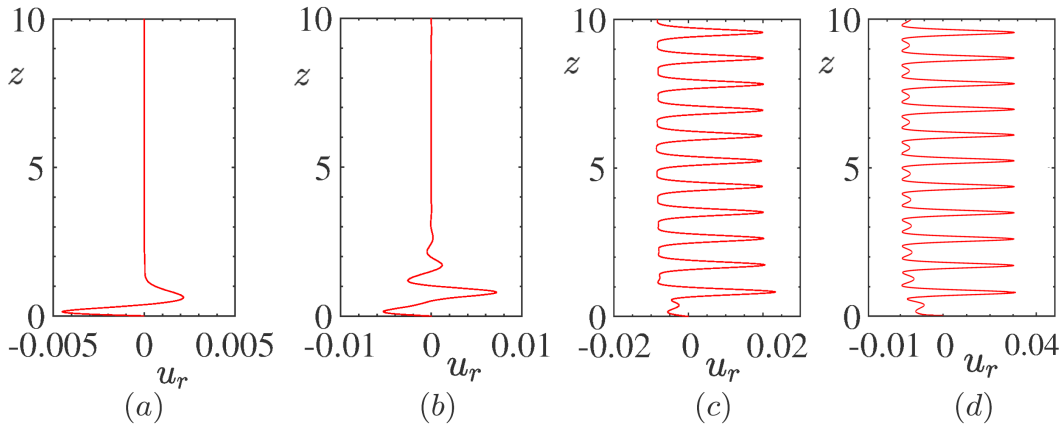


FIGURE 3.3 – Carreau fluid with $n_c = 0.2$ and $\lambda = 200$. Radial velocity component along the axial line, $r = 0.8$, passing through the center of vortices. **(a)** $\epsilon = -0.1$, **(b)** $\epsilon = -0.01$, **(c)** $\epsilon = 0.03$ and **(d)** $\epsilon = 0.06$. For $n_c = 0.2$, $\lambda = 200$, the linear theory assuming infinite cylinders gives $\mathrm{Re}_c = 1.1643$ [33].

axial position is scaled with the corresponding wavelength calculated from the distance between two successive outflow boundaries and a single wavelength is represented. It is interesting to note that with increasing shear-thinning effects, Taylor vortices are squeezed against the inner wall [30, 32, 33]. The periodicity of the cells around the middle of the annular domain can be estimated from the measurement of the wavelength. This yields wavenumbers $k = 3.15 \pm 0.1$ for glycerol solution, $k = 3.5 \pm 0.15$ for xanthan gum solution 1000 ppm and $k = 4.9 \pm 0.3$ for xanthan gum 2000 ppm. These values are in agreement with the linear theory [33] : $k_c = 3.1836$, 3.4601 and 4.7109 respectively.
As already mentioned, above the TVF onset, the maximum of the outflow velocity is larger than the maximum inflow velocity. This is particularly true for shear-thinning fluids [33]. For instance for the xanthan gum 2000 ppm, the measured ratio between the maximum outflow velocity and the minimum inflow is $\approx 4.3$ at $\epsilon = 6.5\%$.
The agreement of the measurements with theoretical results (not accounting for elasticity) tend to show that the viscoelastic properties of the fluid do not play any role in the transition to TVF.

### 3.6.3 Visualization

Visualization is the most widely used technique to determine the onset of the TVF regime. However, as it will be shown later, some artifacts require special caution particularly for shear-thinning fluids. They are due to the anisotropic shape of the particles used for visualization. Guided by the results of the linear theory, the conclusions of the numerical simulation and the PIV measurements, and after several preliminary experimental tests, we have found that the following three criteria allow us to determine reliably the onset of the TVF : (i) Taylor vortices are first observed in the middle of the

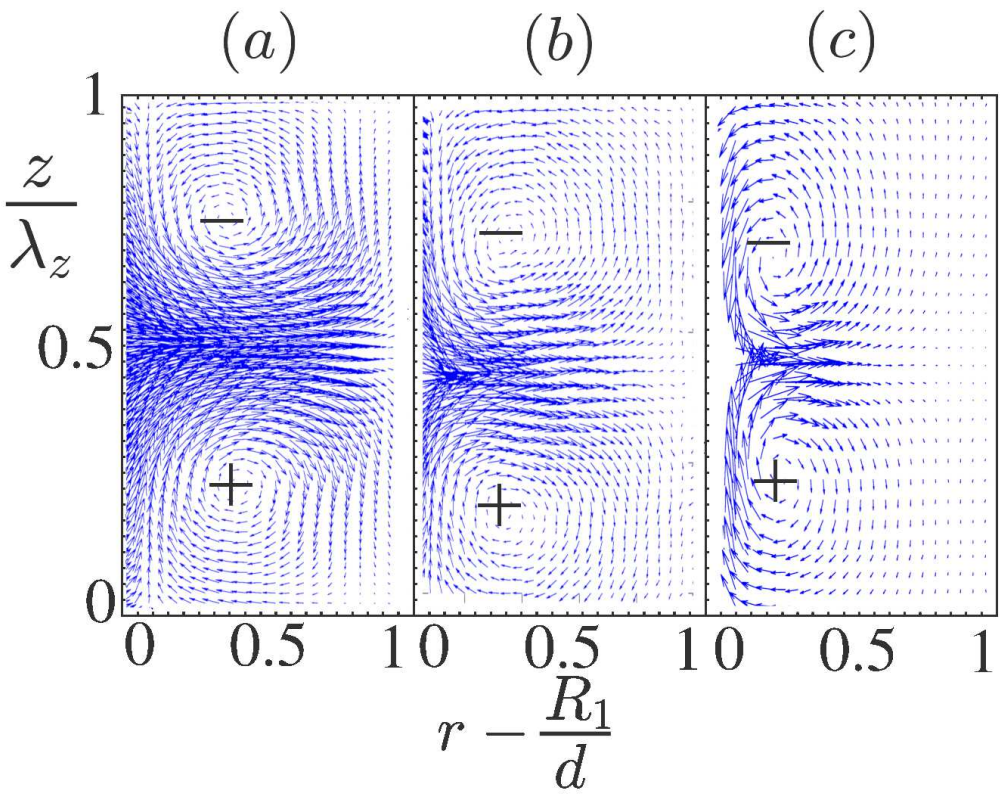


FIGURE 3.4 – Radial-axial velocity vectors in a radial-axial plane for Taylor vortex flow measured at $\epsilon \approx 0.01$. (Left frame) glycerol solution with $\lambda_z = 2$ ; (middle frame) xanthan gum solution 1000 ppm with $\lambda_z = 1.8$ ; (right frame) xanthan gum solution 2000 ppm with $\lambda_z = 1.3$. For the same length vector, the dimensionless velocity in the frames (b) and (c) is two times lower than that in the frame (a), respectively.

apparatus ($z = L/2$), (ii) the topology remains stable during a sufficiently long time and (iii) there is no variation in the topology after an increase of the velocity of rotation of the inner cylinder by $\Delta\Omega_1 = 0.21\,\mathrm{rad/s}$.

- *Glycerol aqueous solution*

Experiments were first carried out with a Newtonian fluid. The annular space was filled with 80 % glycerol aqueous solution. The velocity of rotation of the inner cylinder was increased slowly from rest as described in the protocol given in §3.5.5. Close to the onset of the TVF regime, $\Delta\Omega_1$ was reduced to $0.105\,\mathrm{rad/s}$ ($\Delta\mathrm{Re} = 0.86$) in order to determine accurately the critical Reynolds number. To avoid effects associated with the cylinder ends such as the strong Eckman vortex at the rigid bottom boundary, we focused mainly on the flow structure in the central zone of length $12\,d$. Figure 3.5 displays the spatio-temporal diagram at five values of Re, each developed over a time span of 50 s. At each time, the image is averaged over 10 pixels in the azimuthal direction. With account of the three criteria given above, we find that the transition to TVF occurs at a critical Reynolds number $67.88 < \mathrm{Re}_c^{exp} < 68.74$. This value is in good agreement with that obtained from linear theory assuming infinite cylinders, $\mathrm{Re}_c = 68.2961$. As expected, for the configuration used here, $L = 32$, the value of the critical Reynolds number for the onset of Taylor vortices is practically unaffected by end effects. This result is in agreement with that of Cole [7] in the case of a narrow gap ($0.85 \leq \eta \leq 0.95$). Basing on torque measurements and visual observations, Cole [7] found that there is no variation of the critical speed for the onset of Taylor vortices, with the annulus length, so that theoretical predictions are applicable for an aspect ratio as small as 8 and probably still smaller. The vortices observed at $\mathrm{Re} = 67.88$ and at $\mathrm{Re} = 66.18$ are to be put on account of end effects, i.e. Eckman vortices penetrate progressively the annular space with increasing Re.
In order to determine the critical wavenumber $k_c^{exp}$, a Fourier transform has been applied to the gray-scale spatio temporal diagram $I(z) = \sum_k \bar{I}(k)\exp(ikz)$ corresponding to $\mathrm{Re} = 68.74$. Figure 3.6 (left frame) shows the variation of the signal $I(z)$ in arbitrary units as a function of the axial position. The resulting value of the squared modulus of the Fourier coefficient $\left|\bar{I}\right|^2$ is plotted as a function of $k$ in figure 3.6 (right frame). The maximum of $\left|\bar{I}\right|^2$ is reached at $k = k_c^{exp} = 3.27$ which is close to the critical axial wavenumber $k_c = 3.1834$ obtained from the linear stability analysis. The second largest peak is the first harmonic. Actually, one has to note that for a finite system, only discrete states with an integer number of vortices can occur. With one rigid and one free boundary, our system normally contains an odd number of vortices $(2N + 1)$ [68, 69]. We designate by $k_c^{finite}$ the closest value to $k_c$ compatible with an odd number of vortices. We obtain $k_c^{finite} = 3.24$, which is very close to our experimental result $k_c^{exp} = 3.27$. The stationarity of TVF is evident from figure 3.5.
Once the primary bifurcation is reached, the velocity of rotation of the inner cylinder was increased gradually by a small step following the protocol given in section

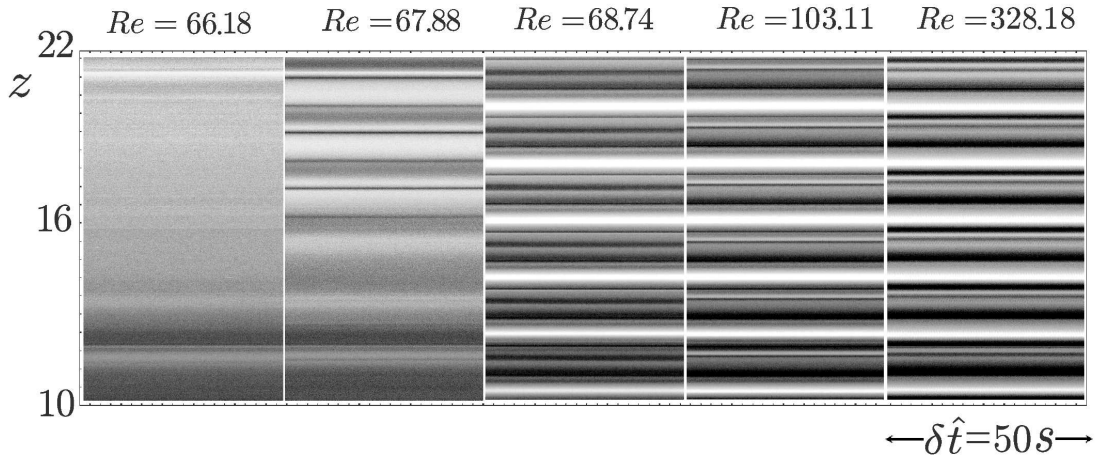


FIGURE 3.5 – Spatio-temporal diagrams for a 80% by volume of glycerol aqueous solution at Re = 66.18, 67.88, 68.74, 103.11 and Re = 328.18. They are constructed from images taken at 10 frames $s^{-1}$. Note that for a Newtonian fluid with $\eta = 0.4$, $\mathrm{Re}_c = 68.2965$.

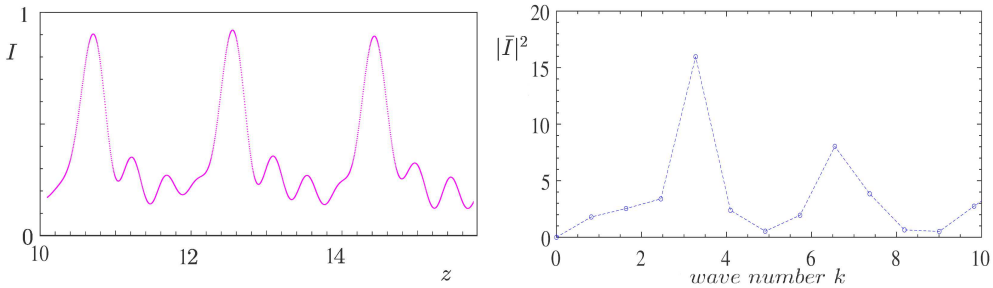


FIGURE 3.6 – 80% glycerol aqueous solution at Re = 68.74. Left frame : plot of the amplitude registered light emission in arbitrary units as a function of the axial position $z$. Right frame : squared modulus of the Fourier coefficient as a function of the wavenumber.

3.5.5. Space-time diagrams obtained from visualization at $\mathrm{Re} \in [\mathrm{Re}_c^{exp}, 5\,\mathrm{Re}_c^{exp}]$ do not present any visible variation as it is shown in figure 3.5. The wavenumber remains constant with $k = k_c^{exp} = 3.27$. This is in agreement with experimental observations of Snyder & Lambert [14] and Burkhalter & Koschmieder [70] using an apparatus of radius ratio $\eta = 0.5$ and an aspect ratio $L \approx 30$ and increasing quasisteadily the Reynolds number. According to Guo & Finlay [25], this suggests that perturbations with $k = k_c$ grow faster than others and become dominant in the fully vortex flow. However, the flow structure is modified. Indeed, PIV measurements show that at Re sufficiently far from $\mathrm{Re}_c$, the center of vortices moves towards the outflow boundaries and the outer cylinder wall, in agreement with the numerical observations of Fasel & Booz [49].

- *Aqueous solution of xanthan gum at* 1000 *ppm*

Figure 3.7 shows spatio-temporal diagrams recorded from visualization images obtained for aqueous solution of xanthan gum at 1000 ppm, with $n_c = 0.5$ and $\lambda = 3.1$. Starting from rest, the velocity of rotation of the inner cylinder is increased quasi-steadily, following the protocol previously described. Stationary patterns are observed at $\mathrm{Re} = 5.72$, much lower than the critical Reynolds number predicted by the linear theory, $\mathrm{Re}_c = 11.1064$ [33]. These patterns are illustrated by the space-time plot shown in the left frame of figure 3.7. They account for a variation of the orientation of reflective particles along the axial position which can be related to Taylor-like vortices. From $\mathrm{Re} = 0.8\,\mathrm{Re}_c$, the velocity of rotation of the inner cylinder was increased by step of $\Delta\Omega_1 = 0.21$ rad/s which corresponds here to $\Delta\mathrm{Re} = 0.38$. At $\mathrm{Re} = 11.05$, the three criteria suggested for the onset of Taylor vortices are satisfied. Therefore, $10.67 < \mathrm{Re}_c^{exp} < 11.05$. This value is in agreement with the linear theory. A fast-Fourier transform of the space-time plot $\mathrm{Re} = 11.05$ was performed. The most energetic wavenumber found $k = k_c^{exp} = 3.72$. This value is in a good agreement with the linear theory taking into account the finite length of the system, $k_c^{finite} = 3.6306$. For infinite cylinders, we have $k_c = 3.5235$ [33].

- *Aqueous solution of xanthan gum at* 2000 *ppm*

Figure 3.8 shows spatio-temporal diagrams for aqueous solution of xanthan gum at 2000 ppm, with $n_c = 0.34$ and $\lambda = 197$. Stationary patterns are first observed at $\mathrm{Re} = 1.12$, much lower than the critical Reynolds number predicted by the linear theory, $\mathrm{Re}_c = 1.6944$. These patterns are illustrated by the space-time plot shown in the left frame of figure 3.8. At $Re = 1.69$, the three criteria for the onset of TVF are satisfied. Here, $\Delta\Omega_1 = 0.21$ rad/s corresponds to $\Delta\mathrm{Re} = 0.026$. The experimental Reynolds number for the onset of TVF $1.67 < \mathrm{Re}_c^{exp} < 1.69$ is in agreement with the linear theory. Applying a fast Fourier transform to the space-time plot corresponding to $\mathrm{Re} = 1.69$, it is found that the most energetic mode is obtained at $k = k_c^{exp} = 4.37$ as it is shown in figure 3.9. This value is again in a very good agreement with that obtained using a linear stability analysis, $k_c = 4.5160$. If we take into account the finite length of the system, a closer value is obtained, $k_c^{finite} = 4.4156$.

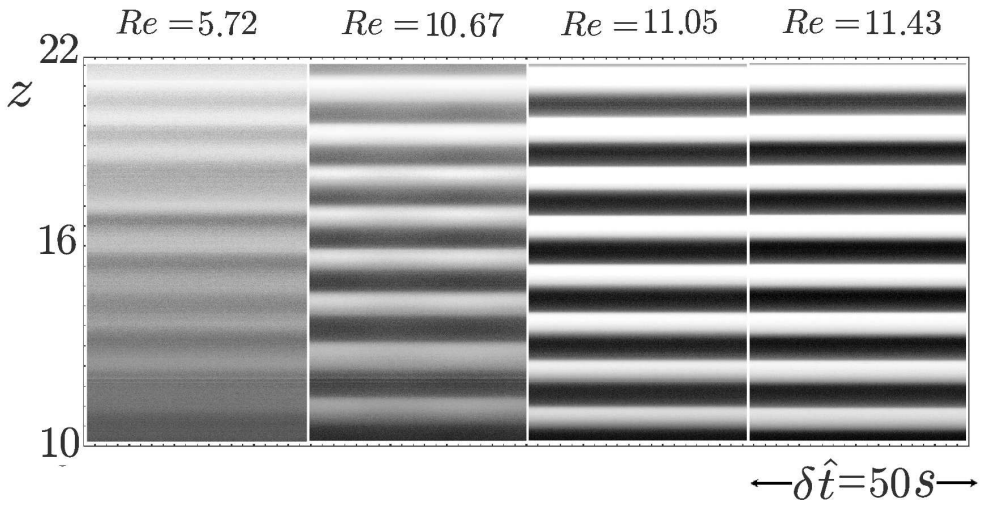


FIGURE 3.7 – Space-time diagrams for aqueous solution of xanthan gum at 1000 ppm for $Re = 5.72, 10.67, 11.05$ and 11.43. The rheological parameters are $n_c = 0.5$, $\lambda = 3.1$. For these parameters, the linear theory assuming infinite cylinders gives $\mathrm{Re}_c = 11.1064$ [33].

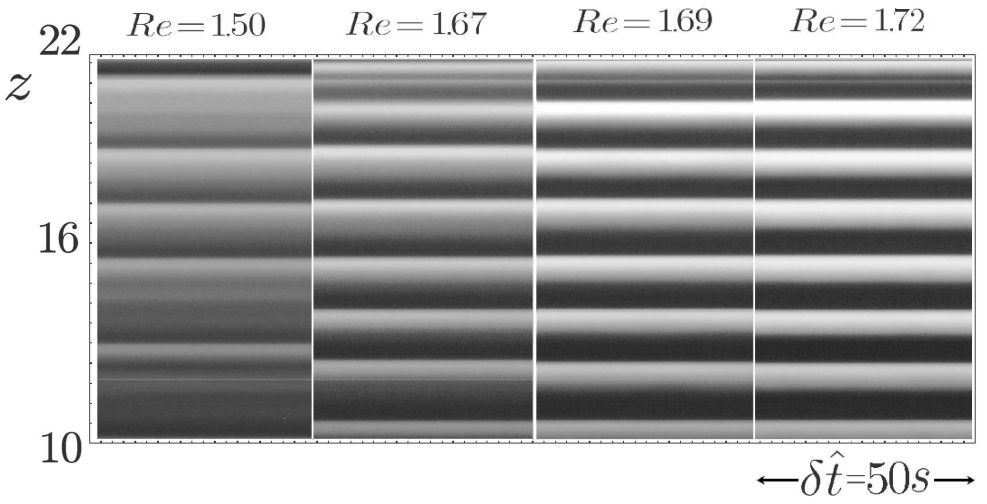


FIGURE 3.8 – Space-time diagrams of xanthan gum 2000 ppm for $\mathrm{Re} = 1.5, 1.67, 1.69$ and 1.72. The rheological parameters are $n_c = 0.34$, $\lambda = 197$. For this case, the linear theory gives $\mathrm{Re}_c = 1.6944$.

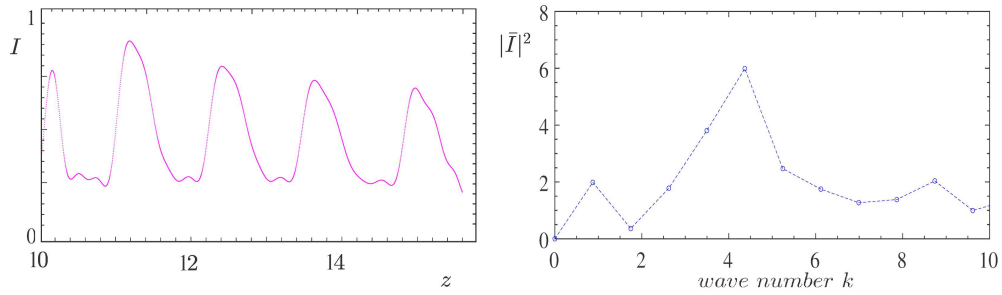


FIGURE 3.9 – Aqueous solution of xanthan gum at 2000 ppm at Re = 1.69. (Left frame) is a plot of the amplitude of the signal as a function of the axial position in units of pixels. (Right frame) Fourier coefficient squared as a function of the wavenumber.

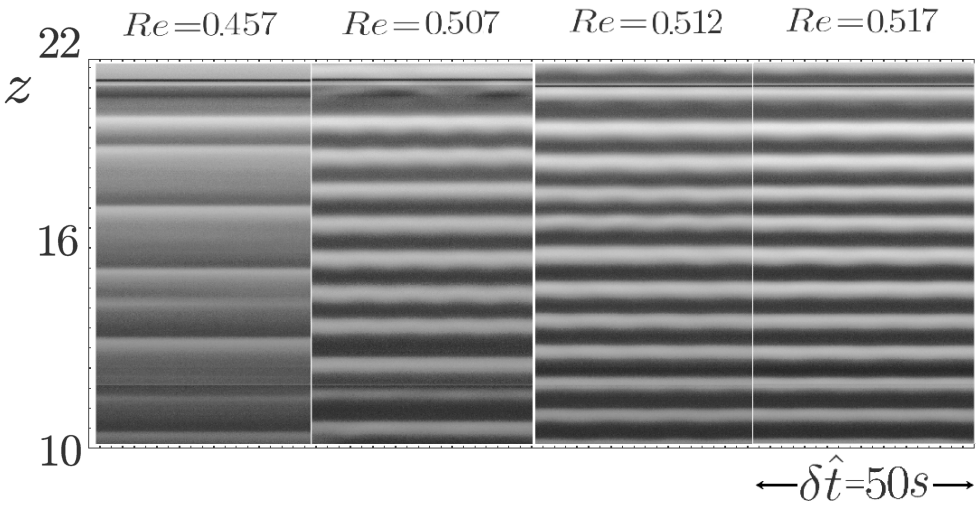


FIGURE 3.10 – Space-time diagrams of xanthan gum 3000ppm at $Re = 0.457, 0.507, 0.512$ and 0.517. The rheological parameters are $n_c = 0.23$ and $\lambda = 1455$. For this case, the linear theory gives $\mathrm{Re}_c = 0.5180$.

- *Aqueous solution of xanthan gum at* 3000 *ppm*

Similar results are obtained for aqueous solution of xanthan gum at 3000ppm, with $n_c = 0.23$ and $\lambda = 1455$ as it is shown by figure 3.10. Patterns which can be related to Taylor-like vortices are first observed at $\mathrm{Re} = 0.114$, much lower than $\mathrm{Re}_c = 0.5180$. The relative difference $\epsilon = (\mathrm{Re} - \mathrm{Re}_c)/\mathrm{Re}_c \approx -0.78$, is larger in absolute value than the previous case (2000 ppm concentration). These patterns are illustrated by the left frame of figure 3.10. At $\mathrm{Re} = 0.512$, the centrifugal instability comes into play. Applying fast Fourier transform to the spatio-temporal diagram $\mathrm{Re} = 0.512$, it is shown that the wavenumber associated with the most energetic mode corresponds to a wavenumber $k_c^{exp} = 6.55$, which is very good agreement with the linear theory, $k_c = 6.8418$ [33] and $k_c^{finite} = 6.7701$

### 3.6.4 Discussion

From the experimental results, two points can be underlined : (i) for the geometrical configuration used, the critical conditions are practically not affected by the end effects in agreement with Cole [7], nor by the viscoelasticity of the fluids used ; (ii) for sufficiently strong shear-thinning effects, patterns which can be related to counter-rotating vortices are observed at Re much lower than $\mathrm{Re}_c^{exp}$. The value of Re at which these patterns appear decreases with increasing shear-thinning effects. Elcicek & Guzel [35] have also reported, from visualization experiments, the existence of axisymmetric vortices at $\epsilon \approx -15\%$ (before TVF regime, Figure 10 in their paper) and they attributed it to Eckman vortices.

Basing on the above results, we think that the patterns observed for xanthan gum solutions at $Re$ much below $Re_c$ are not induced by the vortices generated by the endwall boundary condition. These patterns might be related to an instability induced by anisotropic particles in form of disks used in the visualization. This conclusion is supported by three facts : (i) PIV experiments using spherical particles did not detect radial or axial velocity at $Re$ much below $Re_c$ ; (ii) Strong destabilization of Taylor-Couette flow with large vortex size in shear-thinning clay suspension was evidenced by Philippe et al.[71] using Synchrotron small angle x-ray scattering technique. The clay particles can be assimilated (in average) to disks. (iii) The theoretical study of Gillissen & Wilson[72] demonstrated that suspensions of disks have destabilizing effect in Taylor-Couette flow. This destabilization is due to anisotropic viscous stress induced by suspended disk-shaped particle. Experimental evidence of this destabilization was recently provided by Gillissen et al.[73]

## 3.7 Secondary bifurcations

### 3.7.1 Newtonian fluid : Instability to travelling azimuthal wave mode

Visualization experiments show that in the TVF regime, Taylor vortices are stationary and their axial periodicity is the same as at the onset (figure 3.5). At $\mathrm{Re} = \mathrm{Re}_s^{exp} = 361 = 5.28\,\mathrm{Re}_c$, a secondary instability occurs with a transition from steady axisymmetric Taylor vortices to time-dependent non-axisymmetric flow. Typical spatio-temporal diagrams of reflected light intensity obtained, in this regime, at $\mathrm{Re} = 361\,(5.28\,\mathrm{Re}_c)$ and $\mathrm{Re} = 452\ (6.62\,\mathrm{Re}_c)$ are shown in figure 3.11 from the front view and in figure 3.12 from the cross-sectional view. A zoom on a short time interval is used to account for vertical oscillations due to rotating waves. Indeed, the amplitude of oscillations is weak and the frequency is quite high. In the represented time interval, $20\,\mathrm{s} \approx 700\ (d/R_1\Omega_1)$, 33 periods are visible at $\mathrm{Re} = 452$. Applying the 2D fast Fourier transform (FFT) to spatio-temporal diagrams, it is possible to obtain the axial wavenumber and the frequency of oscillations. The axial wavenumber remains the same as in TVF regime, $k \approx k_c^{finite} = 3.27$. The period $T$ of oscillations in non-dimensional time units and the ratio of the frequency of oscillations to the inner cylinder frequency at different Re is given in Table 3.6. It can be noted that

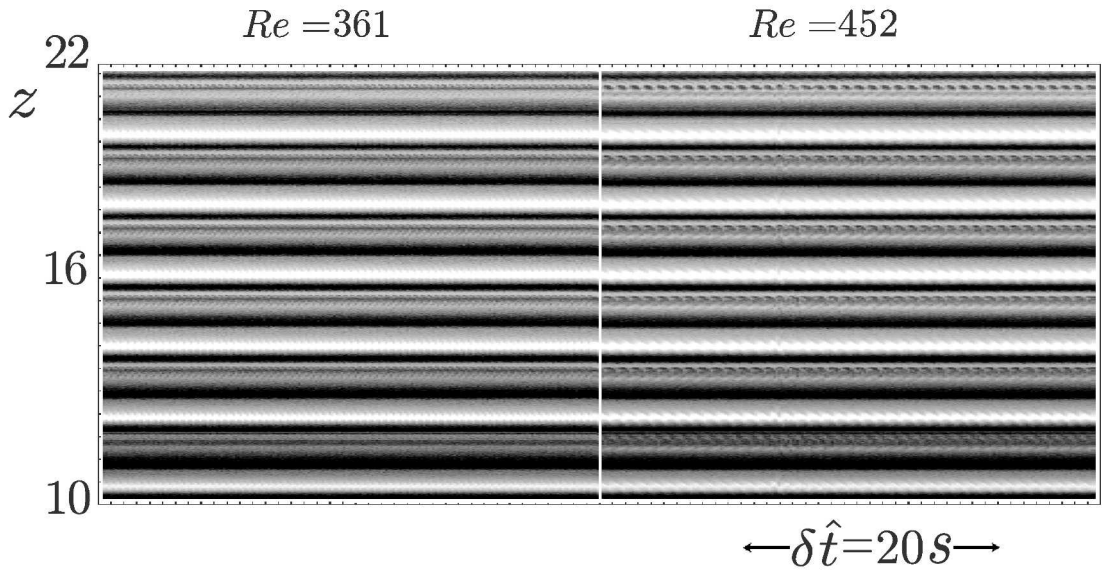


FIGURE 3.11 – Aqueous glycerol solution. Spatio-temporal diagram in TVF regime at Re = 361 and in the case of WVF I at Re = 452. The black parallel lines are inflow and outflow boundaries. The vortices are situated between these lines. Adjacent to each vortex is another vortex that circulates in the opposite sense. Neighboring vortices appear darker or lighter. Below each bright vortex there is an outflow boundary and above each bright vortex an inflow boundary.

in the regime called here *wavy vortex flow I* (WVF I), the period (frequency) of oscillations increases (decreases) as the Reynolds number is increased. This time dependent flow regime is observed for Re ranging from 5.28 to $\approx 6.9\,\mathrm{Re}_c$. Additional information about this regime are obtained from PIV measurements. Figure 3.13 shows the instantaneous velocity field in the radial-axial plane at $\mathrm{Re} = 6.5\,\mathrm{Re}_c$ through one cycle. One period is represented. The axial motion of the vortices is evident based on the location of the vortex centers marked by a cross. One can also observe that : (i) the outflow boundary oscillates with a very small amplitude ; (ii) the inflow boundary has a significant amplitude of oscillations ; (iii) the radial outflow is much stronger than the radial inflow. By numbering the vortices 1 to 3 from the bottom, and analyzing the orientation of vectors velocity in different frames of figure3.13, it can be shown that there is a weak transfer of the fluid from the vortex 2 to the vortex 1 in the frame (b) and from the vortex 1 to the vortex 2, in the frame (d). Of course, the net volume of fluid transferred axially over one cycle must be zero.

At $\mathrm{Re} = 472 \approx 6.9\,\mathrm{Re}_c$, an abrupt increase (decrease) in period (frequency) of oscillations occurs as indicated in Table 3.6 associated to an abrupt increase in the amplitude oscillations as shown in figure 3.14. The axial wavenumber is not modified $k = k_c^{finite} \approx 3.27$. The flow field through one cycle of an azimuthal wave passing the measurement plane represented in figure 3.15 is quite similar to that described previously and will be called here *wavy vortex flow II* (WVF II). However, the oscillations amplitude of the outflow

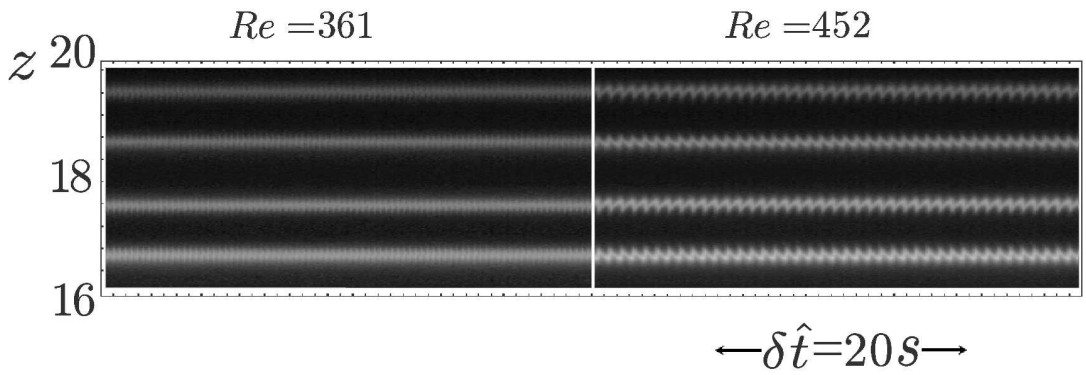


FIGURE 3.12 – Aqueous glycerol solution. Visualization of the cross-section of the flow in the $r-z$ plane. Spatio-temporal diagrams taken in the mid gap. TVF regime at Re $=$ 361 and WVF I at Re $=$ 452.

| $\mathrm{Re}/\mathrm{Re}_c^{exp}$ | Type of mode | $T\,(d/R_1\Omega_1)$ | $f/f_i$ |
|---|---|---|---|
| 5.28 | wavy vortex flow I | 8.2 | 0.51 |
| 6.05 | wavy vortex flow I | 13.5 | 0.31 |
| 6.58 | wavy vortex flow I | 20.2 | 0.206 |
| 6.85 | wavy vortex flow I | 25.8 | 0.16 |
| 6.97 | wavy vortex flow II | 105 | 0.04 |
| 7.23 | wavy vortex flow II | 109 | $\approx 0.04$ |

TABLE 3.6 – Period $T$ of oscillations in non-dimensional time-unit and ratio of the frequency of oscillations to the inner cylinder frequency $f_i$.

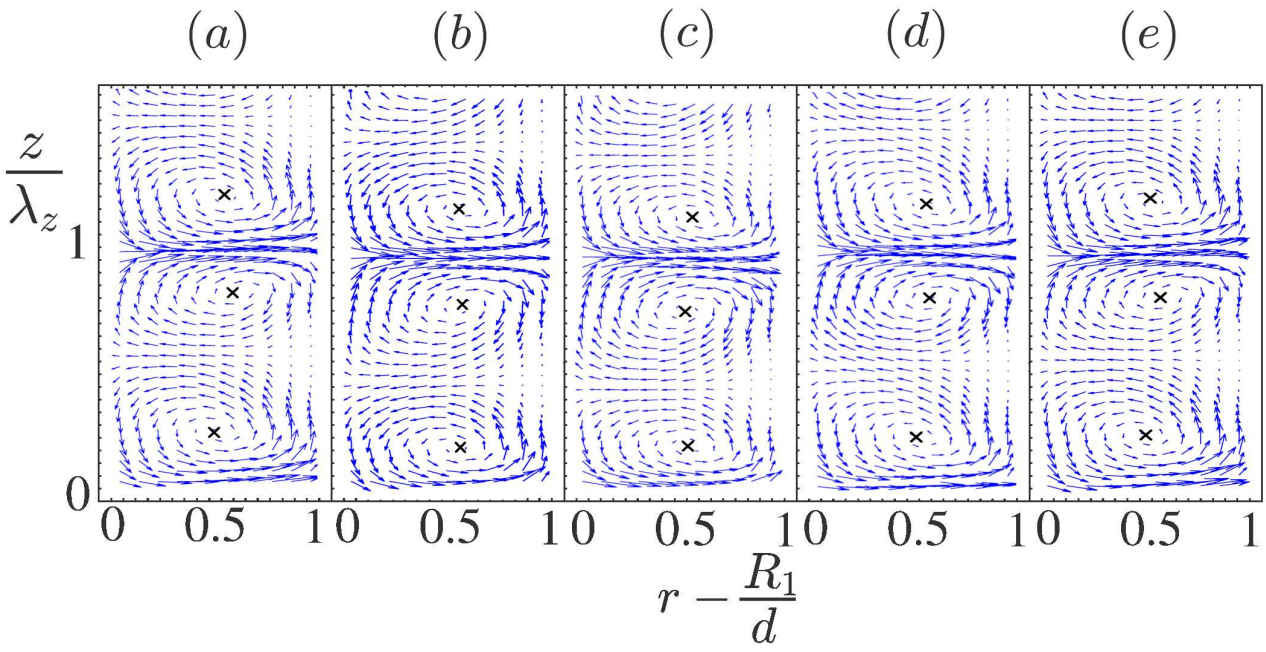


FIGURE 3.13 – Aqueous glycerol solution. Instantaneous radial-axial velocity vectors in radial-axial plane for wavy vortex flow I at $\mathrm{Re} = 6.5\,\mathrm{Re}_c$. The time progresses from left to right through one cycle of an azimuthal wave passing the measurement plane. (a) $t = 0$, (b) $t = 5.3\,(d/R_1\Omega_1)$, (c) $t = 13.25\,(d/R_1\Omega_1)$, (d) $t = 21.2\,(d/R_1\Omega_1)$, (e) $t = 26.5\,(d/R_1\Omega_1)$.

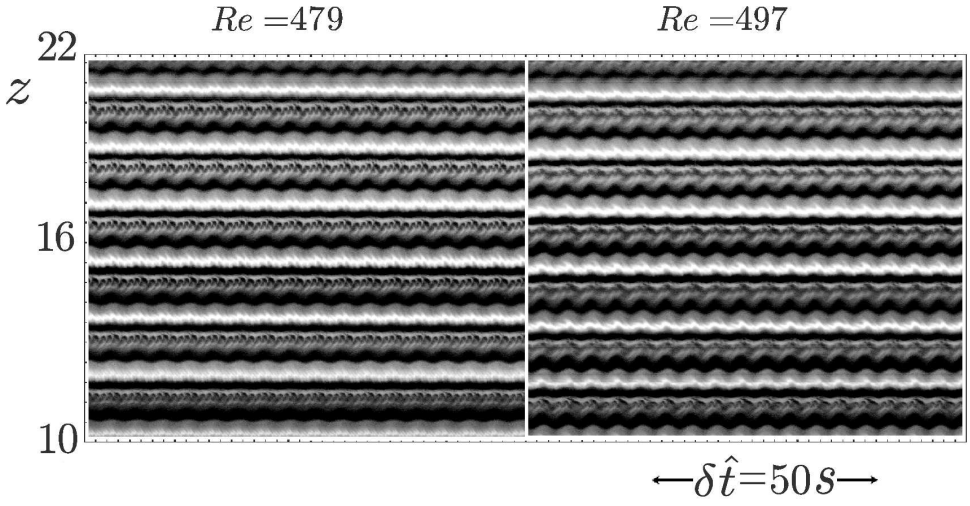


FIGURE 3.14 – Aqueous glycerol solution. Spatio-temporal diagram in WVF II at Re = 479 and 497.

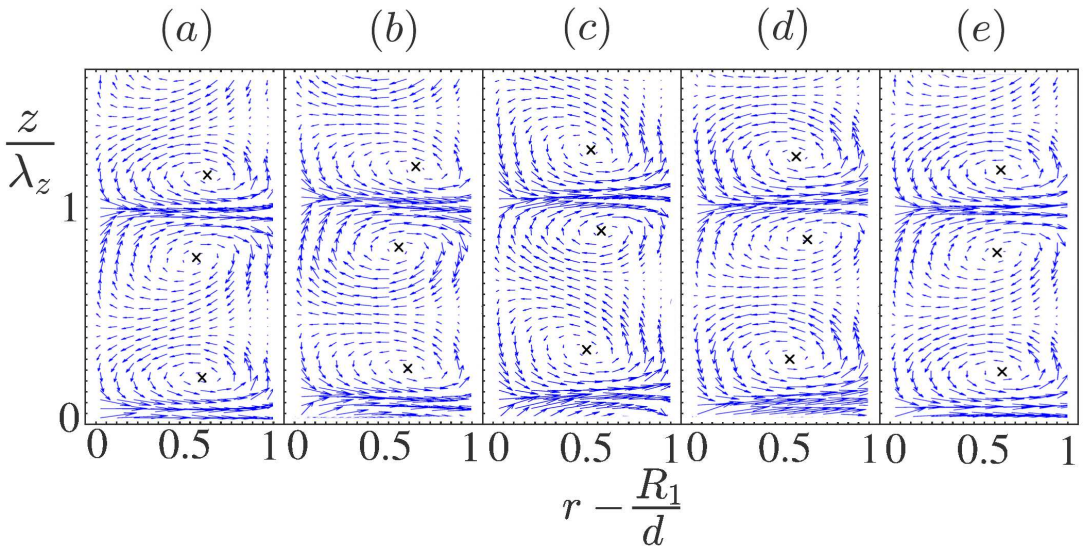


FIGURE 3.15 – Aqueous glycerol solution. Instantaneous radial-axial velocity vectors in radial-axial plane for wavy vortex flow II at $\mathrm{Re} = 7.0\,\mathrm{Re}_c$. The time progresses from left to right through one cycle of an azimuthal wave passing the measurement plane. (a) $t = 0$, (b) $t = 14.4\,(d/R_1\Omega_1)$, (c) $t = 28.8\,(d/R_1\Omega_1)$, (d) $t = 43.2\,(d/R_1\Omega_1)$, (e) $t = 51.8\,(d/R_1\Omega_1)$.

boundary is stronger than previously as well as the transfer of the fluid between vortices 1 and 2 in the frames (a), (c) and (e). The wavy vortex flow II has the same features as the wavy vortex flow described by Wereley & Lueptow [74] for a narrow gap geometry ($\eta = 0.83$). However, in their case, the experimental results do not show any jump in the frequency nor in the amplitude oscillations.

The case of a wide gap geometry was investigated numerically by Razzak et al. [17] using OpenFoam code. Periodic boundary conditions were adopted with a radius ratio $\eta = 0.5$ and an aspect ratio $L = 8$. Razzak et al. [17] found that stationary axisymmetric Taylor vortices occur when Re is between 68 and $425 = 6.25\,\mathrm{Re}_c$. As the Reynolds number is increased beyond 425, the flow structure becomes non axisymmetric. In this regime, the axial flow between two vortices, in the inflow region, increases with Re and reaches its maximum value at $\mathrm{Re} \approx 500 = 7.3\mathrm{Re}_c$. Beyond this last value, a strong decrease is observed until $\mathrm{Re} = 575 \approx 8.4\mathrm{Re}_c$ to be followed by a gradual decrease. Two regimes are distinguished by Razzak et al. [17] called transitional flow to WVF and WVF. The former ranges from Re = 425 to 575 and the last is observed at Re > 575. This description is not completely aligned with our analysis. It seems that our WVF I has not been found in their numerical simulation.

### 3.7.2 Shear-thinning fluids : creation and merging of vortices

For the used shear-thinning fluids, visualization, PIV measurements as well as axisymmetric numerical simulations show that starting from a secondary critical Reynolds number, $\mathrm{Re}_s$, the regular arrangement of Taylor vortices with an axial wavenumber $k = k_c$ becomes unstable in a fundamentally different way from that discussed in the

Newtonian case, since the flow remains axisymmetric. The instability is characterized by a creation of a new pair of vortices in the inflow region, where the inward flow is weak, causing a local increase of the wavenumber. This new state is in its turn unstable and two vortex pairs merge to form one pair reducing the wavenumber. This process of creation and annihilation of vortex pairs repeats continuously. The axial position at which a new vortex pair is created is random. Furthermore, once a new extra vortex pair appears, or once two vortex pairs start to merge to form one pair, neighbouring vortex pairs will move modifying the wavenumber and consequently the axial positions of the following events of creation and merging. A complex pattern may then result. Note also that it is possible to have more than one defect in the system.

**Results of axisymmetric numerical simulations**

As mentioned in section 3.3.2, a continuation method is used to solve the unsteady axisymmetric momentum equations. Each new simulation is started with the converged solution of the steady regime corresponding to the closest set of parameters as initial condition. This procedure is followed before and after the onset of TVF. In the TVF regime, Taylor vortices are steady and their axial periodicity remains the same as at the onset. As we have seen, with increasing Reynolds number, the outflow becomes stronger than the inflow and the extent of the inflow zone where the vorticity is low increases accordingly.

For a Carreau fluid with $n_c = 0.5$, $\lambda = 200$ and periodic boundary conditions in the axial direction, the steady axisymmetric vortices lose their stability at $\mathrm{Re} = 1.69\,\mathrm{Re}_c$. A continuous creation and merging of vortices is observed. This is illustrated by figure 3.16 where contours of stream functions for three base vortex pairs are represented at different times. The choice of three base vortex pairs rather than the whole system is adopted only for a better illustration of creation and merging process. At $t = T_0$ (frame a), a new vortex pair, denoted C and D, emerges. It grows radially and reaches its maximum strength at $t \approx T_0 + 25$ (frame d). The development of the vortices leads to a local increase of the wavenumber. At $t = T_0 + 36$ (frame e) the merging process starts : two vortices B and C in frames (e) and (f) appear to collide and disappear completely at $t = T_0 + 64$. A new pair formed by the vortices A and D is obtained. A short time after, a new vortex pair emerges between two other base vortex pairs, it increases radially then merges with one of the adjacent base vortex pairs by the same mechanism. Another illustration of creation and merging events is given in figure 3.17. The distribution of the azimuthal vorticity along the line $r = R_1/d + 0.44$ (passing near the center of vortices) is represented as a function of time. It can be observed how the vortices B and C are weakened and then annihilated. A representation of the vorticity distribution on a longer interval of time and for the whole system in figure 3.18 shows the repetitive appearance of creation and merging of vortex pairs. Simultaneous defects may occur at the same time. Similar phenomenon is observed

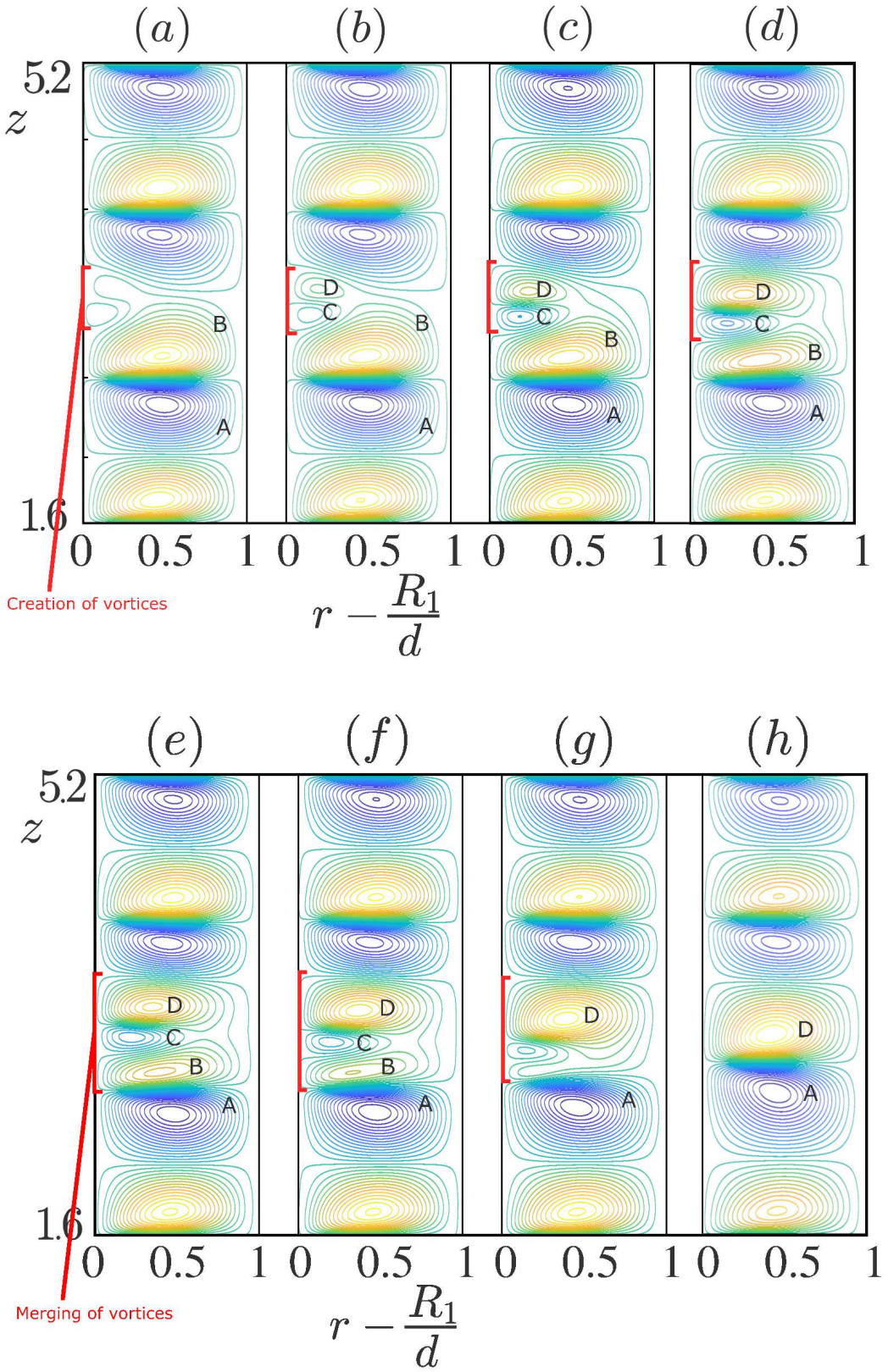


FIGURE 3.16 – Secondary instability for a Carreau fluid with $n_c = 0.5$, $\lambda = 200$ at $\mathrm{Re} = 1.67\,\mathrm{Re}_c$. Periodic boundary conditions in the axial direction, with $\lambda_z = 1.7974$, $L = 7\,\lambda_z = 12.582$. Contours of stream function at different times : (a) $t = T_0$, (b) $t = T_0 + 6$, (c) $t = T_0 + 15$, (d) $t = T_0 + 30$, (e) $t = T_0 + 36$, (f) $t = T_0 + 45$, (g) $t = T_0 + 57$, (h) $t = T_0 + 64$.

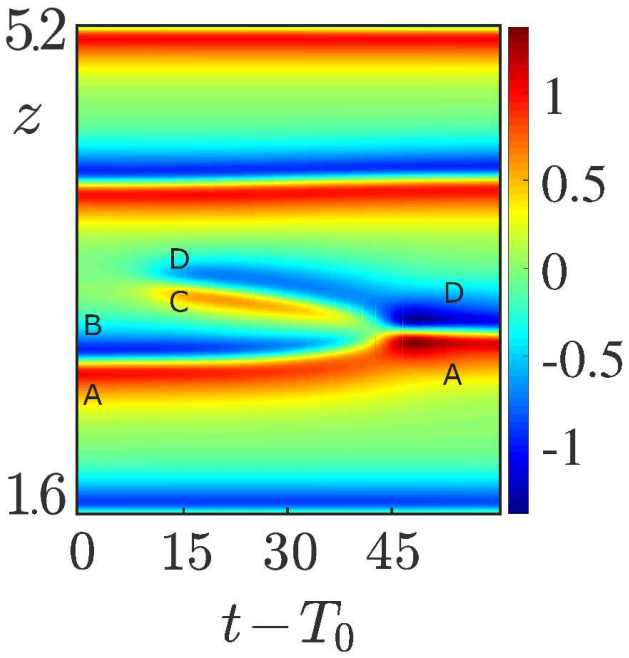


FIGURE 3.17 – Secondary instability for a Carreau fluid with $n_c = 0.5$, $\lambda = 200$ at $\mathrm{Re} = 1.69\,\mathrm{Re}_c$. Periodic boundary conditions in the axial direction with $\lambda_z = 1.7974$, $L = 7\,\lambda_z = 12.582$. Distribution of the azimuthal vorticity along the line $r = R_1/d + 0.44$ as a function of time : zoom on three pairs of vortices.

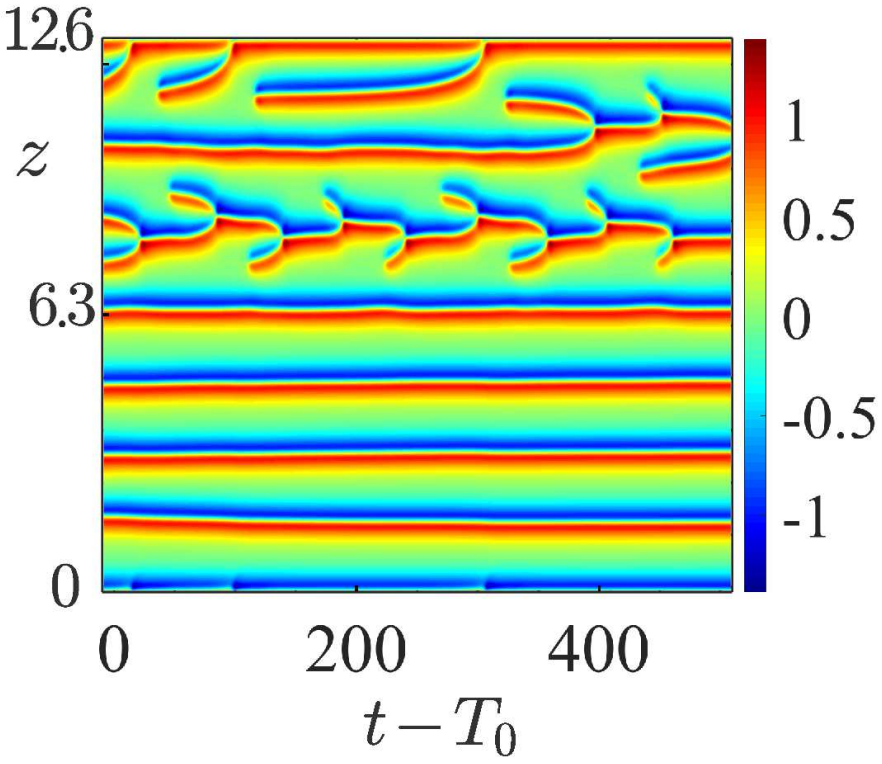


FIGURE 3.18 – Secondary instability for a Carreau fluid with $n_c = 0.5$, $\lambda = 200$ at $\mathrm{Re} = 1.69\,\mathrm{Re}_c$. Periodic boundary conditions in the axial direction with $\lambda_z = 1.7974$, $L = 7\,\lambda_z = 12.582$. Distribution of the azimuthal vorticity along the line $r = R_1/d + 0.44$ as a function of time.

for fixed bottom endwall and stress-free at the top endwall, the secondary critical Reynolds number $\mathrm{Re}_s = 1.67\,\mathrm{Re}_c$ is also pratically the same to that obtained for periodic boundary conditions.

With increasing shear-thinning effects, the range of Reynolds numbers for which the Taylor vortices remain stable shrinks. For instance, for $n_c = 0.2$, $\lambda = 200$, Taylor vortices lose their stability at Reynolds number $1.07\,\mathrm{Re}_c < \mathrm{Re}_s < 1.08\,\mathrm{Re}_c$. Similar events of creation and merging of vortices are observed as shown in figure 3.19 where contours of stream functions are shown at different times at $\mathrm{Re} = 1.08\,\mathrm{Re}_c$. A new pair of vortices C and D forms at $t \approx T_0 + 20$. It grows in size, and reaches a maximum at $t \approx T_0 + 70$. From this time, two vortices of opposite sign of vorticity C and B appear to collide and then cancel at $t \approx T_0 + 117$. A new pair of vortices A and D is obtained. Note that the process lasts longer than for $n_c = 0.5$, $\lambda = 200$. The repetitive appearance of creation and merging of vortex pairs is illustrated in figure 3.20 by the evolution of the azimuthal vorticity along the line $r = R_1/d + 0.123$ in time. It is interesting to observe how the process of creation and merging modifies the local wavenumber of the neighbouring vortices and consequently the following events of creation and merging. For $n_c = 0.2$ and $\lambda = 200$, and for both types of boundary conditions, we observed up to four defects maximum at the same time. We

think that the number of simultaneous defects depends on the aspect ratio.

Because of repetitive creation and merging process, the torque applied on the inner cylinder experiences fluctuations. In figure 3.21 we have plotted the variation of the ratio of the torque to that obtained in a purely Couette flow as a function of time. The simulation parameters are $n_c = 0.5, \lambda = 200, Re = 1.69\, Re_c$, periodic boundary conditions in the axial direction and $L = 8\,\lambda_z$. The dashed line before $t = 0$ is the converged solution at $\mathrm{Re} = 1.62\,\mathrm{Re}_c$. Figure 3.22(a) is a zoom of the curve $C(t)/C_b$ showing when creation and merging events occur. Examining $C(t)/C_b$ and the velocity field, we have placed, on the curve $C(t)/C_b$, letters C, D and M for torque at times of creation of a new pair of vortices, of full development of the new pair of vortices and of the end of merging, respectively. It can be observed that $C(t)/C_b$ increases when the new pair of vortices araises and decreases when the merging process is underway. It happens, that we have a creation of two pairs of vortices at the same time and at two different axial positions, with different times of raising and merging. Similar results are obtained using fixed bottom endwall and stress free at the top endwall (figure 3.22b). Starting from $t = 1000$, a Fourier transform of the plot in figure 3.18 presents a dominant peak at $f = 0.0153$ corresponding to a period $T = 65$. It is visible 3.22(a) and can be related to the frequency of generation of defects along the line $z \approx 7$ in figure 3.18. Similar analysis applies to figure 3.22(b). A dominant peak at $f = 0.007$ corresponding to $T \approx 140$ is obtained and can be related in the generation of defects in figure 3.20.

It is not surprising to observe that the period of creation and merging is longer for a Carreau fluid with $n_c = 0.2$, $\lambda = 200$ than that for $n_c = 0.5, \lambda = 200$, since with increasing shear-thinning effects, the inward flow in the inflow region becomes weaker. The same tendency is observed for fixed $n_c$ and larger $\lambda$. This may explain the difference in time of creation and merging of vortices between figures 3.16 and 3.23.

**Experimental results : PIV measurements and visualization**

Instability of Taylor vortices in shear-thinning fluids was also investigated experimentally by PIV measurements and by visualization. In agreement with the numerical simulation, a secondary bifurcation sets in at $\mathrm{Re} = \mathrm{Re}_s$ depending on the rheological properties of the fluid. The fluid stays axisymmetric but becomes time-dependent with repetitive sequences of creation and merging of vortices. Such process is shown in figure 3.23 where we have plotted, for xanthan gum 1000 ppm with $n_c = 0.51$ and $\lambda = 5.3$, snapshots of instantaneous velocity field in the vertical plane $(r, z)$ at $\mathrm{Re} = 16.5 = 1.7\,\mathrm{Re}_c$. Emergence of a new vortex pair at the inner wall is evident in the frame(a). It grows in size with increasing time as indicated by the frames (b) and (c). The new vortex pair and one base vortex pair collide. The vortices B and C of opposite sign of vorticity in the frame (d) weaken and disappear. In the frame (e) a new vortex pair is formed by the vortices A and D. The process of creation and merging lasts approximately $2\mathrm{s} = 21\, d/(R_1\Omega_1)$ and repeats continuously. During this process, several defects exist out

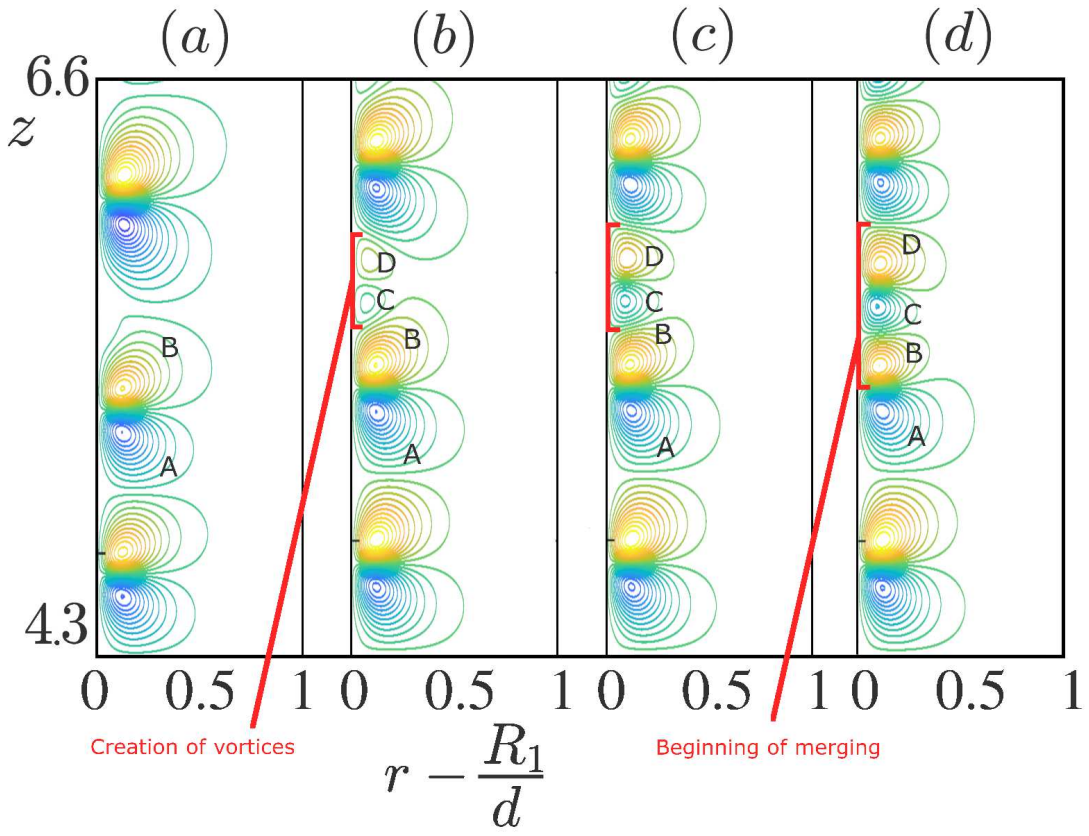


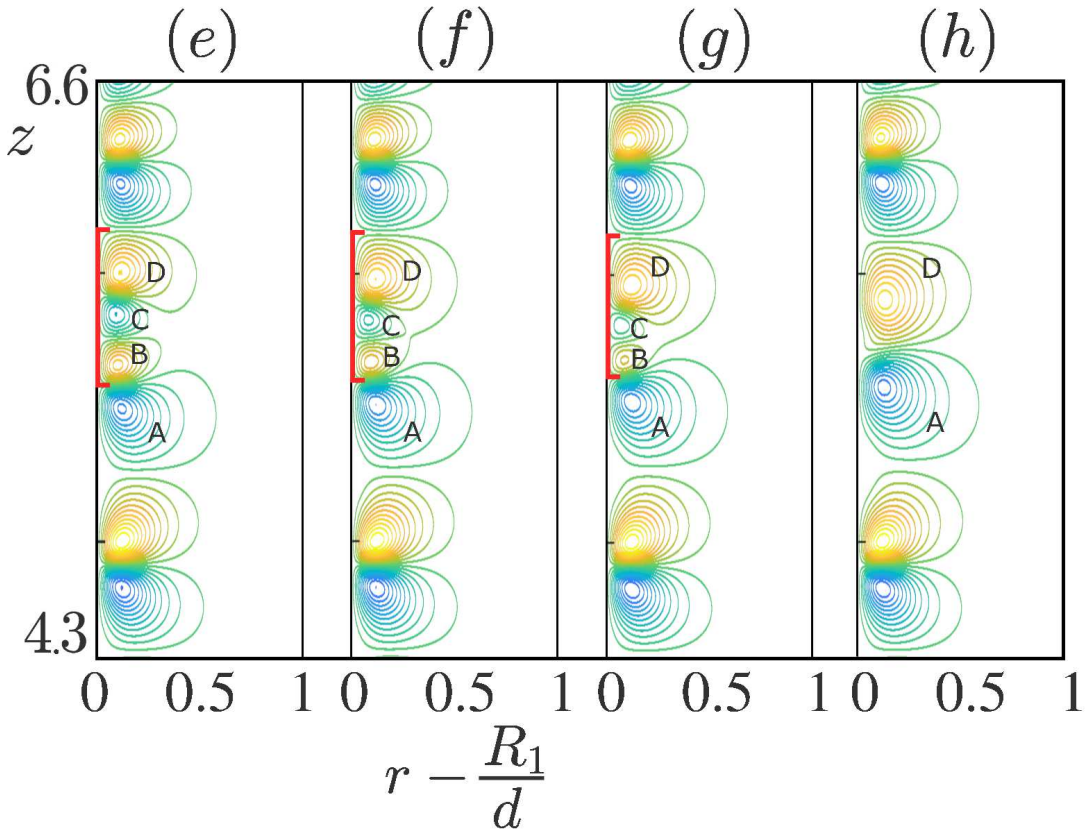


FIGURE 3.19 – Secondary instability for a Carreau fluid with $n_c = 0.2$, $\lambda = 200$, fixed bottom endwall, stress-free at the top endwall at $\mathrm{Re} = 1.08\,\mathrm{Re}_c$. Contours of stream function at different times. (a) $t = T_0$, (b) $t = T_0 + 20$, (c) $t = T_0 + 49$, (d) $t = T_0 + 69$, (e) $t = T_0 + 96$, (f) $t =$, (g) $t = T_0 + 110$, (h) $t = T_0 + 117$.

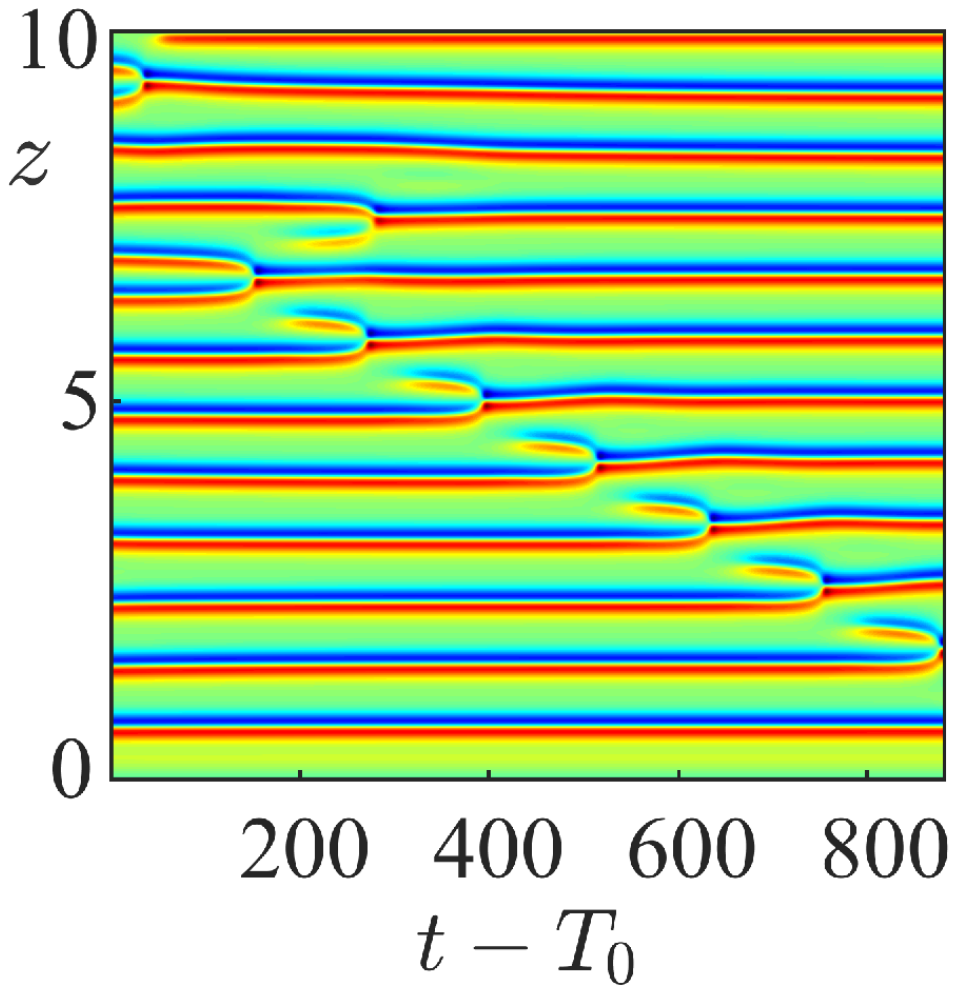


FIGURE 3.20 – Secondary instability for a Carreau fluid with $n_c = 0.2$, $\lambda = 200$, fixed bottom endwall, stress-free at the top, at $\mathrm{Re} = 1.08\,\mathrm{Re}_c$. Distribution of the azimuthal vorticity along the line $r = R_1/d + 0.123$ as a function of time.

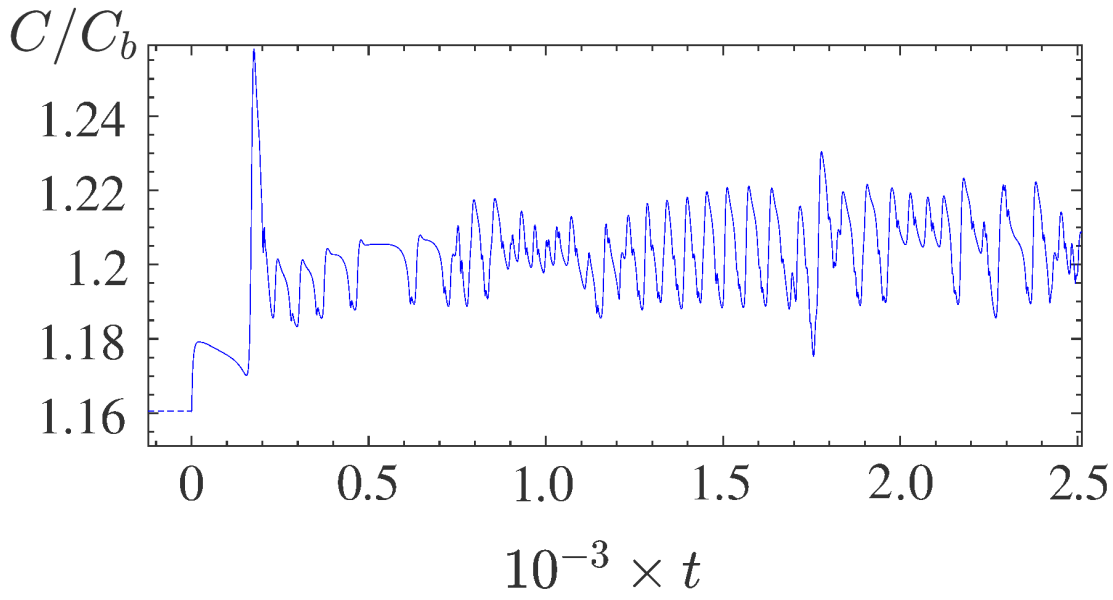


FIGURE 3.21 – Secondary instability for a Carreau fluid with $n_c = 0.5$, $\lambda = 200$. Variation of the ratio of the torque to that obtained for a purely Couette flow with periodic boundary conditions at $\mathrm{Re} = 1.69\,\mathrm{Re}_c$. The dashed line before $t = 0$, is the converged solution at a lower Reynolds number.

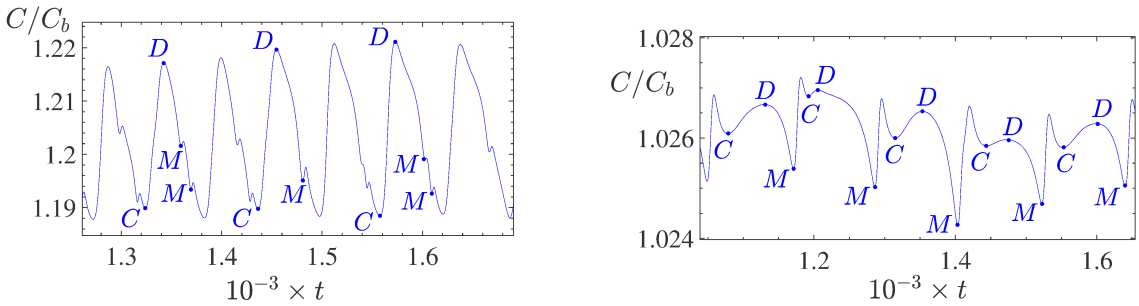


FIGURE 3.22 – Secondary instability for a Carreau fluid. Variation of the ratio of the torque to that obtained for a purely Couette flow. **(a)** $n_c = 0.5$, $\lambda = 200$, $\mathrm{Re} = 1.69\,\mathrm{Re}_c$, periodic boundary conditions in the axial direction. **(b)** $n_c = 0.2$, $\lambda = 200$, $\mathrm{Re} = 1.08\,\mathrm{Re}_c$, fixed bottom endwall and stress-free at the top endwall.

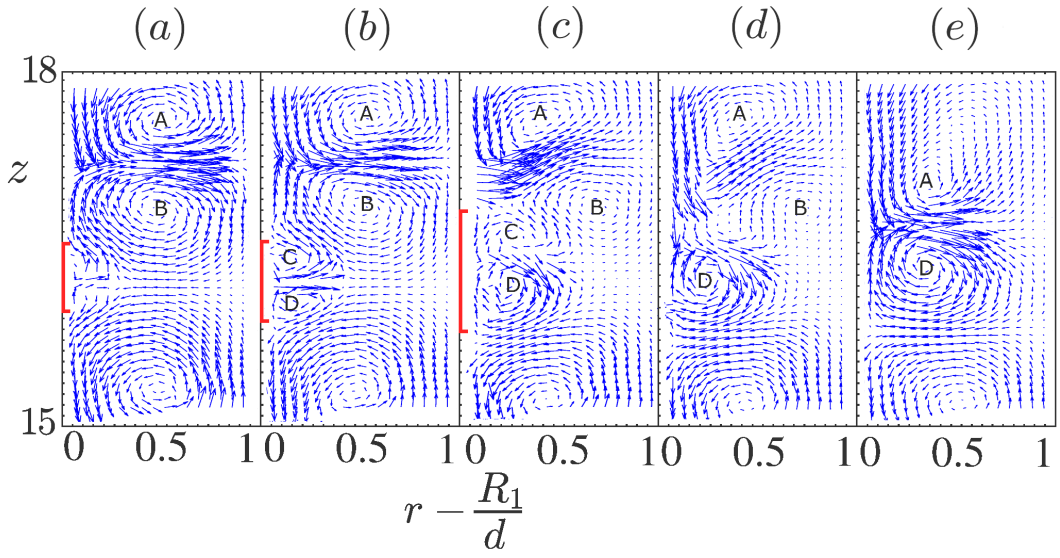


FIGURE 3.23 – Xanthan gum 1000 ppm with $n_c = 0.51$, $\lambda = 5.3$. Velocity field in the plane $(r, z)$. (a) $\hat{t} = T_0$, (b) $\hat{t} = T_0 + 0.2\,s = T_0 + 2.1\,d/(R_1\Omega_1)$, (c) $\hat{t} = T_0 + 1.5\,s = T_0 + 15.8\,d/(R_1\Omega_1)$, (d) $\hat{t} = T_0 + 1.7\,s = T_0 + 17.9\,d/(R_1\Omega_1)$, (e) $\hat{t} = T_0 + 2\,s = T_0 + 21\,d/(R_1\Omega_1)$.

of the measurement zone. Comparison between frames (a) and (e) shows an axial shift of the outflow boundaries which will lead to a modification of the local axial wavenumber of the neighboring vortices.

Qualitatively, the same phenomena are observed for higher concentration of xanthan gum, i.e. for stronger shear-thinning effects. However, three fundamental differences have to be stressed, by comparison with xanthan gum 1000 ppm : (i) the outward radial flow is much stronger and narrower than the radial inward flow, (ii) the new vortex pair reaches practically the same size as the base vortex pair and (iii) the time before merging is much larger. An illustration is given in figure 3.24 where the flow field in the $(r, z)$ plane, obtained for xanthan gum 2000 ppm with $n_c = 0.33$, $\lambda = 262$ at $\mathrm{Re} = 1.08\,\mathrm{Re}_c$, is represented at different times. A new vortex pair C, D is formed in frame (b). It is bigger in frame (c). Its development is accompanied by a splitting of the two neighboring vortex pairs. It remains aligned with the base vortex pairs during significant amount of time, here $30\,s \approx 350\,d/\,(R_1, \Omega_1)$, before merging. The process of merging by collision starts from frame (d). The vortices B and C weaken and disappear in frames (e)-(g). A new vortex pair A, D is formed in frame (h). The creation and merging process lasts $42\,s = 490\,d/(R_1\Omega_1)$, much longer than xanthan gum 1000 ppm, in addition more defects may appear at the same time.

In the visualization experiments, the flow is recorded in the front view plane with a CCD camera (10 frames/second). These experiments allow : (i) to determine the secondary critical Reynolds number from which the stationary TVF regime bifurcates

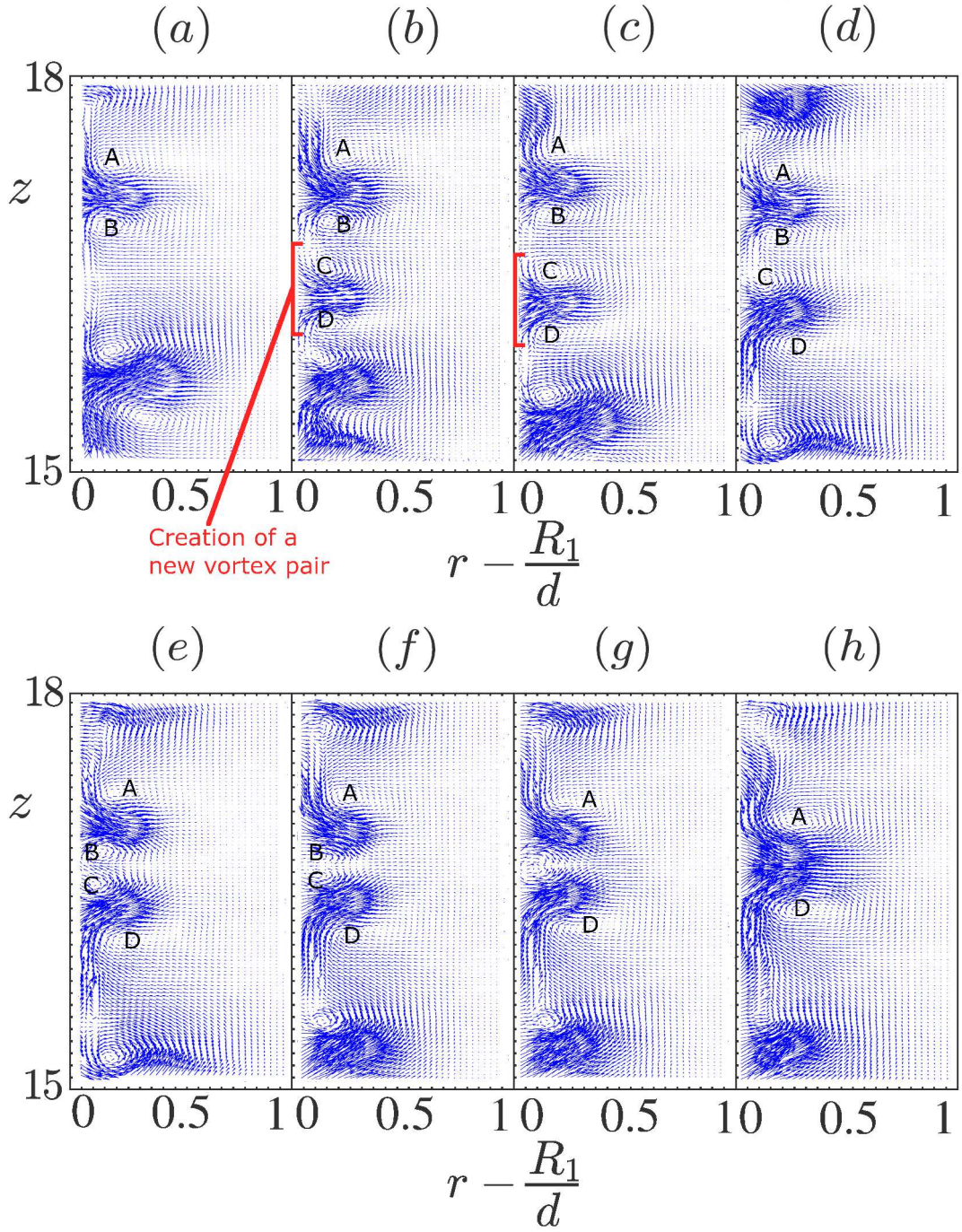


FIGURE 3.24 – Xanthan gum 2000 ppm with $n_c = 0.33$, $\lambda = 262$. Velocity field in the plane $(r, z)$. (a) $\hat{t} = T_0$, (b) $\hat{t} = T_0 + 1.5\,s = T_0 + 17.5\,d/(R_1\Omega_1)$, (c) $\hat{t} = T_0 + 3.3\,s = T_0 + 38.7\,d/(R_1\Omega_1)$, (d) $\hat{t} = T_0 + 33.1\,s = T_0 + 385\,d/(R_1\Omega_1)$, (e) $\hat{t} = T_0 + 38.1\,s = T_0 + 443\,d/(R_1\Omega_1)$, (f) $\hat{t} = T_0 + 39.2\,s = T_0 + 456\,d/(R_1\Omega_1)$, (g) $\hat{t} = T_0 + 40.4\,s = T_0 + 470\,d/(R_1\Omega_1)$, (h) $\hat{t} = T_0 + 42.1\,s = T_0 + 490\,d/(R_1\Omega_1)$.

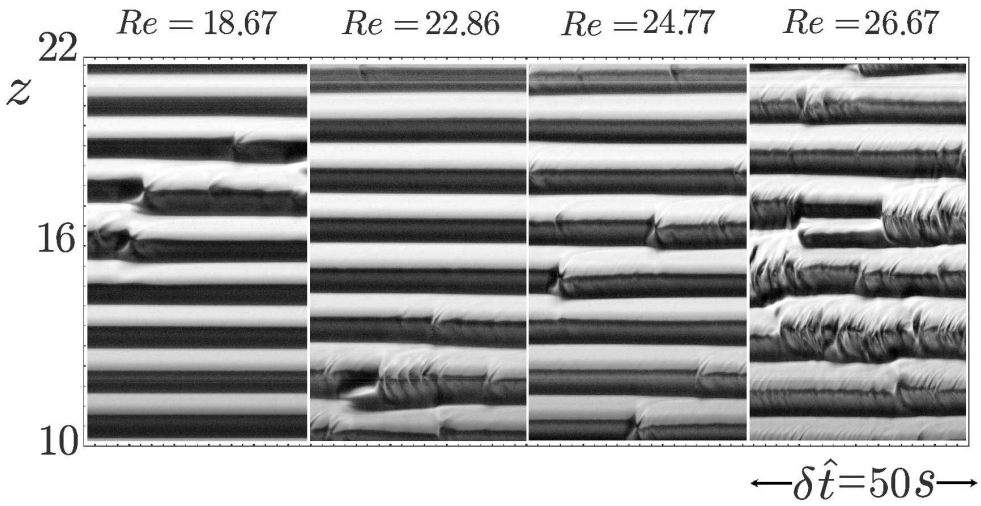


FIGURE 3.25 – Xanthan gum 1000 ppm, $n_c = 0.5$ and $\lambda = 3.1$. Spatio-temporal diagrams at different Reynolds numbers : front view of repetitive creation and merging events. At $\mathrm{Re} = 18.67$, $50\,s = 342d/(R_1\Omega_1)$.

towards an unsteady regime where creation and merging of vortices happens repetitively, (ii) to provide another view of the creation and merging process and (iii) to account for the complexity of the patterns with increasing Reynolds number because of the nonlinear interactions between vortex pairs.

For xanthan gum 1000 ppm with $n_c = 0.5$, $\lambda = 3.1$, the secondary critical Reynolds number found experimentally is $1.65\,\mathrm{Re}_c < \mathrm{Re}_s < 1.7\,\mathrm{Re}_c = 18.67$. It is quite close to that obtained numerically for higher value of $\lambda$ and lower aspect ratio. Visualization of creation and merging events is tricky as expected from the analysis of figure 3.23, in addition the process is fast ($\approx 3\,s$). Figure 3.25 shows spatio-temporal diagrams of the reflected light intensity at different values of Re. In the frame, $\mathrm{Re} = 18.67$, emergence of a small bright spot in a dark zone at $z \approx 16$ and $z \approx 18$ corresponds to a creation of a new vortex pair. Merging of the new bright spot with a large bright band corresponds to merging of vortices. It is followed by an abrupt axial shift of the outflow boundary. In the frame $\mathrm{Re} = 22.86$, continuous creation and merging events occur at $z \approx 12$, probably similar to the numerical simulations in figure 3.18. As the Reynolds number increases, the defects become more frequent and complex pattern arise. Nevertheless, the bright bands remain horizontal.

For xanthan gum 2000 ppm with $n_c = 0.34$ and $\lambda = 197$, the onset of the secondary instability occurs earlier than for xanthan gum 1000 ppm. Experimentally, we have $1.05\,\mathrm{Re}_c < Re_s < 1.07\,\mathrm{Re}_c = 1.81$. Front view of repetitive sequences of creation and merging of vortices is illustrated in figure 3.26, where spatio-temporal diagrams are shown at different values of Re. As previously, at $\mathrm{Re} = \mathrm{Re}_s \approx 1.81$, one observes emergence of

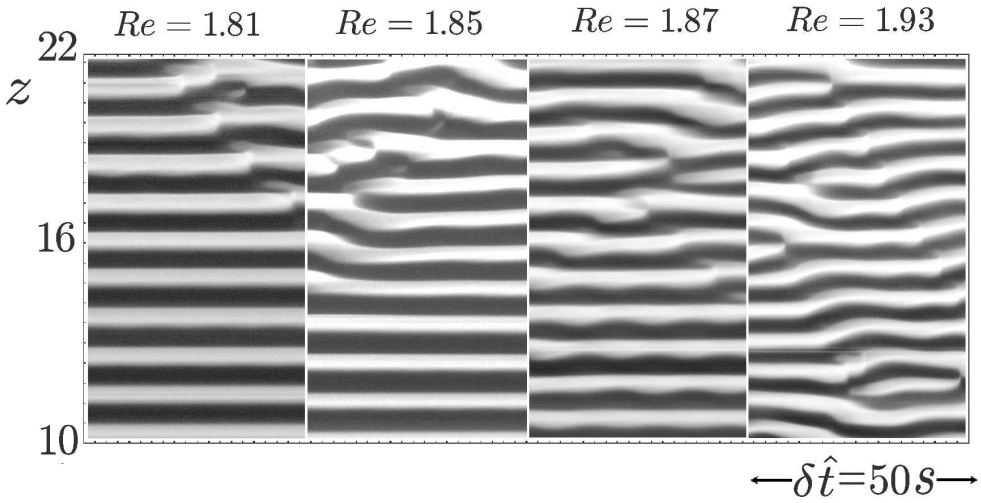


FIGURE 3.26 – Xanthan gum 2000 ppm, $n_c = 0.34$ and $\lambda = 197$. Spatio-temporal diagrams at different Reynolds numbers : front view of repetitive creation and merging events. At Re = 1.81, $50\,s = 523\,d/(R_1\Omega_1)$.

a weakly bright spot in a dark region, corresponding to emergence of new vortex pairs, at different axial positions, (here, $z \approx 18$, 19 and 20). They grow in size and merge with a larger neighboring base vortex pair after a quite short time. The creation and merging last approximately $7\,s = 80\,d/(R_1\Omega_1)$. At the end of the process, the axial position of the vortices is abruptly shifted axially. This axial shift of the vortices modifies the local wavenumber and favors subsequently the formation of a new vortex pair, similarly as in figure 3.20. By increasing slightly the Reynolds number, it is observed that : (i) the formation of the new vortex pair and its development leads to a significant splitting of the neighboring vortices, as shown in the frame Re = 1.93 at $z \approx 12$, (ii) the new vortex pair may remain aligned for some time, $(20 - 40\,s = 230 - 460\,d/(R_1\Omega_1))$ before merging and (iii) the bright bands are no longer horizontal, i.e. their axial position evolves, as a consequence of a number of defects splitting and merging simultaneously.

At still higher concentration of xanthan gum, the onset of creation and merging of vortices occurs very close to $Re_c$, i.e. the range of stable TVF shrinks strongly. For xanthan gum 3000 ppm with $n_c = 0.23$, $\lambda = 1255$, creation and merging of vortices happen at $Re = 1.02\,Re_c$. For a slightly larger Reynolds number, the phenomena described previously, i.e. (i) the increasing number of defects and (ii) the non horizontal bright bands, become more pronounced as shown in figure 3.27. However, the creation and merging of vortices is the main mechanism that drives the flow structure. It can be still better illustrated by applying a complex demodulation technique to the reflected light intensity $I(z,t)$ [75, 76]. The real signal $I(z,t)$ is transformed in its complex equivalent expression by means of Hilbert transform [75, 76]. In practice, the complex demodulation is performed by computing a two-dimensional fast-Fourier-transform of $I(z,t)$, keeping the most energetic modes and performing an inverse FFT. The modulus $|A(z,t)|$ and the

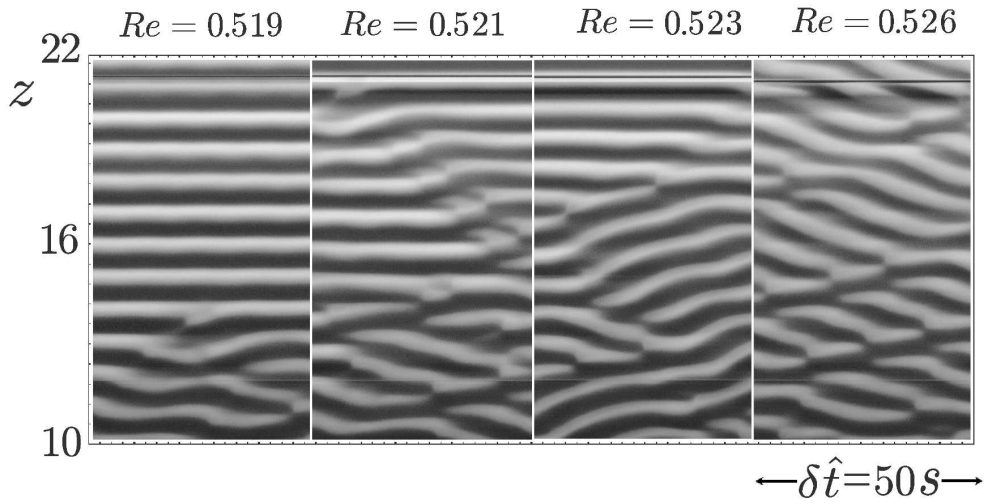


FIGURE 3.27 – Xanthan gum 3000 ppm, $n_c = 0.23$ and $\lambda = 1255$. Spatio-temporal diagrams at different Reynolds numbers. At Re $= 0.519$, $50\,s = 809\,d/(R_1\Omega_1)$.

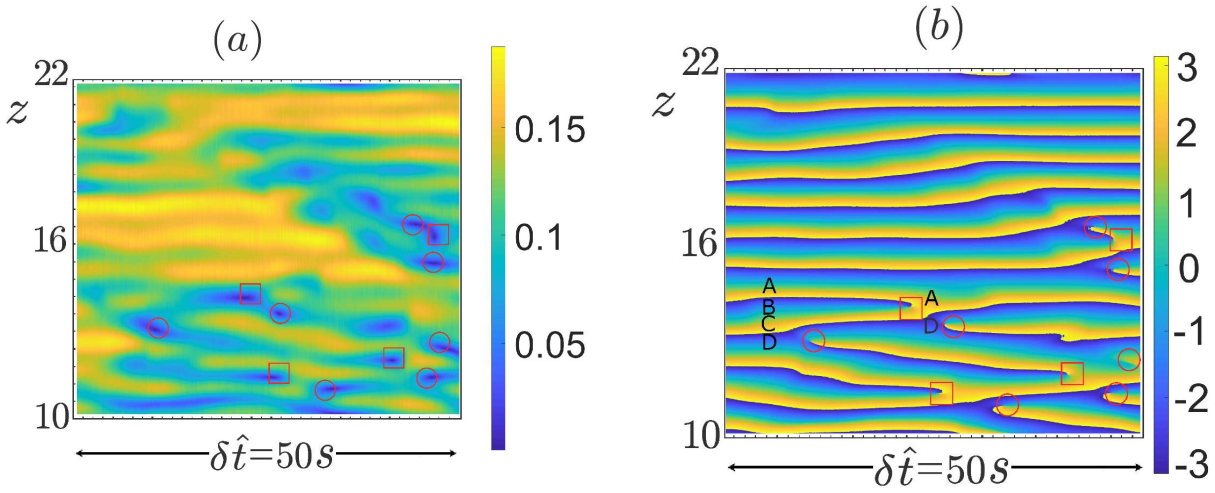


FIGURE 3.28 – Xanthan gum 3000 ppm, $n_c = 0.23$ and $\lambda = 1255$. Complex demodulation of a spatio-temporal diagram at Re $= 0.521$ : **(a)** amplitude demodulation – dark zones corresponds to the core of the defects where the amplitude vanishes ; **(b)** phase demodulation. Circles and squares show the position of creation and merging processes respectively.

| $n_c$ | $\lambda$ | Boundary conditions | Num/Exp | $Re$ | Figures | Time $(d/(R_1\Omega_1))$ |
|---|---|---|---|---|---|---|
| 0.5 | 200 | periodic | numerical | $1.69Re_c$ | 16-18,22(a) | 64 |
| 0.51 | 5.3 | realistic | PIV | $1.70Re_c$ | 23 | 21 |
| 0.5 | 3.1 | realistic | visual | $1.69Re_c$ | 25 | 21 |
| 0.33 | 262 | realistic | PIV | $1.08Re_c$ | 24 | 490 |
| 0.34 | 197 | realistic | visual | $1.07Re_c$ | 26 | 80 |
| 0.34 | 197 | realistic | visual | $1.09Re_c$ | 26 | 230-460 |
| 0.2 | 200 | realistic | numerical | $1.08Re_c$ | 19 | 117 |
| 0.2 | 200 | realistic | numerical | $1.08Re_c$ | 20,22(b) | 140 |
| 0.23 | 1455 | realistic | visual | $1.02Re_c$ | 28 | $> 100$ |
| 0.23 | 1455 | realistic | visual | $1.03Re_c$ | 27-28 | $> 400$ |

TABLE 3.7 – Durations of creation and merging process for different rheological parameters : numerical and experimental results.

phase $\phi(z,t)$ of the complex signal are then determined. Figure 3.28 shows such a result for xanthan gum 3000 ppm at $Re = 0.52$. The phase varies from -$\pi$ (dark colour) to $+\pi$ (bright colour). The phase jump from -$\pi$ to $+\pi$ at the boundary between dark and bright colours corresponds to the boundary between two counter rotating vortices. The main feature of the space-time diagrams displayed in figure 3.28 is the occurrence of topological defects : points where the amplitude $|A|$ vanishes (dark points in the amplitude space time diagram) and the phase is no longer defined. Two types of defects are clearly observed. The first one shown by a square is a merging by two vortex pairs. The phase jumps by $-2\pi$ after a loss of one pair of rolls. The second type of defect is shown by a circle, where the phase jumps by $+2\pi$ corresponds to a creation of one vortex pair. The process described previously can again be observed in figure 3.28(b) : two vortices B and C weaken with time, then disappear and a new vortex pair A and D is formed.

Our experimental and numerical results are summarized in figure 3.29 and Table 3.7. In figure 3.29, we have reported the stability diagram in the plane $(\epsilon = Re - Re_c)/Re_c, n_c)$. The primary bifurcation occurs at $\epsilon = 0$ and the TVF regime is stable when $0 < \epsilon < \epsilon_s$, i.e. $Re_c < Re < Re_s$. The variation of $\epsilon_s$ with $n_c$ is shown by a dashed line. From $\epsilon > \epsilon_s$, the TVF regime is no longer stable. It is interesting to note that there is a quite good agreement between the numerical and the experimental results even if the experimental aspects ratio is three times higher than the numerical one.
In Table 3.7, we have reported the times $T$ between creation and merging. Close to the onset of secondary bifurcation, globally, $T$ increases with increasing shear-thinning effects. As the Reynolds number increases further from $Re_s$, this process lasts significantly longer time, particularly for low $n_c$.

**Remark**
For a Carreau fluid with $n_c = 0.5$ and $\lambda = 3.1$, a reduction of the wavelength was observed at two Reynolds numbers $Re = 14.48$ and 16.77 below $Re_s$. In these cases, a new

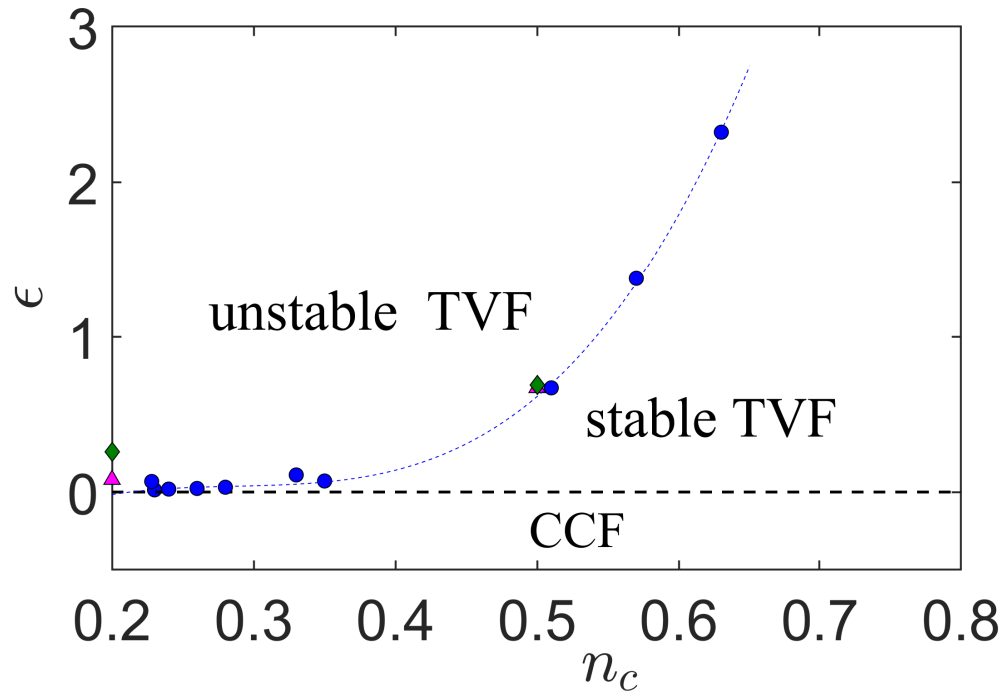


FIGURE 3.29 – Stability diagram of the TVF regime for a Carreau fluid with $\eta = 0.4$ in the plane $(\epsilon = (Re - Re_c)/Re_c)$, $n_c)$. The thin dashed line joins the experimental results represented by filled circles. Numerical results are represented by a filled triangle for realistic boundary conditions and filled diamonds for periodic boundary conditions.

steady-state with an additional vortex pair appears. Such reduction of the wavelength has also been detected using PIV measurements, i.e. it is not an effect of the shape of the particles used in the visualization. Such reduction of the wavelength has also been detected by PIV measurements using spherical particles. Therefore, one may conjecture that this reduction of the wavelength i not an artifact induced by the anisotropic shape of the particles used in flow visualization.
-Creation, propagation and annihilation of vortices was observed by Hoffmann et al. [77] in a Newtonian fluid, in the case of a short Taylor-Couette system ($L = 4 and L = 8$) with counter-rotating cylinders, non rotating end walls and before the centrifugal instability. The radius ratio is $\eta = 0.5$. In their study : (i) the vortices are generated by the shear flow near the Ekman cells and (ii) the phenomenon of creation and merging is not observed in the case of periodic boundary conditions. The physical mechanisms involved in their study is fundamentally different from the ours. Indeed, in our study, repetitive creation and merging of vortices is observed even with periodic boundary conditions.
- In the work of Cagney et al. [40] where $\eta = 0.77$ and $L = 21$, merger events, followed by drifting and splitting of vortices are observed in the WVF regime. They occur at the ends of the geometry and at some particular Reynolds numbers. In our case, $\eta = 0.4$ and $L = 32$, repetitive creation and merging are observed at $Re > Re_s$ as a consequence of an instability of the TVF regime with respect to axisymmetric perturbations.
- Good agreement between the experimental and the theoretical and numerical results assuming purely viscous shear-thinning fluid suggests that the shear-thinning behavior of aqueous solutions of xanthan-gum play a major role in controlling the stability of Taylor-Couette system. Furthermore, it is argued in the literature (Dutcher & Muller [6], [10] and Lacassagne et al. [78]) that the higher the polymer-to-solvent viscosity ratio the stronger the pure shear-thinning. According to these authors, the shear-thinning may act to reduce or suppress elastic and elasto-inertial instabilities observed for Boger fluids.

### 3.7.3 Possible mechanisms of instability of the TVF regime

For the used shear-thinning fluids, experimental and numerical results show that from $Re = Re_s$, the steady TVF regime with a wavenumber $k = k_c$ bifurcates to an axisymmetric unsteady regime with repetitive creation and merging of vortices. We believe that this process is associated with the instability of Taylor vortices to axial perturbations. The most relevant mechanism mechanism is that of Eckhaus instability or generalized Eckhaus instability [25, 79]. If the axial wavenumber is too large, two vortex pairs will merge to form one pair and the wavenumber will be reduced. If it is too small, a new pair of vortices will be created between existing pairs, causing the wavenumber to increase. The classical Eckhaus criterion obtained from an amplitude expansion at the third order is only valid in the region very close to $Re_c$. For a Newtonian fluid, the Eckhaus criterion is valid up to $Re = 1.1Re_c$ [21] and much less for a shear-thinning fluid.

At $Re = Re_s$, the numerical simulations and the experimental tests show that for shear-thinning fluids, the flow resulting from either creation or merging of vortices is as unstable as before the creation or the merge. It is also possible to observe creation and merging at the same time separated by one wavelength (figure 3.20 at $0 < z < 6$ and figure 3.26 at $Re = 1.81$, $16 < z < 22$). Such situation may happen, if the Eckhaus boundary is a closed loop and there is no wavenumber more stable than another. Thus a recurrent creation and merging will occur.

## 3.8 Conclusion

In this paper, we have investigated the influence of shear-thinning effects on the stability of Taylor vortex flow (TVF) in a wide gap geometry with a radius ratio $\eta = 0.4$. With such radius ratio, the Taylor vortices remain stable with respect to non axisymmetric perturbations in a large range of Reynolds numbers for a Newtonian fluid, for which we found $Re_s \approx 5.3\, Re_c$. The inner cylinder is rotating and the outer one is at rest. Aqueous solutions of xanthan gum solutions are used as shear-thinning fluids and aqueous solution of glycerol as a Newtonian fluid reference. The shear-thinning behavior is described by the Carreau model. The originality of the present work consists in simultaneous experimental observations and numerical simulations conveying credit to the presented new results.
For shear-thinning fluids, we have shown experimentally and numerically that the range of Reynolds numbers (defined with the zero shear-rate viscosity) where the Taylor vortices are stable shrinks with increasing shear-thinning effects (figure 3.29). The dominant feature of the secondary instability is the repetitive sequences of formation and merging of vortices. Close to the onset of the secondary instability, $Re_s$, the duration of the creation and merging process increases globally with increasing shear-thinning effects. For $Re$ larger than $Re_s$, the new vortex formed may remain aligned with the neighboring vortices during many number of rounds of the rotating cylinder before merging, particularly for low values of $n_c$. This effect combined with the increase of the number of defects and splitting of vortices leads to complex patterns. We believe that the process of creation and merging of vortices is due to a generalized Eckhaus instability of the TVF regime. If the Eckhaus boundary becomes a closed loop, repetitive sequences of creation and merging will occur [25].
An important open issue is to clarify the physical mechanism behind the secondary instabilities illustrated in this paper. In §3.7.3, we have proposed a possible mechanism based on generalized Eckhaus instability. Therefore, in our future work, we intend to examine numerically, using the linear stability analysis, the influence of the shear-thinning behavior on the stability of Taylor vortices with respect to axial and to non axisymmetric perturbations. For a wide gap, the axial mode is dominant, and it will be possible to determine the Eckhaus boundary and how it is modified by shear-thinning effects. For a thin gap, the non axisymmetric one will be dominant, and it is possible to analyze the influence of shear-thinning behavior on the stability of the TVF regime to non axisymmetric pertur-

bations. For intermediate radius ratios, the competition between the axisymmetric mode and the non axisymmetric mode could be investigated.

## Bibliographie

[1] E. L. Koschmieder. Bénard cells and Taylor vortices. *Cambridge Monogr. Mech.*, 844 :37–51, 1993.

[2] R. Tagg. The Couette-Taylor problem. *Nonlinear Sci. Today*, 4 :1–25, 1994.

[3] G. I. Taylor. Stability of a viscous liquid contained between two rotating cylinders. *Trans. R. Soc. Lond. A*, 223 :289–343, 1923.

[4] RC DiPrima, PM Eagles, and BS Ng. The effect of radius ratio on the stability of Couette flow and Taylor Vortex flow. *Phys. Fluids*, 27(10) :2403–2411, 1984.

[5] A. Esser and S. Grossmann. Analytic expression for Taylor-Couette stability boundary. *Phys. Fluids*, 8(7) :1814–1819, 1996.

[6] C.S. Dutcher and S.J. Muller. Explicit analytic formulas for Newtonian Taylor-Couette primary instabilities. *Phys. Rev. E*, 75(4) :047301, 2007.

[7] J.A. Cole. Taylor-Vortex instability and annulus-length effects. *J. Fluid Mech.*, 75(1) :1–15, 1976.

[8] D. Coles. Transition in circular Couette flow. *J. Fluid Mech.*, 21(3) :385–425, 1965.

[9] T. Mullin. Onset of time dependence in Taylor-Couette flow. *Phys. Rev. A*, 31(2) :1216, 1985.

[10] C.S. Dutcher and S. J. Muller. Spatio-temporal mode dynamics and higher order transitions in high aspect ratio Newtonian Taylor–Couette flows. *J. Fluid Mech.*, 641 :85–113, 2009.

[11] D. Martinand, E. Serre, and R. M. Lueptow. Mechanisms for the transition to waviness for Taylor vortices. *Phys. Fluids*, 26(9) :094102, 2014.

[12] T. Dessup, L.S. Tuckerman, J.E. Wesfreid, D. Barkley, and A.P. Willis. Self-sustaining process in Taylor-Couette flow. *Phys. Rev. Fluids*, 3(12) :123902, 2018.

[13] C.A. Jones. The transition to wavy Taylor vortices. *J. Fluid Mech.*, 157 :135–162, 1985.

[14] H.A. Snyder and R.B. Lambert. Harmonic generation in Taylor vortices between rotating cylinders. *J. Fluid Mech.*, 26(3) :545–562, 1966.

[15] O. Meincke and C. Egbers. Routes into chaos in small and wide gap Taylor-Couette flow. *Phys. Chem. Earth Pt. B*, 24(5) :467–471, 1999.

[16] G.P. King, Y. Li, W. Lee, H. L. Swinney, and P. S. Marcus. Wave speeds in wavy Taylor-Vortex flow. *J. Fluid Mech.*, 141 :365–390, 1984.

[17] M. A. Razzak, B. C. Khoo, and K. B. Lua. Numerical study on wide gap Taylor Couette flow with flow transition. *Phys. Fluids*, 31(11) :113606, 2019.

[18] A. Lorenzen, G. Pfister, and T. Mullin. End effects on the transition to time-dependent motion in the Taylor experiment. *Phys. Fluids*, 26(1) :10–13, 1983.

[19] O. Czarny, E. Serre, P. Bontoux, and R. M. Lueptow. Interaction of wavy cylindrical Couette flow with endwalls. *Phys. Fluids*, 16(4) :1140–1148, 2004.

[20] S. Kogelman and R. C. DiPrima. Stability of spatially periodic supercritical flows in hydrodynamics. *Phys. Fluids*, 13(1) :1–11, 1970.

[21] H. Riecke and H-G. Paap. Stability and wave-vector restriction of axisymmetric Taylor vortex flow. *Phys. Rev. A*, 33(1) :547, 1986.

[22] H-G. Paap and H. Riecke. Wave-number restriction and mode interaction in Taylor vortex flow : Appearance of a short-wavelength instability. *Phys. Rev. A*, 41(4) :1943, 1990.

[23] M. Dennin, D. S. Cannell, and G. Ahlers. Measurement of a short-wavelength instability in Taylor vortex flow. *Phys. Rev. E*, 49(1) :462, 1994.

[24] M.A. Dominguez-Lerma, G. Ahlers, and D.S. Cannell. Marginal stability curve and linear growth rate for rotating Couette–Taylor flow and Rayleigh–Bénard convection. *Phys. Fluids*, 27(4) :856–860, 1984.

[25] Y. Guo and W.H. Finlay. Splitting, merging and wavelength selection of vortices in curved and/or rotating channel flow due to Eckhaus instability. *J. Fluid Mech.*, 228 :661–691, 1991.

[26] R. Meyer-Spasche and H. B. Keller. Some bifurcation diagrams for Taylor Vortex flows. *Phys. Fluids*, 28(5) :1248–1252, 1985.

[27] C.D. Andereck, S.S. Liu, and H.L. Swinney. Flow regimes in a circular Couette system with independently rotating cylinders. *J. Fluid Mech.*, 164 :155–183, 1986.

[28] A. Brandstäter, J. Swift, H.L. Swinney, A. Wolf, J.D. Farmer, E. Jen, and P.J. Crutchfield. Low-dimensional chaos in a hydrodynamic system. *Phys. Rev Lett.*, 51(16) :1442, 1983.

[29] A. Lindner, D. Bonn, and J. Meunier. Viscous fingering in a shear-thinning fluid. *Phys. Fluids*, 12(2) :256–261, 2000.

[30] B. Alibenyahia, C. Lemaître, C. Nouar, and N. Ait-Messaoudene. Revisiting the stability of circular Couette flow of shear-thinning fluids. *J. Non-Newtonian Fluid. Mech.*, 183 :37–51, 2012.

[31] Z. Li and R.E. Khayat. A non-linear dynamical system approach to finite amplitude Taylor-Vortex flow of shear-thinning fluids. *Int. J. Numer. Methods Fluids*, 45(3) :321–340, 2004.

[32] Y. Agbessi, B. Alibenyahia, C. Nouar, and L. Choplin. Linear stability of Taylor-Couette flow of shear-thinning fluids : modal and non-modal approaches. *J. Fluid Mech.*, 775 :354–389, 2015.

[33] S. Topayev, C. Nouar, D. Bernardin, A. Neveu, and S.A. Bahrani. Taylor-vortex flow in shear-thinning fluids. *Phys. Rev. E*, 100(2) :023117, 2019.

[34] H. Masuda, T. Horie, R. Hubacz, M. Ohta, and N. Ohmura. Prediction of onset of Taylor-Couette instability for shear-thinning fluids. *Rheol. Acta*, 56 :73–84, 2017.

[35] H. Elçiçek and B. Güzel. Effect of shear-thinning behavior on flow regimes in Taylor-Couette flows. *J. Non-Newtonian Fluid. Mech.*, 279 :104277, 2020.

[36] V. Sinevic, R. Kuboi, and A.W. Nienow. Power numbers, Taylor numbers and Taylor vortices in viscous Newtonian and non-Newtonian fluids. *Chem. Eng. Sci.*, 41(11) :2915–2923, 1986.

[37] M. P. Escudier, I. W. Gouldson, and D. M. Jones. Taylor vortices in Newtonian and shear-thinning liquids. *Proc. Roy. Soc. Lond. A.*, 449 :155–176, 1995.

[38] N. Cagney and S. Balabani. Influence of shear-thinning rheology on the mixing dynamics in Taylor-Couette flow. *Chem. Eng. Technol*, 42(8) :1680–1690, 2019.

[39] N. Cagney and S. Balabani. Taylor-Couette flow of shear-thinning fluids. *Phys. Fluids*, 31(5) :053102, 2019.

[40] N. Cagney, T. Lacassagne, and S. Balabani. Taylor-Couette flow of polymer solutions with shear-thinning and viscoelastic rheology. *J. Fluid Mech.*, 905, 2020.

[41] K. Park and G. L. Crawford. Deterministic transitions in Taylor Wavy-Vortex flow. *Phys. Rev. Letters*, 50(5) :343, 1983.

[42] G. Ahlers, D. S. Cannell, and M.A. Dominguez-Lerma. Possible mechanism for transitions in wavy taylor-vortex flow. *Phys. Rev. A*, 27(2) :1225, 1983.

[43] G. L. Crawford, K. Park, and R.J. Donnelly. Vortex pair annihilation in Taylor Wavy-Vortex flow. *Phys. Fluids*, 28(1) :7–9, 1985.

[44] P.J. Carreau. Rheological equations from molecular network theories. *T. Soc. Rheol.*, 16(1) :99–127, 1972.

[45] R. B. Bird, R. Amstrong, and O. Hassager. *Dynamics of polymeric liquids.* Wiley-Interscience, New York, 1987.

[46] R. Tanner. Engineering rheology. Oxford University Press, New York, 2000.

[47] J.H. Ng, R.K. Jaiman, and T.T. Lim. Interaction dynamics of longitudinal corrugations in Taylor-Couette flows. *Phys. Fluids*, 30(9) :093601, 2018.

[48] H. Teng, N. Liu, X. Lu, and B. Khomami. Direct numerical simulation of Taylor-Couette flow subjected to a radial temperature gradient. *Phys. Fluids*, 27(12) :125101, 2015.

[49] H. Fasel and O. Booz. Numerical investigation of supercritical Taylor-vortex flow for a wide gap. *J. Fluid Mech.*, 138 :21–52, 1984.

[50] F. Hecht. New development in freefem++. *J. Numer. Math*, 20(3-4) :251–266, 2012.

[51] M. Jenny, E. Plaut, and A. Briard. Numerical study of subcritical rayleigh–bénard convection rolls in strongly shear-thinning carreau fluids. *J. Non-Newtonian Fluid. Mech.*, 219 :19–34, 2015.

[52] J. Cahouet and J-P. Chabard. Some fast 3d finite element solvers for the generalized stokes problem. *Int. J. Numer. Methods Fluids*, 8(8) :869–895, 1988.

[53] A. Davey. The growth of Taylor vortices in flow between rotating cylinders. *J. Fluid Mech.*, 14(3) :336–368, 1962.

[54] R.J. Donnelly and N.J. Simon. An empirical torque relation for supercritical flow between rotating cylinders. *J. Fluid Mech.*, 7(3) :401–418, 1960.

[55] K. Atkhen, J. Fontaine, and J.E. Wesfreid. Highly turbulent Couette–Taylor bubbly flow patterns. *J. Fluid Mech.*, 422 :55–68, 2000.

[56] C. Nore, F. Moisy, and L. Quartier. Experimental observation of near-heteroclinic cycles in the Von Kármán swirling flow. *Phys. Fluids*, 17(6) :064103, 2005.

[57] M. Smieszek, O. Crumeyrolle, I. Mutabazi, and C. Egbers. Instabilities with polyacrylamide solution in small and large aspect ratios Taylor-Couette systems. In *Journal of Physics : Conference Series*, volume 137, page 012021. IOP Publishing, 2008.

[58] J.J. Hegseth. Turbulent spots in plane Couette flow. *Phys. Rev. E*, 54(5) :4915, 1996.

[59] K.W. Schwarz. Phase slip and turbulence in superfluid He 4 : A vortex mill that works. *Phys. Rev. Lett.*, 64(10) :1130, 1990.

[60] F. Daviaud, J. Hegseth, and P. Bergé. Subcritical transition to turbulence in plane Couette flow. *Phys. Rev. Lett.*, 69(17) :2511, 1992.

[61] M. V. Majji, S. Banerjee, and J. F. Morris. Inertial flow transitions of a suspension in Taylor-Couette geometry. *J. Fluid Mech.*, 835 :936–969, 2018.

[62] E. Choppe, F. Puaud, T. Nicolai, and L. Benyahia. Rheology of xanthan solutions as a function of temperature, concentration and ionic strength. *Carbohy. Polym.*, 82(4) :1228–1235, 2010.

[63] G. Cuvelier and B. Launay. Concentration regimes in xanthan gum solutions deduced from flow and viscoelastic properties. *Carbohyd. Polym.*, 6(5) :321–333, 1986.

[64] O. Czarny, E. Serre, P. Bontoux, and R. M. Lueptow. Interaction between Ekman pumping and the centrifugal instability in Taylor-Couette flow. *Phys. Fluids*, 15(2) :467–477, 2003.

[65] G. Ahlers, D.S. Cannell, M.A. Dominguez-Lerma, and R. Heinrichs. Wavenumber selection and Eckhaus instability in Couette-Taylor flow. *Phys. D : Nonlinear Phenom.*, 23(1-3) :202–219, 1986.

[66] M. Lücke, M. Mihelcic, and K. Wingerath. Front propagation and pattern formation of Taylor vortices growing into unstable circular Couette flow. *Phys. Rev. A*, 31(1) :396, 1985.

[67] G. Pfister and I. Rehberg. Space-dependent order parameter in circular Couette flow transitions. *Phys. Lett. A*, 83(1) :19–22, 1981.

[68] M. Linek and G. Ahlers. Boundary limitation of wave numbers in Taylor-Vortex flow. *Phys. Rev. E*, 58(3) :3168, 1998.

[69] T. Watanabe and Y. Toya. Vertical Taylor–Couette flow with free surface at small aspect ratio. *Acta Mech.*, 223(2) :347–353, 2012.

[70] J.E. Burkhalter and E.L. Koschmieder. Steady supercritical Taylor vortex flow. *J. Fluid Mech.*, 58(3) :547–560, 1973.

[71] A.M. Philippe, C. Baravian, M. Jenny, F. Meneau, and L.J. Michot. Taylor-Couette instability in anisotropic clay suspensions measured using small-angle x-ray scattering. *Phys. Rev. letters*, 108(25) :254501, 2012.

[72] J. Gillissen and H.J. Wilson. Taylor-Couette instability in disk suspensions. *Phys. Rev. Fluids*, 3(11) :113903, 2018.

[73] J. Gillissen, N. Cagney, T. Lacassagne, A. Papadopoulou, S. Balabani, and H. Wilson. Taylor-Couette instability in disk suspensions : Experimental observation and theory. *Phys. Rev. Fluids*, 5(8) :083302, 2020.

[74] S. T. Wereley and R. M. Lueptow. Spatio-temporal character of non-wavy and wavy Taylor-Couette flow. *J. Fluid Mech.*, 364 :59–80, 1998.

[75] P. Bot and I. Mutabazi. Dynamics of spatio-temporal defects in the Taylor-Dean system. *Eur. Phys. J. B.*, 13(1) :141–155, 2000.

[76] O. Crumeyrolle, A. Latrache, I. Mutabazi, and A.B. Ezersky. Instabilities with shear-thinning polymer solutions in the Couette-Taylor system. In *J. Phys. Conf. Ser.*, volume 14, page 78. IOP Publishing, 2005.

[77] C. Hoffmann, S. Altmeyer, M. Heise, J. Abshagen, and G. Pfister. Axisymmetric propagating vortices in centrifugally stable taylor–couette flow. *J. Fluid Mech.*, 728 :458–470, 2013.

[78] T. Lacassagne, N. Cagney, J. Gillissen, and S. Balabani. Vortex merging and splitting : A route to elastoinertial turbulence in Taylor-Couette flow. *Phys. Rev. Fluids*, 5(11) :113303, 2020.

[79] A. Bottaro. On longitudinal vortices in curved channel flow. *J. Fluid Mech.*, 251 :627–660, 1993.

# Chapitre 4

# Secondary instabilities in Taylor Couette flow of shear-thinning fluids

**Sommaire**

## 4.1 Introduction

Viscoplastic material behaves as a "solid" from kinematic point of view when the applied stress is below a threshold value $\tau_y$ and flows like a viscous fluid for stresses higher than $\tau_y$. The solid-like behavior is associated with elasticity, whereby the continuum deforms when subject to a given stress and there is a complete strain recovery when the forcing is removed. In many cases, it is acceptable to neglect the elastic behavior by considering that the strain-rate vanishes when the stress is below the $\tau_y$ [1].
In the present work, we follow this assumption. Many materials exhibit a yield-stress [2], like drilling mud in the oil industry, cement, paints, cosmetic preparations as well as a large variety of food products. Although, many models have been proposed to describe the behavior of such materials, the Bingham model is the most well known and simple and contains all the ingredients of viscoplastic materials namely a yield stress and a nonlinear variation of the effective viscosity. In this model, the material is considered to be rigid below a yield criterion described by von Mises criterion and is nonlinear viscous above the yield criterion. The determination of these two regions is not a trivia task, especially in two- and three-dimensional flows. A review on yield-stress fluids can be found in [3, 4, 5]. Although commonly used as industrial fluids, there are surprisingly little published works that focus on the stability of yield-stress fluid flows.
In the present work, we consider the stability of a circular Couette flow for a Bingham fluid. The first linear stability analysis was done by [6] using a narrow gap approximation. He found that the yield-stress has a stabilizing effect. This problem was later reconsidered by [7] assuming axisymmetric disturbances. The most interesting feature of the results is the nonmonotonicity of the critical inner cylinder Reynolds number mainly for a wide gap co-rotating cylinders as the Reynolds number is increased, much like that observed in the case of spiral-Couette flow by [8]. The linear transient growth of perturbation energy and the shape of optimal perturbation was studied by [9] and [10]. It is shown in particular that the yield stress reduces strongly the transient growth.
A numerical simulation of Taylor Couette flow of Bingham fluids was performed by [11], in the case of a wide gap : the radius ratio $\eta = R_1/R_2 = 0.5$. To overcome the discontinuity in Bingham's constitutive equation, a regularization procedure is used and Papanastasiou model is adopted [12]. It is found that when the outer cylinder is fixed, the intensity of vortex flow decreases with increasing the yield stress. However, for the co-rotation situation, the vortex flow is initially strengthened with an increase of yield stress, and then weakened as the yield stress is raised large enough.
This article is organized as follows. In §2 we formulate the physical problem, state the governing equations and define the dimensionless parameters. The velocity and viscosity profiles of the base state are discussed and the disturbance equations are derived. Subsequently, the linearization of the disturbance equations and the eigenvalue problem derivation for the linear stability analysis are presented in §3. In §4, the weakly nonlinear scheme based on multiple scales method is described in detail as well as the method to

derive the Ginzburg-Landau equation and to obtain the first Landau constant. We focus mainly on the situation where a static layer is attached to the outer wall. Section 5 presents and discusses the numerical results dealing with the influence of the Bingham number on the nature of the primary bifurcation and the flow structure. Finally, §6 summarizes the salient concluent of the present study.

## 4.2 Problem formulation

We consider the flow between two infinitely long concentric cylinders with inner and outer radii, $\hat{R}_1$ and $\hat{R}_2$ that rotate independently with angular velocity speed $\hat{\Omega}_1$ (inner) and $\hat{\Omega}_2$ (outer). The scaled momentum and mass conservation equations are

$$\partial_t \boldsymbol{U} + Re_1 \left(\boldsymbol{\nabla U}\right) \cdot \boldsymbol{U} = -\boldsymbol{\nabla} P + \boldsymbol{\nabla} \cdot \boldsymbol{\tau} \tag{4.1}$$

$$\boldsymbol{\nabla} \cdot \boldsymbol{U} = 0, \tag{4.2}$$

where $\boldsymbol{U}$ is the velocity, P the pressure, $\boldsymbol{\tau}$ the deviatoric stress tensor, and $Re_1$ is the inner cylinder Reynolds number :

$$Re_1 = \frac{\hat{\rho}\hat{R}_1\hat{\Omega}_1\hat{d}}{\hat{\mu}_p}\,. \tag{4.3}$$

Here $\hat{\rho}$ and $\hat{\mu}_p$ are the density and the plastic viscosity. The velocity vector is of the form $\boldsymbol{U} = U\boldsymbol{e}_r + V\boldsymbol{e}_\theta + W\boldsymbol{e}_z$, where $U$, $V$, $W$ are the velocity components and $\boldsymbol{e}_r$, $\boldsymbol{e}_\theta$, $\boldsymbol{e}_z$ are unit vectors in the radial ($r$), azimuthal ($\theta$) and axial ($z$) directions. Lengths are scaled with the annular gap $\hat{d} = \hat{R}_2 - \hat{R}_1$. The velocities are scaled with $\hat{\Omega}_1\hat{R}_1$ (velocity of the inner cylinder). The time is scaled with the viscous diffusion time $\hat{\rho}\,\hat{d}^2/\hat{\mu}_p$. The pressure and stresses are scaled with $\hat{\mu}_p\hat{R}_1\hat{\Omega}_1/\hat{d}$. By convention, we take $\hat{\Omega}_1 > 0$.
Using Von Mises yield criterion, the dimensionless constitutive equations for Bingham fluids are :

$$\tau_{ij} = \left(1 + \frac{B}{\dot{\gamma}}\right)\dot{\gamma}_{ij} \qquad \Longleftrightarrow \qquad \tau > B \tag{4.4}$$

$$\dot{\gamma} = 0 \qquad \Longleftrightarrow \qquad \tau \leq B, \tag{4.5}$$

where $\dot{\gamma} = \sqrt{\dot{\gamma}_{ij}\dot{\gamma}_{ij}/2}$ and $\tau = \sqrt{\tau_{ij}\tau_{ij}/2}$ are the second invariant of the strain rate $\dot{\boldsymbol{\gamma}}$ and deviatoric stress $\boldsymbol{\tau}$ tensors respectively. The components of $\dot{\boldsymbol{\gamma}}$ are $\dot{\gamma}_{ij} = U_{i,j} + U_{j,i}$. The Bingham number $B$ is defined as

$$B = \frac{\hat{\tau}_y\,\hat{d}}{\hat{\mu}_p\hat{R}_1\hat{\Omega}_1}\,, \tag{4.6}$$

which represents the ratio of the yield stress $\hat{\tau}_y$ to a nominal viscous stress $\hat{\mu}_p\hat{R}_1\hat{\Omega}_1/\hat{d}$. In the regions where the yield stress is not exceeded, the rate of strain tensor is identically zero (i.e. no local deformation occurs) and the stress tensor is undetermined. The fluid

within these regions is constrained to move as a rigid body and will be hereinafter referred to as "plug region".
Two further dimensionless parameters will be used : the outer Reynolds number $Re_2$ and the radius ratio $\eta$ :

$$Re_2 = \frac{\hat{\rho}\hat{R}_2\hat{\Omega}_2\hat{d}}{\hat{\mu}_p}\,, \quad \eta = \frac{\hat{R}_1}{\hat{R}_2}\,. \tag{4.7}$$

### 4.2.1 Basic flow

The base Couette flow velocity, $\boldsymbol{U}_b = (0, V_b(r), 0)$, is derived from

$$0 = \frac{1}{r^2}\frac{d}{dr}\left(r^2\tau_{r\theta}\right)\,, \quad r \in \left[\frac{\eta}{1-\eta}, \frac{1}{1-\eta}\right] \tag{4.8}$$

$$\tau_{r\theta} = \left[1 + \frac{B}{|\dot{\gamma}_{r\theta}|}\right]\dot{\gamma}_{r\theta} \qquad \Longleftrightarrow \qquad |\tau_{r\theta}| > B \tag{4.9}$$

$$|\dot{\gamma}_{r\theta}| = 0 \qquad \Longleftrightarrow \qquad |\tau_{r\theta}| \leq B\,, \tag{4.10}$$

$$\dot{\gamma}_{r\theta} = \frac{dV_b}{dr} - \frac{V_b}{r}\,, \tag{4.11}$$

with boundary conditions :

$$V_b = 1 \qquad \text{at} \qquad r = R_1 = \frac{\eta}{1-\eta}\,, \tag{4.12}$$

$$V_b = \frac{Re_2}{Re_1} \qquad \text{at} \qquad r = R_2 = \frac{1}{1-\eta}\,. \tag{4.13}$$

The basic flow equations are fully determined by the set of parameters $B$, $\eta$ and $Re_2/Re_1$. From equation (4.8)

$$\tau_{r\theta} = \frac{\tau_i\,\eta^2}{r^2\,(1-\eta)^2} \qquad \text{where} \qquad \tau_i = \tau_{r\theta}(r = R_1)\,. \tag{4.14}$$

Therefore $\tau_{r\theta}$ does not change sign in the annulus and $|\tau_{r\theta}|$ decreases with $r$. Consequently, if there is an unyielded plug region in the annulus, it must be bounded inside by a yield surface, say at $r = R_y$, and must extend to the outer wall. The position of $R_y$ is defined by $|\tau_{r\theta}| = B$ :

$$R_y = \frac{\eta}{1-\eta}\sqrt{\frac{|\tau_i|}{B}} \tag{4.15}$$

The base solutions are of three types : (1) the inner and the outer cylinders rotate with the same angular velocity, the fluid is fully unyielded in the annular gap ; (ii) there may be a layer of unyielded fluid attached to the outer wall ; (iii) the fluid may be fully yielded through the annular gap. The regions where the three solutions may be found can be

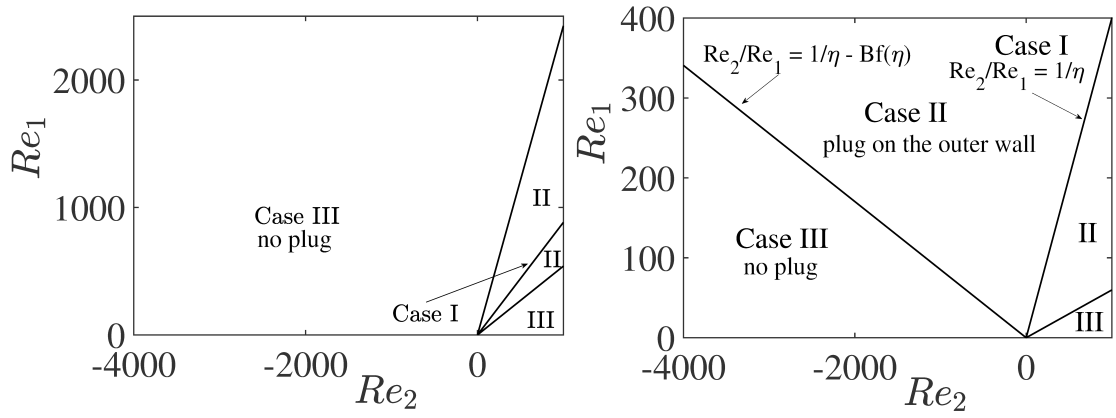


FIGURE 4.1 – Flow regimes in the plane $(Re_2, Re_1)$ at $B = 5$ : **(a)** narrow gap $\eta = 0.881$ and **(b)** wide gap $\eta = 0.4$ .

visualized in the plane $(Re_1, Re_2)$. Fully unyielded flows are found along the line

$$Re_1 = \eta Re_2 \,. \tag{4.16}$$

Partially yielded flows are found in the domains bounded by the above line and the lines

$$\frac{Re_2}{Re_1} = \frac{1}{\eta} \pm B\, f(\eta) \tag{4.17}$$

where $f\,(\eta)$ is defined by

$$f(\eta) = \frac{1+\eta}{2\eta^2} - \frac{ln(1/\eta)}{1-\eta} \tag{4.18}$$

As an example, figure 4.1 shows the domains where the three solutions hold in the plane $(Re_2, Re_1)$ in the case of a narrow gap $\eta = 0.881$ and a wide gap $\eta = 0.4$. The Bingham number is fixed $B = 5$. Additional calculations done at $\eta = 0.75$ and $B = 10$ are in very good agreement with [7]. In the case II of base solutions, the effective viscosity increases from the inner wall and tends to infinity as $r \to R_y$. In the domain of the plane $(Re_2, Re_1)$ where the fluid is fully yielded and partially yielded, the velocity profile $V_b(r)$ is given by

$$V_b(r) = \begin{cases} \dfrac{Re_2}{Re_1}\dfrac{r}{R_2} + \dfrac{\tau_i R_1^2}{2} r \left[\dfrac{1}{R_0^2} - \dfrac{1}{r^2}\right] + Br \ln\left(\dfrac{R_0}{r}\right) sgn(\tau_i) & R_1 \le r \le R_0 \\ \dfrac{Re_2}{Re_1}\dfrac{r}{R_2} & R_0 \le r \le R_2 \,, \end{cases} \tag{4.19}$$

where $R_0 = min(R_y, R_2)$. An illustration of basic velocity profiles $V_b(r)$ at different values of $B$ in the case of co-rotating ($Re_1 = 1000$, $Re_2 = 100$) and counter-rotating cylinders ($Re_1 = 1000$, $Re_2 = -100$) for a narrow and a wide gap is given by figure 4.2. The position $R_y$ of the yield surface is indicated by a vertical dotted line. In the static layer ($R_y \le r \le R_2$), $V_b$ varies linearly with $r$. The nonlinear variation of the viscosity $\mu = 1 + B/\dot{\gamma}$ in the

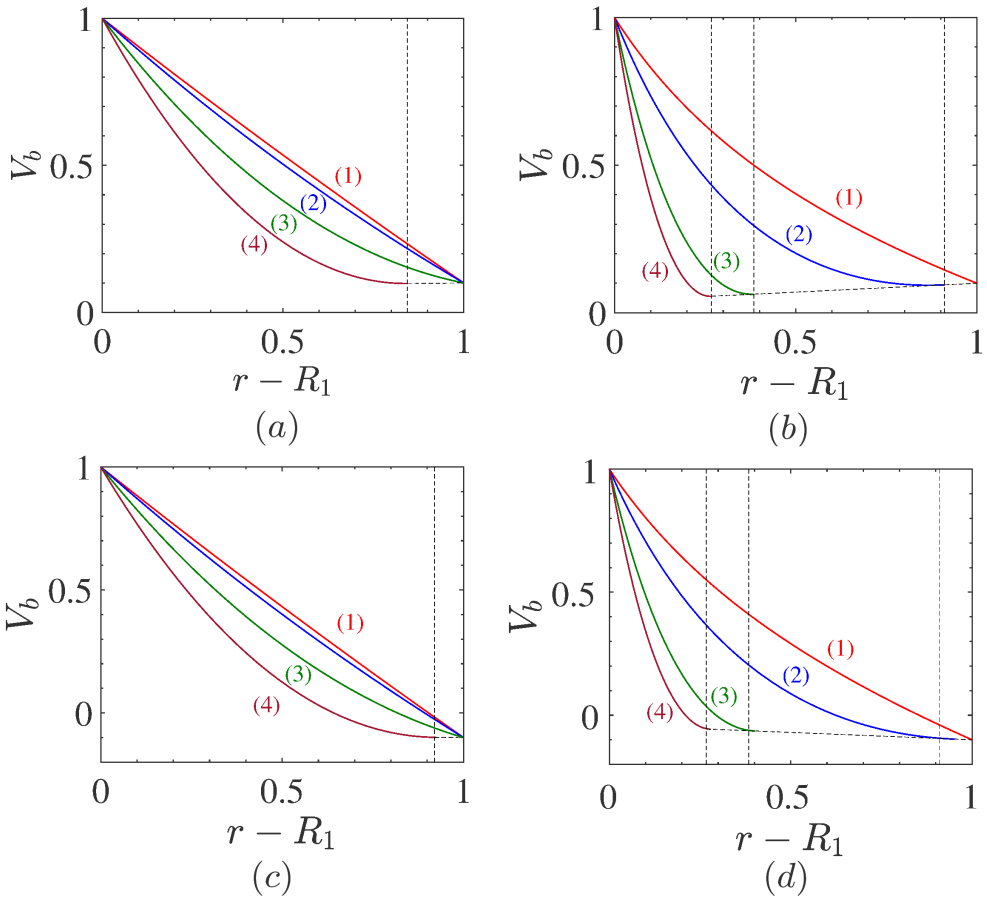


FIGURE 4.2 – Basic velocity profiles, $V_b(r)$. Case of corotating cylinders with $Re_2 = 100; Re_1 = 1000$ for **(a)** $\eta = 0.881$ and **(b)** $\eta = 0.4$. Case of counter-rotating cylinders with $Re_2 = -100; Re_1 = 1000$ for **(c)** $\eta = 0.881$ and (d) $\eta = 0.4$ : (1) $B = 0$, (2) $B = 1$, (3) $B = 5$, (4) $B = 10$.

yielded zone is shown in figure 4.3. According to Bingham model, $\mu$ increases from the inner wall and tends to infinity near the yield surface. The degree of nonlinearity of the rheological behavior becomes stronger with increasing $B$.

### 4.2.2 Perturbation equations

We consider the perturbation of the basic flow $(\boldsymbol{U}_b, P_b)$ :

$$\boldsymbol{U}_b = (0, V_b(r), 0)\,, \quad P_b(r) = Re_1 \int^r \frac{V_b^2(r)}{r} \mathrm{d}r + constant \tag{4.20}$$

by a small disturbance

$$\boldsymbol{u}(r, \theta, z, t), \quad p = P(r, \theta, z, t) \tag{4.21}$$

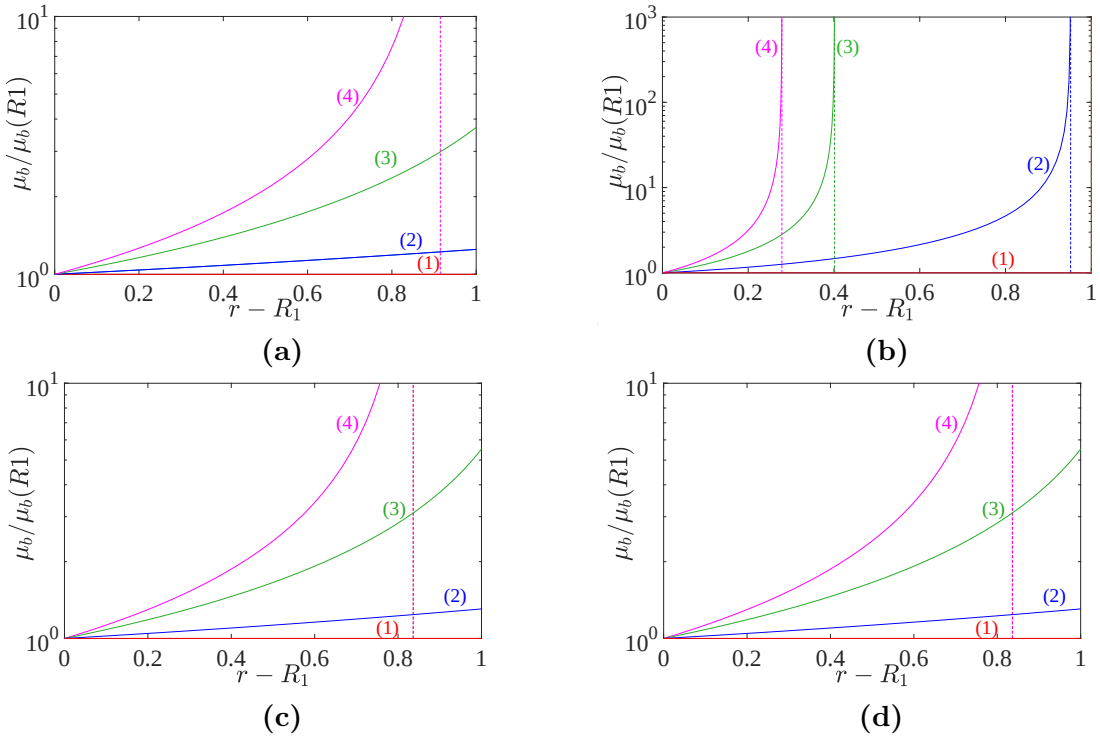


FIGURE 4.3 – Basic viscosity, $\mu_b(r)$. Case of corotating cylinders with $Re_2 = 100; Re_1 = 1000$ for **(a)** $\eta = 0.881$ and **(b)** $\eta = 0.4$. Case of counter-rotating cylinders with $Re_2 = -100; Re_1 = 1000$ for **(c)** $\eta = 0.881$ and (d) $\eta = 0.4$ : (1) $B = 0$, (2) $B = 1$, (3) $B = 5$, (4) $B = 10$.

The perturbation equations in the yielded parts of the flow are straightforwardly derived :

$$\boldsymbol{\nabla} \cdot \boldsymbol{u} = 0\,, \tag{4.22}$$

$$\frac{\partial \boldsymbol{u}}{\partial t} = \boldsymbol{\mathcal{L}}(\boldsymbol{u}, p) + \boldsymbol{\mathcal{N}}(\boldsymbol{u})\,. \tag{4.23}$$

The operator $\boldsymbol{\mathcal{L}}(\boldsymbol{u}, p)$ denotes the linear part of the perturbation equations, which consists of 4 parts :

$$\boldsymbol{\mathcal{L}}(\boldsymbol{u}, p) = Re_1 \boldsymbol{\mathcal{LI}}(\boldsymbol{u}) - \boldsymbol{\nabla} p + \boldsymbol{\mathcal{LV}}(\boldsymbol{u}) + B\boldsymbol{\mathcal{LY}}(\boldsymbol{u}) \tag{4.24}$$

describing inertial, pressure, viscous and yield stress effects. The inertial, pressure and viscous operators are identical with those for a Newtonian fluid :

$$\boldsymbol{\mathcal{LI}}(\boldsymbol{u}) = -\left[(\boldsymbol{U}_b \cdot \boldsymbol{\nabla})\,\boldsymbol{u} + (\boldsymbol{u} \cdot \boldsymbol{\nabla})\,\boldsymbol{U}_b\right]\,, \tag{4.25}$$

$$\boldsymbol{\mathcal{LV}}(\boldsymbol{u}) = \boldsymbol{\nabla} \cdot \dot{\boldsymbol{\gamma}}\,. \tag{4.26}$$

The yield stress term is adressed below along with the nonlinear parts. The terms in $\boldsymbol{\mathcal{N}}$ are significant for nonlinear perturbations. This includes contribution from the inertial terms and from perturbations of shear-stress tensor, where only the yield stress contributions are nonlinear. This can be written as :

$$\boldsymbol{\mathcal{N}}(\boldsymbol{u}) = Re_1 \boldsymbol{\mathcal{NI}}(\boldsymbol{u}) + B\boldsymbol{\mathcal{NY}}(\boldsymbol{u})\,, \tag{4.27}$$

where,

$$\boldsymbol{\mathcal{NI}}\,(\boldsymbol{u}) = -\,(\boldsymbol{u} \cdot \boldsymbol{\nabla})\,\boldsymbol{u}\,. \tag{4.28}$$

### 4.2.3 Yield-stress terms

The components of the shear-stress tensor can be written as :

$$\tau_{ij} = \dot{\gamma}_{ij} + BM_{ij}\,. \tag{4.29}$$

In a part of the fluid where the yield stress is not exceeded, $\tau_{ij}$ are indeterminate. In a part of the fluid, where the yield stress is exceeded, the $M_{ij}$ is given by

$$M_{ij} = \frac{\dot{\gamma}_{ij}}{\dot{\gamma}}\,. \tag{4.30}$$

The contributions to the yield stress in the perturbation equations all come from the expressions, $M_{ij}\,(\boldsymbol{U}_b + \boldsymbol{u}) - M_{ij}\,(\boldsymbol{u})$, which for small finite $\boldsymbol{u}$, can be expressed about the base flow in a Taylor series :

$$M_{ij}\,(\boldsymbol{U}_b + \boldsymbol{u}) - M_{ij}\,(\boldsymbol{U}_b) = m1_{ij}(\boldsymbol{u}) + m2_{ij}(\boldsymbol{u}, \boldsymbol{u}) + m3_{ij}\,(\boldsymbol{u}, \boldsymbol{u}, \boldsymbol{u})\,, ... \tag{4.31}$$

The terms in $mk_{ij}$ contain products of $k$ components of $\boldsymbol{u}$. For $k = 1, 2, 3...$, where,

$$m1_{ij} = \frac{\dot{\gamma}_{ij}(\boldsymbol{u})}{\dot{\gamma}(\boldsymbol{U}_b)} - \frac{\dot{\gamma}_{ij}(\boldsymbol{U}_b)}{2\dot{\gamma}^3(\boldsymbol{U}_b)} \sum_{\ell m} \dot{\gamma}_{\ell m}(\boldsymbol{u})\dot{\gamma}_{\ell m}(\boldsymbol{U}_b)\,, \tag{4.32}$$

$$\begin{aligned} m2_{ij} &= \frac{\dot{\gamma}_{ij}(\boldsymbol{U}_b)}{8} \sum_{k\ell}\sum_{mn} \dot{\gamma}_{k\ell}(\boldsymbol{u})\dot{\gamma}_{mn}(\boldsymbol{u}) \left[\frac{3\dot{\gamma}_{k\ell}(\boldsymbol{U}_b)\dot{\gamma}_{mn}(\boldsymbol{U}_b)}{\dot{\gamma}^5(\boldsymbol{U}_b)} - \frac{2}{\dot{\gamma}^3(\boldsymbol{U}_b)}\frac{\partial\dot{\gamma}_{k\ell}(\boldsymbol{U}_b)}{\partial\dot{\gamma}_{mn}(\boldsymbol{U}_b)}\right] \\ &\quad -\frac{\dot{\gamma}_{ij}(\boldsymbol{u})}{2} \sum_{\ell m} \frac{\dot{\gamma}_{\ell m}(\boldsymbol{u})\dot{\gamma}_{\ell m}(\boldsymbol{U}_b)}{\dot{\gamma}^3(\boldsymbol{U}_b)} \end{aligned} \tag{4.33}$$

$$\begin{aligned} m3_{ij} &= \frac{\dot{\gamma}_{ij}(\boldsymbol{u})}{8} \sum_{k\ell}\sum_{mn} \dot{\gamma}_{k\ell}(\boldsymbol{u})\dot{\gamma}_{mn}(\boldsymbol{u}) \left[\frac{3\dot{\gamma}_{k\ell}(\boldsymbol{U}_b)\dot{\gamma}_{mn}(\boldsymbol{U}_b)}{\dot{\gamma}^5(\boldsymbol{U}_b)} - \frac{2}{\dot{\gamma}^5(\boldsymbol{U}_b)}\frac{\partial\dot{\gamma}_{k\ell}(\boldsymbol{U}_b)}{\partial\dot{\gamma}_{mn}(\boldsymbol{U}_b)}\right] \\ &+ \frac{\dot{\gamma}_{ij}(\boldsymbol{U}_b)}{48} \sum_{k\ell}\sum_{mn}\sum_{ef} \dot{\gamma}_{k\ell}(\boldsymbol{u})\dot{\gamma}_{mn}(\boldsymbol{u})\dot{\gamma}_{ef}(\boldsymbol{u}) \left[-\frac{15\dot{\gamma}_{k\ell}(\boldsymbol{U}_b)\dot{\gamma}_{ef}(\boldsymbol{U}_b)}{\dot{\gamma}^7(\boldsymbol{U}_b)}\right. \\ &+ \left.\frac{6}{\dot{\gamma}^8(\boldsymbol{U}_b)}\left(\frac{\partial\dot{\gamma}_{k\ell}}{\partial\dot{\gamma}_{mn}}(\boldsymbol{U}_b)\dot{\gamma}_{ef}(\boldsymbol{U}_b) + \frac{\partial\dot{\gamma}_{ef}}{\partial\dot{\gamma}_{mn}}(\boldsymbol{U}_b)\dot{\gamma}_{ef}(\boldsymbol{U}_b) + \frac{\partial\dot{\gamma}_{mn}}{\partial\dot{\gamma}_{ef}}(\boldsymbol{U}_b)\dot{\gamma}_{k\ell}(\boldsymbol{U}_b\right)\right] \end{aligned} \tag{4.34}$$

For clarity, we have made the summations above explicite. For the specific base flow that we have, where only $\dot{\gamma}_{r\theta}(\boldsymbol{U}_b) \neq 0$, some simplifications are done :

$$m1_{ij} = 0, \qquad ij = r\theta, \theta r \tag{4.35}$$

$$m1_{ij} = \frac{\dot{\gamma}_{ij}(\boldsymbol{u})}{\dot{\gamma}(\boldsymbol{U}_b)} \qquad ij \neq r\theta, \theta r \tag{4.36}$$

$$m2_{ij} = \frac{sgn(\dot{\gamma}_{r\theta}(\boldsymbol{U})_b)}{2\dot{\gamma}^2(\boldsymbol{U}_b)} \left[\dot{\gamma}^2_{r\theta}(\boldsymbol{u}) - \dot{\gamma}^2(\boldsymbol{u})\right] \qquad ij = r\theta, \theta r \tag{4.37}$$

$$m2_{ij} = -\frac{sgn\left(\dot{\gamma}_{r\theta}(\boldsymbol{U}_b)\right)}{\dot{\gamma}^2(\boldsymbol{U}_b)} \dot{\gamma}_{ij}(\boldsymbol{u})\dot{\gamma}_{r\theta}(\boldsymbol{u}) \qquad ij \neq r\theta, \theta r \tag{4.38}$$

$$m3_{ij} = \frac{\dot{\gamma}_{r\theta}\left(\boldsymbol{u}\right)}{\left[\dot{\gamma}(\boldsymbol{U}_b)\right]^3} \left[\dot{\gamma}^2(\boldsymbol{u}) - \dot{\gamma}^2_{r\theta}(\boldsymbol{u})\right] \qquad ij = r\theta, \theta r \tag{4.39}$$

$$m3_{ij} = \frac{1}{2\left[\dot{\gamma}(\boldsymbol{U}_b)\right]^3} \left[\frac{3}{2}\dot{\gamma}^2_{r\theta}(\boldsymbol{u}) - \dot{\gamma}^2(\boldsymbol{u})\right] \dot{\gamma}_{ij}(\boldsymbol{u}) \qquad ij \neq r\theta, \theta r \tag{4.40}$$

In terms of $mk_{ij}$, $k = 1, 2, 3$, we may now define the linear and non linear Bingham perturbation terms as follows :

$$\boldsymbol{\mathcal{LY}} = \boldsymbol{\nabla} \cdot \boldsymbol{m1} = \begin{pmatrix} \mathcal{LY}_r \\ \mathcal{LY}_\theta \\ \mathcal{LY}_z \end{pmatrix} = \begin{pmatrix} \frac{1}{r}\frac{\partial}{\partial r}\left(rm1_{rr}\right) + \frac{\partial}{\partial z}m1_{rz} - \frac{m1_{\theta\theta}}{r} \\ \frac{1}{r}\frac{\partial}{\partial\theta}m1_{\theta\theta} + \frac{\partial}{\partial z}m1_{\theta z} \\ \frac{1}{r}\frac{\partial}{\partial r}\left(rm1_{rz}\right) + \frac{1}{r}\frac{\partial}{\partial\theta}m1_{\theta z} + \frac{\partial}{\partial z}m1_{zz}. \end{pmatrix} \tag{4.41}$$

and

$$\boldsymbol{\mathcal{N}\mathcal{Y}} = \boldsymbol{\nabla}\cdot\boldsymbol{mk} = \begin{pmatrix}\mathcal{L}\mathcal{Y}_r\\ \mathcal{L}\mathcal{Y}_\theta\\ \mathcal{L}\mathcal{Y}_z\end{pmatrix} = \begin{pmatrix}\frac{1}{r}\frac{\partial}{\partial r}\left(rmk_{rr}\right)+\frac{1}{r}\frac{\partial}{\partial\theta}mk_{r,\theta}+\frac{\partial}{\partial z}mk_{rz}-\frac{mk_{\theta\theta}}{r}\\ \frac{1}{r^2}\frac{\partial}{\partial r}\left(r^2mk_{r\theta}\right)+\frac{1}{r}\frac{\partial}{\partial\theta}mk_{\theta\theta}+\frac{\partial}{\partial z}mk_{\theta z}\\ \frac{1}{r}\frac{\partial}{\partial r}\left(rmk_{zr}\right)+\frac{1}{r}\frac{\partial}{\partial\theta}mk_{z\theta}+\frac{\partial}{\partial z}mk_{zz}.\end{pmatrix} \tag{4.42}$$

Note that the expressions for k = 1,2,3 are identical, except that $m1_{r\theta} = m1_{\theta r} = 0$.

## 4.3 Linear stability analysis

The basic flow is supposed to be perturbed by an infinitesimal disturbance. The linearized perturbation equations can be written formally as :

$$\boldsymbol{\nabla}\cdot\boldsymbol{u} = 0\,, \tag{4.43}$$

$$\frac{\partial\boldsymbol{u}}{\partial t} = Re_1\boldsymbol{\mathcal{L}\mathcal{I}}(\boldsymbol{u}) + \boldsymbol{\mathcal{L}\mathcal{V}}(\boldsymbol{u}) + B\boldsymbol{\mathcal{L}\mathcal{Y}}(\boldsymbol{u})\,. \tag{4.44}$$

### 4.3.1 Boundary conditions

If the fluid is fully yielded in all the annular space (case III in Fig. 4.1), the no-slip conditions at both walls are imposed :

$$\boldsymbol{u} = 0 \qquad \text{at} \qquad r = R_1 \tag{4.45}$$

$$\boldsymbol{u} = 0 \qquad \text{at} \qquad r = R_2. \tag{4.46}$$

If the fluid is partially yielded (case II figure. 4.1), in the region where the yield stress is exceeded, the components of the deviatoric stress tensor are assumed linearly perturbed and $|M_{ij}(\boldsymbol{U}_b+\boldsymbol{u}) - M_{ij}(\boldsymbol{U}_b)| = |m1_{ij}(\boldsymbol{u})|$. Therefore, it can be assumed that the yield surface will be also linearly perturbed from its initial position $R_0$ :

$$R_y = R_0 + h \qquad \text{with} \qquad h << 1\,. \tag{4.47}$$

The continuity of the velocity components at the yield surface $R_y$ gives

$$(\boldsymbol{U}_b+\boldsymbol{u})\left([R_0+h]^-\,,z,t\right) = (\boldsymbol{U}_b+\boldsymbol{u})\left([R_0+h]^+\,,z,t\right)\,, \tag{4.48}$$

Where the superscripts $\pm$ indicate that the limit is taken from each side of the yield surface. Since $\boldsymbol{u} = 0$ uniformly in the plug zone, the linearization of the boundary conditions at the yielded side reads

$$\boldsymbol{u} = 0 \qquad \text{at} \qquad r = R_0\,. \tag{4.49}$$

Additional conditions arise from the continuity of the stress components at the perturbed yield surface ([13], [14], [7], [15]). This results in :

$$\dot{\gamma}_{rr}(\boldsymbol{u}) = \dot{\gamma}_{\theta\theta}(\boldsymbol{u}) = \dot{\gamma}_{zz}(\boldsymbol{u}) = 0 \qquad \text{at} \qquad r = R_0\,, \tag{4.50}$$

$$\dot{\gamma}_{rz}(\boldsymbol{u}) = \dot{\gamma}_{\theta z}(\boldsymbol{u}) = 0 \qquad \text{at} \qquad r = R_0\,, \tag{4.51}$$

$$\dot{\gamma}_{r\theta}(\boldsymbol{u}) = \frac{2hBsgn(\tau_i)}{R_0} \qquad \text{at} \qquad r = R_0\,. \tag{4.52}$$

These conditions are not strictly boundary conditions. Instead (4.50) & (4.51) are compatibility conditions. Indeed, each $\dot{\gamma}_{ij}(\boldsymbol{u})$ in (4.50) & (4.51) also appears in the Bingham terms (4.36) divided by $\dot{\gamma}(\boldsymbol{U}_b)$. Conditions (4.50) & (4.51) are therefore necessary conditions for the linear stability equations to be well defined as $r \to R_0^-$. One may observe that (4.52) is not required for compatibility, instead it defines the perturbation of the yield surface $h$. Note also that the yield surface is not a material surface or interface, so there is no kinematic condition.
Lastly, note for the case I basic flow, the finite plug that fills the annulus cannot be perturbed by an infinitesimal perturbation. Therefore, in this case there is no linear stability problem.

### 4.3.2 Normal mode approach

The perturbation is assumed periodic and of the form

$$(u, v, w, p, h) = (u(r,t), v(r,t), w(r,t), p(r,t), h(t))e^{i(m\theta+kz)}\,, \tag{4.53}$$

where $m$ (integer) and $k$ (real) are the azimuthal and the axial wavenumber respectively. The perturbation equations in terms of the complex amplitude $\boldsymbol{u} = (u, v, w, p)$ are

$$D_* u + \frac{imv}{r} + ikw = 0\,, \tag{4.54}$$

$$\frac{\partial u}{\partial t} = -Dp - Re_1 \frac{V_b}{r}(imu - 2v) + \left(DD_* - k^2 - \frac{m^2}{r^2}\right)u + B\Phi_r \tag{4.55}$$

$$\frac{\partial v}{\partial t} = -\frac{imp}{r} - Re_1\left(uD_*V_b + imv\frac{V_b}{r}\right) + \left(DD_* - k^2 - \frac{m^2}{r^2}\right)u + \frac{2imu}{r^2} + B\Phi_\theta \tag{4.56}$$

$$\frac{\partial w}{\partial t} = -ikp - Re_1 im\frac{V_b}{r}w + \left(DD_* - k^2 - \frac{m^2}{r^2}\right)w + B\Phi_z\,, \tag{4.57}$$

where

$$\Phi_r = \frac{2}{r} D\left(\frac{rDu}{\dot{\gamma}_b}\right) + \frac{1}{\dot{\gamma}_b}\left(ikDw - k^2 u - \frac{2\left(imv + u\right)}{r^2}\right) \tag{4.58}$$

$$\Phi_\theta = \frac{1}{\dot{\gamma}_b}\left[\frac{2\left(imu - m^2 v\right)}{r^2} - \frac{kmw}{r} - k^2 v\right], \tag{4.59}$$

$$\Phi_z = \frac{1}{r} D\left(\frac{r\left(iku + Dw\right)}{\dot{\gamma}_b}\right) - \frac{1}{\dot{\gamma}_b}\left(\frac{m^2 w}{r^2} + \frac{kmv}{r} + 2k^2 w\right). \tag{4.60}$$

In the above equations, $D = d(.)/dr$ and $D_* = d(.)/dr + (.)/r$.
If the fluid is fully yielded in all the annular space, the boundary conditions are :

$$u = v = w = 0 \qquad \text{at} \qquad r = R_1, R_2\,. \tag{4.61}$$

If the fluid is partially yielded, the boundary conditions are

$$u = v = w = 0 \qquad \text{at} \qquad r = R_1, R_0 \tag{4.62}$$

We have also to add the compatibility conditions at the yield surface as well as the associated equation to its perturbation $h$ :

$$Du = Dw = 0 \qquad \text{at} \qquad r = R_0\,, \tag{4.63}$$

$$Dv = -hD^2 V_b \qquad \text{at} \qquad r = R_0\,. \tag{4.64}$$

In the usual fashion, we consider a normal mode approach and we assume the solution of the form

$$(u, v, w, p, h) = (U_{11}(r), V_{11}(r), W_{11}(r), P_{11}(r), H_{11})\, e^{st}\,. \tag{4.65}$$

The initial value problem (4.55-4.57) is transformed into a generalized eigenvalue problem, where the complex frequency $s$ is the eigenvalue. Its real part is the growth rate of the perturbation and its imaginary part is its oscillation frequency. The eigenvalue value problem can be re-written in terms of $u$ and $v$ if $k \neq 0$ or in terms of $u$ and $w$ if $m \neq 0$. The spatial discretization is achieved through a standard Chebyshev spectral collocation method [16]. At a fixed $Re_2$, the critical values of the axial wavenumber $k$ and the azimuthal wavenumber $m$ are associated with the minimum value of $Re_1$ for which $s_{r,max} = 0$ with an accuracy of $10^{-4}$. The numerical computations were validated by comparison with [9, 10, 7]

### 4.3.3 Results

Examples of marginal stability curves in the plane ($Re_2$, $Re_1$) are shown in figures 4.4 and 4.5 for a narrow ($\eta = 0.881$) and a wide gap ($\eta = 0.4$). The marginal stability curves are above the rigid rotation line $Re_1 = \eta Re_2$ (line I in figure 4.5). The transition

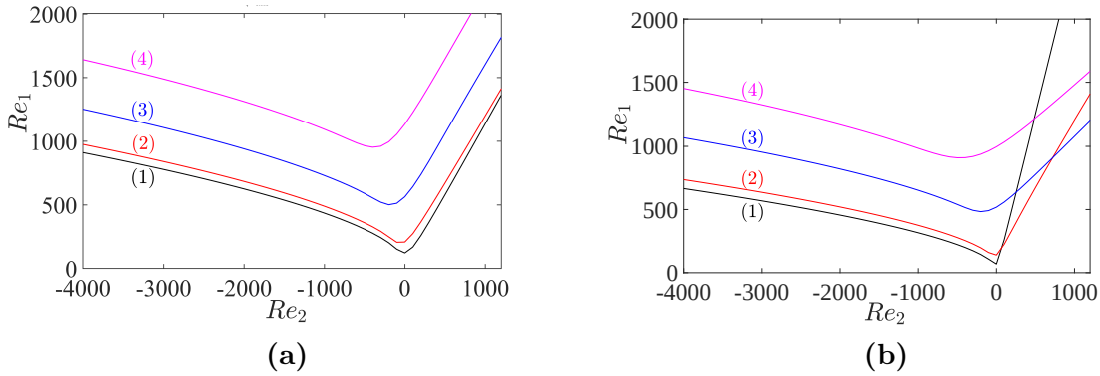


FIGURE 4.4 – Marginal stability curves at (a) $\eta = 0.883$ and (b) $\eta = 0.4$. Effect of Bingham number : (1) $B = 0$, (2) $B = 1$, (3) $B = 5$ and (4) $B = 10$

is smooth along the marginal stability curve between the base flows III (fully yielded) and II (partially yielded). The minimum of the marginal stability curves moves slightly towards counter-rotating cylinders as $B$ increases. By comparison between figures 4.4(a) and 4.4(b), it can be observed that for the same value of $B$ and $Re_2$, the value of $Re_{1c}$ for $\eta = 0.883$ is much greater than that for $\eta = 0.4$. Actually as the gap between cylinders decreases, the azimuthal velocity profile approaches that of a plane Couette flow, which is linearly stable.

In the case of counter-rotating cylinders, the critical Reynolds number $Re_{1c}$ increases monotonically with increasing Bingham number for a narrow and for a wide gap. However for co-rotating cylinders, a nonmonotonicity of $Re_{1c}$ is observed. For a narrow gap, and from $Re_2 = 2000$, the yield stress has a destabilizing effect. Indeed, it can be observed in figure 4.4(a) that $Re_c(B = 0) > Re_c(B = 1)$. This behavior appears more earlier for a wide gap. Indeed for $\eta = 0.4$, when $Re_2 > 80$, we have $Re_{1c}(B = 0) > Re_{1c}(B = 1)$ and from $Re_2 > 700$, $Re_{1c}(B = 1) > Re_{1c}(B = 5)$. It is the only one situation where the yield stress has a destabilizing effect. This result was first observed by [17] and [8]. An explanation based on the energy equation was proposed by [7]. Globally, the destabilizing effect corresponds to the situation where the production term in the energy equation is amplified via the increase the strain-rate at the inner wall and dominates the increase of the viscous dissipation.

Concerning the critical azimuthal and axial wavenumbers (figure 4.6), for a narrow gap, in the co-rotating regime, the critical mode remains axisymmetric at least up to $Re_2 = 2000$, i.e. the primary bifurcation leads to stationary TVF. In the case of counter-rotating regime, the critical azimuthal wavenumber increases with $|Re_2|$. There is a limit $Re_{2\ell}$, under which the primary bifurcation leads to spiral vortices ($m_c > 1$). Spiral vortices are traveling waves in axial and azimuthal directions. It is worthy to note that with increasing the yield stress, the primary bifurcation is axisymmetric for a long range negative $Re_2$. The axial wavelength decreases with increasingly negative $Re_2$. This may be attributed to the decrease of the "effective gap" where the Rayleigh instability criterion holds, i.e. the

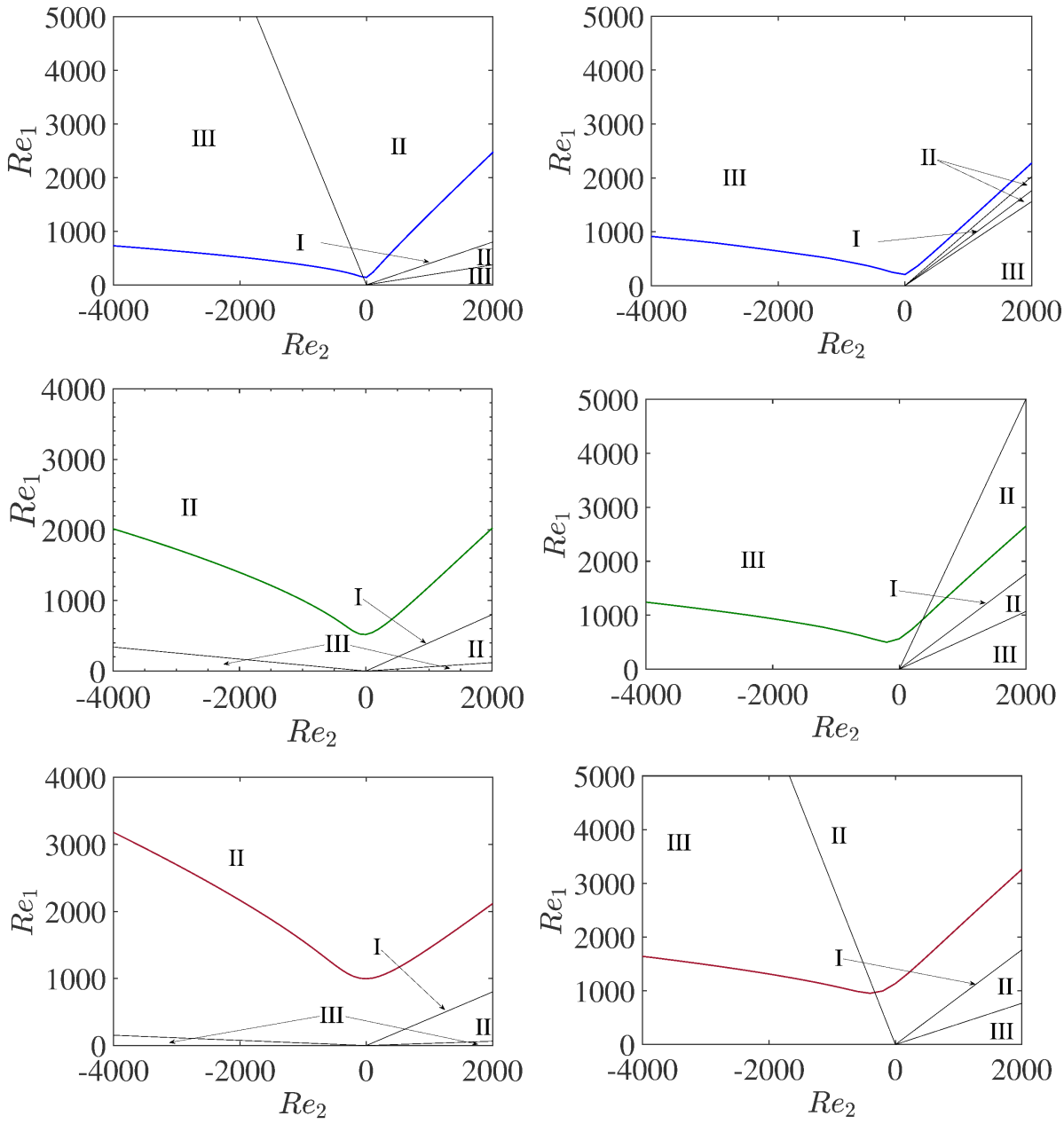


FIGURE 4.5 – Marginal stability curves with flow types for $\eta = 0.883$ (left frame and $\eta = 0.4$ (right frame) and three values of $B$ : 1, 5 and 10 from top to bottom.

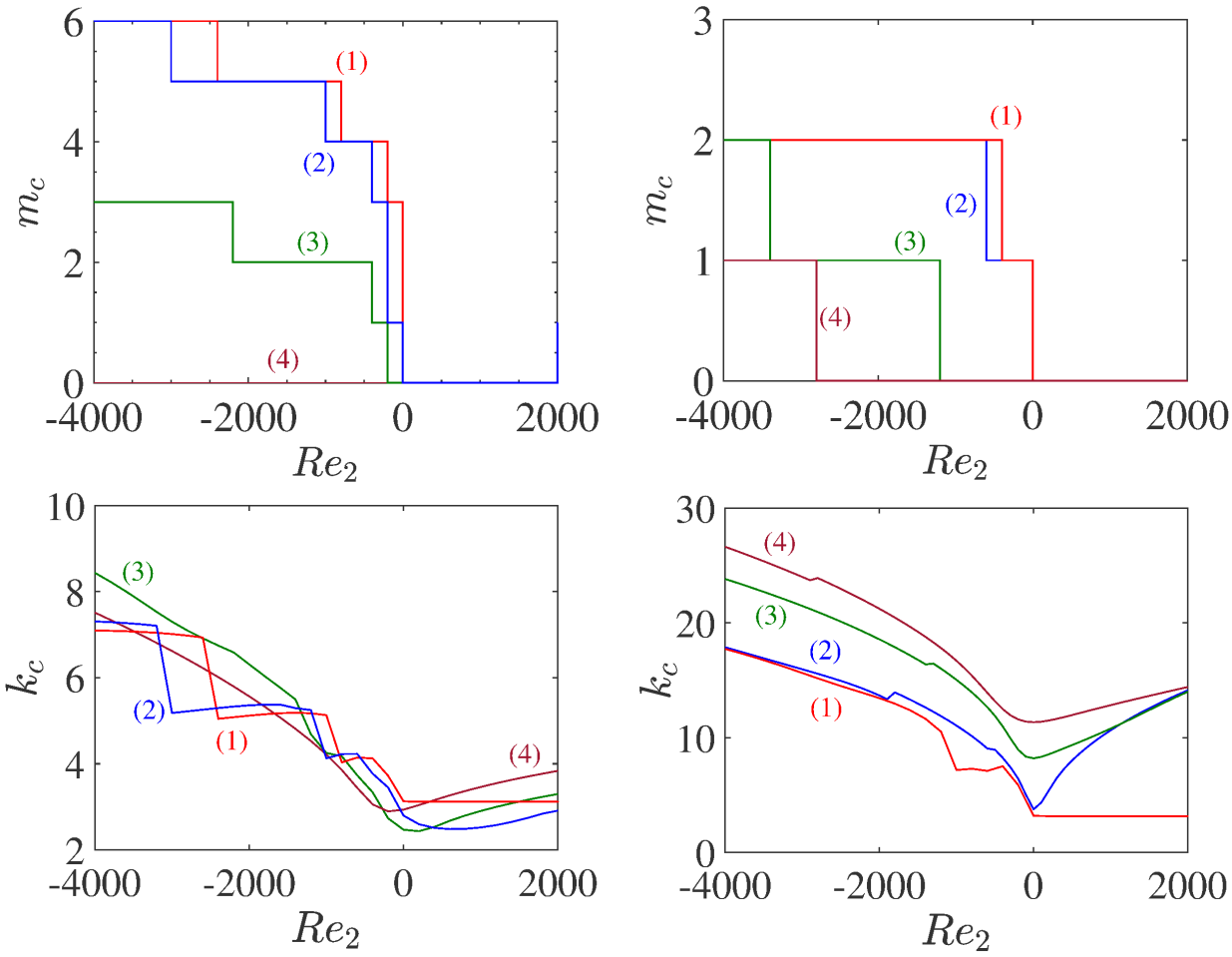


FIGURE 4.6 – Critical azimuthal and axial wave numbers for a Bingham fluid with two radius ratios $\eta = 0.883$ (figures on the left) and $\eta = 0.4$ (figures on the right). Effect of Bingham number : (1) $B = 0$, (2) $B = 1$, (3) $B = 5$ and (4) $B = 10$.

gap between the inner cylinder and the "nodal surface" where $V_b = 0$. Similar trends are observed for a wide gap, except that the axial wavelength is shorter and decreases significantly with increasing Bingham number. This is due to the appearance of a plug zone attached to the outer wall.

Some features of the critical mode are shown in figure 4.7 for Newtonian and Bingham fluids. We have represented isolines of constant $w$ on one wavelength. Positive and negative values of $w$ correspond to anticlockwise and clockwise rotation. It can be noted that the isolines are more concentrated near the inner wall with increasing Bingham number, indicating the presence of steep velocity gradient as well as an unaffected plug zone attached to the outer wall. In figure 4.8(a) we have represented the yield surface perturbations of the linear mode $\mathcal{R}eal(H_{11}E^1)$, in the case II of the base flow, for different values of Bingham number. Along the axial position, the minimum of $\mathcal{R}eal\left(H_{11}E^1\right)$ corresponds to the jet

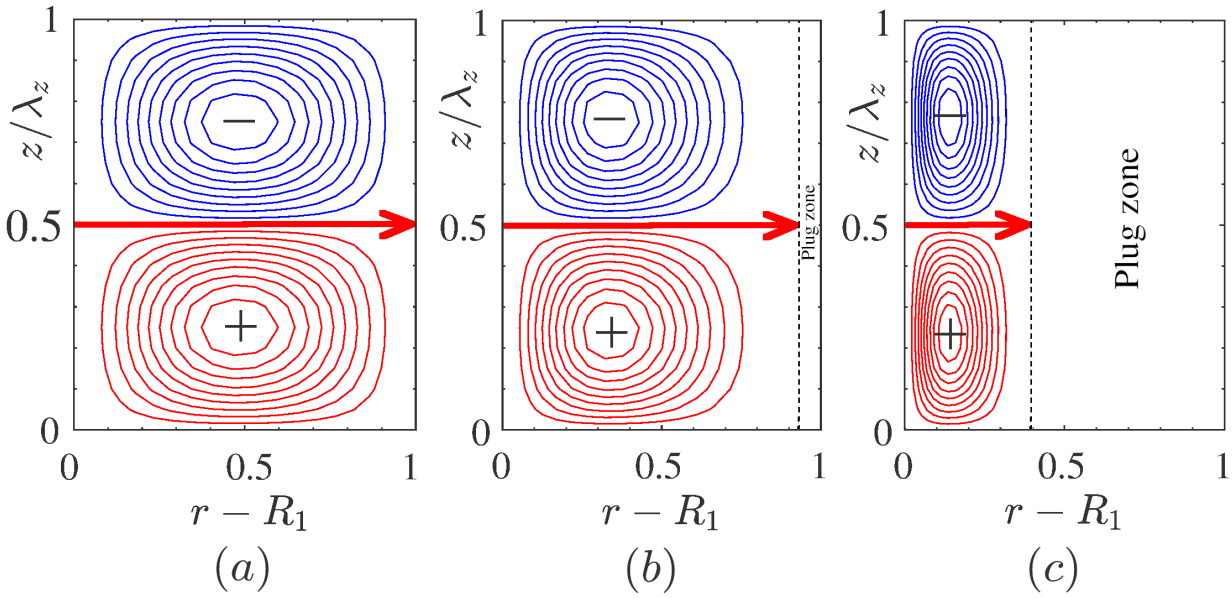


FIGURE 4.7 – Contours of iso-values of the axial velocity $w$ associated with the critical mode at $Re_2 = 0$, $\eta = 0.4$ for three values of Bingham numbers **(a)** $B = 0$, **(b)** $B = 1$, **(c)** $B = 5$. The arrows indicate the rotation direction of the rolls.

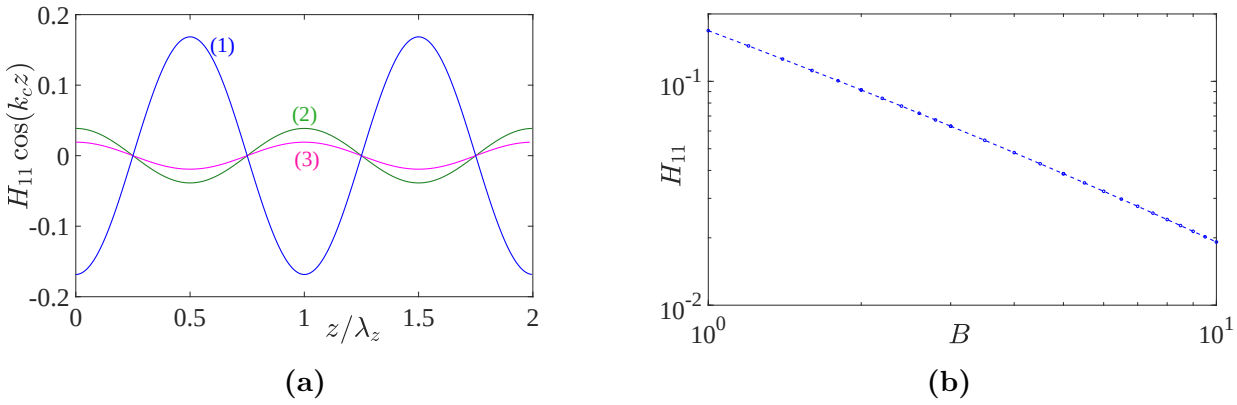


**(a)** **(b)**

FIGURE 4.8 – **(a)** Perturbation of the yield surface at the linear order at $\eta = 0.4$ and three different values of Bingham number. **(b)** Variation of $H_{11}$ as a function of $B$

impingement near the yield surface. The maximum of $\mathcal{R}eal\left(h_{11}E^1\right)$ corresponds to the radial flow from the outer to the inner cylinder. It can also be noticed in figure 4.8(b) that $H_{11}$ decreases significantly with Bingham number. For $\eta = 0.4$, we have $H_{11} \propto B^{-0.96}$.

## 4.4 Weakly nonlinear analysis

From here on we consider only axisymmetric disturbances. In this case, the continuity equation simplifies and is satisfied via introduction of a function $\phi$ such that

$$u = -\frac{\partial \phi}{\partial z} \quad \text{and} \quad w = \frac{1}{r}\frac{\partial}{\partial r}(r\phi)\,. \tag{4.66}$$

The pressure is eliminated by cross-differentiating the radial and axial momentum equations. Finally, the perturbation equations are written in terms of $\boldsymbol{f} = (\phi, v)^T$ as follows

$$\boldsymbol{\mathcal{C}}\frac{\partial \boldsymbol{f}}{\partial t} = \boldsymbol{L}\boldsymbol{f} + \boldsymbol{N}(\boldsymbol{f})\,, \tag{4.67}$$

where again $\boldsymbol{L}$ and $\boldsymbol{N}$ denote linear and nonlinear operators, respectively. They are splitted into inertial, viscous and yield stress parts as :

$$\boldsymbol{L} = Re_1 \boldsymbol{LI} + \boldsymbol{LV} + B\,\boldsymbol{LY}\,, \tag{4.68}$$

$$\boldsymbol{N} = Re_1\,\boldsymbol{NI} + B\,\boldsymbol{NY}\,. \tag{4.69}$$

### 4.4.1 Multiple scales method

As the Reynolds number is increased above the onset $Re_c$, the growth rate of the perturbation is positive for any wavenumber $k$ within a band $\sqrt{\epsilon}$ around the critical wavenumber, where $\epsilon = (Re - Re_c)/Re_c$ is the distance from the onset. Taylor expansion of the dispersion curve near its maximum shows that $s \propto \epsilon$ and $(k - k_c) \propto \sqrt{\epsilon}$. For $\epsilon > 0$, emergent patterns are described by a sum of unstable modes of the form $\exp(s\,t/\tau_0)\,\exp(i\,k_c z)\,\exp(i\sqrt{\epsilon}z/\xi_0)$, where $\tau_0$ is the characteristic time for the instability to grow and $\xi_0$ the coherence length. For small $\epsilon$, we can separate the dynamics into fast eigenmodes and slow modulation of the form $\exp(s\,\epsilon/\tau_0)$ and $\exp(i\sqrt{\epsilon}z)/\xi_0$. We denote $\delta = \sqrt{\epsilon}$. The multiple-scales approach is used to obtain the amplitude equation, which describes the slow temporal and spatial variation of the variables. The slow scales

$$Z = \delta\, z \quad \text{and} \quad T = \delta^2\, t \tag{4.70}$$

are treated as independent of the fast scales $z$ and $t$. The derivatives with respect to the new variables are

$$\frac{\partial}{\partial t} \to \frac{\partial}{\partial t} + \delta^2\frac{\partial}{\partial T}, \quad \frac{\partial}{\partial z} \to \frac{\partial}{\partial z} + \delta\frac{\partial}{\partial Z}\,. \tag{4.71}$$

The fast spatial variables vary on the order of a typical wavelength. The slow variables describe the temporal and the spatial modulations of these fast variables. Futhermore, as the marginal mode is stationary, then

$$\frac{\partial}{\partial t} \rightarrow \delta^2 \frac{\partial}{\partial T}\,. \tag{4.72}$$

The solution of the nonlinear problem in the neighborhood of the critical conditions, corresponding to the onset of convection is developed with respect to the parameter $\delta$ by

$$\boldsymbol{f} = \delta \boldsymbol{f}_1 + \delta^2 \boldsymbol{f}_2 + \delta^3 \boldsymbol{f}_3 + O\left(\delta^4\right) \tag{4.73}$$

$$Re = Re_c + \delta^2 Re^{(2)} + O(\delta^4)\,. \tag{4.74}$$

The Reynolds is increased by increasing the rotation rate of the inner cylinder. Therefore, the Bingham number will be perturbed as

$$B = B_c - \delta^2 \frac{B_c}{Re_c} Re^{(2)} + O(\delta^4)\,, \tag{4.75}$$

where, $B_c$ is the value of the Bingham number at the critical conditions. Actually, in Eq. 4.75, we have written $B = He/Re$, where $He$ is the Hedström number. In the case (II), where the fluid is partially yielded, the yield surface at $r = R_y$ is disturbed to :

$$r = R_y + \delta\, h_1 + \delta^2 \tilde{h}_2 + \delta^3 h_3 + O(\delta^4)\,. \tag{4.76}$$

It is worthy to note that the 2nd order perturbation term above $\tilde{h}_2$ includes the change in the Bingham number due to the change in $Re$ from $Re_c$ to $Re_c + \delta^2 Re^{(2)}$, as the angular rotation of the inner cylinder is increased. This second order change in Reynolds number effectively leads to a change in the dimensionless yield stress, which in turn shifts the position of the yield surface :

$$\tilde{h}_2 = h_2 - \frac{B_c}{Re_c} Re^{(2)} \left(\frac{dR_0}{dB}\right)_c\,. \tag{4.77}$$

Since there are temporal and spatial derivatives $\partial/\partial t$ and $\partial/\partial z$ in operators $\boldsymbol{\mathcal{C}}$, $\boldsymbol{L}$ and $\boldsymbol{N}$ as introduced in equations (4.67)-(4.69), these operators also need to be expanded as series of $\delta$ :

$$\boldsymbol{C} = \boldsymbol{C}_0 + \delta \boldsymbol{C}_1 + O(\delta^2)\,, \tag{4.78}$$

$$\boldsymbol{LI} = \boldsymbol{LI}_0 + \delta \boldsymbol{LI}_1 + \delta^2 \boldsymbol{LI}_2 + O\left(\delta^3\right) \tag{4.79}$$

$$\boldsymbol{NI} = \delta^2 \boldsymbol{NI}_2 + \delta^3 \boldsymbol{NI}_3 + O(\delta^4) \tag{4.80}$$

$$\boldsymbol{NY} = \delta^2 \boldsymbol{NY}_2 + \delta^3 \boldsymbol{NY}_3 + O(\delta^4)\,. \tag{4.81}$$

Formally, Taylor expansion of $\boldsymbol{LV}$ and $\boldsymbol{LY}$ is similar to that of the inertia linear operator $\boldsymbol{LI}$. The explicit expressions of $\boldsymbol{C}$, $\boldsymbol{LI}$, $\boldsymbol{LV}$, $\boldsymbol{LY}$, $\boldsymbol{NI}$ and their subscales are given in

Appendix A.

### 4.4.2 Derivation of Ginzburg Landau equation

We substitute equations (4.71), (4.72) and (4.78)-(4.81) into equation (4.67) and collect the terms at the same order of $\delta$. In the following, the first three orders are developed at $\delta$ : adjoint equations are formulated and at $\delta^3$, the solvability condition is discussed and the Ginzburg-Landau equation is derived.
For axisymmetric perturbations, the linear stability analysis suggests an exchange of stability as we traverse $Re_{1c}$. Thus in the classical way, we look for periodic solutions of form :

$$\begin{aligned} \boldsymbol{f} = \quad & \delta\left[A\boldsymbol{f}_1^{(1)}E^1 + c.c.\right] + \delta^2\left[|A|^2\boldsymbol{f}_2^{(0)}E^0 + A^2\boldsymbol{f}_2^{(2)}E^2 + c.c.\right], \\ & +\delta^3\left[|A|^2\boldsymbol{f}_3^{(1)}AE^1 + A^3\boldsymbol{f}_3^{(3)}E^3 + c.c.\right] + ..., \end{aligned} \tag{4.82}$$

where the subscript refers to the order in $\delta$ and the superscript to the corresponding Fourier mode, with :

$$\boldsymbol{f}_j^{(i)} = [F_{ij}, V_{ij}] \quad \text{and} \quad E^n = e^{ink_c z}\,. \tag{4.83}$$

In equations (4.82), the amplitude $A = A(Z,T)$ of the perturbation depends on slow variables. Furthermore, we have assumed that the amplitudes of the higher frequency spatial modes, which require interactions between lower frequecy modes will scale accordingly. Similarly, the perturbation $h$ of the yield surface is assumed of form

$$\begin{aligned} h = \quad & \delta\left[AH_{11} + c.c.\right] + \delta^2\left[|A|^2\tilde{H}_{02}E^0 + A^2H_{22}E^2 + c.c.\right] \\ & +\delta^3\left[|A|^2AE^1H_{13} + A^3E^3H_{33} + c.c.\right] + ..., \end{aligned} \tag{4.84}$$

Gathering powers of $E$ at each order in $\delta$, we derive the following hierarchical structure.

#### Solution at order $\delta$

At the first order, we recover the linear problem

$$\boldsymbol{L}_0\boldsymbol{f}_1^{(1)} = 0 \tag{4.85}$$

The boundary and compatibility conditions in terms of $\boldsymbol{u}$ are given in details in Appendix B. They are translated here in terms of $F_{ij}$ and $V_{ij}$. In the case III of base solutions (fully yielded) the no-slip conditions at the walls give :

$$F_{11} = DF_{11} = V_{11} = 0, \quad \text{at} \quad r = R_1, R_2\,. \tag{4.86}$$

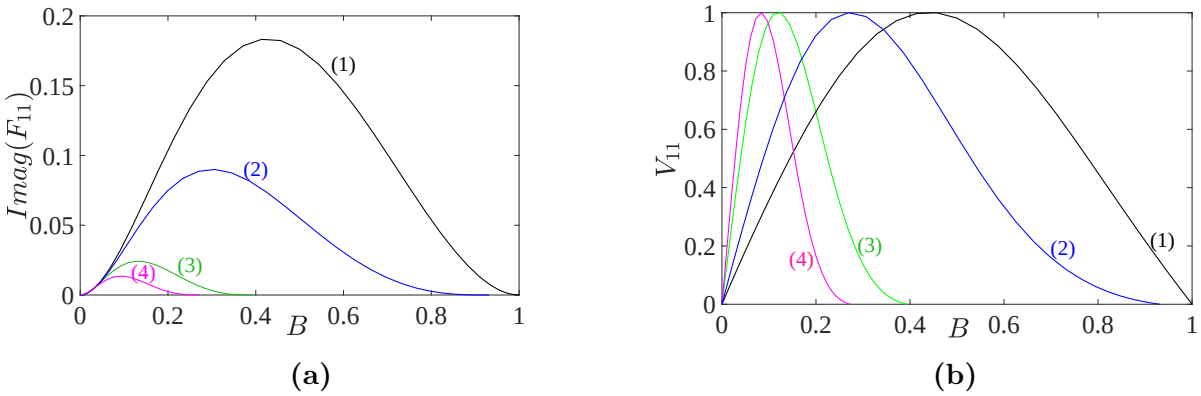


FIGURE 4.9 – Eigenfunctions at critical conditions for different values of $B$ with $\eta = 0.4$. **(a)** $\mathcal{I}mag\,(F_{11})$, **(b)** $V_{11}$. (1) $B = 0$, Newtonian ; (2) $B = 1$ ; (3) $B = 5$ ; (4) $B = 10$.

In the case II of base solutions (partially yielded), the boundary conditions at the inner wall are identical to that in the case III. At the yield surface, combining the continuity of velocity and yield conditions leads to :

$$F_{11} = DF_{11} = D^2F_{11} = 0 \quad \text{at} \quad r = R_y, \tag{4.87}$$

$$V_{11} = 0 \quad \text{at} \quad r = R_y \tag{4.88}$$

$$DV11 = -H_{11}D^2V_b \quad \text{at} \quad r = R_y\,. \tag{4.89}$$

$$\tag{4.90}$$

Since any multiple of an eigenfunction is also a solution of the linear problem (4.85) and in order to define a reference solution, $F_{11}$ and $V_{11}$ can be normalized such that

$$max(V_{11}) = 1\,, \tag{4.91}$$

which fixes the amplitude of the perturbation. Computations indicate that the eigenfunction $F_{11}$ is a pure imaginary valued while $V_{11}$ is real. The structure of the critical eigenfunctions is depicted in figure 4.9. One notices that the maximum of $\mathcal{I}mag\,(F_{11})$ decreases strongly with inceasing $B$.

### Linear adjoint mode

The adjoint mode is required to obtain the Ginzburg-Landau equation. Its definition is given as

$$\langle \boldsymbol{f}_{ad}, \boldsymbol{L}\boldsymbol{f}_1 \rangle = \langle \boldsymbol{L}_{ad}\boldsymbol{f}_{ad}, \boldsymbol{f}_1 \rangle\ , \tag{4.92}$$

where $\boldsymbol{f}_{ad} = [F_{ad}, V_{ad}]^T$ is the adjoint eigenfunction, $\boldsymbol{L}$ is the linear stability operator and $\boldsymbol{L}_{ad} = Re_1\boldsymbol{L}\boldsymbol{I}_{ad} + \boldsymbol{L}\boldsymbol{V}_{ad} + B\,\boldsymbol{L}\boldsymbol{Y}_{ad}$ is the corresponding adjoint operator. In this definition,

the inner product is given as

$$\langle \boldsymbol{f}, \boldsymbol{g} \rangle = \int_{R_1}^{R_0} \boldsymbol{f}^* \cdot \boldsymbol{g}\, r\, dr\,, \tag{4.93}$$

where $\boldsymbol{f}^*$ is the complex conjugate of $\boldsymbol{f}$. We find that $\boldsymbol{C}_{(\ell)}, \boldsymbol{LV}_{(\ell)}$ and $\boldsymbol{LY}_{(\ell)}$, $(\ell = 0, 1, 2)$, are real and self-adjoint whereas $\boldsymbol{LI}_{(\ell)}$ is not self-adjoint. We have :

$$\boldsymbol{LI}_{ad} = \begin{pmatrix} 0 & -ik_c D_* V_b \\ 2ik_c V_b / r & 0 \end{pmatrix} \tag{4.94}$$

The linear adjoint problem,

$$\boldsymbol{L}_{ad}\,(\boldsymbol{f}_{ad}) = 0\,, \tag{4.95}$$

is subject to appropriate boundary conditions, matching those of the linear problem, i.e. (4.86), (4.87) and (4.88). As the adjoint is linear and can be arbitrarily scaled, we normalize the adjoint eigenfuctions so that the maximum of the adjoint azimuthal velocity $max\,(V_{ad}) = 1$.

**Solution at order $\delta^2$ : Quadratic modes**

At order $\delta^2$, the solution has two components. The first component proportional to $|A|^2 E^0$ arises from the nonlinear interaction of the fundamental mode with its complex conjugate and the second one proportional to $A^2 E^2$ arises from the nonlinear interaction of the fundamentalmode with itself.

- Mode 0, factor $|A|^2 E^0$

This harmonic is a correction at the second order of the base flow. It is obtained by solving the following system of equations

$$\boldsymbol{L}_0 \boldsymbol{f}_2^{(0)} = -Re_{1c} \boldsymbol{NI}\left(\boldsymbol{f}_1^{(1)} | \boldsymbol{f}_1^{(-1)}\right) - B\boldsymbol{NY}\left(\boldsymbol{f}_1^{(1)} | \boldsymbol{f}_1^{(-1)}\right), \tag{4.96}$$

where $\boldsymbol{f}_1^{(-1)} = \boldsymbol{f}_1^{(1)*}$ is the complex conjugate of $\boldsymbol{f}_1^{(1)}$. As previously, the boundary conditions are of two types.

In the case (II) of base solutions, the no-slip condition at the walls gives

$$F_{02} = DF_{02} = V_{02} = 0 \quad \text{at} \quad r = R_1, R_2\,. \tag{4.97}$$

In the case (III) of base solutions, the boundary conditions and yield conditions at the yield surface lead to :

$$F_{02} = DF_{02} = 0 \qquad \text{at} \quad r = R_y\,, \tag{4.98}$$

$$D2F_{02} = -\left[H_{11} D^3 F_{11}^* + H_{11}^* D^3 F_{11}\right] \quad \text{at} \quad r = R_y\,, \tag{4.99}$$

$$V_{02} = H_{11} H_{11}^* D^2 V_b \qquad \text{at} \quad r = R_y\,. \tag{4.100}$$

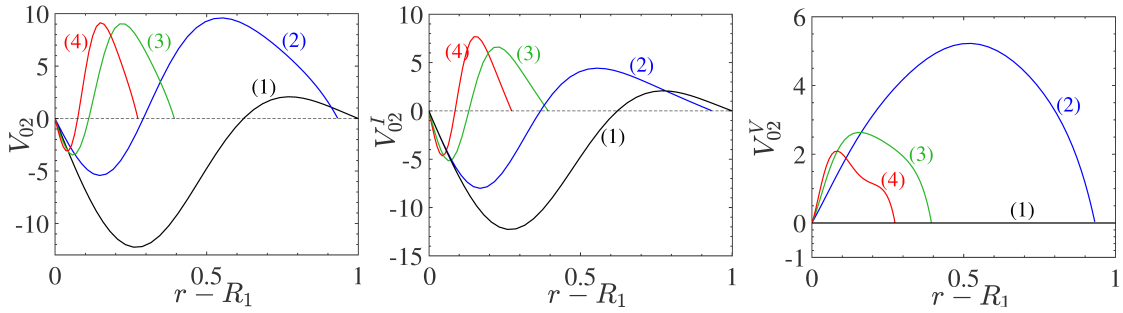


FIGURE 4.10 – **(a)** Modification of the base flow at the second order in $\delta$, for a geometry with $\eta = 0.4$, **(b)** contribution of the nonlinear inertia terms and **(c)** contribution of the nonlinear viscous terms : (1) $B = 0$, (2) $B = 1$, (3) $B = 5$ and (4) $B = 10$.

As for the linear eigenfunction, the nonlinear corrections are computed numerically. The results show, as expected, that $F_{02} = 0$, i.e. there is no radial or axial mean flow. The correction at the second order of the azimuthal velocity profile of the base state is illustrated by the profiles of $V_{02}$ represented in figure 4.10(a) for different values of $B$. The velocity is reduced near the inner cylinder and increased near the outer cylinder or the yield surface. The contribution of nonlinear inertia and viscous terms are shown in figures 4.10(b) and 4.10(c) respectively. As in the case of shear-thinning fluids [18] the interaction of the fundamental mode with its complex conjugate through nonlinear viscous terms accelerate the fluid in the whole yielded domain. A positive correction of the basic azimuthal flow leads to a destabilizing effect and therefore may be considered as a precursor to the emergence of a subcritical bifurcation.

The perturbation of the yield surface by the mode $\tilde{H}_{02}E^0$ is obtained from the yield condition. It is given by :

$$\tilde{H}_{02}D^2V_b = -DV_{02} - \left[H_{11}D^2V_{11}^* + H_{11}^*D^2V_{11}\right] - H_{11}H_{11}^*D^3V_b \quad \text{at} \quad r = R_0\,, \quad (4.101)$$

with, $\tilde{H}_{02} = H_{02} + \tilde{H}_0$. The first term arises from the interaction of the fundamental mode with its complex conjugate and the second one arises from the variation of the Bingham number as the Reynolds number is increased. The variation of $\tilde{H}_{02}$ with Bingham number is shown in figure 4.11. Positive values of $\tilde{H}_{02}$ mean that the width of the plug zone is reduced. The reduction is weaker with increasing $B$. Nevertheless, one can highlight the high values of $\tilde{H}_{02}$ compared with $H_{11}$. This result reveals probably the limited range of validity of the weakly nonlinear approach.

- Mode 2 factor of $A^2E^2$

The second harmonic mode is solution of the following system of equations :

$$\boldsymbol{L}_0\boldsymbol{f}_2^{(2)} = -Re_{1c}\boldsymbol{NI}\left(\boldsymbol{f}_1^{(1)}|\boldsymbol{f}_1^{(1)}\right) - B\boldsymbol{NY}\left(\boldsymbol{f}_1^{(1)}|\boldsymbol{f}_1^{(1)}\right)\,, \quad (4.102)$$

with the appropriate boundary conditions :

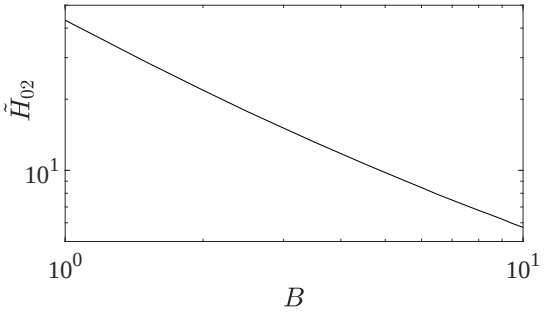


FIGURE 4.11 – Couette flow with $\eta = 0.4$. Modification at the second order in $\delta$ of the width of the static layer as a function of the Bingham number.

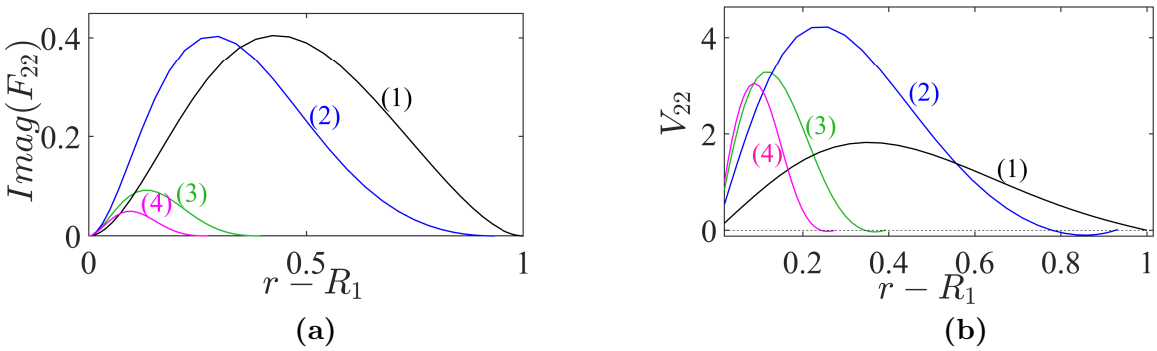


FIGURE 4.12 – Correction of the linear mode at the second order in $\delta$ at critical conditions for different values of $B$ with a radius ratio $\eta = 0.4$. **(a)** $\mathcal{I}mag(F_{22}(r))$ and **(b)** $V_{22}(r)$ : (1) $B = 0$, (2) $B = 1$, (3) $B = 5$ and (4) $B = 10$.

In the case (III) of base solutions, the no-slip condition at the walls gives

$$F_{22} = DF_{22} = V_{22} = 0 \quad \text{at} \quad r = R_1, R_2\,. \tag{4.103}$$

In the case (II) of base solutions, the boundary conditions and yield conditions at the yield surface lead to :

$$F_{22} = DF_{22} = 0 \qquad \text{at} \qquad r = R_y\,, \tag{4.104}$$

$$D^2F_{22} = -H_{11}D^3F_{11} \qquad \text{at} \qquad r = R_y\,, \tag{4.105}$$

$$V_{22} = \frac{1}{2}H_{11}^2D^2V_b \qquad \text{at} \qquad r = R_y\,. \tag{4.106}$$

The influence of Bingham number $B$ on the profiles $\mathcal{I}mag(F_{22}(r))$ and $V_{22}(r)$ is shown in figure 4.12. The maximum of these profiles decreases with increasing $B$. This is probably a consequence of the reduction of energy exchange between the fundamental and its harmonic via the nonlinear viscous terms.

The perturbation of the yield surface by the mode $H_{22}A^2E^2$ is obtained from yield condi-

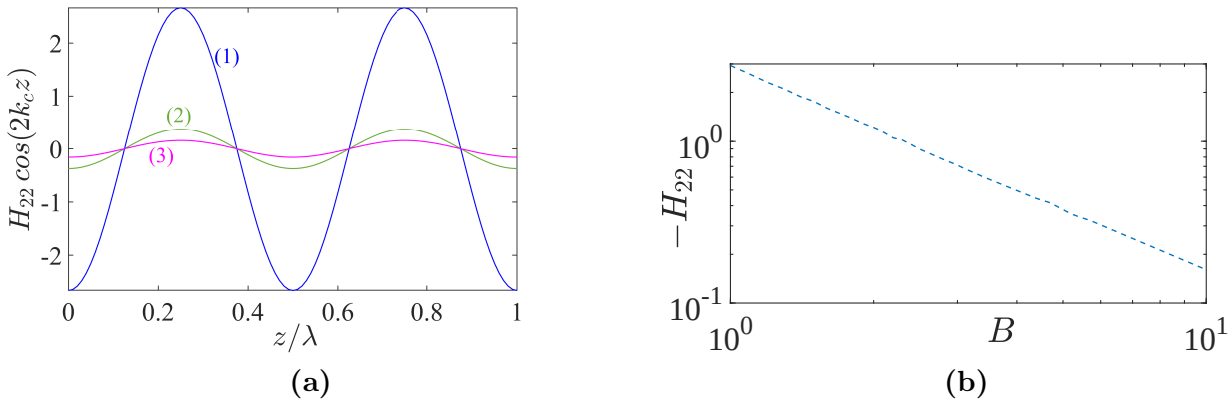


FIGURE 4.13 – (a) Yield surface perturbation of mode 2 for $\eta = 0.4$ and three different values of $B$ : (1) $B = 1$, (2) $B = 5$ and (3) $B = 10$. (b) Amplitude $H_{22}$ of the second harmonic of the yield surface perturbation as a function of Bingham number.

tions and is given by :

$$H_{22}D^2V_b = -DV_{22} - H_{11}D^2V_{11} - \frac{H_{11}^2}{2}D^3V_b \qquad \text{at} \qquad r = R_y\,. \quad (4.107)$$

It is represented in figure 4.13 as a function of $B$. One notices that : (i) $H_{22}$ decreases with increasing the width of the static layer and (ii) $H_{22}$ is one magnitude order larger than $H_{11}$.

### Solution at order $\delta^3$ : Ginzburg-Landau equation

At order $\delta^3$, the solution has two components. The first one proportional to $|A|^2AE^1$ represents the feedback at order $(\delta^3)$ on the fundamental mode through the nonlinear interactions of the fundamental with the second harmonic and with the modification of the basic state. The second one is the third harmonic.
The first component, $\boldsymbol{f}_1^{(3)} = [F_{13}, V_{13}]^T$ satisfies the following non-homogeneous equation :

$$\begin{aligned} |A|^2A\,\boldsymbol{L}_0\boldsymbol{f}_3^{(1)} = \quad & \boldsymbol{C}_0\frac{\partial A}{\partial T}\boldsymbol{f}_1^{(1)} - Re^{(2)}A\left(\boldsymbol{LI}_0 - \frac{B}{Re_c}\boldsymbol{LY}_0\right)\boldsymbol{f}_1^{(1)} - A\,\boldsymbol{L}_2\boldsymbol{f}_1^{(1)} \\ & -Re_{1c}\,|A|^2A\left[\boldsymbol{NI}\left(\boldsymbol{f}_1^{(1)}|\boldsymbol{f}_2^{(0)}\right) + \boldsymbol{NI}\left(\boldsymbol{f}_1^{(-1)}|\boldsymbol{f}_2^{(2)}\right)\right] \\ & -B\,|A|^2A\left[\boldsymbol{NY}\left(\boldsymbol{f}_1^{(1)}|\boldsymbol{f}_2^{(0)}\right) + \boldsymbol{NY}\left(\boldsymbol{f}_1^{(-1)}|\boldsymbol{f}_2^{(2)}\right)\right] \\ & -B\,|A|^2A\,\boldsymbol{NY}\left(\boldsymbol{f}_1^{(1)}, \boldsymbol{f}_1^{(1)}|\boldsymbol{f}_1^{(-1)}\right)\,. \end{aligned} \quad (4.108)$$

Concerning the boundary conditions :
For the case III of base solutions, we have :

$$F_{13} = DF_{13} = 0 \qquad \text{at} \quad r = R_1, R_2\,, \quad (4.109)$$

$$V_{13} = 0 \qquad \text{at} \quad r = R_1, R_2\,. \quad (4.110)$$

For the case II of base solutions, the boundary conditions combined with the yield conditions at the yield surface are :

$$F_{13} = 0\,, \tag{4.111}$$

$$DF_{13} = H_{11}H_{11}^{*}D^3F_{11} + \frac{H_{11}^2}{2}D^3F_{11}^{*}\,, \tag{4.112}$$

$$\begin{aligned} D^2F_{13} = &-H_{11}H_{11}^{*}D^4F_{11} - H_{11}^{*}D^3F_{22} - \tilde{H}_{02}D^3F_{11} - H_{22}D^3F_{11}^{*} \\ &-\frac{H_{11}^2}{2}D^4F_{11}^{*} - \frac{H_{11}}{R_0}\left[H_{11}D^3F_{11}^{*} + H_{11}^{*}D^3F_{11}\right]\,, \end{aligned} \tag{4.113}$$

$$V_{13} = H_{11}H_{11}^{*}D^2V_{11} + \frac{H_{11}^2}{2}D^2V_{11}^{*} + H_{11}^2H_{11}^{*}D^3V_b, \tag{4.114}$$

$$+\left(H_{11}^{*}H_{22} + H_{11}\tilde{H}_{02}\right)D^2V_b\,. \tag{4.115}$$

The condition on $DV_{13}$ defines $H_{13}$, but is lengthy and omitted for brevity.
The amplitude equation is found in the usual way, as a solvability condition on the 3rd order problem. In the case where the annular space is fully yielded, the boundary conditions for $\boldsymbol{f}_1^{3)}$ are homogeneous. The solvability condition leads to :

$$\begin{aligned} 0 = \quad &\left\langle \boldsymbol{f}_{ad}, \boldsymbol{C}_0\boldsymbol{f}_1^{(1)}\right\rangle \frac{\partial A}{\partial T} \\ &-Re^{(2)}\left\langle \boldsymbol{f}_{ad}, \left(\boldsymbol{L}\boldsymbol{I}_0 - \frac{B}{Re_{1c}}\boldsymbol{L}\boldsymbol{Y}_0\right)\boldsymbol{f}_1^{(1)}\right\rangle A - \left\langle \boldsymbol{f}_{ad}, \boldsymbol{L}_2\boldsymbol{f}_1^{(1)}\right\rangle A \\ &-Re_{1c}\left\langle \boldsymbol{f}_{ad}, \boldsymbol{N}\boldsymbol{I}\left(\boldsymbol{f}_2^{(0)}|\boldsymbol{f}_1^{(1)}\right)\right\rangle |A|^2A - Re_{1c}\left\langle \boldsymbol{f}_{ad}, \boldsymbol{N}\boldsymbol{I}\left(\boldsymbol{f}_2^{(2)}|\boldsymbol{f}_1^{(-1)}\right)\right\rangle |A|^2A \\ &-B\left\langle \boldsymbol{f}_{ad}, \boldsymbol{N}\boldsymbol{Y}\left(\boldsymbol{f}_2^{(0)}|\boldsymbol{f}_1^{(1)}\right)\right\rangle |A|^2A - B\left\langle \boldsymbol{f}_{ad}, \boldsymbol{N}\boldsymbol{Y}\left(\boldsymbol{f}_2^{(2)}|\boldsymbol{f}_1^{(-1)}\right)\right\rangle |A|^2A \\ &-B\left\langle \boldsymbol{f}_{ad}, \boldsymbol{N}\boldsymbol{Y}\left((\boldsymbol{f}_1^{(1)}, \boldsymbol{f}_1^{(1)})|\boldsymbol{f}_1^{(-1)}\right)\right\rangle |A|^2A. \end{aligned} \tag{4.116}$$

Using the departure from the linear threshold

$$\epsilon = \frac{Re_1 - Re_{1c}}{Re_{1c}} = \delta^2\frac{Re^{(2)}}{Re_{1c}}, \tag{4.117}$$

and after returning to the fast variables $\delta A(Z,T) = A'(z,t)$, $\dfrac{\partial}{\partial Z} = \dfrac{1}{\delta}\dfrac{\partial}{\partial z}$ and $\dfrac{\partial}{\partial T} = \dfrac{1}{\delta^2}\dfrac{\partial}{\partial t}$, the following Ginzburg-Landau equation is derived :

$$\frac{\partial A}{\partial T} = \frac{\epsilon}{\tau_0}A + \frac{\xi_0^2}{\tau_0}\frac{\partial^2 A}{\partial z^2} + g_1|A|^2A, \tag{4.118}$$

where $\tau_0$ is the characteristic time for the instability to grow,

$$\tau_0^{-1} = Re_{1c}\frac{\left\langle \boldsymbol{f}_{ad}, \left(\boldsymbol{L}\boldsymbol{I}_0 - \dfrac{B}{Re_{1c}}\boldsymbol{L}\boldsymbol{Y}_0\right)\boldsymbol{f}_1^{(1)}\right\rangle}{\left\langle \boldsymbol{f}_{ad}, \boldsymbol{C}_0\boldsymbol{f}_1^{(1)}\right\rangle} \tag{4.119}$$

$\xi_0$ the coherence length

$$\xi_0^2 = \frac{1}{Re_{1c}} \frac{\left\langle \boldsymbol{f}_{ad}, \boldsymbol{L}_2 \boldsymbol{f}_1^{(1)} \right\rangle}{\left\langle \boldsymbol{f}_{ad}, \left( \boldsymbol{L}\boldsymbol{I}_0 - \frac{B}{Re_{1c}} \boldsymbol{L}\boldsymbol{Y}_0 \right) \boldsymbol{f}_1^{(1)} \right\rangle} \tag{4.120}$$

and $g_1$ the first Landau coefficient

$$\begin{aligned} g_1 &= Re_{1c} \frac{\left\langle \boldsymbol{f}_{ad}, \boldsymbol{N}\boldsymbol{I} \left( \boldsymbol{f}_2^{(0)} | \boldsymbol{f}_1^{(1)} \right) \right\rangle}{\left\langle \boldsymbol{f}_{ad}, \boldsymbol{C}_0 \boldsymbol{f}_1^{(1)} \right\rangle} + Re_{1c} \frac{\left\langle \boldsymbol{f}_{ad}, \boldsymbol{N}\boldsymbol{I} \left( \boldsymbol{f}_2^{(2)} | \boldsymbol{f}_1^{(-1)} \right) \right\rangle}{\left\langle \boldsymbol{f}_{ad}, \boldsymbol{C}_0 \boldsymbol{f}_1^{(1)} \right\rangle} \\ &+ B \frac{\left\langle \boldsymbol{f}_{ad}, \boldsymbol{N}\boldsymbol{Y} \left( \boldsymbol{f}_2^{(0)} | \boldsymbol{f}_1^{(1)} \right) \right\rangle}{\left\langle \boldsymbol{f}_{ad}, \boldsymbol{C}_0 \boldsymbol{f}_1^{(1)} \right\rangle} + B \frac{\left\langle \boldsymbol{f}_{ad}, \boldsymbol{N}\boldsymbol{Y} \left( \boldsymbol{f}_2^{(2)} | \boldsymbol{f}_1^{(-1)} \right) \right\rangle}{\left\langle \boldsymbol{f}_{ad}, \boldsymbol{C}_0 \boldsymbol{f}_1^{(1)} \right\rangle} \\ &+ B \frac{\left\langle \boldsymbol{f}_{ad}, \boldsymbol{N}\boldsymbol{Y} \left( (\boldsymbol{f}_1^{(1)}, \boldsymbol{f}_1^{(1)}) | \boldsymbol{f}_1^{(-1)} \right) \right\rangle}{\left\langle \boldsymbol{f}_{ad}, \boldsymbol{C}_0 \boldsymbol{f}_1^{(1)} \right\rangle}. \end{aligned} \tag{4.121}$$

The integrals are evaluated numerically by means of Clenshaw and Curtis method [19]. At critical conditions, and assuming that the amplitude does not vary with the axial position, $\boldsymbol{f}_1^{(3)} = \boldsymbol{f}_{1H}^{(3)}$ satisfies equation of the form

$$\boldsymbol{L}_0 \boldsymbol{f}_{1H}^{(3)} = g_{1H}\, \boldsymbol{C}_0 \boldsymbol{f}_1^{(1)} - Re_{1C}\, \boldsymbol{N}\boldsymbol{I} - B\, \boldsymbol{N}\boldsymbol{Y}\,. \tag{4.122}$$

In the case, where there is a static layer on the outer wall, the boundary conditions at the yield surface (defined in (4.112)-(4.115)) are inhomogeneous. In order to derive the solvability condition, we decompose, as in [20] and [21], $\boldsymbol{f}_1^{(3)}$ into homogeneous $\boldsymbol{f}_{1H}^{(3)}$ and inhomogeneous parts $\boldsymbol{f}_{1NH}^{(3)}$

$$\boldsymbol{f}_1^{(3)} = \boldsymbol{f}_{1H}^{(3)} + \boldsymbol{f}_{1NH}^{(3)}, \tag{4.123}$$

where, $\boldsymbol{f}_{1NH}^{(3)}$ is a correction term that accounts for the non-homogeneity of the boundary conditions. Furthermore at critical conditions $\boldsymbol{f}_1^{(3)}$ satisfies an equation that can be written as :

$$\boldsymbol{L}_0 \boldsymbol{f}_1^{(3)} = g_1\, \boldsymbol{C}_0 \boldsymbol{f}_1^{(1)} - Re_{1C}\, \boldsymbol{N}\boldsymbol{I} - B\, \boldsymbol{N}\boldsymbol{Y}. \tag{4.124}$$

Substituting (4.123) into (4.124), we obtain

$$\boldsymbol{L}_0 \boldsymbol{f}_{1H}^{(3)} = g_1\, \boldsymbol{C}_0 \boldsymbol{f}_1^{(1)} - Re_{1C}\, \boldsymbol{N}\boldsymbol{I} - B\, \boldsymbol{N}\boldsymbol{Y} - \boldsymbol{L}_0 \boldsymbol{f}_{1H}^{(3)}, \tag{4.125}$$

By applying the solvability condition to (4.125), we get

$$g_1 = g_{1H} + \frac{\left\langle \boldsymbol{f}_{ad}, \boldsymbol{L}_0 \boldsymbol{f}_{1NH}^{(3)} \right\rangle}{\left\langle \boldsymbol{f}_{ad}, \boldsymbol{C}_0 \boldsymbol{f}_1^{(1)} \right\rangle}. \tag{4.126}$$

The technique of solution adopted is to iterate a few times between (4.123) and (4.126). At the start, $\boldsymbol{f}_{1NH}^{(3)}$ is assumed to be identically zero in (4.126). A first approximation of $g_1$ is then obtained : $g_1^{(1)} = g_{1H}$. This is put into (4.124), which is solved at the critical conditions, with non-homogeneous boundary conditions, to obtain a first approximation of $\boldsymbol{f}_1^{(3)}$. Using (4.123) a first approximation of $\boldsymbol{f}_{1NH}^{(3)}$ is deduced. Then $\boldsymbol{f}_{1NH}^{(3)}$ is put into (4.126). This process is repeated until it converges to a desired level of accuracy. Note that equation (4.124) is solved with an additional condition

$$\boldsymbol{f}_1^{(3)} = 0 \quad \text{at} \quad r = r_{max}, \tag{4.127}$$

where $r_{max}$ the radial position at which $V_{11}(r_{max}) = 1$. This normalization was suggested by [22, 23, 20, 24]. Without this normalization, $\boldsymbol{f}_1^{(3)}$ is defined up to an arbitrary multiple of the solution $\boldsymbol{f}_1^{(1)}$.

### 4.4.3 Results and discussion

The variation of the characteristic time $\tau_0$ as a function of Bingham number is shown in figure 4.14 (a) for two radius ratios $\eta = 0.4$ and $\eta = 0.88$. For $\eta = 0.4$, we can distinguish two zones : in the first one, $0 < B < 0.85$, the annular space is fully yielded and $\tau_0$ decreases slightly with $B$. In the second one $B > 0.85$, the annular space is partially yielded and $\tau_0$ decreases practically as $(1/B)$. The same behavior is observed for $\eta = 0.88$, where the annular space becomes partially yielded when $B \geq 8.5$. The same trend is observed for the coherence length in figure 4.14(b).

#### Transition from supercritical to subcritical bifurcation

In figure 4.15 we have represented the variation of $g_1$ as a function of the Bingham number in the case of a wide gap ($\eta = 0.4$ and $\eta = 0.5$). The sign of $g_1$ determines whether we are dealing with a supercritical or a subcritical bifurcation.
Consider the case where $\eta = 0.4$, figure 4.15(a). At $B = 0$, (Newtonian fluid) $g_1$ is negative and the bifurcation is supercritical. With increasing $B$, $g_1$ decreases, reaches a minimum at $B \approx 0.4$, then increases rapidly until a static layer appears on the outer wall $atB = 0.88$. At this point, the increase of $g_1$ with $B$ is significantly reduced. At $B = B^* = 4.03$ which corresponds to $R_1/R_0 = 0.6$, $g_1$ becomes positive and the primary bifurcation becomes subcritical. Then, $g_1$ continues to increase with $B$ at least in the range of the values of $B$ considered. Note that at $B = 10$, we have $R_1/R_0 = 0.71$.
Similar variation of $g_1$ as a function of $B$ is observed at $\eta = 0.5$ (figure 4.15(b)). For this

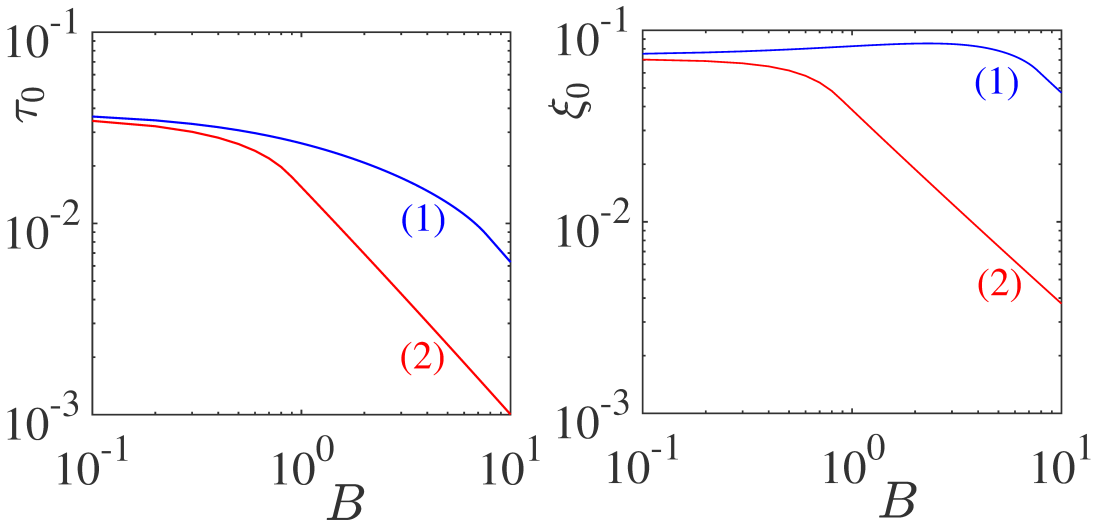


FIGURE 4.14 – Variations of the characteristic time of instability (left frame) and the coherence length (right frame) as a function of Bingham number for a wide and a narrow gap : (1) $\eta = 0.88$, (2) $\eta = 0.4$

radius ratio, the bifurcation becomes subcritical at $B = B^* = 2.7$ which corresponds as previously to $R_1/R_0 = 0.6$. For $\eta = 0.6$, it is may be not surprising to observe that $g_1$ becomes positive as soon as a static layer appears on the outer wall which corresponds to $B = B^* = 1.8$.

For a narrower gap, it is possible to have a subcritical bifurcation when the annular space is fully yielded, as it is illustrated in figure 4.16(a) obtained for $\eta = 0.8$, where $g_1$ becomes positive from $B = B^* = 4.18$. However, unlike the case of a wide gap, with increasing $B$ and once a static layer appears, $g_1$ remains practically constant and even starts to decrease from $B = 9.2$ which corresponds to $R_1/R_0 = 0.85$. For an even narrower gap, $\eta = 0.9$, the primary bifurcation remains supercritical as it can be observed in figure 4.16(b). Furthermore, in presence of a static layer, $g_1$ decreases with increasing $B$. The variation of $B^*$, i.e. the Bingham number from which the primary bifurcation becomes positive, as a function of $\eta$ is shown in figure 4.17. It is interesting to note that the minimum of $B^*$ is reached at $\eta = 0.6$.For $\eta < 0.6$, the subcritical bifurcation occurs in presence of a static layer, whereas for $\eta > 0.6$, a subcritical bifurcation can be observed when the annular space is fully yielded. However, for $\eta \geq 0.9$, the primary bifurcation is supercritical. Therefore for a given $\eta < 0.9$, the bifurcation is supercritical for $B < B^*$, subcritical for $B > B^*$, but for sufficiently large value of $B$, such that $R_1/R_0 \geq 0.9$, the bifircation becomes supercritical again.

To shed more light on the mechanism of supercritical/subcritical instability, the first Landau constant is decomposed as

$$g_1 = g_{1I} + g_{1V} + g_{1NH} = \left(g_{1I}^{1,0} + g_{1I}^{-1,2}\right) + \left(g_{1V}^{1,0} + g_{1V}^{-1,2} + g_{1V}^{1,1,-1}\right) + g_{1NH}, \quad (4.128)$$

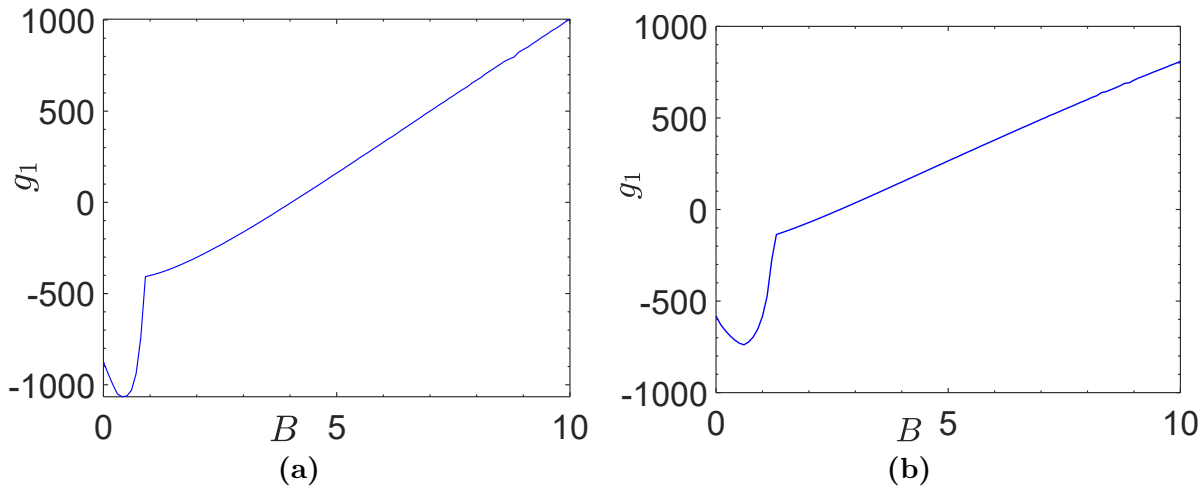


FIGURE 4.15 – Case of a wide gape. Variation of the first Landau constant as a function of the Bingham number for two radius ratios : **(a)** $\eta = 0.4$ and **(b)** $\eta = 0.5$

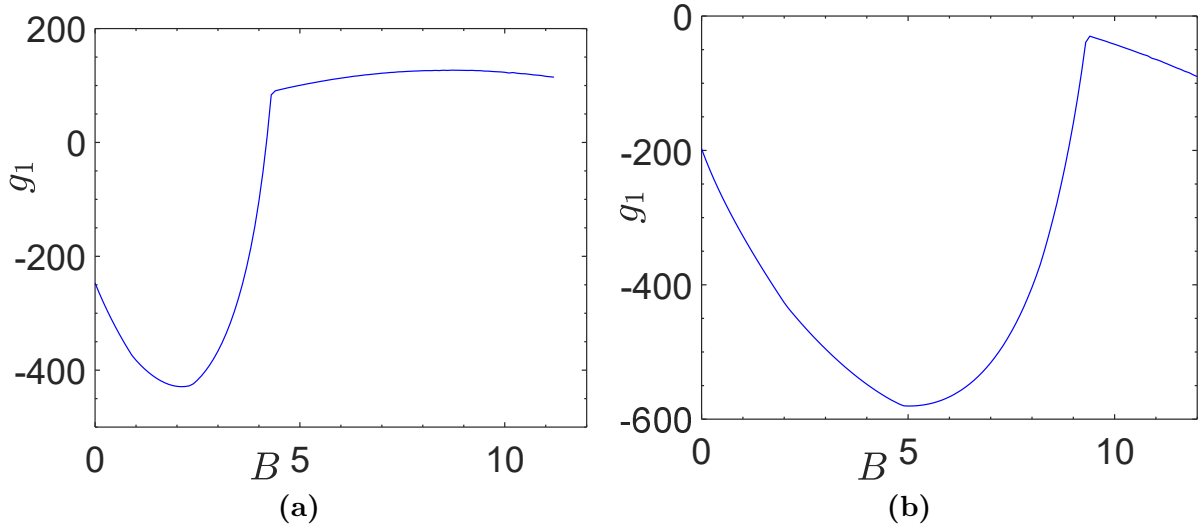


FIGURE 4.16 – Case of a narrow gape. Variation of the first Landau constant as a function of the Bingham number for two radius ratios : **(a)** $\eta = 0.8$ and **(b)** $\eta = 0.9$

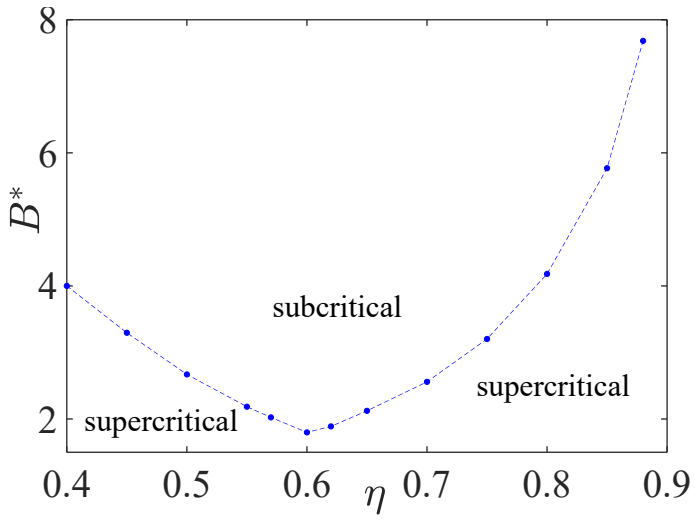


FIGURE 4.17 – Variation of the Bingham number from which the primary bifurcation becomes subcritical as a function of the radius ratio.

where $g_{1I}^{1,0}$ and $g_{1V}^{1,0}$ are the feedback of the mean flow correction onto the fundamental through the nonlinear inertial and nonlinear viscous terms, $g_{1I}^{-1,2}$ is the feedback of the second harmonic onto the fundamenal, $g_{1V}^{1,1,-1}$ arises from the cubic nonlinear viscous term and $g_{1NH}$ is the contribution of the inhomogeneity of the boundary conditions on $g1$. These terms are straightforwardly identified by comparison (4.128) with (4.126) and (4.122). In figure 4.18, we have represented the contribution of nonlinear inertial terms (Reynolds terms) and nonlinear viscous terms (Bingham terms), respectively, $g_{1I} = g_{1I}^{1,0} + g_{1I}^{-1,2}$ and $g_{1V} = g_{1V}^{1,0} + g_{1V}^{-1,2} + g_{1V}^{1,1,-1}$ on the first Landau constant for a wide $\eta = 0.4$ and a narrow gap $\eta = 0.88$. For the range of tested values, $g_{1I} < 0$ and $g_{1V} > 0$, i.e. the nonlinear inertial terms promote a supercritical bifurcation and the nonlinear viscous terms promote a subcritical bifurcation. For $B < B^*$, the contribution of nonlinear inertial terms is dominant and for $B > B^*$, it is the contribution of nonlinear viscous terms which is dominant. As the Bingham number is raised large enough, $g_{1I}$ becomes dominant and the bifurcation returns to supercriticality, as it is shown in figure 4.18(b).
The contributions of the different terms that control the value of $g_1$ are given in appendix. The results indicate that $g_{10}^I$ and $g_{10}^V$, i.e. the terms that arise from the interaction of the fundamental mode with the distortion of the mean flow have the largest values. Furthermore, $g_{10}^V$ increases strongly once a static layer appears on the outer cylinder.

**Stationary amplitudes**

A steady solution of equation (4.118) is

$$A = A_0 e^{iqz} \quad \text{with} \quad A_0 = \left| \frac{\epsilon - \xi_0^2 q^2}{\tau_0(-g_1)} \right|^{1/2} \quad \text{and} \quad q = k - k_c \,. \tag{4.129}$$

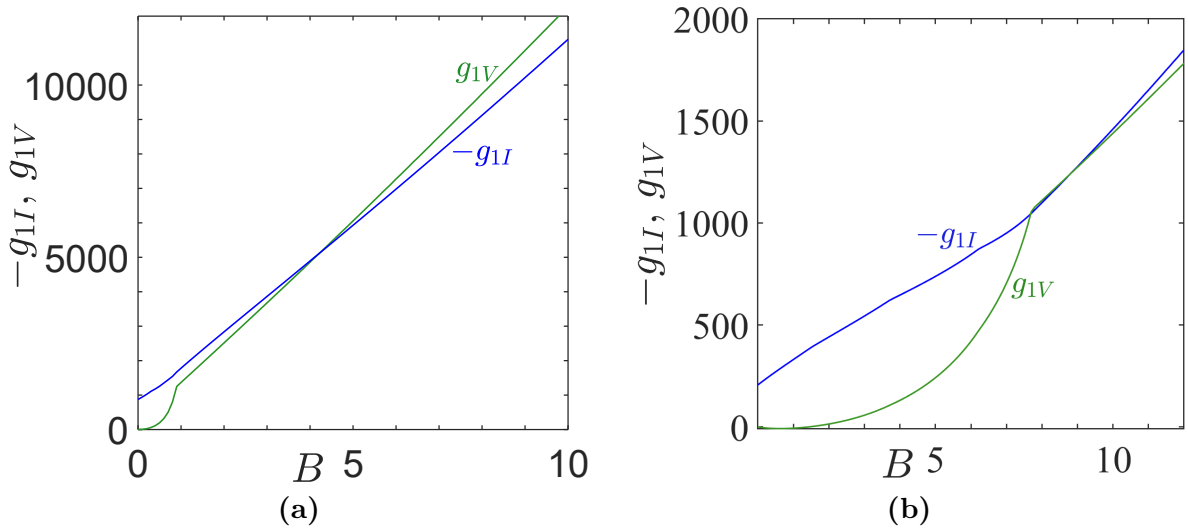


FIGURE 4.18 – Contributions of nonlinear inertial terms $g_{1I}$ and nonlinear viscous terms $g_{1V}$ on the first Landau constant as a function of $B$ for **(a)** a wide gap $\eta = 0.4$ and **(b)** a narrow gap $\eta = 0.88$

Figure 4.19 shows the bifurcation diagram obtained in the case where $k = k_c$, i.e. $q = 0$, at different Bingham numbers. For a wide gap, $\eta = 0.4$, 4.19(a), near the critical conditions, when the bifurcation is supercritical, the equilibrium amplitude shown in continuous line, increases with increasing $B$. When the bifurcation is subcritical, the threshold amplitude, that limits the basin of attraction of the circular Couette flow, shown in dashed line, decreases with increasing $B$, i.e. the basic flow becomes more sensitive to finite amplitude perturbations. However, this variation can not continue. Indeed, when the width of the yielded zone is sufficiently narrow, $R_1/R_y \geq 0.9$, the bifurcation again becomes supercritical. This is illustrated by figure 4.19(b) obtained for $\eta = 0.881$. At $B = 8$, $R_1/R_y = 0.883$, the bifurcation is subcritical and at $B = 12$, $R_1/R_y = 0.902$, the bifurcation again becomes supercritical.
Note that in the suspecritical regime, the stationary solutions obtained for $k \neq k_c$ are unstable to long-wavelength perturbations when $\epsilon > 3\xi_0^2 q^2$.

**Flow structure**

One has to note that the numerical values of the Landau constant and hence the values of the amplitude depend on the normalization condition used for the eigenfunctions in the linear theory. However, the physical velocity component, i.e. the product of the amplitude with the eigenfunctions of the linear theory are independent of the normalization. In figure 4.20, we have represented the profiles of the radial velocity component

$$u = -\left(ik_c A F_{11} E^1 + 2ik_c A^2 F_{22}^* E^2 + c.c.\right) + O(A^3), \tag{4.130}$$

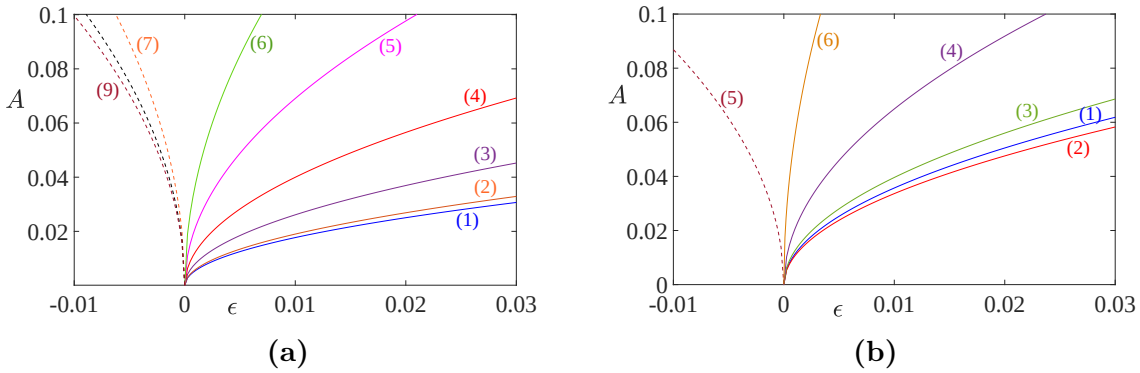


FIGURE 4.19 – Stationary amplitude as a function of the distance $\epsilon$ to criticality.
**(a)** Wide gap, $\eta = 0.4$, (1) $B = 0$, (2) $B = 0.5$, (3) $B = 0.8$, (4) $B = 1$, (5) $B = 2$, (6) $B = 3$, (7) $B = 6$, (8) $B = 8$ and (9) $B = 10$.
**(b)** Narrow gap, $\eta = 0.881$, (1) $B = 0$, (2) $B = 1$, (3) $B = 5$, (4) $B = 7$, (5) $B = 8$, (6) $B = 12$.

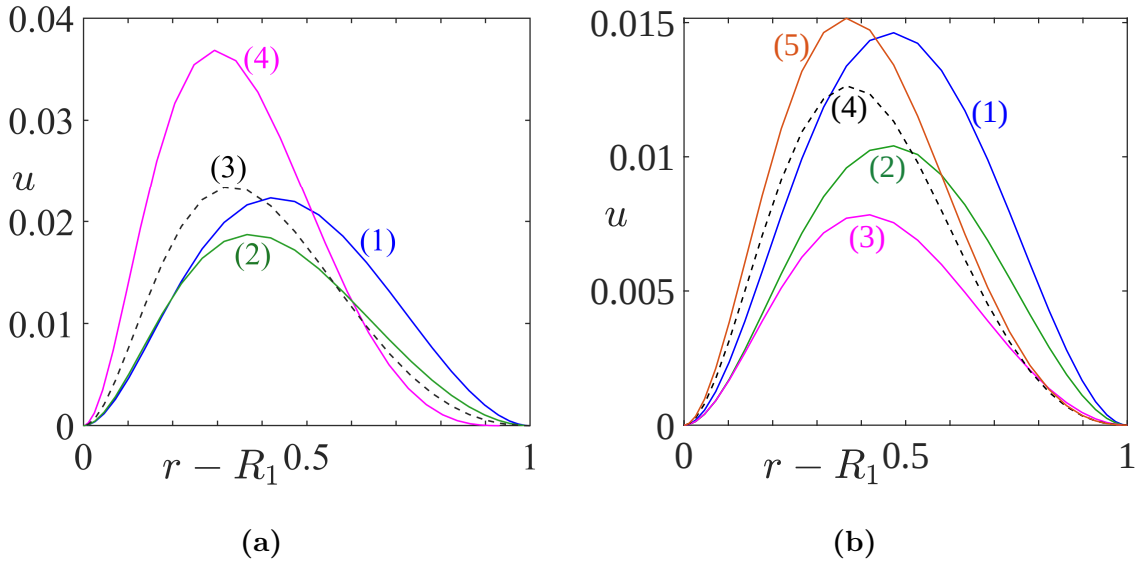


FIGURE 4.20 – Velocity component $u$ across the gap at $\epsilon = 0.01$ and for different Bingham numbers. **(a)** Wide gap, $\eta = 0.4$, (1) $B = 0$, (2) $B = 0.5$, (3) $B = 0.8$, (4) $B = 1$. **(b)** Narrow gap, $\eta = 0.881$, (1) $B = 0$, (2) $B = 1$, (3) $B = 5$, (4) $B = 7$, (5) $B = 7.2$.

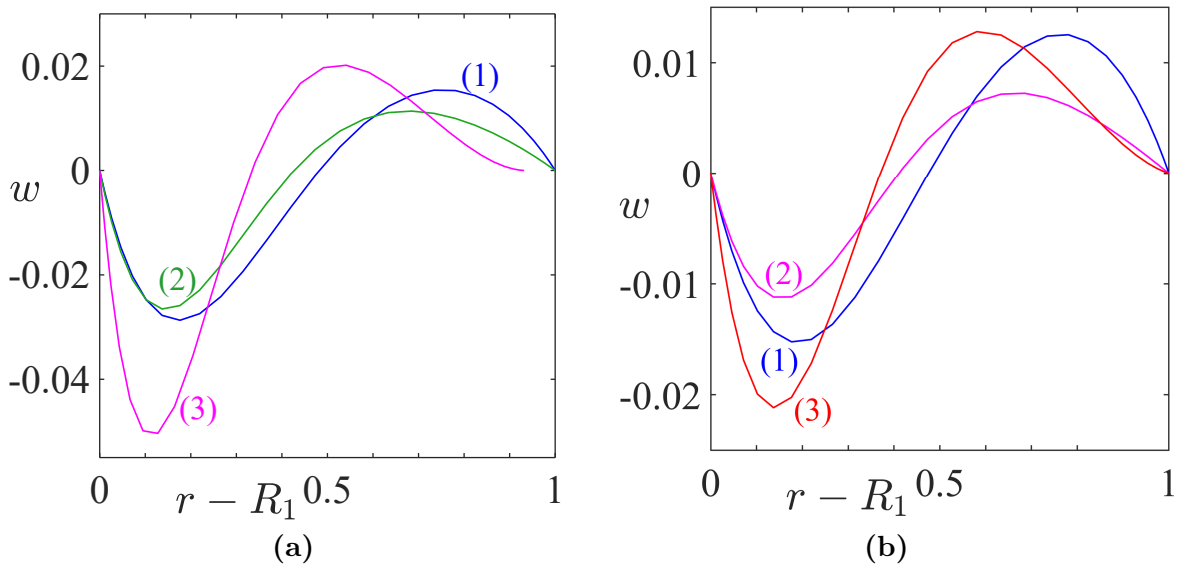


FIGURE 4.21 – Velocity component $w$ across the gap at $\epsilon = 0.01$ and for different Bingham numbers. **(a)** Wide gap, $\eta = 0.4$, (1) $B = 0$, (2) $B = 0.5$, (3) $B = 1$. **(b)** Narrow gap, $\eta = 0.881$, (1) $B = 0$, (2) $B = 5$, (3) $B = 7.2$.

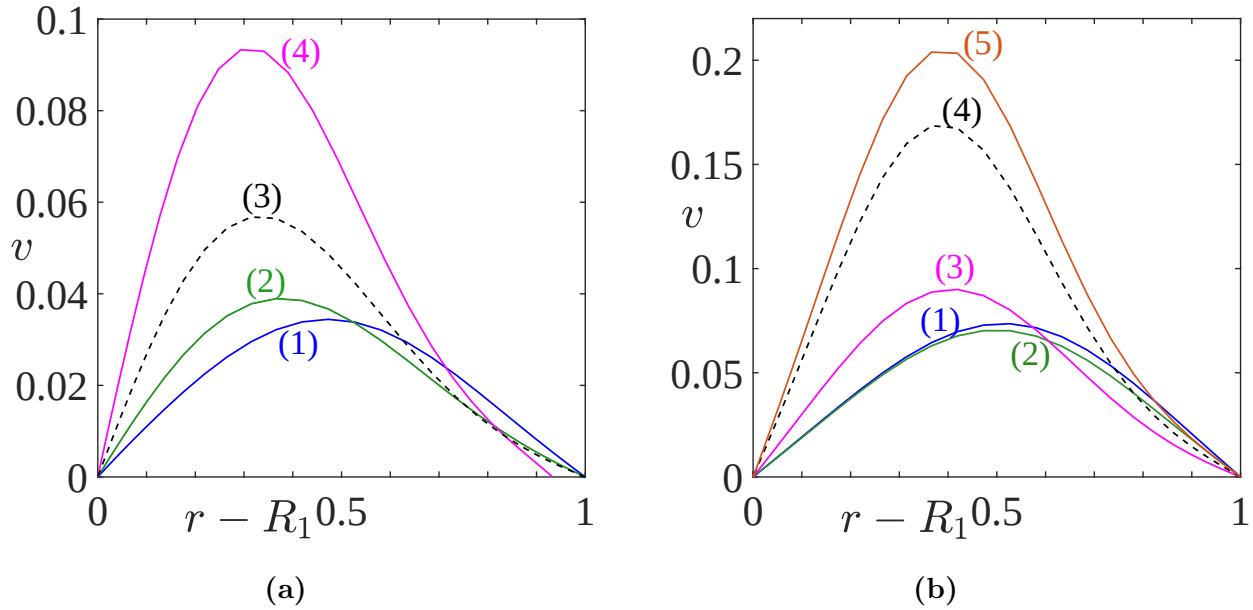


FIGURE 4.22 – Velocity component $v$ across the gap at $\epsilon = 0.01$ and for different Bingham numbers. **(a)** Wide gap, $\eta = 0.4$, (1) $B = 0$, (2) $B = 0.5$, (3) $B = 1$, (4) $B = 1.4$. **(b)** Narrow gap, $\eta = 0.881$, (1) $B = 0$, (2) $B = 1$, (3) $B = 5$, (4) $B = 7$, (5) $B = 7.2$.

at $z = 0$, $\epsilon = 0.01$, in a wide and a narrow gap and for different Bingham numbers. As it can be observed, at low values of $B$, the maximum of the radial velocity component decreases and the intensity of the vortex flow is weakened (see for instance, curves 1, 2 and 3 in figure 4.20(b). However, for sufficiently large values of $B$, the maximum of $u$ increases, and the intensity of the vortex flow is strengthened. This is probably a consequence of the reduction of the viscous dissipation by the viscosity perturbation.
Concerning the azimuthal velocity,

$$v = AV_{11} + A^2V_{22} + |A|^2V_{02} + c.c. + O(A^3) \tag{4.131}$$

figure 4.22 shows that globally, the intensity of the azimuthal streaks increases with increasing B. It is interesting to note for a wide gap, at $B = 1$, (curve 4), the shear rate, $\dot{\gamma}_{r\theta}$ at the yield surface does not cancel. The perturbation azimuthal velocity at $r = R_0$ is too small, and can not be distinguished in the figure. figure 4.22 shows that globally, the intensity of the azimuthal streaks increases with increasing B. It is interesting to note for a wide gap, at $B = 1$, (curve 4), the shear rate, $\dot{\gamma}_{r\theta}$ at the yield surface does not cancel. The perturbation azimuthal velocity at $r = R_0$ is too small, and can not be distinguished in the figure.

### Torque

The determination of the torque $\hat{T}$ applied on the inner cylinder is of great interest. It provides information about the energy dissipation. [25] and [26] defined a dimensionless torque as the ratio of $\hat{T}$ to a nominal torque $2\pi\hat{\rho}\hat{\nu}^2\hat{\ell}$, where $\hat{\nu}$ is the kinematic viscosity and $\hat{\ell}$ the height of the inner cylinder immersed in the fluid. By analogy with the heat transfer in Rayleigh-Bénard convection, the previous authors defined a pseudo-Nusselt number, $Nu_*$ for a Taylor Couette flow as the ratio of $G$ to the dimensionless torque evaluated in the laminar regime $G_b$ :

$$Nu_* = \frac{G}{G_b} = \frac{\int_0^{2\pi/k_c} \left(\tau_{r\theta}\left(\boldsymbol{U}_b + \boldsymbol{u}\right)\right)_{R_1} \mathrm{d}z}{\left(2\pi/k_c\right)\left(\tau_{r\theta}\left(\boldsymbol{U}_b\right)\right)_{R_1}}. \tag{4.132}$$

The pseudo-Nusselt number, $Nu_*$, represents the dimensionless angular velocity flux or momentum flux (CCF)[26]. Greater $Nu_*$ implies that that the torque per unit height or the momentum flux is larger.
In the laminar regime, the radial flux of the angular momentum is diffusive and $Nu_* = 1$. In the TVF regime, using equations (4.29), (4.31), (4.35) and (4.37), $Nu_*$ can be written as

$$Nu_* = 1 + \left[\frac{DV_{02}}{\tau_{r\theta}\left(\boldsymbol{U}_b\right)}\right]_{R_1} |A|^2 - Bsgn\left(\dot{\gamma}_{r\theta}\left(\boldsymbol{U}_b\right)\right)\left[\frac{|D^2F_{11}|^2}{\tau_{r\theta}\left(\boldsymbol{U}_b\right)\left[\dot{\gamma}\left(\boldsymbol{U}_b\right)\right]^2}\right]_{R_1} |A|^2 + O\left(|A|^4\right). \tag{4.133}$$

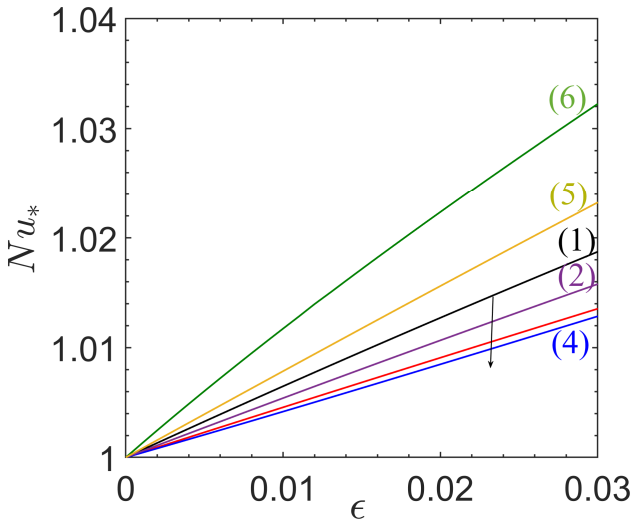


FIGURE 4.23 – Torque applied on the inner cylinder as a function of $\epsilon$ for different values of $B$ with $\eta = 0.4$. (1) $B = 0$, (2) $B = 0.2$, (3) $B = 0.5$, (4) $B = 1$, (5) $B = 3$ and (6) $B = 5$.

In the case where $k = k_c$, using equation (4.129), the pseudo-Nusselt number can be written formally as :

$$Nu_* = 1 + K\epsilon, \tag{4.134}$$

where $K$ depends on Bingham number. For a Newtonian fluid, we have

$$K = -\frac{1}{\tau_0 g_1}\left[\frac{DV_{02}}{\dot{\gamma}_{r\theta}\left(\boldsymbol{U}_b\right)}\right]_{R_1} \quad \text{with} \quad \left(\dot{\gamma}_{r\theta}\left(\boldsymbol{U}_b\right)\right)_{R_1} = -\frac{2}{\eta\left(1+\eta\right)} \tag{4.135}$$

## 4.5 Conclusion

We have invstigated the Taylor vortex flow regime in a yield stress fluid. A Bingham fluid model is used. After a characterization of the base flow and determination the range of Reynolds numbers for which we have a static layer on the outer cylinder, a three-dimensional linear stability analysis is performed for a narrow and a wide gap. We recover the results of [8] and [7] where for co-rotating cylinder, the yield stress may have a destabilizing effect. We have also determined the ranges of $Re_1$ and $Re_2$ where the assumption of axisymmetric perturbations can be used.

A weakly nonlinear analysis based on the multiple scales method is performed. Amplitude equation is derived and the first Landau coefficient $g_1$ is determined for different values of $B$. It is shown that the variation of $g_1$ with $B$ is nonmonotonic. For a wide gap, $\eta = 0.4$, $|g_1|$ first increases with $B$ due to the dominant contribution of the nonlinear inertia terms, reaches a maximum at $B \approx 4$, then decreases due to the contribution of the nonlinear viscous terms. For a sufficiently large values of $B$, here $B = 10.5$, the primary bifurcation

becomes subcritical. The variation of the dimensionless torque, pseudo Nusselt number $Nu^*$, with B is fundamentally different from that observed for shear-thinning fluids. In the case where the fluid is fully yielded in the annular space, $Nu^*$ decreases with increasing $B$. However in the case of partially yielded, $Nu^*$ increase with increasing $B$.
The erosion of the plug zone arises mainly from the quadratic mode due to the interaction of the fundamental mode with its complex conjugate.
To our knowledge a weakly nonlinear analysis was not performed previously. We believe that this analysis expanded for a higher order can become as basis for a future research as it was done for the shear-thinning fluids.

## 4.A Operators and matrix coefficients

### 4.A.1 The operator $C$

$$\boldsymbol{C} = \begin{pmatrix} DD_* + \dfrac{\partial^2}{\partial z^2} & 0 \\ 0 & 1 \end{pmatrix} \tag{4.136}$$

**The sub-scales $\boldsymbol{C}_0$ and $\boldsymbol{C}_1$**

$$\boldsymbol{C}_0 \equiv \boldsymbol{C} \quad , \quad \boldsymbol{C}_1 = \begin{pmatrix} 2\dfrac{\partial^2}{\partial z \partial Z} & 0 \\ 0 & 0 \end{pmatrix} \tag{4.137}$$

### 4.A.2 The operator $LI$

$$\boldsymbol{LI} = \begin{pmatrix} 0 & -2\dfrac{V_b}{r}\dfrac{\partial}{\partial z} \\ D_* V_b \dfrac{\partial}{\partial z} & 0 \end{pmatrix} \tag{4.138}$$

**The sub-scales $\boldsymbol{LI}_0$, $\boldsymbol{LI}_1$ and $\boldsymbol{LI}_2$**

$$\boldsymbol{LI}_0 \equiv \boldsymbol{LI} \quad , \quad \boldsymbol{LI}_1 = \begin{pmatrix} 0 & -2\dfrac{V_b}{r}\dfrac{\partial}{\partial Z} \\ D_* V_b \dfrac{\partial}{\partial Z} & 0 \end{pmatrix} \quad , \quad \boldsymbol{LI}_2 = \boldsymbol{0}. \tag{4.139}$$

### 4.A.3 The operator $LV$

The coefficients of the $2 \times 2$ matrix $\boldsymbol{LV}$ are :

$$\boldsymbol{LV} = \begin{pmatrix} \boldsymbol{LV}_{11} & 0 \\ 0 & \boldsymbol{LV}_{22} \end{pmatrix} \tag{4.140}$$

with

$$\boldsymbol{LV}_{11}(\phi) = (DD_*)^2 \phi + 2\frac{\partial^2}{\partial z^2} DD_* \phi + \frac{\partial^4 \phi}{\partial z^4}, \tag{4.141}$$

$$\boldsymbol{LV}_{22}(v) = \frac{1}{r^2}\frac{\partial}{\partial r}\left[r^2\left(Dv - \frac{v}{r}\right)\right] + \frac{\partial^2 v}{\partial z^2} \tag{4.142}$$

**The sub-scales $LV_0$, $LV_1$ and $LV_2$**

$$\boldsymbol{LV}_0 \equiv \boldsymbol{LV} \tag{4.143}$$

$$\boldsymbol{LV}_{11}^{(1)}(\phi) = 4DD_* \frac{\partial^2 \phi}{\partial z \partial Z} + 4 \frac{\partial^4 \phi}{\partial z^3 \partial Z} \tag{4.144}$$

$$\boldsymbol{LV}_{22}^{(1)}(v) = 2 \frac{\partial^2 v}{\partial z \partial Z} \tag{4.145}$$

$$\boldsymbol{LV}_{11}^{(1)}(\phi) = 2DD_* \frac{\partial^2 \phi}{\partial Z^2} + 6 \frac{\partial^4 \phi}{\partial z^2 \partial Z^2} \tag{4.146}$$

$$\boldsymbol{LV}_{22}^{(2)}(v) = \frac{\partial^2 v}{\partial Z^2} \tag{4.147}$$

## 4.B Boundary conditions

### 4.B.1 Case (III) of the base solution

In the case where the fluid is fully yielded in the annular space (case III of the base solution), appropriate boundary conditions come from the no-slip conditions at the wall :

$$\boldsymbol{u} = 0 \quad \text{at} \quad r = R_1, R_2 \,. \tag{4.148}$$

### 4.B.2 Case (II) of the base solution

In the case where we have a partially yielded fluid, i.e. a case (II) of base solution, the condition (4.148) is satisfied at the inner wall. However, the outer wall is no longer the boundary of the computational domain for the stability problem : it is the yield surface. The yield surface position has been perturbed from $R_0$ to

$$r = R_0 + \delta h_1 + \delta^2 \tilde{h}_2 + \delta^3 h_3 + O(\delta^4) \,. \tag{4.149}$$

Both continuity and yield conditions need to be evaluated at the perturbed yield surface, then linearized onto $r = R_0$.
The continuity of the velocity through the yield surface reads

$$[\boldsymbol{U}_b + \boldsymbol{u}] \left( \left[ R_0 + \delta h^{(1)} + \delta^2 h^{(2)} + \delta^3 h^{(3)} + ... \right]^- , z, t \right) = [\boldsymbol{U}_b + \boldsymbol{u}] \left( \left[ R_0 + \delta h^{(1)} + \delta^2 h^{(2)} + \delta^3 h^{(3)} + ... \right]^+ , z, t \right)$$

Here the superscripts $\pm$ indicate that the limit is taken from each side of the yield surface. The condition of the velocity continuity has to be linearized onto $r = R_0$. Note that we

retain the base flow in these expressions, since the base flow is discontinuous in its second derivative at the yield surface. By continuity from the outer wall, $\boldsymbol{u} = 0$ uniformly within the plug. On writting

$$\boldsymbol{u} = \delta \boldsymbol{u}_1 + \delta^2 \boldsymbol{u}_2 + \delta^3 \boldsymbol{u}_3 + ... \tag{4.151}$$

the following conditions on the primitive variables are derived at $r = R_0^-$

$$\boldsymbol{u}_1 = \boldsymbol{0}\,, \tag{4.152}$$
$$\boldsymbol{u}_2 = -h_1 \frac{\partial \boldsymbol{u}_1}{\partial r} - \frac{h_1^2}{2}\frac{d^2 V_b}{dr^2}\boldsymbol{e}_\theta \tag{4.153}$$
$$\boldsymbol{u}_3 = -h_1 \frac{\partial \boldsymbol{u}_2}{\partial r} - \tilde{h}_2 \frac{\partial \boldsymbol{u}_1}{\partial r} - \frac{h_1^2}{2}\frac{\partial^2 \boldsymbol{u}_1}{\partial r^2} - h_1 \tilde{h}_2 \frac{d^2 V_b}{dr^2}\boldsymbol{e}_\theta - \frac{h_1^3}{6}\frac{d^3 V_b}{dr^3}\boldsymbol{e}_\theta\,. \tag{4.154}$$

Additional compatibility conditions are also imposed at the yield surface. Indeed, due to the yield criterion, each component of the strain rate tensor of the perturbed flow vanishes at the yield surface. Expanding both about the base solution and about the base flow yield surface, we obtain the following hierarchical system of compatibility conditions :

$$\dot{\gamma}_{ij}(\boldsymbol{u}_1) = 0 \qquad ij \neq r\theta, \theta r \tag{4.155}$$
$$\dot{\gamma}_{ij}(\boldsymbol{u}_1) + h_1 \frac{\partial}{\partial r}\dot{\gamma}_{ij}(\boldsymbol{U}_b) = 0\,, \qquad ij = r\theta, \theta r\,, \tag{4.156}$$
$$\dot{\gamma}_{ij}(\boldsymbol{u}_2) + h_1 \frac{\partial}{\partial r}\dot{\gamma}_{ij}(\boldsymbol{u}_1) = 0\,, \qquad ij \neq r\theta, \theta r\,, \tag{4.157}$$
$$\dot{\gamma}_{ij}(\boldsymbol{u}_2) + h_1 \frac{\partial}{\partial r}\dot{\gamma}_{ij}(\boldsymbol{u}_1) + h_2 \frac{\partial}{\partial r}\dot{\gamma}_{ij}(\boldsymbol{U}_b) + \frac{h_1^2}{2}\frac{\partial^2}{\partial r^2}\dot{\gamma}_{ij}(\boldsymbol{U}_b) = 0 \qquad ij = r\theta, \theta r \tag{4.158}$$
$$\dot{\gamma}_{ij}(\boldsymbol{u}_3) + h_1 \frac{\partial}{\partial r}\dot{\gamma}_{ij}(\boldsymbol{u}_2) + h_2 \frac{\partial}{\partial r}\dot{\gamma}_{ij}(\boldsymbol{u}_1) + \frac{h_1^2}{2}\frac{\partial^2}{\partial r^2}\dot{\gamma}_{ij}(\boldsymbol{u}_1) = 0 \qquad ij \neq r\theta, \theta r \tag{4.159}$$
$$\dot{\gamma}_{ij}(\boldsymbol{u}_3) + h_1 \frac{\partial}{\partial r}\dot{\gamma}_{ij}(\boldsymbol{u}_2) + h_2 \frac{\partial}{\partial r}\dot{\gamma}_{ij}(\boldsymbol{u}_1) + \frac{h_1^2}{2}\frac{\partial^2}{\partial r^2}\dot{\gamma}_{ij}(\boldsymbol{u}_1) +$$
$$h_3 \dot{\gamma}_{ij}(\boldsymbol{U}_b) + h_1 h_2 \frac{\partial^2}{\partial r^2}\dot{\gamma}_{ij}(\boldsymbol{U}_b) + \frac{h_1^3}{6}\frac{\partial^3}{\partial r^3}\dot{\gamma}_{ij}(\boldsymbol{U}_b) = 0 \qquad ij = r\theta, \theta r \tag{4.160}$$

Combining the velocity continuity conditions (4.152-4.154) and yield conditions (4.155-4.160) leads to the following set of conditions at $r = R_0$ :

**At order** $\delta$

$$u_1 = v_1 = w_1 = 0\,, \tag{4.161}$$
$$\frac{\partial u_1}{\partial r} = \frac{\partial w_1}{\partial r} = 0\,, \tag{4.162}$$
$$\frac{\partial v_1}{\partial r} = -h_1 \frac{d^2 V_b}{dr^2}\,. \tag{4.163}$$

**At order $\delta^2$**

$$u_2 = 0\,, \tag{4.164}$$
$$v_2 = \frac{h_1^2}{2}\frac{d^2V_b}{dr^2}\,, \tag{4.165}$$
$$w_2 = 0\,, \tag{4.166}$$
$$\frac{\partial u_2}{\partial r} = -h_1\frac{\partial^2 u_1}{\partial r^2}\,, \tag{4.167}$$
$$\frac{\partial w_2}{\partial r} = -h_1\frac{\partial^2 w_1}{\partial r^2}\,, \tag{4.168}$$
$$\frac{\partial v_2}{\partial r} = -h_1\frac{\partial^2 v_1}{\partial r^2} - \tilde{h}_2\frac{d^2V_b}{dr^2} - \frac{h_1^2}{2}\frac{d^3V_b}{dr^3} \tag{4.169}$$

**At order $\delta^3$**

$$u_3 = \frac{h_1^2}{2}\frac{\partial^2 u_1}{\partial r^2}\,, \tag{4.170}$$
$$v_3 = \frac{h_1^2}{2}\frac{\partial^2 v_1}{\partial r^2} + \frac{h_1^3}{3}\frac{d^3V_b}{dr^3} + h_1\tilde{h}_2\frac{d^2V_b}{dr^2},, \tag{4.171}$$
$$w_3 = \frac{h_1^2}{2}\frac{\partial^2 w_1}{\partial r^2}\,, \tag{4.172}$$
$$\frac{\partial u_3}{\partial r} = -h_1\frac{\partial^2 u_2}{\partial r^2} - \tilde{h}_2\frac{\partial^2 u_1}{\partial r^2} - \frac{h_1^2}{2}\frac{\partial^3 u_1}{\partial r^3}\,, \tag{4.173}$$
$$\frac{\partial v_3}{\partial r} = -h_1\frac{\partial^2 v_2}{\partial r^2} - \tilde{h}_2\frac{\partial^2 u_1}{\partial r^2} - \frac{h_1^2}{2}\frac{\partial^3 u_1}{\partial r^3} - \frac{h_1\tilde{h}_2}{R_0}\frac{d^2V_b}{dr^2} - h_1\tilde{h}_2\frac{d^3V_b}{dr^3} - \frac{h_1^3}{6R_0}\frac{d^3V_b}{dr^3} \tag{4.174}$$
$$\frac{\partial w_3}{\partial r} = -h_1\frac{\partial^2 w_2}{\partial r^2} - \tilde{h}_2\frac{\partial^2 w_1}{\partial r^2} - \frac{h_1^2}{2}\frac{\partial^3 w_1}{\partial r^3} \tag{4.175}$$

## 4.C Contribution of nonlinear inertial and nonlinear viscous terms

The feedback of the mean flow correction and that of the first harmonic on the fundamental mode through the nonlinear inertial and nonlinear viscous terms are given in table 4.1.

| $B$ | $g_1$ | $g_1^I$ | $g_1^V$ | $g_{12}^I$ | $g_{12}^V$ | $g_{10}^I$ | $g_{10}^V$ | $g_{1-11}^V$ |
|---|---|---|---|---|---|---|---|---|
| 0.0 | -874.785 | -874.785 | 0 | -236.14 | 0 | -637.69 | 0 | 0 |
| 0.5 | -1061.4 | -1257.2 | 195.79 | -470.14 | 222.41 | -787.07 | 106.53 | -133.14 |
| 1.0 | -414.4 | -1781.5 | 1367.1 | -686.81 | 621.76 | -1094.6 | 1136.8 | -391.46 |
| 2.0 | -321.2 | -2837 | 2515.8 | -944.78 | 1138.3 | -1892.3 | 2133.1 | -755.58 |
| 3.0 | -186.9 | -3865.4 | 3678.5 | -1168.3 | 1669.3 | -2697.1 | 3150.9 | -1141.7 |
| 4.0 | -34.2 | -4893.1 | 4858.9 | -1374 | 2219.4 | -3519.1 | 4188.9 | -1549.5 |
| 5.0 | 127.1 | -5929.5 | 6056.6 | -1568.8 | 2789.2 | -4360.7 | 5244.7 | -1977.3 |
| 6.0 | 290.9 | -6979.2 | 7270.1 | -1756 | 3377.7 | -5223.2 | 6315.6 | -2423.3 |
| 7.0 | 459.7 | -8041.9 | 8501.6 | -1938.9 | 3986.3 | -6103 | 7402.1 | -2886.8 |
| 8.0 | 623.2 | -9121.9 | 9745.1 | -2117.6 | 4611.7 | -7004.3 | 8498.8 | -3365.5 |
| 9.0 | 790 | -10216 | 11006 | -2294.2 | 5255.6 | -7922.3 | 9609.4 | -3859.4 |
| 10.0 | 952 | -11327 | 12279 | -2469 | 5916.6 | -8857.7 | 10729 | -4366.9 |

TABLE 4.1 – The first Landau constant $g_1$ and the contributions of nonlinear inertial and nonlinear viscous terms for different values of the Bingham number. The radius ratio $\eta = 0.5$.

## Bibliographie

[1] P. Coussot. Saffman-Taylor instability in yield-stress fluids. *J. Fluid Mech.*, 300 :363–376, 1999.

[2] R. B. Bird, G. C. Daii, and B. J. Yarusso. The rheology and flow of viscoplastic materials. *Rev. Chem. Eng.*, 1 :1–110, 1983.

[3] N.J. Balmforth, I.A. Frigaard, and G. Ovarlez. Yielding to stress : recent developments in viscoplastic fluid mechanics. *Annu. Rev. Fluid Mech.*, 46 :121–146, 2014.

[4] P. Coussot. Bingham's heritage. *Rheol. Acta*, 56(3) :163–176, 2017.

[5] D. Bonn, M. Denn, L. Berthier, T. Divoux, and S. Manneville. Yield stress materials in soft condensed matter. *Rev. Mod. Phys.*, 89(3) :035005, 2017.

[6] W.P. Graebel. Stability of a Stokesian fluid in Couette flow. *Phys. Fluids*, 4(3) :362–368, 1961.

[7] M.P. Landry, I.A. Frigaard, and D.M. Martinez. Stability and instability of Taylor–Couette flows of a Bingham fluid. *J. Fluid Mech.*, 560 :321–353, 2006.

[8] J. Peng and K-Q. Zhu. Linear stability of Bingham fluids in spiral Couette flow. *J. Fluid Mech.*, 512 :21–45, 2004.

[9] Y. Agbessi, B. Alibenyahia, C. Nouar, C. Lemaitre, and L. Choplin. Linear stability of Taylor–Couette flow of shear-thinning fluids : modal and non-modal approaches. *J. Fluid Mech.*, 776 :354–389, 2015.

[10] C. Chen, Z-H. Wan, and W-G. Zhang. Transient growth in Taylor-Couette flow of a Bingham fluid. *Phys. Rev. E*, 91(4) :043202, 2015.

[11] J. Jeng and K.Q. Zhu. Numerical simulation of Taylor Couette flow of Bingham fluids. *J. Non-Newtonian Fluid Mech.*, 165(19-20) :1161–1170, 2010.

[12] T.C. Papanastasiou. Flows of materials with yield. *J. Rheol.*, 31(5) :385–404, 1987.

[13] I.A. Frigaard, S.D. Howison, and I.J. Sobey. On the stability of Poiseuille flow of a Bingham fluid. *J. Fluid Mech.*, 263 :133–150, 1994.

[14] I. Frigaard and C. Nouar. On three-dimensional linear stability of Poiseuille flow of Bingham fluids. *Phys. Fluids*, 15(10) :2843–2851, 2003.

[15] C. Nouar, N. Kabouya, J. Dusek, and M. Mamou. Modal and non-modal linear stability of the plane Bingham–Poiseuille flow. *J. Fluid Mech.*, 577 :211–239, 2007.

[16] P.J. Schmid and D.S. Henningson. *Stability and transition in shear flows*, volume 142. Springer Science & Business Media, 2000.

[17] M.P. Landry. *Taylor-Couette instability of a Bingham fluid*. PhD thesis, University of British Columbia, 2003.

[18] S. Topayev, C. Nouar, D. Bernardin, A. Neveu, and S.A. Bahrani. Taylor-vortex flow in shear-thinning fluids. *Phys. Rev. E*, 100(2) :023117, 2019.

[19] L. N. Trefethen. *Spectral methods in MATLAB*. SIAM, 2000.

[20] P.K. Sen and D. Venkateswarlu. On the stability of plane Poiseuille flow to finite-amplitude disturbances, considering the higher-order landau coefficients. *J. Fluid Mech.*, 133 :179–206, 1983.

[21] M. Bouteraa, C. Nouar, E. Plaut, C. Métivier, and A. Kalck. Weakly nonlinear analysis of Rayleigh–Bénard convection in shear-thinning fluids : nature of the bifurcation and pattern selection. *J. Fluid Mech.*, 767 :696–734, 2015.

[22] T. Herbert. Nonlinear stability of parallel flows by high-ordered amplitude expansions. *AIAA Journal*, 18(3) :243–248, 1980.

[23] T. Herbert. On perturbation methods in nonlinear stability theory. *J. Fluid Mech.*, 126 :167–186, 1983.

[24] S. Constantinou Generalis and K. Fujimura. Range of validity of weakly nonlinear theory in the Rayleigh–Bénard problem. *J. Phys. Soc. Japan*, 78(8) :084401, 2009.

[25] B. Dubrulle and F. Hersant. Momentum transport and torque scaling in Taylor-Couette flow from an analogy with turbulent convection. *Eur. Phys. J-B*, 26(3) :379–386, 2002.

[26] B. Eckhardt, S. Grossmann, and D. Lohse. Torque scaling in turbulent Taylor–Couette flow between independently rotating cylinders. *J. Fluid Mech.*, 581 :221–250, 2007.

# Discussion, conclusion and future perspectives

In this work the stability of Taylor-Couette flow in Newtonian and non-Newtonian fluids is studied. A configuration with a wide gap $\eta = 0.4$ is mainly considered. Theoretical, numerical and experimental approaches are used to characterize the flow structure at various Reynolds numbers. From theoretical point of view using linear and weakly-nonlinear analysis the critical conditions and description of the flow structure near the onset of the primary bifurcation are given in the Chapter II. By assuming a purely viscous fluid, the influence of shear-thinning behavior on the primary bifurcation and on the flow structure is analyzed and compared to the Newtonian fluid. The rheological behavior of the fluid is characterized by the Carreau model. Additional nonlinearities coming from the rheology of the shear-thinning fluid are introduced through an amplitude expansion of Stuart-Landau method up to the seventh order.

The critical Reynolds/wave numbers obtained from the linear stability analysis using zero shear-rate viscosity as reference is strongly decreased/increased for a stronger shear-thinning fluid. The critical Reynolds numbers of Newtonian fluid for a different radius ratio $\eta$ are compared with Chandrasekhar's results [1]. Similar comparison for the shear-thinning fluids with various rheological parameters are done with results of Alibenyahia et al.[2]. For both Newtonian and shear-thinning cases a very good agreement was found. By using a weakly nonlinear analysis the changes in the flow structure in the case of shear-thinning fluids have been stressed at Reynolds number $Re$ slightly above the onset of the TVF regime. It was observed that by increasing the strength of shear-thinning behavior the Taylor vortices are shifted towards inner cylinder and by increasing Reynolds number towards the outflow boundaries. The asymmetry between the radial outflow and inflow, that was noted in the literature by Escudier et al. [3], was also observed and it was found a faster increase of the strength of the radial outflow comparatively to the radial inflow. As a consequence of this imbalance the area of the inflow region accordingly increases. For stronger shear-thinning fluids these changes are amplified. The ratio of the dimensionless torque $G$ to the dimensionless torque of the laminar flow $G_b$ called in literature as pseudo-Nusselt number $Nu_*$ is calculated and it was found that $Nu_*$ decreases with increasing shear-thinning effects. These results of $Nu_*$ for Newtonian fluid was compared with that obtained by Donnely & Simon [4]. Again, a good agreement is found. Similar analysis

has been also done for a narrow system with $\eta = 0.9$. It was discussed briefly, since for a narrow system it is well known that the range of Reynolds number at which the Taylor vortices are stable is strongly limited. An instability due to the azimuthal perturbation appears early. This case can be as well characterized by practically linear variation of the azimuthal velocity and quite weak viscosity stratification.

On the other hand the experimental and numerical approaches are used and some results are given in Chapter III. From experimental point of view the visualization experiments and PIV measurements have been done for aqueous solution of glycerol (Newtonian) and aqueous solutions of xanthan gum (shear-thinning) with different concentrations. The rheological behavior of these fluids are given through the Carreau model. An increase of strength of shear-thinning behaviors can be given through decrease of shear-thinning index $n_c$ and increase of the characteristic time $\lambda$. Several sets of experiments are done for Newtonian fluids and shear-thinning fluids varying the concentration of the xanthan gum solution. Beside the fact, that a large number of different concentration of xanthan gum solution was analyzed, in Chapter III only three concentration of 1000, 2000 and 3000 ppm are given to describe the shear-thinning properties. This layout of Chapter III was selected to avoid repetition and representation of unnecessary figures. According recent results of Lacassagne et al. [5] it is believed that for the aqueous solution of xanthan gum the shear-thinning properties dominate over the elastic properties. It means that the origin of secondary instabilities observed are due to the shear-thinning behaviors. The Newtonian fluid was firstly used as a reference fluid to validate the experimental setup. Nevertheless, new results for Newtonian fluid were obtained. By increasing the Reynolds number $Re$ the circular Couette flow bifurcates to a Taylor-Vortex flow and then at sufficiently higher Reynolds number $Re \approx 5.3Re_c$ to a Wavy-Vortex flow as it was observed previously by several authors for a various systems. It was found that the WVF regime could be divided on WVF I, which can be characterized through a weak oscillation of the outflow region and more significant oscillation of the inflow zone, and WVF II with a higher oscillation amplitude and fluid transfer from one vortex to another. It was noted in Chapter III.

At the second step, the shear-thinning fluid is studied. First, the critical conditions are compared with that obtained theoretically ; the relative difference did not exceed more than 2%. The range of stable TVF regime becomes narrower with increase of the shear-thinning behaviors. For a weakly shear-thinning fluid with shear-thinning index $n_c \approx 0.5$ at Reynolds number $Re \approx 1.7Re_c$ the vortices becomes unstable. Repetitive creation and merging processes occurs at different positions along all the height of the annular gap. The number of these processes of creation/merging increases with increase of the Reynolds number. Similar transition to the unstable regime was observed for stronger shear-thinning fluids. For instance, for the strongest shear-thinning fluids discussed in this thesis with $n_c \approx 0.23$ the first process of creation/merging was observed at $Re = 1.02Re_c$. For a larger Reynolds number the number of such changes of the flow structure increases leading to a more complex flow regime.

Numerical analysis was done using partial differential equation solver Freefem++ as-

suming purely viscous fluid. Two cases were introduced : a weakly shear-thinning with $n_c = 0.5$ and sufficiently strong shear-thinning with $n_c = 0.2$. Qualitatively, similar results have been found. The same continuous creation/merging processes were observed and the oscillation of the torque acting on the inner wall was noted. For numerical results a good agreement was found for a critical conditions of the primary bifurcation. The Reynolds number at which the secondary instabilities were first observed is slightly altered because of the difference in the rheology of the fluids used. The possible physical mechanism of the secondary instability observed for a shear-thinning fluids as well as more detailed analysis and some validation of the results were given in Chapter III. To sum up, the origin of the secondary instability comes from an axial perturbation, since the system remains axisymmetric.

It is important to note that for visualization experiments the "Taylor-like" structures were observed at Reynolds number $Re < Re_c$ for shear-thinning fluids. These structures have no effect on the primary bifurcation, since a good agreement with theoretical results and no effect on the secondary instabilities was found. It was found that the origin of these structures is related to the shape of the particles used, since the PIV measurements show purely azimuthal flow at Re below $Re_c$.

The Chapter IV presents the beginning of the theoretical approach to the shear-thinning fluid with a yield-stress. The rheology of such fluids is characterized by the Bingham model. Again the linear stability analysis is done and the values of the critical conditions were compared with the literature. A good agreement is found. A weakly nonlinear analysis has been also performed taking into account the fast and slow modulation of the variables, resulting in the Ginzburg-Landau amplitude equation. The first Landau constant has been obtained. It is found that by increasing the Bingham number $B$ the first Landau constant $g_1$ decreases until certain value of $B \approx 0.6$ and then it starts to increase and reaches a positive value at $B > 4$. The positive Landau constant means that the nonlinear viscous terms dominate over the nonlinear inertia terms. It can be concluded that for the case with $B > 4$ the bifurcation to the TVF regime is subcritical. Similarly as for the Chapter II the flow structure near the onset of the TVF is discussed. It is found that since the yield zone enlarges with the increase of Bingham number $B$, the vortices are shifted towards inner wall. The shape of the interface of static zone is also briefly discussed. Finally, the pseudo-Nusselt number $Nu^*$ has been calculated. A non monotonic variation of the $Nu^*$ with increase of the Bingham number $B$ is found : in the case of fully yielded flow, the $Nu^*$ decreases and in the case, when the flow is partially yielded, the $Nu^*$ increases. Probably, this is due to the low viscosity at the inner wall. We believe, that this chapter expanded for a higher order can become a basis for the future research on the yield-stress fluids.

During research some points were not very clear, which require additional investigations. Several points can be explored in a future :

-In a short term, (i) the influence of the concentration of the particles used for the visualization experiments on the primary and secondary bifurcation of the flow should be

investigated ; (ii) experimental analysis with both visual and torque measurements may give more details how secondary instabilities in the case of shear-thinning fluids act.

-In a middle term, (ii) experimental study of Bingham fluids with different strength, as well as extending the weakly nonlinear analysis to a higher order are required.

-In a long term, (iii) the competition between the non axisymmetric azimuthal perturbation and axisymmetric axial perturbation in the case of moderate radius ratio $\eta$ for the shear-thinning fluids can be explored.

## Bibliographie

[1] S. Chandrasekhar. *Hydrodynamic and hydromagnetic stability.* Dover Publications, 1981.

[2] B. Alibenyahia, C. Lemaître, C. Nouar, and N. Ait-Messaoudene. Revisiting the stability of circular Couette flow of shear-thinning fluids. *J. Non-Newtonian Fluid. Mech.*, 183 :37–51, 2012.

[3] M. P. Escudier, I. W. Gouldson, and D. M. Jones. Taylor vortices in Newtonian and shear-thinning liquids. *Proc. Roy. Soc. Lond. A.*, 449 :155–176, 1995.

[4] R.J. Donnelly and N.J. Simon. An empirical torque relation for supercritical flow between rotating cylinders. *J. Fluid Mech.*, 7(3) :401–418, 1960.

[5] T. Lacassagne, N. Cagney, J. Gillissen, and S. Balabani. Vortex merging and splitting : A route to elastoinertial turbulence in Taylor-Couette flow. *Phys. Rev. Fluids*, 5(11) :113303, 2020.

## Écoulement de Taylor-Couette pour des fluides complexes.

On s'intéresse aux instabilités secondaires dans un écoulement de Taylor-Couette en grand entrefer pour un fluide rhéofluidifiant. Des études théorique, expérimentale et numérique ont été mises en œuvre. D'un point de vue théorique, une analyse faiblement non linéaire a été développée en régime dit TVF (Taylor Vortex Flow) pour rendre compte des premiers effets de la non linéarité de la loi de comportement sur la structure de l'écoulement. Le comportement rhéologique du fluide est décrit par le modèle de Carreau. Des effets significatifs du caractère rhéofluidifiant ont été mis en évidence : Les rouleaux de Taylor ont une taille plus petite et sont écrasés contre le cylindre intérieur. Le jet radial sortant est plus fin et beaucoup plus intense que le jet radial entrant. Par conservation de débit, la zone de jet radial entrant est plus étendue. Ces modifications sont probablement à l'origine des instabilités des rouleaux de Taylor observées expérimentalement et numériquement. Le dispositif expérimental utilisé est constitué de deux cylindres coaxiaux, où le cylindre intérieur est en rotation et le cylindre extérieur est fixe. Le rapport des rayons est $\eta = 0.4$ et le rapport d'aspect $L = 32$. Les fluides utilisés sont des solutions de xanthane à différentes concentrations ainsi qu'une solution de glycérole, comme fluide newtonien de référence. La structure de l'écoulement est déterminée par visualisation et par mesures de vitesse par PIV 2D. Pour la solution de glycérole, après la bifurcation primaire à $Re = Re_c$, le régime TVF stationnaire reste stable jusqu'à pratiquement $7Re_c$. A partir de cette dernière valeur, les rouleaux de Taylor perdent leur stabilité vis-à-vis de perturbations azimutales. Dans le cas des solutions de xanthane, les valeurs du nombre de Reynolds à partir desquelles, les rouleaux de Taylor apparaissent sont en accord avec la théorie linéaire comme dans le cas Newtonien. En augmentant le nombre de Reynolds, les rouleaux de Taylor deviennent instables, mais cette-fois-ci vis-à vis de perturbations axiales. Ces instabilités peuvent être considérées comme des instabilités d'Eckhaus généralisées. Elles se caractérisent par un processus récurrent de création et d'appariement de rouleaux. L'augmentation du nombre de sites où se produit ce processus conduit à un écoulement chaotique (turbulence de phase). Il convient de noter que plus les effets rhéofluidifiants sont importants, et plus la gamme de Re où le régime TVF est stable, est réduite. Ces résultats ont été confirmés par une simulation numérique 2D des équations de conservation instationnaires, en utilisant le solveur de FreeFem++. Le cas des fluides rhéofluidifiants avec seuil de contrainte a été entamé , en se focalisant sur le cas particulier où il existe une zone non-cisaillée attachée au cylindre extérieur.

**Mots clés :** Fluide rhéofluidifiant, Taylor-Couette, instabilité secondaire.

# Abstract

This work deals with secondary instabilities in a Taylor-Couette flow with a wide gap in the case of shear-thinning fluids. Theoretical, experimental and numerical approaches are used. From theoretical point of view, a weakly nonlinear analysis has been done to account for the nonlinear effects of constitutive law on the flow structure of the Taylor Vortex Flow (TVF) regime. The shear-thinning behavior of the fluid are characterized by the Carreau model. Significant effects of shear-thinning have been demonstrated : Taylor vortices are smaller in size and shifted toward the inner cylinder. The radial outflow jet is thinner and stronger than the radial inflow jet. This asymmetry leads to an increase of the radial inflow zone. These changes in the flow structure are probably the origin of the secondary instabilities of Taylor vortices observed experimentally and numerically. The experimental setup consist of two coaxial cylinders where the inner cylinder is rotating and the outer one is at rest. The radius ratio is $\eta = 0.4$ and the aspect ratio is $L = 32$. The fluids used are aqueous xanthan gum solutions at different concentrations and aqueous glycerol solution as a reference Newtonian fluid. The flow structure is analyzed through the visualization and by the 2D PIV velocity measurements. For the aqueous glycerol solution, once the primary bifurcation is reached at $Re = Re_c$, the stationary TVF regime remains stable up to practically $Re = 7Re_c$. From this values the Taylor vortices lose its stability with respect to azimuthal disturbances. In the case of the aqueous xanthan gum solutions the values of the Reynolds number from which the Taylor vortices appear are in agreement with a linear theory as for the case of Newtonian fluid. By increasing the Reynolds number, the Taylor vortices become unstable, but with respect to axial disturbances. There instabilities can be considered as generalized Eckhaus instabilities. They are characterized by the continuous processes of creation and merging of vortices. The increase in the number of axial positions where these processes occur leads to the chaotic flow (phase turbulence). It should be noted that the stronger shear-thinning effects, the smaller the range of stable TVF regime. These results have been confirmed by a 2D numerical simulation of unsteady conservation equations, using PDE solver Freefem++. The case of shear-thinning with a stress-yield was started as well, focusing on the particular case when the unyielded zone is attached to the outer cylinder.



**Keywords :** Shear-thinning, Taylor-Couette, secondary instability